Development of Fibre Optic Evanescent-Wave Fluorescence-Based Sensors

By

David Gerard O'Keeffe B.Sc. (Hons)

A thesis presented

to

Dublin City University

For the degree of Doctor of Philosophy

March 1995

School of Physical Sciences

Dublin City University

Ireland

I hereby certify that this material, which I now submit for assessment on the programme of study leading to the award of Doctor of Philosophy is entirely my own work and has not been taken from the work of others save and to the extent that such work has been cited and acknowledged within the text of my work.

Signed: Gerard Keeffe Date: 4/8/'95

Dedication

To Mom and Katie - the two women in my life!

Acknowledgements

I want to thank Cork County Council, who by providing me with six years of funding made my college years much more bearable than most. I also want to thank Sieger Ltd, Poole, United Kingdom who financed the final years of my post-graduate years and who also afforded me the opportunity of industrial experience, during the summer months of 1994.

The 3½ years that I've spent in the School of Physical Sciences, Dublin City University has been a very enjoyable time. I want to take this opportunity to thank all those people, who by their enthusiasm or help in any way, made this thesis possible. In particular, I want to thank the following Dr. Rob Van Ewyk, Thomas Butler, Fidelma Sheridan, Marian Shortt, Tom Murphy, Dr. Colette McDonagh, Aisling McEvoy, John Maguire, Kay Davin, Dr. Brian Lawless, Fergal McAleavey, Katie Curtin, Dr. Vincent Ruddy, 'The Judester', Des Lavelle, Dr. Fergus Connolly, Jackie McLaughlin, Dr. Padraig McHale, 'The Bird', Dr. Simon McCabe, Teresa McCormack, Fergal Clark, Dr. Han Vos, the optical sensors group, the sol-gel group, the technical staff, my family and friends.

Finally, and most importantly, I want to thank the person who made it all possible - Dr. Brian MacCraith. I'll always be in debt to you Brian!

Abstract

The development of a fibre optic oxygen sensor based on the fluorescence quenching of ruthenium complexes entrapped in a sol-gel-derived microporous silica film is presented. The sensor is based on evanescent wave excitation of the sol-gel film which is coated on a declad portion of optical fibre. Theoretical considerations concerning the efficiency of evanescent wave excitation of fluorescence and its collection are discussed in detail. Experimental measurements which investigate these predictions are presented. The principles of fluorescence quenching are outlined and sensing based on measuring fluorescence intensity or fluorescence decay time are described. In particular the advantages of the phase fluorimetric method of decay time monitoring are highlighted. The ruthenium complex [Ru^{II}-tris(4,7-diphenyl-1,10-phenantroline)] was chosen for this work and was immobilised in a microporous glass, produced by the low temperature sol-gel process. The advantages of using this method of reagent capture are explained and the method of sensor fabrication described. A number of experimental systems have been employed. The progress from an air-cooled argon-ion laser/PMT characterisation system to a compact LED/photodiode system is detailed. The oxygen sensor was found to exhibit fast response times of less than 5 seconds, high sensitivity to oxygen and good repeatability. Sensor response, including dependence on oxygen concentration, temperature and humidity are discussed and the viability of manufacturing this type of sensor as an industrial product is examined. In addition, related work leading to the development of fluorescence-based evanescent-wave immunosensor is presented. Lactate dehydrogenase, a clinically important diagnostic marker enzyme, is detected in concentrations as low as 30ng/ml.

Table of Contents

Chapter One - Introduction

1.1 Introduction

The word 'sensor' is derived from *sentire* meaning 'to perceive'. A sensor is a device capable of continuously recording a physical parameter or the concentration of a chemical or biochemical species. The industrial field has always been dependent on sensors for the measurement of physical parameters. For this reason, the technology of sensors and transducers has a long tradition. Wilhelm Von Siemens built one of the first sensors in 1860, when he made use of the temperature dependence of a resistor made of copper wire for temperature measurements. Between 1920 and 1940, the intensive expansion of large scale processes created problems in measurement and control technology. However, the development of semiconductor technology in the 1950's enabled electronic signal processing and control techniques to be established. Since this time the sensor market has thrived.

A sensor provides a usable output in response to a specified measurand. In terms of analogue and digital electronic instrumentation, a usable output has to be some form of electrical signal which lends itself to digital processing or data acquisition. It is generally the case that the specified measurand is inherently different from the desired output signal. Thus to convert the former quantity to the latter, at least one transduction principle is required to make the sensor work. The sensing process can be explained in terms of conversion of energy from one form to another as illustrated in figure 1.1. These transduction principles are physical or chemical effects. In 1984, Schubert compiled a dictionary containing more than 350 such *effects* [1]. It is convenient to group these effects in terms of the form of energy in which the signals are received and generated. The six classes of signals with some examples are shown in table 1.1.

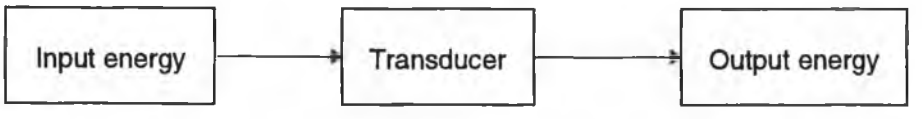

figure 1.1 The sensing process

Energy	Sensing parameter
Mechanical	length, area, volume, force, pressure, acoustic wavelength and intensity
Thermal	temperature, entropy, heat flow, conduction
Electrical	voltage, current, charge, resistance, capacitance, polarization, electric field
Magnetic	field intensity, flux density, magnetic moment, permeability
Chemical	composition, concentration, reaction rate, pH
Radiant	intensity, phase, wavelength, polarization, fluorescence lifetime, fluorescence, reflectance, transmittance, refractive index

table 1.1 Sensing parameters associated with various energy forms.

The classification of sensors may also be achieved using the energy labels of table 1.1. In recent years there has been considerable emphasis on research and development of sensing techniques based on radiant or optical effects. Optical sensors have many operational advantages over other methods. These advantages include:

i) Optical sensors do not present a significant risk of sparking, and are therefore more suitable for use in potentially explosive areas e.g. mining and petroleum industries.

ii) Because the primary signal is optical, it is generally not subject to electrical interference.

iii) Analysis may be performed in real-time.

iv) The ability to measure the radiant parameters listed in table 1.1, offers an extensive range of possible measurands e.g. position, temperature, chemical composition, sound, radiation, vibration, electric and magnetic fields

v) As well as the ability to carry out point sensing, optical sensors offers the ability to perform open path sensing. This offers advantages in certain applications including a reduction in maintenance and installation costs.

vi) The ability to use optical fibres in conjunction with optical sensors offers the possibility of miniaturisation, remote sensing, distributed sensing, invasive sensing as well as many other advantages inherent in optical fibre use (see section 1.2).

However, optical sensors are not without some disadvantages, among which are the interference of ambient light, the lack of light sources in the UV to IR spectrum, and the expense of certain optical components. In the specific case of optical chemical sensors, disadvantages may also include the ability to successfully immobilise reagents, the long term instability due to reagent washout or photobleaching and the lack of selective indicators for various analytes of interest. Despite these and other limitations, optical sensors have the potential of becoming an attractive alternative to other sensing methods and to perform diagnostic, environmental, or clinical functions better, faster, more accurately, and less expensively than existing approaches.

1.2 Optical fibre sensors

The availability of optical fibres has had a significant impact on some scientific disciplines including that of optical sensing. Optical fibres became widely available for use, as an offshoot of the communications industry which emerged in the late 1960's. An optical fibre is a thin low loss glass rod, in which total internal reflection of a beam of light entering at one end, causes the beam to be transmitted completely along the fibre. Step index fibres consist of a core of refractive index n_1, surrounded by a cladding of lower refractive index n_2, as illustrated in figure 1.2. Several other new technologies have accelerated the development of fibre optic sensing. Lasers are now available for routine applications, the range of light emitting diodes (LED's) covers the 400 to 1000nm spectrum with some also available in the mid-IR. Photodetectors and amplifiers have

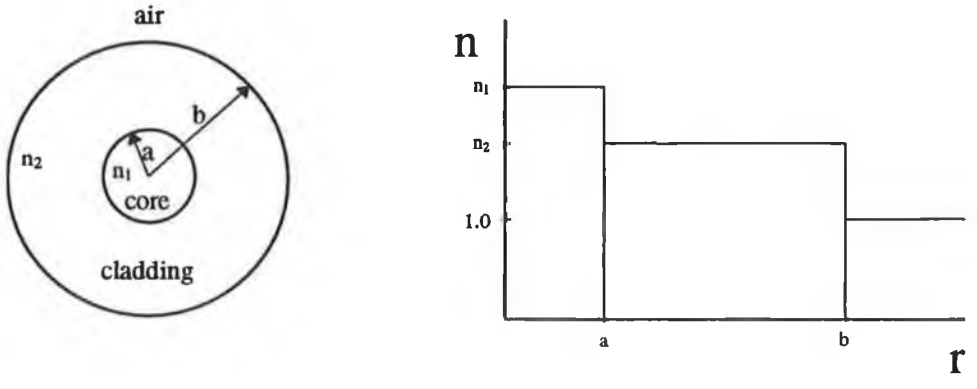

figure 1.2 Variation of the index of refraction n with the radius r of an optical fibre

become routinely available at low prices. Optical fibres are ideal for sensor systems because they are immune to electromagnetic interference that is present in the industrial environment. Among the advantages of using optical fibres for sensing purposes are that they are easy to install, they are non electrical, small in size and can be interfaced with data communications systems if required.

Fibre optic sensors can be divided into two basic categories: phase-modulated and intensity modulated sensors [2]. Intensity modulated sensors detect a change in the amount of light that is a function of a perturbing environment as illustrated in fig 1.3(a). The change in the amount of light can be associated with transmission, reflection, absorption, scattering or fluorescence within the fibre. Phase modulated sensors have attracted considerable research attention because of the extremely high sensitivity achievable using this approach. Generally, the sensor employs a coherent laser light source and two single mode fibres. The light from the laser is then split as illustrated in figure 1.3(b) and launched into each fibre. If a measurand perturbs one fibre relative to the other, a phase shift occurs that can be detected very precisely. The four better known interferometric configurations are the Mach-Zehnder, the Michelson, the Fabry Perot and the Sagnac.

Optical fibre chemical sensors, which are sensors based on the detection and determination of chemical species combine the advantage of the optical fibers with the specificity of chemical reagents for the analyte species of interest. A thorough review of optical fibre chemical sensors has been carried out by Wolfbeis [3,4]. Optical fibre chemical sensors may be categorised as intrinsic or extrinsic sensors. An extrinsic fibre sensor uses the optical fibre purely as an optical signal carrier and often requires coupling optics to interact with the optical sensing device. Extrinsic fibre optic chemical sensors have been designed to measure or detect temperature [5], oxygen [6], pH [7], as well as many other chemicals. An intrinsic optical fibre chemical sensor on the other hand, is one in which the light is perturbed within the fibre, by the parameter to be measured. The

fibre itself is an integral part of the sensing device. Diagrammatic representations of both an intrinsic and extrinsic fibre optic chemical sensor are shown in figure 1.4. Examples of intrinsic fibre optic chemical sensors are i) refractometric sensors which can be used to measure e.g. liquid levels, concentration of dissolved solids or the moisture content of skin [8], ii) core-based sensors developed to sense e.g. relative humidity [9] and ammonia [10], and iii) evanescent wave sensors [4, 11]. Evanescent-wave interactions forms the basis of the work described in this thesis.

The evanescent wave is a consequence of total internal reflection and can be generated at the interface between any two dielectric materials such as the core/cladding interface of an optical fibre. The motivation for using the evanescent wave approach in fibre optic sensing, is derived from a number of advantages offered by the technique in

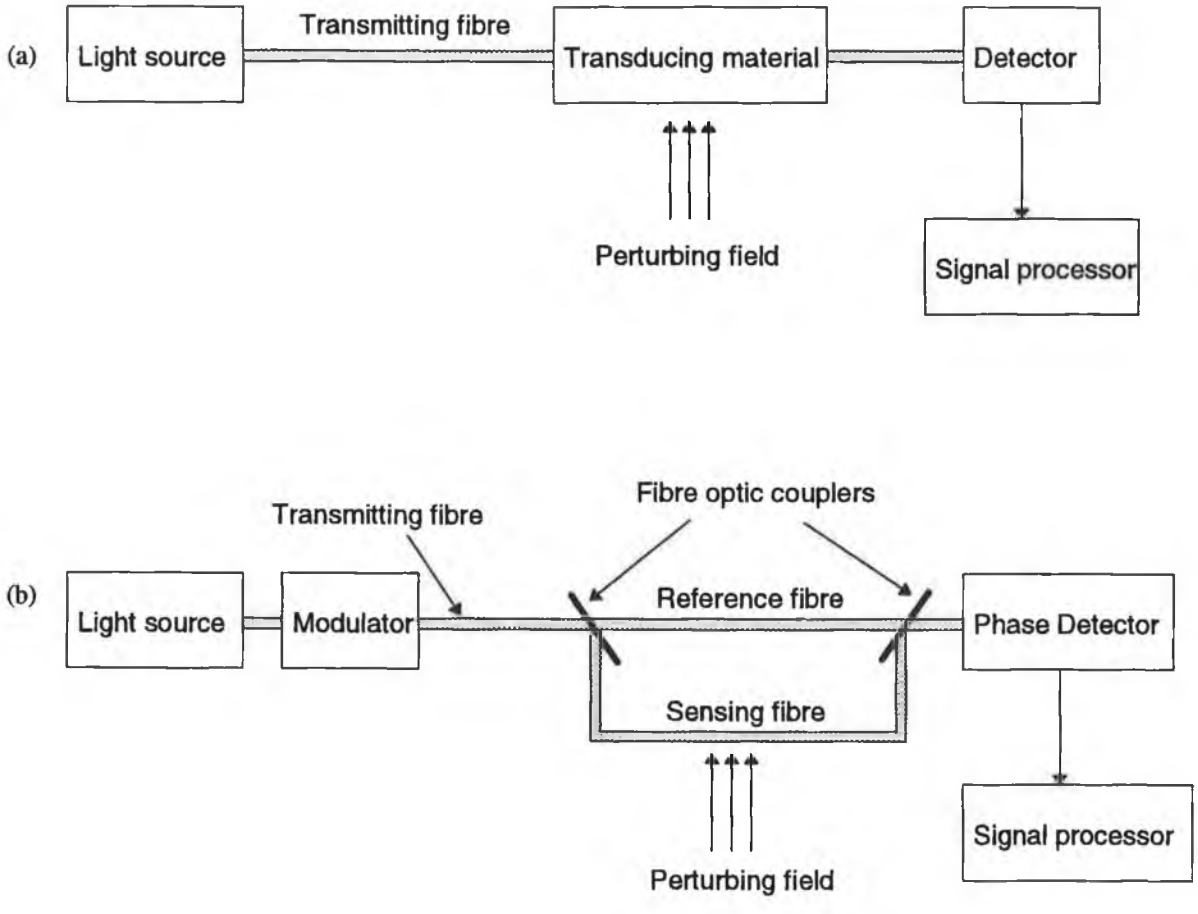

figure 1.3 (a) Intensity sensor (b) phase modulated sensor

particular applications [10]. These advantages include: i) the absence of coupling optics, ii) the confinement of the evanescent field to a short distance from the guiding interface thereby enabling discrimination to a large extent between surface and bulk effects, iii) the possibility of carrying out full or quasi-distributed sensing, iv) the ability to control interaction parameters such as interaction length, sensing volume and response time. Evanescent-wave spectroscopy is treated in detail in chapter 2.

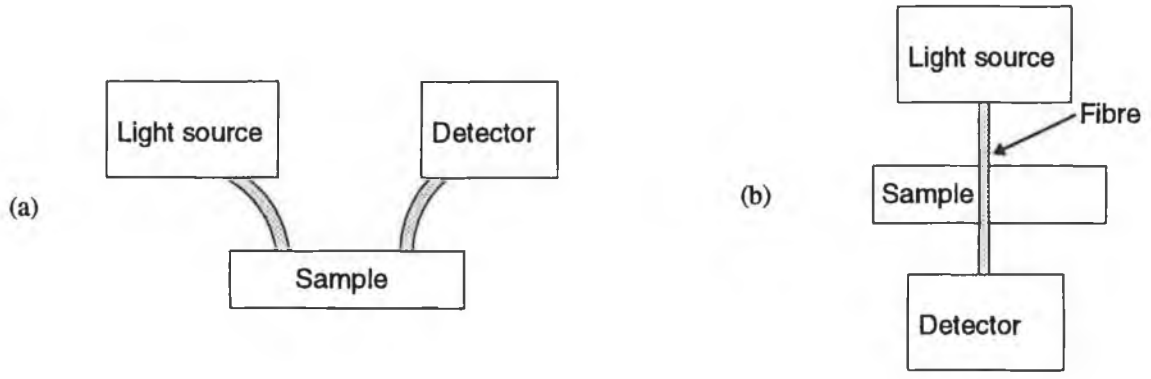

figure 1.4 (a) Extrinsic and (b) Intrinsic fibre optic chemical sensors

1.3 Oxygen sensing

The principal gas hazards encountered in confined places, mining tunnels and heavy industries are a lack of oxygen, and the presence of flammable or toxic gases. In the industrial sector, oxygen detection is important both for anaerobic processing and for quality control (e.g., for monitoring combustion efficiency in car engines [12]). The detection of molecular oxygen, both gaseous and in solution is also of great importance for environmental and biomedical analysis. In the environmental field the concentration of dissolved oxygen in surface water is directly related to the presence of phosphates and nitrates, so that its measurement can give an estimate of pollution of the ecosystem. In the biomedical field, the measurement of the oxygen partial pressure of blood allows the diagnosis of pulmonary diseases and diseases of the respiratory system. Its monitoring is also very important during surgical operations. Moreover, by oxygen measurements it is possible to detect, in an indirect way, many important physiological parameters, such as glucose [13], cholesterol [14], and lactate [15].

The main criteria required for an oxygen gas sensing device may be summarised as follows:

i) Regions of interest in oxygen gas sensing include the 17% to 23% region important for personal monitoring systems. Normal oxygen concentration in the air is 20.9%. Oxygen deficiency is a cause of death resulting in the importance of providing an alarm before oxygen levels become too low. *Crowcon Detection Instruments* provide an alarm at 18% - 19% since at oxygen levels below 17% abnormal behaviour is likely to occur [16]. The enrichment of oxygen in the atmosphere is also dangerous. Oxygen becomes toxic at high concentrations and the flammability of materials also increases. High oxygen concentration alarm level is normally 23% [16]. Other oxygen concentrations of interest include the 0% to 5% range required for monitoring anaerobic processes and the 95% to 100% range which is important for aerobic processes. However, there also exists the necessity for sensing oxygen concentrations other than these regions for specific industrial processing requirements. In most applications the oxygen sensing device would require a measurement accuracy of at least 0.5% of oxygen concentration.

ii) Fast response times of the order of a few seconds are required, especially for the personal monitoring system. Commercial literature for a *Citicel* electrochemical oxygen cell quotes a response time of >20secs, for a 95% signal response in the 0% to 25% range [17].

iii) A problem with many types of sensors is their lack of immunity to ambient temperature variation. *Citicel* quotes a 0.2% signal change per degree Celsius in the temperature range from -15°C to +40°C for a specific oxygen sensing electrochemical cell.

iv) The response of the sensor should be independent of the presence of other gases. CO_2 is a particular problem in the case of electrochemical cells as described below.

v) The sensor response should be repeatable with oxygen concentration, exhibiting high long term stability, resulting in ease of sensor calibration.

vi) Fabrication of the sensing device should be compatable with large scale manufacturing.

One of the most common laboratory methods of measuring dissolved oxygen concentration is the Winkler method [18]. The sample being tested is treated with an

excess of manganese(II), potassium iodide and sodium hydroxide. Manganese(II) hydroxide is formed and reacts with the dissolved oxygen to give manganese (III). When acidified, the manganese(III) oxidises iodide to iodine. The liberated iodine can be titrated using a standard procedure. However, to achieve accurate results the concentration of oxygen in the sample has to remain constant for the duration of the titration. The major problem is that the procedure is quite lengthy. An alternative method of oxygen detection was developed by L.C. Clark in 1956. It consisted of an electrode that could measure the partial pressure of gaseous oxygen, and of oxygen in solution by measuring the current flow between electrodes [19]. Clark cells are to-day the most common device used to detect and measure oxygen concentration. A schematic drawing of a typical Clark electrode is shown in figure 1.5 [17]. At the cathode, oxygen is reduced to hydroxyl ions according to the equation

$$O_2 + 2H_2O + 4e^- \rightarrow 4OH^- \qquad 1.1$$

The hydroxyl ions in turn oxidise the metal anode according to the equation

$$2Pb + 4OH^- \rightarrow 2PbO + 2H_2O + 4e^- \qquad 1.2$$

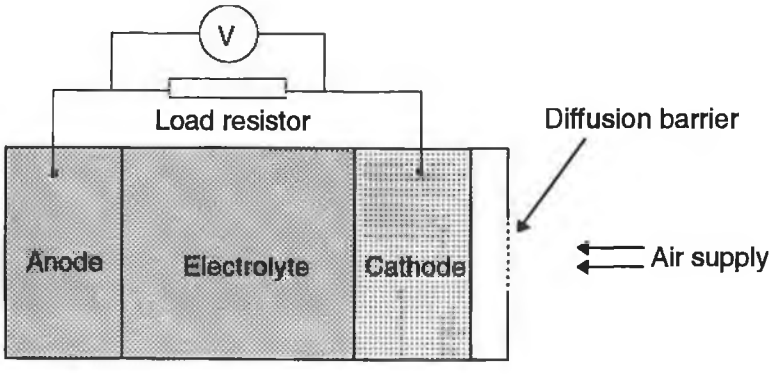

figure 1.5 Clark electrode

The current produced is proportional to the rate of consumption of oxygen, and the oxygen permeability of the diffusion barrier. The response time of the sensor is also limited by the diffusion barrier. Problems associated with the use of such electrodes are as follows:

i) The cells have limited lifetimes and require replacement when the lead anode has been totally oxidised. This lifetime varies with cell usage and typical lifetimes are in the range of 1 to 2 years.

ii) When the carrier gas mixture has a mean molecular weight significantly different from nitrogen, a calibration of the output signal has to be carried out. This is due to the different diffusion rates caused by the molecular weights involved (Graham's law).

iii) Acid gases such as CO_2 and SO_2 can be slightly absorbed by the electrolyte and tend to increase the flux of oxygen to the electrode. This results in an enhanced output signal.

iv) The cells cannot be used in conditions where condensation may occur. Under these conditions, liquids may form in the region of the gas access holes within the membrane, and this may restrict the flow of O_2 to the sensor.

v) Oxygen is consumed during detection, and this can have undesirable effects when small volumes of gas are under investigation.

vi) The signal from a typical cell is slightly non-linear and can be described using the following expression

$$S = K\log_e\left(\frac{1}{1-C}\right) \qquad 1.3$$

where S is the output signal, C is the fractional concentration of oxygen, and K is a constant that varies from cell to cell.

Optical oxygen sensors offer a number of advantages over amperometric type electrodes such as the Clark electrode. These include small size, lack of oxygen consumption and reference cells, and immunity against sample flow rates [3]. In 1968,

Bergman described one of the first oxygen sensors based on fluorescence quenching of long lifetime fluorescence compounds [20]. He used the polycyclic aromatic compound fluoranthene as an indicator. In the past few years, a number of groups have published works describing the use of optical fibres in monitoring oxygen gas and dissolved oxygen in water. In most of these investigations, absorption dyes [21,22] or fluorescence type indicators [6,23,24] have been immobilised in an organic matrix and attached to an optical fibre. The quenching of fluorescence is the process by which a fluorophore molecule is de-excited by collision, or other means, resulting in non-radiative decay of the excited state. The quenching of fluorescence can then be correlated with oxygen concentration. For fluorescence compounds with long excited-state lifetimes, the probability of a collision that will result in quenching is much higher than for one with a short lifetime. An increasingly important class of fluorescence indicators used in these sensors has been luminescence transitional metal complexes, especially those of ruthenium. Ruthenium complexes known as metal to ligand charge transfer (MLCT) materials (see chapter 3), have long lifetimes (in the order of hundred of nanoseconds to tens of microseconds) and high quenching efficiencies which make them suitable for oxygen sensing. The photo-physical and photochemical properties of these compounds have been extensively studied by Demas et al. [25].

One of the problems associated with most of the optical oxygen sensors has been poor chemical and photochemical stability of the sensors due to the use of polymers as host materials for immobilisation of fluorescence indicators. For example, both polystyrene and polyethylene degrade when exposed to environments containing organic solvents or temperatures above 60°C. Both polymers fluoresce in the blue or violet when exposed to UV radiation. The development of inorganic host materials with superior chemical and photochemical stability and good optical properties for immobilisation of organic dyes for sensor applications, has been the subject of much research during recent years. One of the more promising approaches is the use of the sol-gel process for the encapsulation of optically active organic compounds into a silica glass matrix. Compared to polymers, glass provides improved properties as a sensor substrate, such as high surface area, ruggedness, high chemical, photochemical and thermal stability and low

absorption in visible and near infrared range. This approach for reagent immobilisation is pursued in the work reported in this thesis.

1.4 The sol-gel process

The sol-gel process is a method of preparing glasses and ceramics at near ambient temperature by hydrolysis and polymerisation of organic precursors [26]. Materials can be prepared in a variety of forms (i.e. bulk, powder, wire, aerogel, monolith, fibre, thin film etc.) with a wide range of optical, structural and electroceramic applications. The process typically involves a metal alkoxide, water, a solvent and frequently a catalyst, which are mixed thoroughly to achieve homogeneity on a molecular scale. Chemical reactions (hydrolysis and polymerisation) lead to the formation of a viscous gel, which is an amorphous porous material containing liquid solvents in the pores. Low temperature (typically < 100°C) curing expels most of the liquids and leaves the porous oxide. Further curing at higher temperatures leads to the densification of the material. Silica, titania and silica-titania thin films and monoliths can be routinely fabricated by this process. The sol-gel process is particularly attractive in that it allows the user a great deal of flexibility. By alteration of the process parameters and precursors, it is possible to alter a range of material properties such as refractive index and porosity [26]. The sol-gel process provides a means of coating an unclad optical fibre with a porous cladding, within which an analyte-sensitive reagent is entrapped [27]. Under appropriate process parameters the reagent cannot be leached out, but smaller analyte molecules can permeate the interconnecting microporous pores. The sol-gel produced thin films offer many advantages over other immobilisation techniques [10]:

i) Sensor fabrication is simple and involves straight-forward dip-coating of the unclad optical fibre followed by curing at low temperatures.

ii) Curing produces a tough, inert porous film which is considerably more resistant than alternative polymer films.

iii) The flexibility of the sol-gel process enables a range of critical sensor parameters to be optimised, including the coating speed which determines the coating thickness [25].

iv) The technique is particularly suited to gas sensing because the high specific area (i.e. $100m^2/g$) of the microporous structure enhances the sensitivity considerably.

The application of the sol-gel process to fibre optic chemical sensors was first proposed by Badini et al. [28] in 1989, followed by Zusman et al. [29] in 1990. In Badini's work, silica gel incorporating fluorescein isothiocyanate was prepared and coated on a silica glass slide and used as a pH sensitive substrate. However, cracks developed for most of the coatings when heated, and difficulties in the detection of any spectral change were also reported in their work. The idea of using the sol-gel coating technique for application in fiber optic chemical sensors was finally accomplished by two groups in 1991, one by MacCraith et al. [30] and the other by Ding et al. [31]. Both these groups developed fiber optic pH sensors which were the first intrinsic fiber optic chemical sensors prepared by the sol-gel technique. MacCraith's group immobilised the pH sensitive fluorescent indicator fluorescein on a silica fibre. The pH range of interest in their work was in the region of pH3.5 - 6.5. In the approach taken by Ding et al. two absorption type pH indictors (bromocresol green and bromocresol purple) were co-immobilized into silica gel, which was then coated as a thin film onto a porous core silica glass fiber. A dynamic range of pH3-9 was achieved in this work. The work presented in this thesis describes the sol-gel method of immobilisation of fluorescent dyes, for the sensing of gaseous oxygen.

1.5 Thesis overview and objectives

In defining the objectives of this project it should be noted that industrial sponsorship was provided by Sieger Ltd., Poole, England. It was crucial that the completed oxygen gas sensing devices were miniature so as to allow portability, suitable for personal sensing devices. The possibility of carrying out battery operation would also be envisaged. Sensor performance, in particular sensitivity to gaseous oxygen and sensor response time of the completed device, should compare favourably to the specifications of currently available electrochemical cells, which were outlined in section 1.3. Both temperature and relative humidity studies of the oxygen sensor were to be performed.

The work presented in the thesis describes the development of fibre optical oxygen sensors based on evanescent wave excitation of a ruthenium complex entrapped in a thin

microporous coating fabricated by the sol-gel process. The sensors are based on the quenching of fluorescence from ruthenium complexes. A laboratory based characterisation system, using an argon-ion laser as excitation source, PMT as detector and a commercial lock-in amplifier is described. The fluorescence intensity is monitored as a function of oxygen concentration. The same system is tested in phase fluorimetric mode. The detected phase shift as a function of frequency, is compared to the fluorescence lifetimes of the immobilised ruthenium complexes. Comparison between fluorescence intensity and phase fluorimetric operation is carried out as a function of frequency. The development of a portable version of the sensor, using a high intensity blue LED source, and photodiode detection is then described. The miniaturised hand-held oxygen gas sensor exhibits fast response times of less than 5 seconds, high sensitivity to oxygen and good repeatability. Sensor response, including linearity to oxygen concentration, temperature response and humidity dependence are discussed, and the viability of using this type of sensor for industrial production is examined. Finally, the use of the evanescent wave technique for carrying out immunoassays is treated in the final chapter.

References:

1. Schubert J.: '**Physikalische Effekte**', Weinheim, FRG; Physik-Verlag, 1984

2. Krohn D.A: '**Fibre optic sensors : fundamentals and applications**', Instrument Society of America, 1982, 2nd ed., p. 2

3. Wolfbeis O.S. (Ed.): '**Fibre optic chemical sensors and biosensors**', CRC Press, Boco Raton, FL, 1991, Vol. 1

4. Wolfbeis O.S. (Ed.): '**Fibre optic chemical sensors and biosensors**', CRC Press, Boco Raton, FL, 1991, Vol. 2

5. Zhang Z., Grattan K.T.V., Palmer A.W.: '**Thermal characteristics of alexanderite fluorescence decay at high temperatures, induced by a visible laser diode emission**', Journal of Applied Physics, 1993, Vol. 73, No. 7, pp. 3493-3498

6. Peterson J., Golden S.R., Fitzgerald R.V., Buckhold D.K.: '**Fibre-optic probe for in vivo measurement of oxygen partial pressure**', Analytical Chemistry, 1984, Vol. 56, pp. 62-67

7. Peterson J., Golden S.R., Fitzgerald R.V., Buckhold D.K.: '**Fibre optic pH probe for physiological use**', Analytical Chemistry, 1980, Vol. 52, pp. 864-869

8. Takeo T., Hattori H.: '**Application of a fibre optic refractometer for monitoring skin conditions**', R.A Lieberman (ed.), Chemical, Biochemical and Environmental Fibre Sensors III, 1991, Proc. SPIE, Vol. 1587, pp. 284-287

9. Zhou Q., Shahriari M.R., Sigel G.H.: '**The effects of temperature on the response of a porous fibre optic humidity sensor**', R.A. Lieberman and W.T. Wlodarczyk (eds.), Chemical, Biochemical and Environmental Fibre Sensors, 1988, Proc. SPIE, Vol. 990, p. 153

10. Sharhriari M.R., Zhou Q., Sigel G.H.: '**Porous optical fibres for high-sensitivity ammonia-vapour sensors**', Optics Letters, 1988, Vol. 5, No. 13, p. 407

11. Mac Craith B.D.: '**Enhanced evanescent wave sensors based on sol-gel-derived porous glass coatings**', Sensors & Actuators B, 1993, Vol. 11, pp. 29-34

12. Takeuchi T.: '**Oxygen sensors**', Sensors & Actuators, 1988, Vol. 14, pp. 109-125

13. Moreno-Bondi M.C., Wolfbeis O.S., Leiner M.J.P., Schaffer P.H.: '**Oxygen optrode for use in a fibre-optic glucose biosensor**', Analytical Chemistry, 1990, Vol. 62, p. 2377

14. Trettnak W., Wolfbeis O.S.: '**A fibreoptic cholesterol biosensor with an oxygen optrode as transducer**', Analytical biochemistry, 1990, Vol. 184, No. 124.

15. Trettnak W., Wolfbeis O.S.: '**A fibre optic lactate biosensor with an oxygen sensor as the transducer**' Analytical Letters, 1989, Vol. 22, No. 9, pp. 2191-2197

16. Crowcon Detection Instruements, Fixed systems and portable instrumentation for safety gas monitoring, Oxfordshire, England.

17. City Technology Limited: '**Product Data Handbook : Quality gas detection**', 1993, Vol. 1.7, pp. A1-A10

18. Mackereth F.J.H., Heron J., Talling J.F.: '**Water analysis: some revised methods for Limnologists**' Freshwater Biological Association, 1978, pp. 24-35

19. Clark L.C., Journal of Transactions - American Society for Artificial Internal Organisation, 1856, Vol. 2, p41.

20. Bergman I.: '**Rapid-response atmospheric oxygen monitor based on fluorescence quenching**', Nature, 1968, Vol. 218, p. 396

21. Tarasankar P., Nikhil R.J., Das P.K.: '**Spectrophotometric determination of dissolved oxygen in water by the formation of a dicyanoaurate (I) complex with gold sol.**', Analyst, 1991, Vol. 116, pp. 321-322

22. Baldini F., Bucci M., Cosi F., Bianco A. Del,: '**Absorption-based optical-fibre oxygen sensor**', Sensors & Actuators B, 1992, Vol. 7, pp. 752-757

23. Blyler L.L., Lieberman R.A., Cohen L.G., Ferrara J.A., Macschesney J.B.: '**Optical fibre chemical sensors utilising dye-doped silicone polymer claddings**', Polymer Engineering and Science, 1989, Vol. 29, No. 17, pp. 1215-1218

24. Del Bianco A., Baldini F., Bacci M., Klimant I., Wolfbeis O.W.: '**A new kind of oxygen - sensitive transducer based on an immobilised metallo-organic compound**', Sensors & Actuators B, 1993, Vol. 11, pp. 347-350

25. Demas J.N., DeGraff B.A.: '**Design and applications of highly luminescent transition metal complexes**', Analytical chemistry, 1991, Vol. 63, No. 17, pp. 829-837

26. Brinker C.J., Scherer G.W.: '**Sol-gel science**', Academic Press, New York, 1990

27. Mac Craith B.D., McGilp J.F., O'Kelly B., Ruddy V.: '**A waveguide sensor**', PCT Patent application No. PCT/GB92/00428, 1992

28. Badini G.E., Grattan K.T.V., Palmer A.W., Tseung A.C.C.: '**Development of pH-sensitive substrates for optical sensor applications**', Springer Proceeding in Physics, 1989, Vol. 44, pp. 436-442

29. Zusman R., Rottman C., Ottolenghi M., Avnir D.: '**Doped sol-gel glasses as chemical sensors**', Journal of non-crystalline solids, 1990, Vol. 122, pp. 107-109

30. Mac Craith B.D., Ruddy V., Potter C., '**Optical waveguide sensor using evanescent excitation of a fluorescent dye in a sol-gel glass**', Electronic Letters, 1991, Vol. 14, No. 27, pp. 1247-1248

31. Ding J.Y., Shahriari M.R., Sigel Jr. G.H.: '**Fibre-optic pH sensors prepared by sol-gel immobilisation technique**', Electronic Letters, 1991, Vol. 17, No. 27, pp. 1560-1561

Chapter Two - Evanescent Wave Sensing

2.1 Introduction

Newton [1] was one of the first to note the existence of the evanescent field. He observed that total internal reflection in a prism could be frustrated by bringing a second prism close to the point of total reflection. This phenomenon is today known as frustrated total reflection (FTR). However, the properties of the evanescent wave were not discussed in detail until 1933, when Taylor [2] outlined the potential of the evanescent wave for spectroscopic and refractive index measurements. In the early 1960's Fahrenfort [3] and Harrick [4] used total internal reflection as a spectroscopic tool and developed what is today known as internal reflection spectroscopy (IRS). Harrick described IRS as the technique of recording the optical spectrum of a sample material that is in contact with an optically denser but transparent medium. Their published work sparked off a flurry of research into internal reflection spectroscopy, which also became known as attenuated total reflection (ATR). The sensitivity of ATR spectroscopy is normally much less than conventional direct absorption spectroscopy because the interaction occurs at the point of total internal reflection over a relatively short path length. Increasing the number of interaction points, however, increases the sensitivity of ATR in an analogous way to increasing the path length in direct absorption. Optical fibres and waveguides are ideal substrates of use in ATR spectroscopy, because light propagates by means of total internal reflection with a high number of reflections per unit length. An optical fibre has a definite advantage over the planar geometry in this regard, since the internal reflections are confined to two of the three dimensions rather than one. Two distinct approaches may be adopted in evanescent wave sensors. Firstly, the evanescent wave can interact directly with the analyte if the interrogating wavelength coincides with the absorption band of the species. Such *direct spectroscopic* evanescent wave sensors are of particular interest in the infrared region, where many species absorb strongly. In 1987, Tai et al. [5] demonstrated evanescent wave absorption, to determine the concentration of methane gas, using a tapered optical fibre. This work was followed by a large number of others, using both visible and infra-red transmitting fibres for liquid and gas sensing. In 1994 Sanghera et al. [6] published work in which telluride glass fibres were used, to measure

the evanescent absorption spectra of water, methanol, isopropanol, acetone, ethanoic acid, hexane and chloroform. An alternative sensing technique to direct spectroscopy is the use of an intermediate reagent which responds optically (e.g. by fluorescence, or absorption change) to an analyte. This analyte is attached to the waveguide to carry out *reagent-mediated* sensing. The main thrust of the work described in this thesis, is based on the use of such analytes or dyes, whose fluorescence characteristics alter in the presence of a measurand. This family of optical sensors is known as evanescent wave fluorosensors.

2.2 Review of sensors based on evanescent wave excited fluorescence

Evanescent wave fluorosensors based on the principle of total internal reflection were first described by Hirschfeld [7] in 1965, wherein fluorescein was excited using the planar geometry of either a prism or waveguide. Kronick et al. [8] in 1975 and Sutherland et al. [9] in 1987 used evanescent wave excitation, but collected the fluorescence emission in free propagation. Evanescent excitation and evanescent collection using an optical fiber was first proposed by Block and Hirshfeld in 1984 [10,11]. In 1985, Sutherland et al. [12] and Andrade et al. [13] described fluoroimmunosensing experiments in which serum- or water-based samples replaced a conventional cladding. The subject of evanescent-wave theory is reviewed by Harrick [14] and a detailed description of the optical characteristics of optical fiber evanescent wave fluorosensors is described by Wise and Wingard [15].

2.3 The evanescent field

An evanescent wave is generated when the conditions for total internal reflection are satisfied. Although geometric optics provide the conditions for total internal reflection to occur, it offers no explanation of the phenomenon or any information about the energy distribution at reflection. The results of electromagnetic theory must be applied to the case. A representation of a plane wave reflection at an interface is shown in figure 2.1. The monochromatic incident plane wave shown is polarised normal to the plane of incidence. In order to obtain a mathematical description of what occurs at the interface, it is convenient to take the simple case of linear, isotropic, homogeneous and non-magnetic

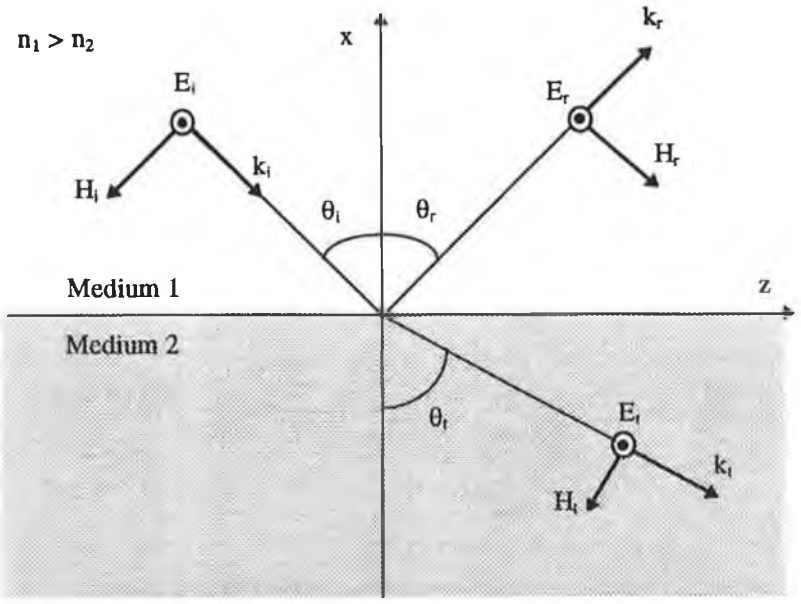

figure 2.1 Plane wave reflection from a dielectric interface is represented in terms of the E, H and k vectors (⊙ represents the direction perpendicular to the page)

dielectric media. The incident (i), reflected (r) and transmitted (t) plane waves are then represented by the following equations:

$$\mathbf{E}_i = A_i \cdot e^{-j(\mathbf{k}_i \cdot \mathbf{r} - \omega t)} \qquad 2.1$$

$$\mathbf{E}_r = A_r \cdot e^{-j(\mathbf{k}_r \cdot \mathbf{r} - \omega t)} \qquad 2.2$$

$$\mathbf{E}_t = A_t \cdot e^{-j(\mathbf{k}_t \cdot \mathbf{r} - \omega t)} \qquad 2.3$$

where A is the electric field amplitude, **k** is the propagation vector of the plane wave with angular frequency ω, the components of **r** specify the co-ordinate point at which the field is observed and t is the time. Using Maxwell's equations, it can be shown that the tangential components of the **E** and **H** fields must be continuous across the boundary between the two media i.e. the phase variation along the interface must be the same for the incident, reflected and transmitted fields. That is, at the interface and neglecting time variance

$$\mathbf{k}_i \cdot \mathbf{r} = \mathbf{k}_r \cdot \mathbf{r} = \mathbf{k}_t \cdot \mathbf{r} \qquad 2.4$$

Each wave propagation vector may be resolved into cartesian components k_x, k_y and k_z where x and z are oriented as in figure 2.1 and y is the direction perpendicular to the page. The interface is defined as the yz plane at x = 0. The co-ordinate system has been drawn with the incident k vector in the xz plane, and therefore the y component of $\mathbf{k}_i$ is 0. In this situation the phase variation along the interface depends only on z. Equating the phases of the incident, reflected and transmitted waves at the interface results in

$$k_i \sin\theta_i = k_r \sin\theta_r = k_t \sin\theta_t \qquad 2.5$$

which are the z components of the incident, reflected and transmitted vectors respectively. Since the incident and reflected waves are in the same medium, $k_i = k_r$, we can conclude that

$$\theta_i = \theta_r \qquad 2.6$$

i.e. the reflected and incident angles measured with respect to the normal are equal. Further, using the relation $k_m = 2\pi n_m/\lambda_0$ (where k_m is the plane wave propagation constant in medium m, n_m is the refractive index of the medium and the subscript m denotes medium 1, or 2) and equation 2.5, it can be shown that

$$\begin{aligned} n_1 \sin\theta_i &= n_2 \sin\theta_t \\ \Rightarrow \sin\theta_t &= n_{12} \sin\theta_i \end{aligned} \qquad 2.7$$

which is commonly known as Snell's law.

Total internal reflection occurs at the interface between two media where n_2 is less than n_1. This happens in a step-index fibre at the core-cladding interface. As the angle of incidence, θ_i , is increased, the transmitted angle, θ_t , also increases. When $n_1 > n_2$, θ_t is greater than θ_i. There is therefore a critical angle of incidence, θ_c, for which $\theta_t = 90°$. For incident angles greater than this critical angle, no light propagates into medium 2. The equation for the propagation vector in medium 2 is

$$\mathbf{k}_t = k_{tx} + k_{tz} = k_t \cos\theta_t + k_t \sin\theta_t \qquad 2.8$$

Using Snell's law and the trigonometric identity $\cos^2\theta + \sin^2\theta = 1$, we may write[1] $\cos\theta_t = [1 - (n_{12})^2 \sin^2\theta_i)]^{1/2}$. The x and z components of the propagation vector of the transmitted wave can then be described in terms of the angle of incidence and the refractive indices of media 1 and 2

$$k_{tz} = k_t \sin\theta_t = k_t n_{12} \sin\theta_i \qquad 2.9$$

$$k_{tx} = k_t \cos\theta_t = k_t\left(1 - n_{12}^2 \sin^2\theta_i\right)^{1/2} \qquad 2.10(a)$$

$$= k_t n_{12}\left(\sin^2\theta_c - \sin^2\theta_i\right)^{1/2} \qquad 2.10(b)$$

For incident angles θ_i greater than the critical angle, θ_c, where $\theta_c = \sin^{-1}(n_{21})$, the x component, k_{tx}, of the propagation constant is complex and may be written as $i\delta$ where δ is real. The transmitted wave electric field is then given by

$$\mathbf{E}_t = A_t \cdot e^{j(k_t n_{12} \sin(\theta_i) z - \omega t)} e^{\pm\delta x} \qquad 2.11$$

where

$$\delta = k_t\left(n_{12}^2 \sin^2\theta_i - 1\right)^{1/2} \qquad 2.12$$

δ is known as the attenuation constant and can take positive or negative solutions. The solutions are physically constrained such that the product δx is negative; otherwise the field would increase exponentially with distance into the second medium. This solution describes a non-propagating electric field which decays exponentially in medium 2. The exponentially decaying field is called the evanescent field. The penetration depth of the

[1] $n_{12} = n_1/n_2$ and $n_{21} = n_2/n_1$

evanescent field d_p , is defined as the distance required for the electric field amplitude to fall to exp(-1) or 37% of its value at the interface and is expressed as

$$d_p = \frac{1}{\delta} = \frac{\lambda_0}{2\pi n_2 (n_{12}^2 \sin^2\theta_i - 1)^{1/2}} \qquad 2.13(a)$$

$$= \frac{\lambda_0}{2\pi n_1 (\sin^2\theta_i - \sin^2\theta_c)^{1/2}} \qquad 2.13(b)$$

where k_t has been written in terms of the free space wavelength λ_0. The direction of propagation of the evanescent field is parallel to the dielectric interface, as indicated by the arrows in figure 2.2.

In evanescent wave sensing, it is often important to optimise penetration depth to achieve high sensitivity. According to equation 2.13, the factors that influence the penetration depth are the wavelength of the incident light, the refractive index ratio and the launch angle θ_i. Although d_p is typically less than λ_0, it is clear from equation 2.13(b) that its value rises sharply as the angle of incidence approaches the critical angle $\theta_c = \sin^{-1} n_{21}$, indicating the transition from an evanescent wave to a refracting wave in the surrounding medium. Figure 2.3 illustrates the dependence of penetration on angle of incidence for various refractive indices. It is clear from the graph that the penetration

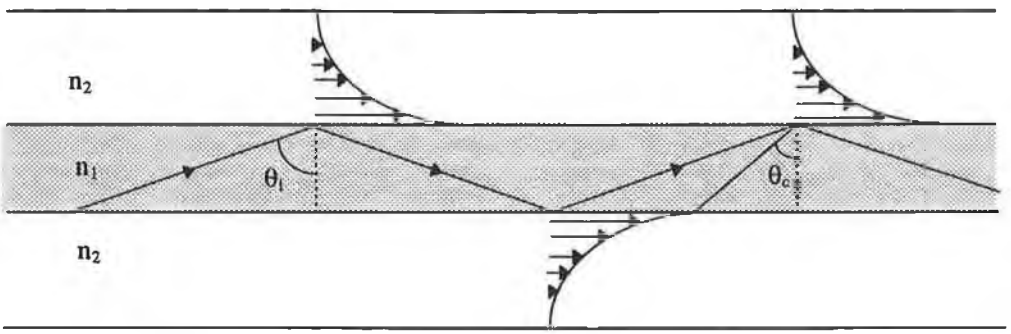

figure 2.2 The field amplitude of the evanescent wave decays exponentially further from the media interface, its direction of propagation is parallel to the interface as illustrated [16].

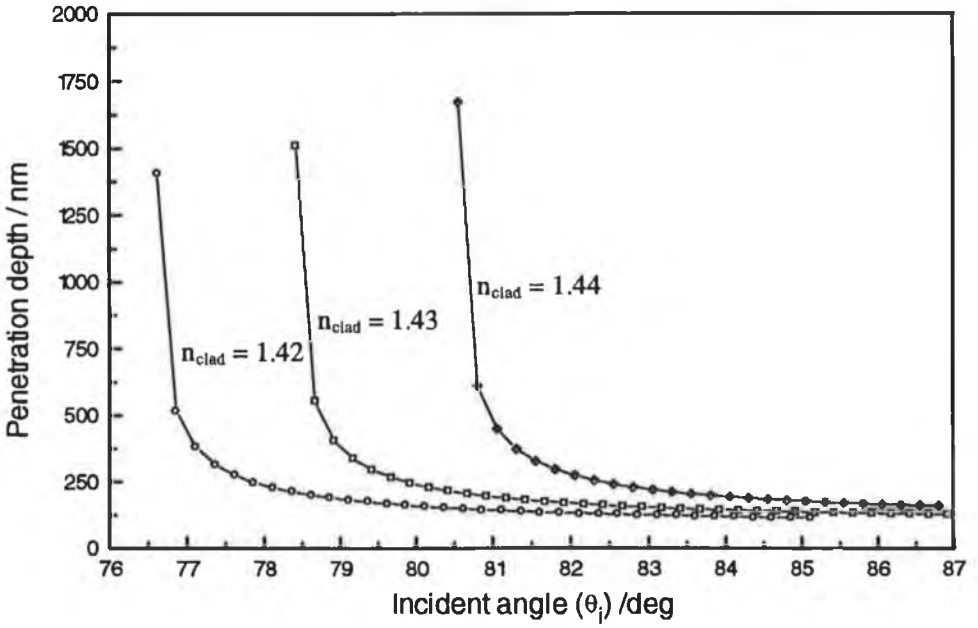

figure 2.3 Penetration depth dependence on incident angle for various refractive indices as shown. n_{core} = 1.46, wavelength of incident light 450nm.

depth is maximum when the angle of incidence approaches the critical angle. This dependence will be taken into account in the design of the optical system which is described in chapter 5.

2.4 Evanescent wave interactions

The penetration of the evanescent field into the rarer medium as described above may lead to evanescent wave interactions. There are two distinct ways in which perturbations of the evanescent fields can result in a reduction of the reflected optical power. These are frustrated total reflection (FTR) and attenuated total reflection (ATR). If a lossless dielectric with a refractive index n_3 overlaps the exponentially decaying field in medium two and if $n_3 > n_1 \sin\theta_i$, where θ_i is the angle of incidence of the wavefront, then the evanescent condition is not satisfied and k_z in medium 3 is real. Therefore the wave propagates in medium 3. This reduces the intensity of the reflected wave and so the reflection condition is frustrated. By controlling the distance between medium 1 and medium 3, or the angle of incidence of the plane wave, the amounts of transmitted and reflected light may be adjusted [14,17].

The case of ATR is depicted in figure 2.4, where medium 3 is replaced with an absorbing medium with a complex refractive index n_3, with real component $n_{3r} < n_1 \sin\theta_i$. The reflected wave is attenuated as the lossy medium absorbs a portion of the optical power through interaction with the evanescent field. Power absorption is a function of the absorption coefficient of the material and the depth of penetration of the evanescent field in the medium. The evanescent wave can also be used to excite electronic transitions in molecules located sufficiently close to the waveguide, while molecules located at distances large relative to d_p will not experience the evanescent wave, and so remain unaffected. If the absorbing species are capable of re-emitting the absorbed energy by means of fluorescence decay, then the evanescent wave may be employed as an excitation source. This technique is often referred to as total internal reflection fluorescence (TIRF). In this situation medium 2 is normally very thin compared to medium 3 as illustrated in fig 2.4, or else does not exist. A review of the theory behind this phenomena forms the basis for the next section of this thesis [17].

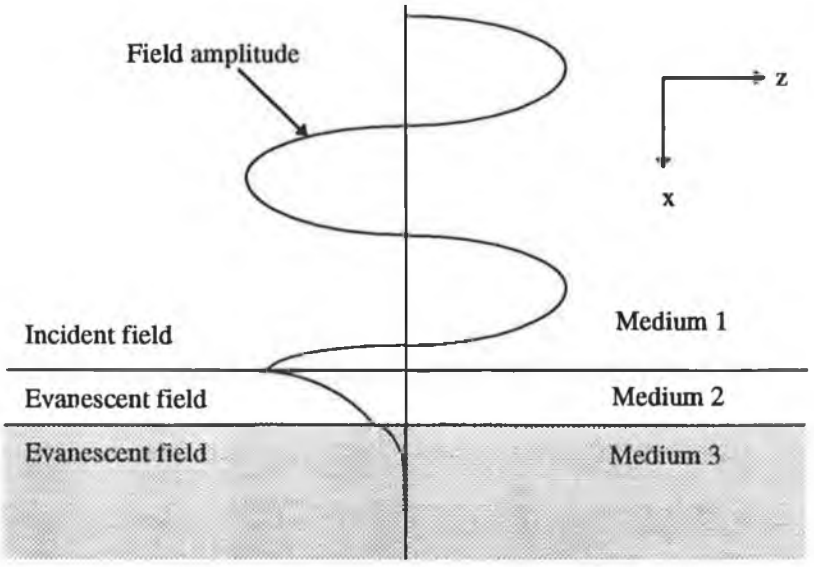

figure 2.4 ATR geometry, $n_1 \sin\theta_i > n_2 > n_{3r}$ [17].

2.5 Theory of Evanescent Wave Excitation and Detection of Fluorescence

2.5.1 Introduction

Love et al. [19] used ray-optics to analyse the excitation and collection of fluorescence from thin coatings on short optical fibre probes. The theory developed, in his work was shown to be in good agreement with experimental results. However, the approach is accurate only when the waveguide diameter is very large compared to the wavelength of light. A review of this work is carried out in section 2.5.2. A more complete approach based on the electromagnetic wave theory was described in 1988 by Marcuse using the weakly guiding approximation for optical fibres [20]. His results were applied to a sensor described by Lieberman at al. [21], from which agreement between theory and experiment was within an order of magnitude for a single experimental data point. The development of Marcuse's model is outlined in section 2.5.3. Marcuse's model, however, can not predict the behaviour of a fibre that has a large difference between the core and cladding indices of refraction. More recently, however, Marcuse's model has been extended by Egalon to include the case of waveguides with arbitrarily large refractive index difference [16]. He has calculated evanescent power collection efficiency using the exact field solution of the optical fibre. Egalon's work is described in section 2.5.4.

2.5.2 Evanescent coupling efficiency - geometric optic approach

A detailed description of the physical parameters involved in developing a model of evanescent wave excitation and fluorescence detection was carried out by Love et al. in 1991 [19]. In this model, a cylindrical sensor is approximated as a planar interface where the waveguide diameter, d, is much greater than the wavelength of light. It is also assumed that a geometrical ray optics approach is valid. The fluorescent molecules are situated on the lower refractive index side of the planar dielectric interface. In the absence of absorbing molecules, light is reflected off the interface for incident angles $\theta_i > \theta_c$, so that total internal reflection occurs without loss of power. However, power may be removed from the incident beam as a result of the interactions between evanescent field and the electric dipole moments located in the medium of lower refractive index. The power absorbed from a ray, is calculated using the magnitude of the electric field

obtained from the Fresnel transmission coefficients, and the optical absorption coefficient of the fluorescent medium. Assuming each ray to be randomly polarised as it approaches the interface, and using Beer-Lambert's absorption law, an expression for the local power absorption, P_{abs}, at a distance δ from the interface and for a ray at incident angle θ, was derived [19]

$$P_{abs}(\delta;\theta) = 2\gamma I_{ray}\cos\theta\left\{\frac{n_{12}\exp\left(\frac{-2\delta}{d_p}\right)}{n_{12}^{\,2}-1}\right\}[1+g(\theta)] \qquad 2.14$$

with

$$1+g(\theta) = 1 + \frac{2n_{12}^{\,2}\sin^2\theta - 1}{(n_{12}^{\,2}+1)\sin^2\theta - 1} \qquad 2.15$$

where γ is the absorption coefficient for the cladding material and I_{ray} is the power flux of the ray normal to the interface. The quantity $n_{12} = n_1/n_2$ and d_p is the evanescent penetration depth as defined in section 2.3. The factor $1 + g(\theta)$ arises from averaging the 2 possible incident polarizations and is found to vary by about 2% over the range of θ values of interest. This calculation also assumes that the absorbed power is small compared to the incident power. Equation 2.14 allows the incident flux of the ray and the absorption factor to be factored out, and thus one can define a dimensionless 'geometrical absorption factor' F_{abs} by

$$F_{abs}(\delta;\theta) = \frac{P_{abs}(\delta;\theta)}{\gamma I_{ray}(\theta)}$$

2.16

$$= 2\cos\theta \left\{ \frac{n_{12} \exp\left(\frac{-2\delta}{d_p}\right)}{n_{12}^{\,2} - 1} \right\} [1 + g(\theta)]$$

The most significant feature of equation 2.16 is its exponential dependence on $-\delta/d_p$ i.e. the absorption factor is much greater for angles near the critical angle. A plot of F_{abs} versus incident angle for various distances from the interface, δ, is shown in figure 2.5, for the specific case where $n_1 = 1.46$, $n_2 = 1.43$ (i.e. $\theta_c = 78.36°$) and $\lambda_0 = 450$nm.

There is also a finite probability that radiation emitted by a dipole located in the medium of lower refractive index will propagate as a plane wave above the critical angle

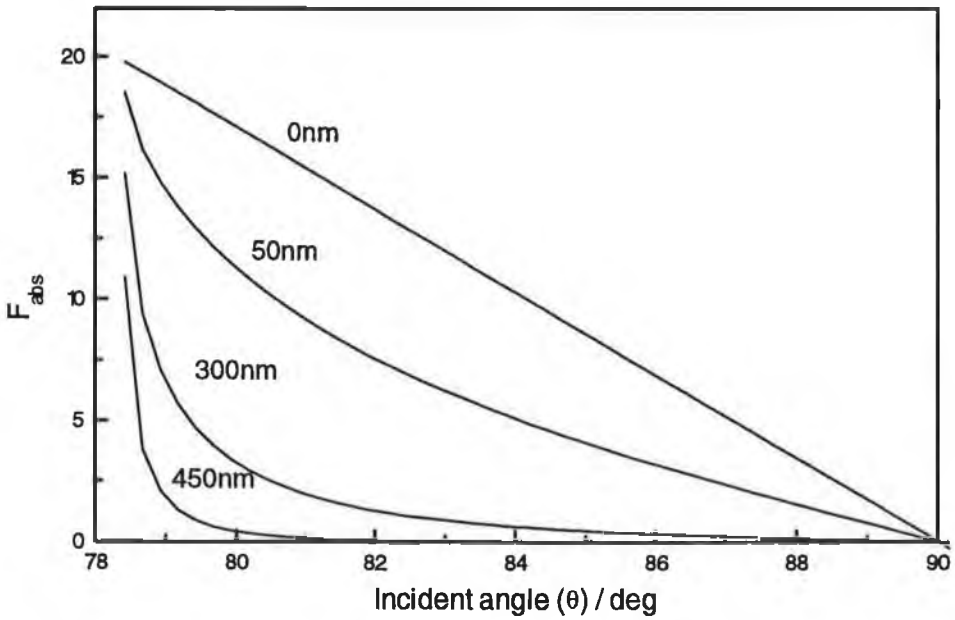

figure 2.5 Calculated geometrical absorption factor F_{abs}, for various values of δ, as a function of angle of incidence.

within the denser medium. The emission probability into any range of solid angles is obtained from the classical radiation pattern for a dipole near a dielectric interface. This has been calculated in detail by Lukosz et al. [22,23]. The optical power emitted in a given direction per unit solid angle for the specific case of angles within the region $\theta_c \leq \theta \leq \pi/2$ was found to have the form

$$\frac{dP}{d\Omega} = \left(\frac{cn_2k^4D_0^4}{6\pi}\right)\left(\frac{n_{12}^3\cos\theta}{n_{12}^2-1}\right)\exp\left(\frac{-2\delta}{d_p}\right)[1+g(\theta)] \qquad 2.17$$

where D_0 is the dipole strength. The probability of injection into a bound mode was found to be maximum near the critical angle, and to exhibit a rapid decrease with angle for large δ/λ in the evanescent region. Using the cylindrical co-ordinates of the specific waveguide and by taking the angular probability distribution for photon emission into account, the total probability that a photon emitted by a dipole will propagate as a detectable forward ray was found to be described by a function $p_{emit}(\delta;\theta_0^{max})$, given by

$$p_{emit}(\delta;\theta_0^{max}) = \left(\frac{2}{P_{tot}}\right)\int_{\theta_{min}}^{\pi/2}\cos^{-1}\left(\frac{\sin\theta_{min}}{\sin\theta}\right)\left(\frac{dP}{d\Omega}\right)\sin\theta d\theta \qquad 2.18$$

where θ_0^{max} is the maximum incident angle of the launch and detection lens, and θ_{min} is its corresponding incident at the core-cladding interface. P_{tot} is the power radiated in all directions by the fluorescent sources. Analysis of equation 2.18 shows that p_{emit} becomes large for a collection cone with a maximum angle approaching the critical angle. This situation is similar to the response found for the absorption function (i.e. equation 2.16) which also indicates the importance of high angle collection.

The fluorescence signal, I_{fluor}, per unit area of interface from a single incident plane wave may be calculated from equations 2.16 and 2.18. I_{fluor} is the power absorbed at a depth, δ, in the fluorescent medium times the probability that a photon emitted at δ will propagate as a detectable ray. For a bulk fluorescent medium, I_{fluor} may be given by [19]

$$I_{fluor}^{(bulk)}(\theta) = \gamma I_{ray}(\theta) \int_0^{\infty} F_{abs}(\delta;\theta)\, p_{emit}\left(\delta;\theta_0^{max}\right) d\delta \qquad 2.19$$

For the case of a thin fluorescent layer of thickness h, I_{fluor} is obtained by integrating over the layer. If h is smaller than the wavelength so that P_{abs} and p_{emit} are approximately constant over the layer then I_{fluor} may be written as [19]

$$I_{fluor}^{(film)}(\theta) = \gamma h I_{ray}(\theta)\, F_{abs}(\delta = 0;\theta)\, p_{emit}\left(\delta = 0;\theta_0^{max}\right) d\delta \qquad 2.20$$

Equations 2.19 and 2.20 consider only the signal from a single reflection from a given ray. The total signal from such a ray may be calculated by taking into account the number of reflections from such a ray. The rays that are excited into the waveguide are dependent on the illumination of the fibre end face. Love et al. assume that the fibre end is illuminated by a diffuse Lambertian light source. The light is focused so that it uniformly illuminates a spot centered on the end face of the fibre. The radius of the spot is r_{max}, where r_{max} is less than or equal to the radius of the fibre as illustrated in figure 2.6. The optical flux per unit area with in the spot, per unit angle $d\Omega$, is given by [19]

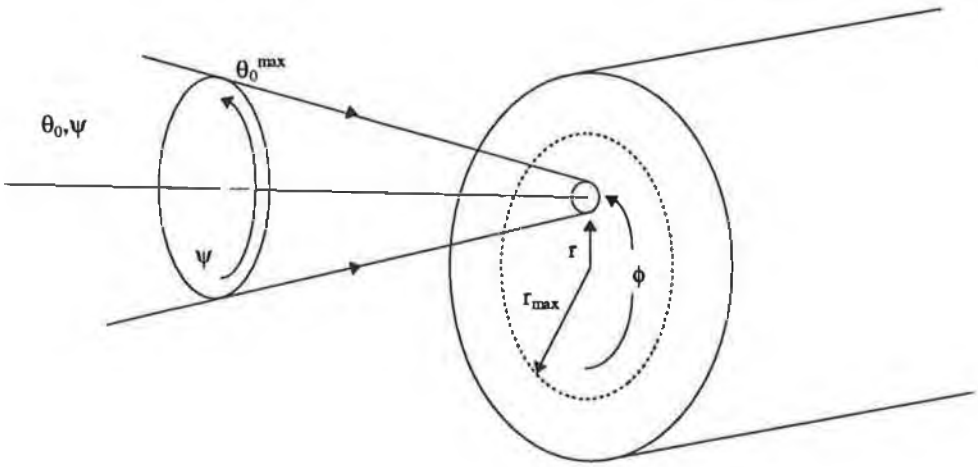

figure 2.6 Definition of launch variables; incident ray angles are described by θ_0, ψ, and the fiber end faces described by polar co-ordinates r,ϕ; $r_{max} \leq$ fiber radius a [19].

$$dP_{inc} = I_0 \cos\theta_0 \, dA \, d\Omega \qquad 2.21$$

where θ_0 is the polar angle measured from the fibre axis, dA is the area element on the fibre end face and I_0 is the optical radiance of the source. The launch lens has a NA that cuts off the power at an angle θ_0^{max}. The polar co-ordinates (r,ϕ) define the position of the entering ray on the fibre end face and (θ,ψ) describe the spherical polar directions for rays entering at the point (r,ψ).

Using mainly equations 2.19 to 2.21 and invoking standard trigonometric relationships, Love et al. obtained an expression for the total fluorescence signal, S_{tot}, over the rays launched within the illuminated spot on the fibre end face and within the cone of angles $\theta_0 \leq \theta_0^{max}$ [19]

$$S_{tot} = \left(\frac{\pi\gamma I_0 L}{a n_1}\right) \int_0^{r_{max}} r dr \int_0^{2\pi} d\psi \int_0^{\theta_0^{max}} \sin^2\theta_0 \cos\theta_0 \, d\theta_0 \qquad 2.22$$

$$\times \begin{cases} \int_0^{\infty} F_{abs}\left(\delta;\theta[\theta_0,\psi,r/a]\right) p_{emit}\left(\delta;\theta_0^{max}\right) d\delta & (bulk\ case) \\ h \times F_{abs}\left(\delta=0;\theta[\theta_0,\psi,r/a]\right) p_{emit}\left(\delta=0;\theta_0^{max}\right) & (thin-film\ case) \end{cases}$$

The dependence of the normalised fluorescence signal, S_{tot}, on $\sin\theta_0^{max}$ was obtained by numerical integration of equation 2.22, for a bulk solution of fluorescence molecules and also for two surface coatings of thickness 0.1λ and 0.01λ. The relationship between S_{tot} and $\sin\theta_0^{max}$ displayed an approximately eighth power dependence, except for the bulk case at higher values of $\sin\theta_0^{max}$. This agrees closely with experimental results also published by Love et al. [24], where they carried out a series of experiments to consider the effect of launch angle, spot size and numerical aperture of the material (NA_{mat}) upon the detected fluorescence signal, S_{tot}. It appears from these data that there is very little difference in detected fluorescence signal between a surface coating of $\theta.1\lambda$ and the bulk situation. The evaluation of detected fluorescence signal, S_{tot}, for various spot sizes, r_{max}/a, was also carried out by Love et al. [19]. Results indicate an approximate $(r_{max}/a)^2$ dependence which agrees with their experimental measurements.

Finally, S_{tot} was found to be proportional to NA_{matl}^{-4} for surface molecules, and to NA_{matl}^{-4} - NA_{matl}^{-7} for the bulk case over the range 0.6 to 0.45 for NA_{matl}. Their experimental results tend to agree more consistently with the surface case i.e. a NA^{-4} dependence, which are attributed to adsorption of the fluorescein dye to the fibre surface. Therefore, for fluorescent molecules close to the core-cladding interface, the total fluorescence signal is given by

$$S_{tot} \propto I_0 \gamma L a \left(\frac{r_{max}}{a}\right)^2 \sin^8 \theta_0{}^{max} (NA)_{matl}{}^{-4} \qquad 2.23$$

Equation 2.23 emphasises the importance of launching and maintaining high angle light through the fibre. Sensitivity with an eight power dependence on launch aperture was also demonstrated by Hirschfeld [24], and the importance of maintaining high angle light propagation for maximum fluorescence signal was demonstrated both experimentally and theoretically by Glass et al.[18]

2.5.3 Evanescent coupling efficiency - Weakly guiding approximation

A number of workers studied the particular issues of collection of fluorescence into guided modes of an optical fibre. A more rigorous approach to this problem of evanescent wave coupling efficiency based on electromagnetic wave theory, was carried out by Marcuse in 1988 [20]. He used the weakly guiding approximation and Maxwell's equations to model the coupling efficiency of light into the cores of optical fibres, from fluorescent sources that are located in its cladding region. In his work the 'collection efficiency' is defined as the ratio of light collected in the fiber core relative to the total amount of light radiated by the fluorescent sources. The fiber was assumed to have an infinite cladding and both positively and negatively guiding fibers, i.e. $n_{core} > n_{clad}$ and $n_{clad} > n_{core}$ were treated. Assuming each source in the cladding to be an infinitesimal electric current, with random phase and orientation, which excite radiation fields and bound modes, Marcuse analysed two different source distributions:

1. sources that are concentrated in the core cladding boundary
2. sources that are uniformly distributed in the cladding

The bound modes are trapped inside the core and propagate in both forward and backward directions [25].To calculate the power only in the forward propagating modes, the total electric field in the core, **E**, can be expressed as the superposition of the modal fields, $\mathbf{E}_\upsilon$, with expansion coefficients c_υ [20,25].

$$\mathbf{E} = \sum_{\upsilon} c_\upsilon \mathbf{E}_\upsilon \qquad 2.24$$

The sum in equation 2.24 extends over all propagating modes; the modal fields $\mathbf{E}_\upsilon$ are given by Snyder and Love [25] in table 12-3. The expansion coefficients of the modes are obtained as an integral over the product of the source current density **j** and the electric field vector of the mode [25]. They can be expressed as [20]

$$c_\upsilon = \frac{1}{4P_\upsilon}\int_{V\text{source}} \mathbf{j}.\mathbf{E}_\upsilon \, dV \qquad 2.25$$

where V_{source} is the volume occupied by the cladding sources and P_υ is the power carried by each mode. Taking the sum over all modes, the total power due to the bound modes, P_{core}, is given by

$$P_{core} = \sum_{\upsilon} |c_\upsilon|^2 P_\upsilon \qquad 2.26$$

However, since there are many sources distributed in the cladding and they have random phase and orientation, the ensemble average of the total power of the field can be written as

$$P_{core} = \sum_{\upsilon} \left\langle |c_\upsilon|^2 \right\rangle P_\upsilon \qquad 2.27$$

The correlation function of the current density vector of the light sources is assumed to have the form [20]

$$\langle \mathbf{j}(\mathbf{r})\,\mathbf{j}(\mathbf{r}')\rangle = IS\delta(\mathbf{r}-\mathbf{r}') \qquad 2.28$$

where S indicates the source strength, I is a unit tensor and $\delta(\mathbf{r} - \mathbf{r}')$ is a three dimensional Dirac delta function. The ensemble average of the absolute square of the field expansion coefficients follows from equations 2.25 and 2.28 as [20]

$$\langle |c_\upsilon|^2 \rangle = \frac{1}{16P_\upsilon^2}\int_{V_{source}} S\,|\mathbf{E}_\upsilon|^2\,dV \qquad 2.29$$

The volume integral extends over the region occupied by light sources. Therefore the power injected into bound modes may be written as follows [20,27]

$$P_{core} = \sum_\upsilon \frac{1}{16P_\upsilon}\int_{V_{source}} S|\mathbf{E}_\upsilon|^2\,dV \qquad 2.30$$

Marcuse has shown that the source strength, S, is related to the power, R, that is radiated by a unit volume of source filled material into the unit element of solid angle in homogeneous space filled with the cladding material, as follows [26]

$$S = \frac{16\pi^2}{\omega\mu_0 nk}R \qquad 2.31$$

where μ_0 is the magnetic permeability of the vacuum. The total power radiated into the homogenous space of refractive index n by sources uniformly distributed between radii a and b along a length L of fibre is related to R as follows [20]

$$P_{rad} = 4\pi^2(b^2-a^2)LR \qquad 2.32$$

Using equations 2.30 to 2.32 and the weak-guidance approximation[1] for the description of a guided modes, the excitation efficiency of the positively guiding fiber, for an infinitesimally thin source-filled region at the core-cladding interface is described by [20]

$$\frac{P_{core}}{P_{rad}} = \frac{1}{2n_{core}{}^2 k^2 V^2 a^2} \sum_{\upsilon} \frac{(W)^2 J^2{}_{\upsilon}(U)}{\left|J_{\upsilon-1}(U) J_{\upsilon+1}(U)\right|} \qquad 2.33$$

where J_υ is the Bessel function of order υ, V is the normalised frequency parameter[2]. The propagation constant, β, of the mode for a core of radius a, is related to its radial propagation constant by

$$U = a\sqrt{n_{core}{}^2 k^2 - \beta^2} \qquad 2.34$$

while the cladding decay parameters of the guided mode field in the cladding is defined as

$$W = a\sqrt{\beta^2 - n_{clad}{}^2 k^2} \qquad 2.35$$

Marcuse also treats the case in which the sources are uniformly distributed between radii a and b, where the outer radius b is large enough to ensure that the evanescent field tails of the modes have decayed to insignificant values. He calculated the collection efficiency in this case to have the following form [20]:

$$\frac{P_{core}}{P_{rad}} = \frac{1}{2n_{clad}^2 k^2 V^2 \left(b^2 - a^2\right)} \sum_{\upsilon} \left\{ \frac{(W)^2 J_{\upsilon}^2(U)}{\left|J_{\upsilon-1}(U) J_{\upsilon+1}(U)\right|} \cdot \left[\frac{K_{\upsilon-1}(W) K_{\upsilon+1}(W)}{K_{\upsilon}^2(W)} - 1 \right] \right\} \qquad 2.36$$

[1] The magnitude n_1 and n_2 are assumed to be close together, so that the waveguide is weakly guiding i.e. $\Delta = (n_1{}^2 - n_2{}^2)/2n_1{}^2 \leq 1$, where Δ is the refractive index difference.

[2] Normalised frequency parameter, or fibre V-number is defined as $V=(2\pi a/\lambda_0)NA$, where λ_0 is the vacuum wavelength, a is the core radius and NA is the numerical aperture.

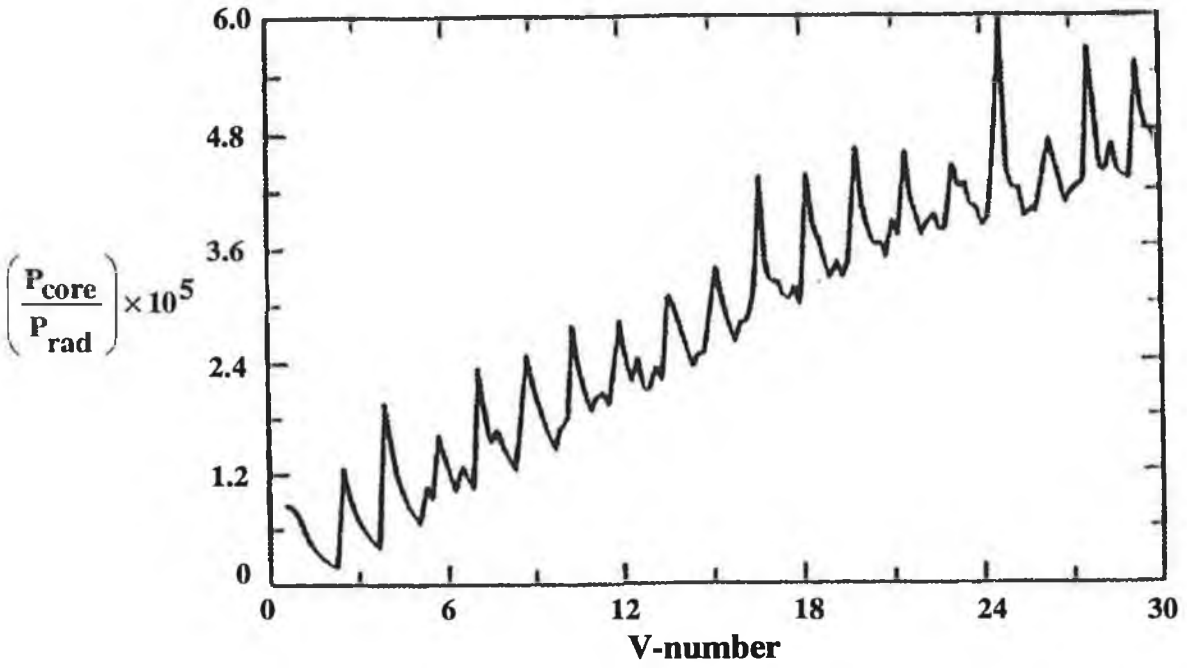

figure 2.7 Light collection efficiency of a positively guiding fiber as a function of V. The wavelength and core radius are set at 1.3μm and 10μm. The light sources are distributed between a < r < b with b/a = 5 [20].

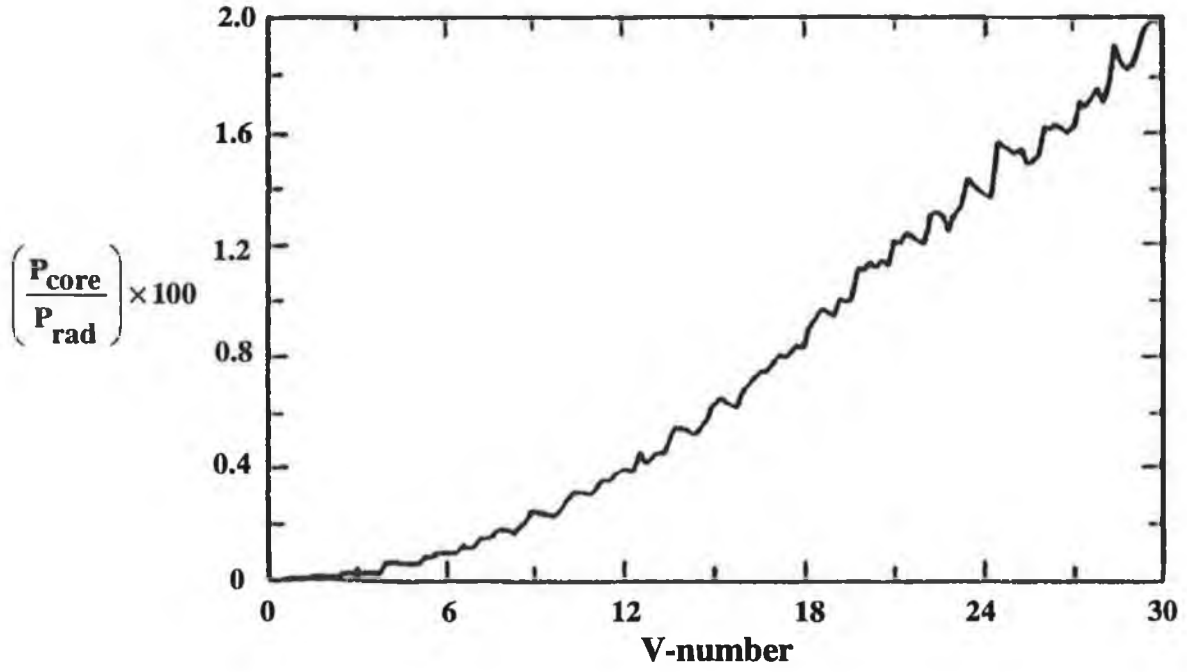

figure 2.8 . This data is similar to figure 2.7 except that the light sources are concentrated in a thin layer at the core-cladding interface [20].

where K_υ is the modified Bessel function of the second kind of order υ.

Analysis of Marcuse's work shows that the cladding to core coupling coefficient increases linearly with V-number for the bulk film case as shown in figure 2.7. However, a parabolic dependence was found for the thin film situation as shown in figure 2.8. The coupling coefficient also scales inversely as the cladding cross sectional area and the square of the wavenumber of light. The thin film case was found to have a coupling coefficient higher than the bulk by a factor of 10^3. The jagged appearance for the bulk case is due to the fact that a sharp increase occurs in the penetration depth as the mode group approaches cut-off.

2.5.4 Evanescent coupling efficiency - Exact solutions to the fields

Egalon extended Marcuse's work in a treatment of positively guiding fibers for both thin film [27] and bulk distribution [28] of fluorescence sources within the cladding. Egalon used the exact solution of the cylindrical optical fibre with an infinite cladding and thus allowed arbitrary differences between the refractive indices of the core and cladding to be taken into account. Such an approach is not limited to weakly-guiding fibres. The derivation of the expressions for the power associated with both the radiation field, P_{rad}, and bound modes, P_{core}, can be found in publications by Egalon [16,27,28] and are given by

$$P_{rad} = \sqrt{\frac{\mu_0}{\varepsilon_0}} \frac{n_{clad} k^2 SL}{4} \left(r_{out}^{\,2} - r_{in}^{\,2} \right) \qquad 2.37$$

$$P_{core} = \sum_{\upsilon,\mu} \frac{1}{16 P_{\upsilon,\mu}} \int_{V_{source}} S \left| \mathbf{E}_{\upsilon,\mu}(r) \right|^2 dV \qquad 2.38$$

where L is the length of the fibre coated with fluorescent sources, S is the source strength, k is the wavenumber of the fluorescent light, n_{clad} is the refractive index of the cladding, $\mathbf{E}_{\upsilon,\mu}$ is the modal electric field as described by Synder and Love[24] , and r_{out} and r_{in} are the inner and outer radii of source distribution as illustrated in figure 2.9.

As previously defined, the power efficiency for a fibre coated with fluorescent

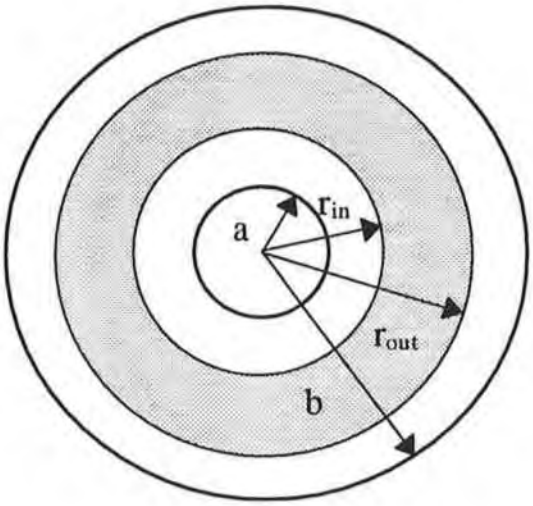

figure 2.9 Sources uniformly distributed in the cladding between r_{in} and r_{out} [28]

sources at the core/cladding interface, where $P_{rad} >> P_{core}$ can be written as [27]

$$\frac{P_{core}}{P_{rad}} = \frac{\sqrt{\varepsilon_0 / \mu_0}}{8a\delta Ln_{clad}k^2} \sum_{\upsilon,\mu} \frac{1}{P_{\upsilon,\mu}} \int_{V_{source}} \left|\mathbf{E}_{\upsilon,\mu}\right|^2 dV \qquad 2.39$$

where δ is the thickness of the fluorescent film. For the weakly guiding case, the integral in equation 2.39 has the same functional form for every mode and when calculated is similar to those of Marcuse [20] i.e. equations 2.33 and 2.36. However, for the exact case, the integral in equation 2.39 has to be calculated for each mode separately i.e. transverse electric ($TE_{0,\mu}$), transverse magnetic ($TM_{0,\mu}$) and hybrid modes ($HE_{0,\mu}$ and $HE_{0,\mu}$). The results for a thin-film distribution [27] and bulk distribution [28] were developed by Egalon.

Egalon uses his model to examine the behaviour of coupling efficiency while varying the fibre V-number parameters. Marcuse increased the V-number in his work, by increasing the difference in the core-cladding index difference i.e. Δn, with the other fibre parameters held constant. Egalon examined variations in V-number by changing

wavelength, core diameter and refractive index difference, and also included the case where the V-number is kept constant by changing two of its variables.

Egalon's model predicts that a thin film distribution in the core-cladding boundary is more efficient than a bulk one. However, the total power radiated by the thin film is lower than in the bulk case, because there are fewer sources present. The highest probability of excitation into bound modes is found, when the thin film is closest to the core-cladding interface as would be expected. However, Egalon found that for bulk distribution, the longer the wavelength the higher the power efficiency i.e. the lower the V-number the higher the power efficiency, which is contrary to the predictions of Marcuse's model. In the case of a thin film distribution, the coupling efficiency remains almost constant over the spectrum of values chosen by Egalon. In a similar way, Egalon varied the core radius for both thin film and bulk film distributions and examined its dependence on coupling efficiency. For a bulk distribution he found that the power efficiency decreases with increasing core radius. This result is also contrary to Marcuse's model in that the coupling efficiency decreases with V-number. A sharp increase in coupling efficiency was found for thin film distribution at low V-number, but was found to stabilise as the core radius was increased. Egalon also investigated the dependence of power efficiency on Δn, for both bulk and thin film distributions at constant V-number. The model predicted that the greater the difference between the indices of refraction, the higher the power efficiency. Figure 2.10 shows the dependence of the coupling efficiency on Δn for constant V-numbers for a thin-film situation [16]. The results were obtained for four different V-numbers and are plotted on a log-log scale. Using a linear equation, Egalon found a correlation coefficient of 1.0 for the first three V-numbers. For the fourth V-number of 62.83, the correlation coefficient was found to be 0.998 for a linear equation and 1.0 for a quadratic one i.e. the higher the V-number the more the graph deviates from a linear equation on a log-log scale. These data show that the high value of coupling efficiency at high V-number is not due to the increase in V-number but to the bigger differences between the indices of refraction. In 1994 Albin et al. [29] published work that verified this dependence on refractive index difference. The data in figure 2.11 simulates a bare fibre core coated with a thin film of fluorescent material of refractive index 1.0. As expected, the coupling efficiency was found to increase with n_{core}. The

increase in coupling efficiency was found to be almost linear with Δn. Table 2.1 summarises the results of Egalon's model.

Egalon has also carried out an investigation of the dependence of coupling efficiency on the polarization of the fluorescent emission [30]. Results show that sources polarized parallel to one another and perpendicular to the axis of the fibre couple fluorescence emission to guided modes approximately 1.2 times as well as do randomly orientated sources, and nearly twice as well as do sources, that emit photons with their polarisation vectors parallel to the axis of the fibre.

INCREASING PARAMETER	λ	a	Δn
BULK	P_{eff} increases	P_{eff} decreases	P_{eff} increases
THIN FILM	P_{eff} constant	P_{eff} increases at small values, then remains constant	P_{eff} increases

table 2.1 Factors affecting evanescent coupling efficiency, P_{eff}, from cladding to core [16].

2.6 Conclusion

The concept of the evanescent wave and evanescent wave spectroscopy has been introduced. A geometric optic approach to describe the parameters that influence the total captured signal of a fibre optic evanescent wave fluorosensor has been described. The analysis suggests that the captured fluorescent signal increases, i) linearly with length of fluorescent coating, ii) to the square of launch spot size, iii) to minus the fourth power of the material numerical aperture, iv) to the eighth power of sin of the launching angle. The third parameter here describes the effect of increasing the difference between refractive index of fibre core and cladding, whereas the fourth parameter emphasises the importance of designing fluorosensors with high angle collection. A different approach based on the electromagnetic wave theory which describes the coupling efficiency, cladding to core, of fluorescent sources has also been treated. This model uses the weak-guidance approximation and concludes that the coupling efficiency of both thin films and bulk films increase with V-number of optical fibre. This model was later extended to

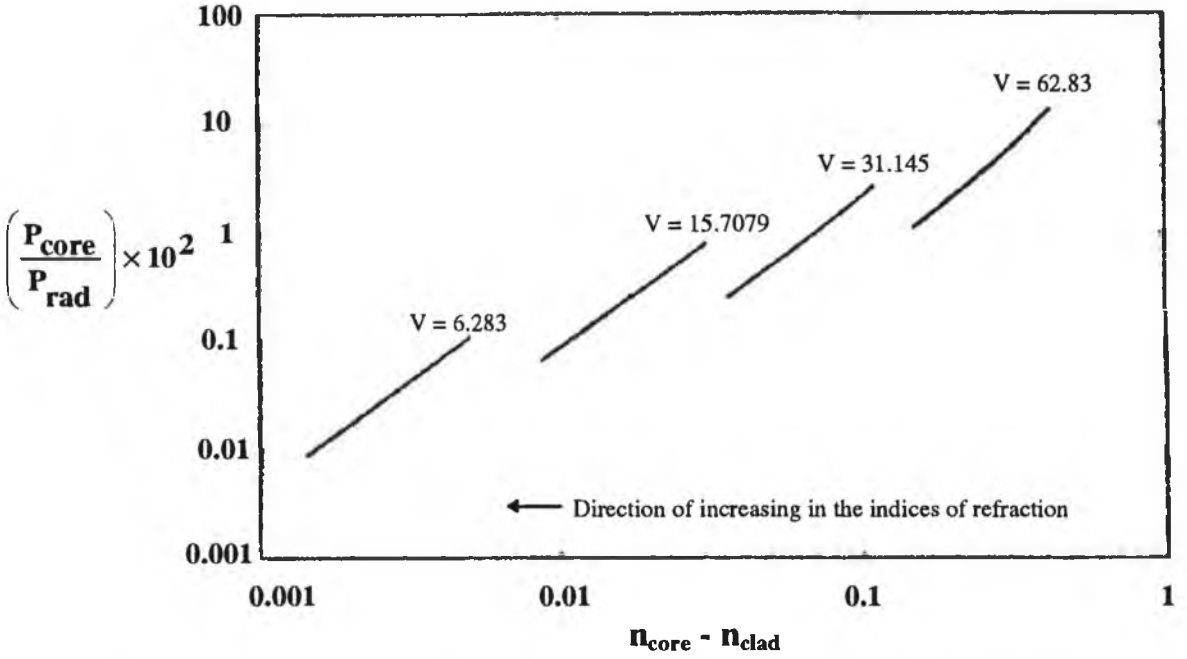

figure 2.10 Coupling efficiency of a thin-film distribution of sources versus the difference n_{core} - n_{clad}. The core radius and the wavelength are held fixed at 6.0μm and 0.6μm respectively [16,29] .

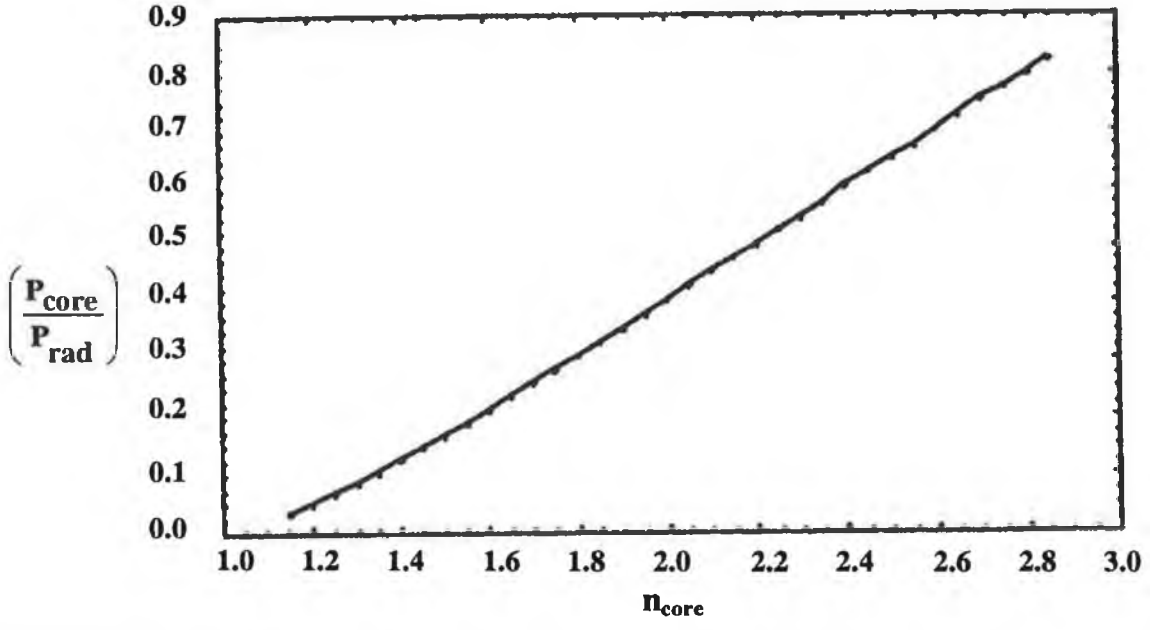

figure 2.11 Coupling efficiency of a thin-film distribution of sources versus the index of refraction of the core n_{core}. The core radius, the wavelength and the index of refraction of the cladding are held constant at 5.0μm, 0.6μm and 1.0 respectively [16,29].

include arbitrary differences between the refractive indices of the core and cladding. This work which calculates the coupling efficiency of each separate mode shows that the fluorescence coupling efficiency does not necessarily increase with fibre V-number. However, it was found to increase with the difference between the refractive index of fibre core and cladding, which is in qualitative agreement with the predictions of the geometric optic model. Experimental evidence of this was reported in 1994. A similar experiment is described in section 5.4.4

References

1. Newton I.: '**Optiks II, Book 8'**,1817, p97

2. Taylor A.M. et al.: '**Studies in refractive index I and II**', Journal of the Optical Society of America, 1933, Vol. 33, p. 202

3. Fahrenfort J.: '**Attenuated total reflection: A new principle for the production of useful infrared reflection spectra of organic compounds**', Spectrochimica Acta, 1962, pp. 698

4. Harrick N.J.: '**Surface chemistry from spectral analysis of totally reflected radiation**', Journal of Physical Chemistry, 1960, Vol. 64, p.1110

5. Tai H., Tanaka H., Yoshino T.: '**Fibre-optic evanescent-wave methane-gas sensor using optical absorption for the 3.392μm line of a HeNe laser**', Optics Letters, 1987, Vol. 12, No. 6, pp. 437-439

6. Sanghera J.S., Kung F.H., Pureza P.C., Nguyen V.Q., Milkos R.E., Aggarwal I.D.: '**Infrared evanescent-absorption spectroscopy with chalogenide glass fibre**', Applied Optics, 1994, Vol. 33, No. 27, pp. 6315- 6322

7. Hirschfeld T.: '**Total reflection fluorescence**', Can. Spectroscopy, Vol. 10, p. 128

8. Kronick M.N., Little W.A.: '**A new immunoassay based on fluorescence by internal reflection spectroscopy**', Journal of Immunological Methods', 1975, Vol. 8, p. 235

9. Sutherland R.M., Dahne C., Slovacek R., Bluestein B.: '**Interface immunoassays using the evanescent wave, nonisotopic immunoassay**', Ngo T.T. (Ed.), Plenum, New York.

10. Hirschfeld T.B., Block M.J.: '**Assay apparatus and method**', 1984, U.S. Patent 4,447,014

11. Hirschfeld T.B., Block M.J.: '**Fluorescent immunoassay employing optical fibres in capillary tube**', 1984, U.S. Patent 4,447,546

12. Sutherland R.M., Dahne C.: '**Optical detection of antibody-antigen reactions at a glass liquid interface**', Clinical Chemistry, 1984, Vol. 30, p. 1533

13. Andrade J.D., Van Wagenan R.A., Gregonis D.E., Newby K., Lin J.N.: '**Remote fibre optic biosensors based on evanescent-excited fluoro-immunoassay: concept and progress**', IEEE Transactions of Electronic Devices, 1985, Vol. 32, p. 1175

14. Harrick N.J.: '**Internal reflection spectroscopy**', 1985, Harrick Scientific Corporation.

15. Wise D.L., Wingard L.B.: '**Biosensors with fiberoptics**', 1991, Humana Press Inc., New Jersey

16. Egalon C.O.: '**Injection efficiency of bound modes**', NASA Contractor Report 4333, 1990

17. McCabe S.: '**An investigation of evanescent wave gas sensing using zirconium fluoride optical fibre**', Ph.D. Thesis, 1994, pp. 18-20

18. Glass T.R., Lackie S., Hirschfeld T.: '**Effect of numerical aperture on signal level in cylindrical waveguide evanescent fluorosensors**', Applied Optics, 1988, Vol. 26, No. 11, pp. 2181-2187

19. Love F.W., Button L.J., Slovacek R.E.,: '**Optical characteristics of fiberoptic evanescent sensors', Biosensors with fiberoptics**', Wise and Winegard (Eds.), 1991, The Humana Press Inc., pp. 139-180

20. Marcuse D.: '**Launching light into fiber cores from sources located in the cladding**', Journal of lightwave technology, 19XX, Vol. 6, No. 8, pp. 1273-1279

21. Lieberman R.A., Blyler L.L., Cohen L.G.: '**Distributed fiber optic sensor based on cladding fluorescence**', IEEE Journal of Lightwave Technology, 1990, Vol. 8, No 2, p. 212

22. Lukosz W., Kunz R.E.: '**Light emission by magnetic and electric dipoles to a plane interface. I. Total radiated power**', Journal of the Optical Society of America, 1979, Vol. 67, pp. 1607-1615

23. Lukosz W., Kunz R.E.: '**Light emission by magnetic and electric dipoles to a plane dielectric interface. II. Radiation patterns of perpendicular dipoles**', Journal of the optical Society of America, 1979, Vol. 69, pp. 1615-1620

24. Hirschfeld T.: '**Apparatus for improving the numerical aperture at the input of a fibre device**', 1987, U.S. Patent 4,654,532

25. Synder A.W., Love J.D.: 'Optical Waveguide Theory', 1983, Chapman and Hall, New York.

26. Marcuse D.: '**Excitation of parabolic-index fibres with incoherent sources**', Bell Syst. Tech. J., 1975, Vol. 54, pp. 1507-1530

27. Egalon C.O., Rogowski R.S.: '**Theoretical model for a thin cylindrical film optical fiber fluorosensor**', Optical Engineering, 1992, Vol. 31, No. 2, pp. 237-244

28. Egalon C.O., Rogowski R.S.: '**Efficiency of core light injection from sources in the cladding: bulk distribution**', Optical Engineering, 1992, Vol. 31, No. 4, pp. 846-851

29. Albin S., Bryant A.L., Egalon C.O., Rogowski R.S.: '**Injection efficiency from a side-excited thin-film fluorescent cladding of a circular waveguide**', Optical Engineering, 1994, Vol. 33, No. 4, pp. 1172-1175

30. Egalon C.O, Rogowski R.S.: '**Source polarization effects in an optical fiber fluorosensor**', Optical Engineering, 1992, Vol. 31, No. 10, pp. 2213-2217

Chapter Three - Fluorescence Spectroscopy

3.1 Introduction

The sensors investigated in this work all involve fluorescence emission. The fluorescence process can be explained by the emission of a photon of light, from a molecule which has been placed in the excited state by the absorption of another photon. The emitted photon is generally of a lower energy than that of the absorbed photon due to energy loss encountered during internal conversion. General features of the absorption and emission of light can be illustrated using an energy level diagram as shown in figure 3.1. Each molecular decay step is characterised by its own rate constant, k. (It is important to note that by convention, the symbol k is used both for the rate constant which is used throughout chapter three, and the propagation constant of an electromagnetic wave used in chapter two). The electronic states of the system are depicted by S_0, S_1 and S_2 respectively. At each of these electronic energy levels the fluorescent substance (fluorophore) can exist in a number of vibrational states as illustrated. The excited state molecule rapidly relaxes, with very high efficiency, to the lowest excited electronic state (S_1). The energy stored in the excited state may then be released in several ways. The electron may return to the electronic ground state with the release of heat, i.e. non-radiative decay (k_{nr}). After relaxing thermally to the lowest

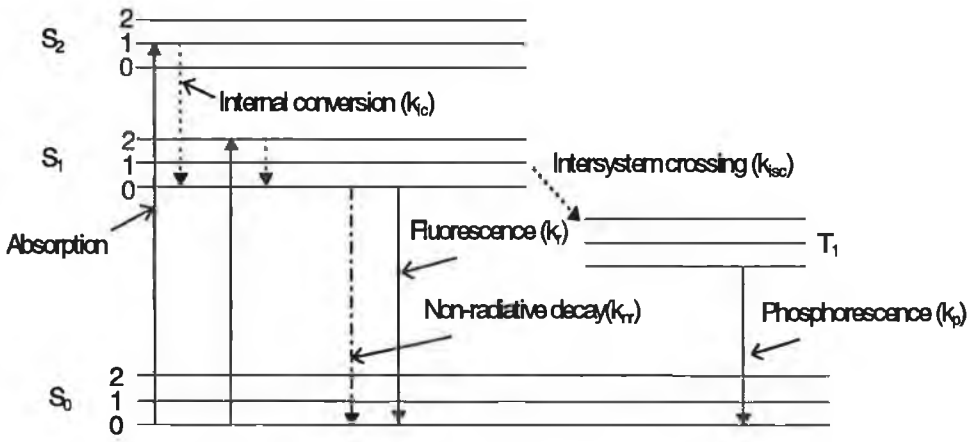

figure 3.1 Energy level diagram showing molecular and electronic energy levels

vibrational level of the S_1 state, the electron may return to the S_0 state with light emission i.e. fluorescence or radiative decay (k_r). Some type of reaction which may occur with another species present may result in de-energization of the excited state i.e. a quenching process. Alternatively, if the molecule is sufficiently long lived in the S_1 state, it may cross into a lower energy triplet state (T_1). Relaxation from this triplet state to the ground state can also occur with light emission, this is known as phosphorescence.

The probability of light absorption or emission from a particular energy level is related to the characteristics of the states involved and particularly to their spin quantum number. Each electron in a molecule carries a spin angular momentum with a spin quantum number s = ½. The total spin angular momentum possessed by a many electron atom or molecule is represented by the total spin quantum number S, which may be calculated as the vector sum of all the individual contributions from each electron. Two electrons possessing s = ½ may be present with their spins parallel or opposed. If the spins are opposed the total spin quantum number S is zero. If the electron spins are parallel the total quantum number is 1. The spin multiplicity gives the number of states expected in the presence of an applied magnetic field and is given as 2S+1. Thus a molecule with all electrons spin-paired possesses S = 0 and a spin multiplicity of 1. Such an electronic state is referred to as a singlet state e.g. S_0, S_1 and S_2 of figure 3.1. If however, there exists a means of changing the spin of the excited electron so that it becomes aligned parallel to the electron "left behind", the excited state will be generated with a total spin quantum number of 1, and therefore a spin multiplicity of 3. This is termed a triplet state, e.g. T_1 of figure 3.1. Transitions from the ground state to excited states having the same spin value are allowed and give rise to intense absorption bands, whereas transitions to excited states of different spin values are forbidden and can hardly be observed in the absorption spectrum. Fluorescence and internal conversion are spin allowed steps whereas phosphorescence and intersystem crossing are spin-forbidden steps and are therefore less likely to be observed [1,2].

As previously stated, all the sensors in this work involve fluorescence emission. A method for monitoring the variation of the concentration of oxygen is by the change of fluorescence intensity or the fluorescence lifetime of a quenchable fluorophore. Oxygen is well known to be a dynamic quencher of fluorescence and can thus be monitored by

fluorescence methods [3]. The observed fluorescence intensity of a fluorophore, in the observation wavelength interval λ_1 to λ_2, can be described by the following expression [4]

$$I_{\lambda_{1,2}} = I_{abs} \cdot \eta \cdot \Gamma \cdot \int_{\lambda_2}^{\lambda_1} f_{em}(\lambda) d\lambda \qquad 3.1$$

where

$$I_{abs} = \int_{\lambda_4}^{\lambda_3} f_{abs}(\lambda) \cdot I_{ex}(\lambda) d\lambda \qquad 3.2$$

and where η is the fluorescence quantum yield, $f_{em}(\lambda)$ the spectral distribution of the fluorescence spectrum, $f_{abs}(\lambda)$ the spectral distribution of the absorbance of the fluorophore, $I_{ex}(\lambda)$ the spectral intensity of the source, and Γ a geometrical factor. The fluorescence quantum yield is defined for a particular fluorophore as the ratio of the number of photons emitted to the number absorbed and can be written in terms of the radiative and non-radiative decay constants as follows:

$$\eta = \frac{k_r}{k_r + k_{nr}} \qquad 3.3$$

It is clear from equation 3.3 that as fluorescence quenching increases, the fluorescence quantum yield decreases. Therefore, from equation 3.1 we can write

$$\frac{\eta_0}{\eta} = \frac{I_0}{I} \qquad 3.4$$

where η_0 is the fluorescence quantum yield in the absence of oxygen, η is the fluorescence quantum yield in the presence of oxygen, I_0 is the fluorescence intensity in the absence of oxygen and I is the fluorescence intensity in the presence of oxygen.

An important parameter in fluorescence spectroscopy is the fluorescence lifetime. The fluorescence lifetime of an excited state is by definition the time required for the excited state population to decay to 1/e of its initial value, following excitation by an impulse of light. The impulse response function, I(t), in the simplest case of a single exponential will have the following form:

$$I(t) = I_0 \exp(-\mathbf{k}t) \qquad 3.5$$

where I_0 is the intensity at t = 0 and **k** represents the overall relaxation rate for the probed excited state. The value of **k** is given by

$$\mathbf{k} = k_r + k_{nr} \qquad 3.6$$

where k_r and k_{nr} are the radiative and non-radiative decay constants. From equation 3.5 it follows that the fluorescence lifetime can therefore be written as [5]

$$\tau = \frac{1}{k_r + k_{nr}} \qquad 3.7$$

The fluorescence lifetime typically has a value in the order of tens or hundreds of nanoseconds. Fluorescence quenching may also take place, during which the excited states are deenergized, without the emission of a photon. This results in a lower fluorescence intensity and a shorter fluorescence lifetime. Demas et al. have shown that a variety of ruthenium(II), osmium(II) and iridium(III) complexes are very susceptible to oxygen quenching in solution [6]. Ruthenium polypyridyl compounds have been shown to be particularly attractive as oxygen sensing species (see section 3.2). The fluorescence quenching process of any such complex, when entirely collisional, can be described by the Stern-Volmer equations, which relate the variation in fluorescence intensity, I, and fluorescence lifetime, τ, with oxygen partial pressure i.e.

$$I_0 / I = 1 + K_{SV}[O_2] \qquad 3.8$$

$$\tau_0 / \tau = 1 + K_{SV}[O_2] \quad 3.9$$

$$K_{SV} = k\tau_0 = \alpha D\tau_0 \quad 3.10$$

where I_0 and τ_0 are, respectively, the fluorescence intensity and excited state lifetime in the absence of oxygen, K_{SV} is the Stern-Volmer quenching constant, k is the bimolecular quenching constant and $[O_2]$ is the oxygen concentration. The bimolecular quenching constant is the product of D, the oxygen diffusion coefficient in the fluorophore environment and, α, the oxygen solubility factor in the environment of the fluorophore [7].

In this chapter, the chemistry of oxygen sensing transition metal complexes is discussed. The process of fluorescence quenching and its dependence on ambient temperature is examined. The influence of heterogeneous environments, such as that of the sol-gel structure, on the fluorescence lifetime of the complex is also discussed. Finally, the principle of phase fluorimetry as a method of lifetime measurement is outlined.

3.2 Transition metal complexes for oxygen sensing

Organic dyes [8,9] and polycyclic aromatic hydrocarbons [10] have been used in the past as luminescent indicators for oxygen sensing. However, an increasingly important class of sensor materials is luminescent metal complexes, especially those of the platinum metals (i.e. Ru, Pd, Os, Ir, Pt). The photochemical and photophysical properties of these materials have been studied extensively by Demas et al. [11,12], Juris et al. [2], Van Houten et al. [13] and Durham et al. [14]. These materials have many desirable features for use as sensing probes. These include high quantum yields and long unquenched lifetimes (microseconds), resulting in high sensitivity as indicated by equations 3.8 to 3.10. Long lifetimes are much simpler and less expensive to measure. These complexes also can absorb intensely in the blue-green region of the spectrum, for which a wide range of suitable laser and light emitting diodes (LED) are available, and

have a large Stokes shift. They also tend to be thermally, chemically and photochemically stable, thus reducing the problem of photodecomposition resulting in extended sensor lifetime [12].

Transition metal complexes are characterised by partially filled d orbitals. The emissive properties of these complexes are determined by the occupancy of these orbitals. A simplified orbital and spectroscopic state diagram, for a typical octahedral structured complex is shown in fig 3.2. The octahedral crystal field of the ligands, splits the five degenerate d orbitals by an amount Δ, into a triply degenerate t_2 level and a doubly degenerate e level as illustrated. The splitting arises because the e orbitals are directed toward the six ligands and the remaining t_2 orbitals points between the ligands. The amount of the crystal field splitting Δ, can therefore, be controlled by altering the ligand geometry or central metal ion [12]. This allows the chemist to control the luminescent properties of the complex to an extent. The distribution of electrons between the t_2 and e levels is strongly affected by Δ. If Δ is large, it is energetically more favourable to pair electrons in the t_2 level than to keep them unpaired by distributing them throughout the t_2

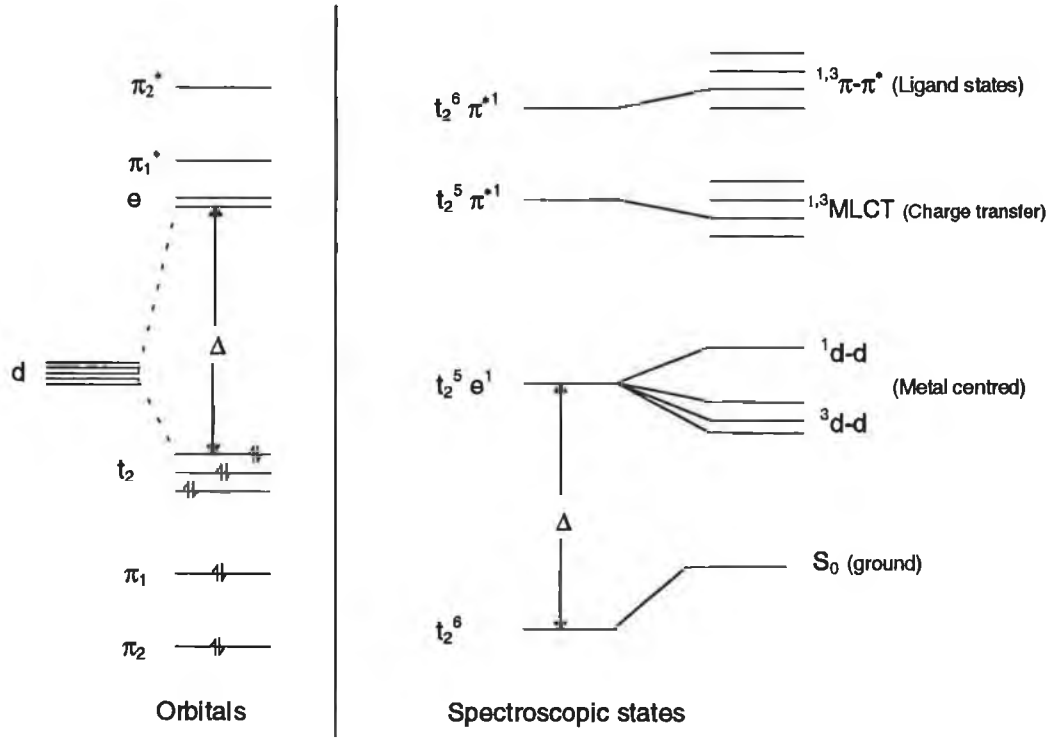

figure 3.2 Simplified orbital and state diagrams for a d^6 metal in an octahedral environment [12].

and e levels. This pairing scheme contradicts Hund's Rule [15]. The ligands have π and σ orbitals but only the π orbitals are spectroscopically important for visible and near ultra violet absorption and emission. There are both π bonding and π antibonding (π^*) levels; however, only the π bonding levels are filled [12].

Within such an octahedral environment, three types of excited states are of spectroscopic importance. Firstly, a d electron can be promoted to another d level i.e. a d-d transition. Secondly, an electron from a π bonding orbital can be promoted to a π^* antibonding orbital i.e. a π-π^* transition. Thirdly, a d electron can be promoted to a π^* antibonding orbital, or an electron in a π bonding orbital can be promoted to an unfilled d orbital. These last two options are known as metal to ligand charge transfer states (MLCT) and ligand to metal charge transfer state (LMCT), respectively [12].

The lowest ligand excited states are π-π^* states derived from promoting a bonding π electron to a π^* level. There are triplet and singlet states possible, the triplet being always below its analogous singlet state. These transitions are localised on the organic ligands and are spectroscopically similar to those of the free ligand [12]. Similarly, singlet and triplet d-d states arise from promoting a t_2 electron to an e level. d-d transitions are formally forbidden, even for the allowed singlet-singlet ones, thus d-d emissions are characterised by long radiative lifetimes and a high susceptibility to environmental quenching. This results in low luminescence yields at room temperature [12]. Charge transfer transitions, however, tend to be more strongly allowed and are less susceptible to intermolecular and environmental quenching. The molar extinction coefficients of the spin-allowed transitions are large, which makes these charge transfer states easier to pump optically [12].

The control of the luminescence properties of the complexes hinges on the control of the relative energies of the excited states and on the nature and energy of the lowest excited state [12]. Choice of an appropriate ion and ligand are factors that determine the relative energies of the excited states. Optimum oxygen sensing characteristics are achieved when the relative positions of the ^{3}d-d, $^3\pi$-π^* and ^{3}MLCT states are as shown in fig 3.3, i.e. the metal to ligand charge transfer transition has the lowest energy with respect to the other possible transitions. This state is therefore largely responsible for the absorption and emission characteristics of the transition metal complex. The relatively

long lifetimes of the charge transfer states are responsible for the high susceptibility to oxygen quenching. Any d-d states must be well above the emitting level so that they cannot be reached by thermal excitation from the emitting state. Thermal excitation of the d-d states results in photochemical instability and excitation state deactivation (see section 3.2.4). In the design of these luminescence probes it is also important that the emitting state is not too close to the ground state in energy. The energy gap law states that radiationless process become more efficient as the emitting state approaches the ground state [2].

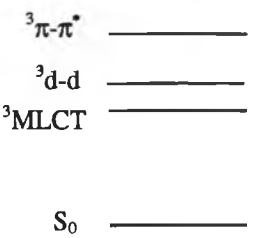

figure 3.3 Lowest triplet state ordering for O_2 sensing

α-diimine ligands such as bipyridine, phenanthroline and tris-diphenylphenanthroline (see figure 3.4), with ruthenium as a central ion, have appropriate crystal field strengths for the energy displacement shown in figure 3.3 to occur. Because these ligands are easily reduced, the system involves only MLCT transitions. The ruthenium complexes most widely used as oxygen sensitive materials are as follows

i) Ru(II) - tris (2,2′-bipyridine) - $Ru(bpy)_3^{2+}$

ii) Ru(II) - tris (1,10-phenanthroline) - $Ru(phen)_3^{2+}$

iii) Ru(II) - tris (4,7-diphenyl-1,10-phenanthroline) - $Ru(Ph_2phen)_3^{2+}$

The photochemistry of these complexes will be discussed in the next section.

3.2.1 Photochemistry of oxygen sensing ruthenium complexes

The bidentate heterocyclic complex $Ru(bpy)_3^{2+}$, has absorption maxima peaks at 450, 344, 322, 285, 240 and 185nm and has a fluorescence peak at 608nm [2]. The absorption bands at 185nm and 285nm have been assigned to π-π^* transitions. The shoulders at 322nm and 344nm are due to d-d transitions. The intense absorption bands at 450nm and 240nm, are assigned to MLCT transitions [2]. Inter system crossing (ISC) can occur from the singlet MLCT state to the triplet MLCT state as illustrated in figure

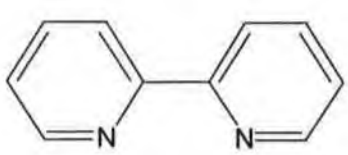

2-2″-bipyridine (bpy)

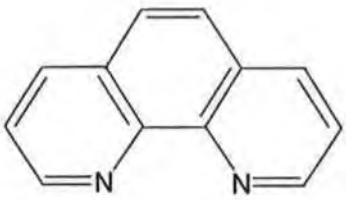

1,10-phenanthroline (phen)

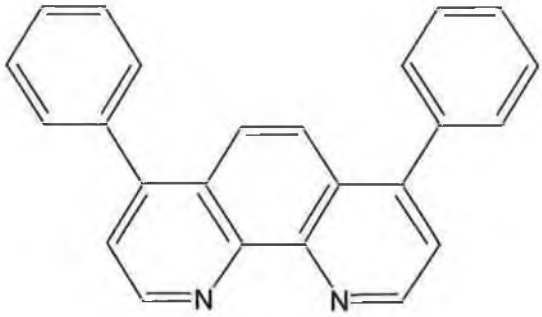

4,7-diphenyl,1,10-phenanthroline (Ph_2phen)

figure 3.4 α-diimine ligands

3.5. Fluorescence emission is due to the radiative decay (k_r) of this excited ^{3}MLCT state [2,12]. Non-radiative emission (k_{nr}), however, can also take place from this level.Another de-activating pathway to the ground state is by de-population via the metal centred (^{3}d-d) excited state. This can give rise to either radiationless deactivation ($k_{nr'}$) or to photodecomposition of the complex (see section 3.2.4). The relatively long lifetime of the ^{3}MLCT state, gives the fluorophore its characteristic long lifetime of 685ns[1] at room temperature [2]. It is this long lifetime of the excited state which results in the dye being oxygen sensitive. The quantum yields of fluorescence for $Ru(bpy)_3^{2+}$ are given as 0.062 in aerated solution and 0.100 in degassed solution at 25°C [14]. $Ru(bpy)_3^{2+}$, however, is not the most suitable of oxygen sensing luminescence probes, because, as mentioned previously, the population of the ^{3}d-d state can lead to photodecomposition and photochemical instability of the complex. Another disadvantage of the $Ru(bpy)_3^{2+}$ is that the excited state is chemically active [14]. Since the excited state is easily oxidised into $Ru(bpy)_3^{3+}$, it will easily form intermediary compounds which change the photophysical properties of the molecule. The oxidised $Ru(bpy)_3^{3+}$ is also an efficient quencher of

[1] water used as solvent

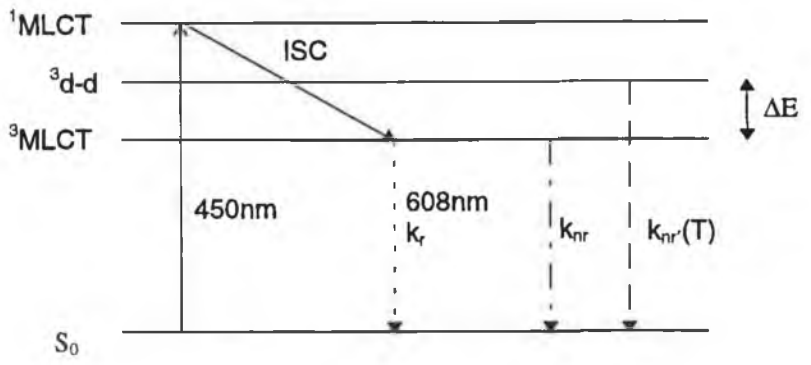

figure 3.5 Excited state properties of $Ru(bpy)_3^{2+}$

$Ru(bpy)_3^{2+}$ by the same quenching process as oxygen [16] and as such can be mistaken as oxygen in a probe designed with $Ru(bpy)_3^{2+}$. The $Ru(bpy)_3^{2+}$ is also easily reduced to $Ru(bpy)_3^{+}$. This can lead to another alternative path for non-radiative energy loss. By altering the ligand system around the ruthenium (II) centre, it is possible to improve the ground-state and excited-state properties of the complex.

The $Ru(phen)_3^{2+}$ complex is quite similar in structure to that of $Ru(bpy)_3^{2+}$, differing only by the type of ligand. As a result, the photophysical characteristics are also quite similar. The $Ru(phen)_3^{2+}$ has absorption peaks at 446, 417, 263 and 224nm [14]. The fluorescence peaks at 603nm and has an excited state lifetime of 962ns in water [2]. The quantum yields are given as 0.0086 in aerated solution and 0.014 in degassed solution at 25°C [14]. The excited state lifetime for $Ru(phen)_3^{2+}$ is about 40% longer than that for $Ru(bpy)_3^{2+}$ and as a result has a potentially greater sensitivity to collisional quenching by oxygen.

However, greater susceptibility to oxygen quenching is found for $Ru(Ph_2phen)_3^{2+}$. A fluorescence lifetime of 5.6μs[1] was measured for this material [17]. The excitation and emission wavelengths of this complex immobilised in sol-gel derived glass were measured to be 450nm and 607.5nm respectively [20,21], with a fluorescence quantum yield of 0.5 [29]. A molar extinction coefficient of 30,000 M^{-1} cm^{-1} implies a 52% higher absorption than that of the bipyridine complex (see table 3.1) [29]. The increase in stability, and stronger absorption coupled with a greater oxygen response makes the $Ru(Ph_2phen)_3^{2+}$ a more efficient dye for use in oxygen sensors. A summary of some relevant photochemical

[1] sol-gel immobilised in 0% oxygen at room temperature

paramters of oxygen sensitive ruthenium complexes is shown in table 3.1, where ε is the molar extinction coefficient and ΔE is the activation energy. References are noted in the brackets.

Ru. Complex	τ_0 (ns)	ε ($M^{-1}cm^{-1}$)	ΔE (cm^{-1})	λ_{abs} (nm)	λ_{em} (nm)	Quantum yield
$Ru(bpy)_3^{2+}$	685 [2][2]	14600 [19][5]	3960 [18][1]	453 [2][2]	608 [2][1]	0.376 [22]
$Ru(phen)_3^{2+}$	962 [2][2]		3157 [18][1]	446 [14]	603 [2][1]	0.584 [22]
$Ru(Ph_2phen)_3^{2+}$	5600 [17][2]	30000 [29][6]		450 [20][3]	607 [21][2]	0.5 [29][4]

table 3.1 Photochemical parameters of oxygen sensitive complexes

3.2.2 Quenching of fluorescence

Fluorescence quenching is the general term for extrinsic processes which depopulate the excited state without the emission of a photon [23]. Five common types of quenching that are observed in fluorescence processes are temperature, solvent, concentration, impurity and oxygen quenching [24]. Depending upon the system, the quenching of the fluorescent emission may result from energy transfer, complex formation, or collisional quenching. It may also result from oxidation or reduction of the excited state. The mechanism by which oxygen quenches fluorescence has been the subject of much research. It is clear, however, that contact between the oxygen molecule and the fluorophore is a requirement for quenching [23]. Quenching resulting from collisional encounters between the fluorophore and quencher is called collisional or dynamic quenching. One of the best known collisional quenchers is molecular oxygen [25]. Collisional quenching of fluorescence is described by the Stern-Volmer equation of section 3.1. The collisional quenching process involves the formation of a non fluorescent complex between the fluorophore and oxygen. This complex sometimes known as an exciplex [26], absorbs the energy from the excited state and results in the non radiative decay of the fluorophore.

[1] water used as solvent
[2] ethanol - methanol mixture (4:1) used as solvent
[3] sol-gel immobilised
[4] measured in an ethanol-methanol (4:1) glass at 77°K
[5] measured at 452nm
[6] measured at 450nm

The second type of fluorescence quenching by oxygen is known as static quenching. This process occurs as a result of the formation of a non-fluorescent ground state complex between the fluorophore and quencher. When this complex absorbs light it immediately returns to the ground state without the emission of a photon.

The lifetimes or temperature dependence of the quenching processes can be used to distinguish the static and collisional quenching contributions. In the case of collisional quenching, the excited state is depopulated resulting in an equivalent decrease in fluorescence intensity and fluorescence lifetime [23], i.e.

3.11

In the case of static quenching a fraction of the fluorophores is removed from observation. The complexed fluorophores are non-fluorescent and the only observed fluorescence is from the uncomplexed fluorophore. The uncomplexed fraction is unperturbed and therefore the fluorescence lifetime in the presence of the quencher remains equal to the lifetime in the absence of the quencher [23], i.e.

$$\frac{\tau_0}{\tau} = 1 \qquad 3.12$$

From equation 3.8 it is clear that I_0/I is expected to be linearly dependent upon the concentration of quencher, with an intercept of 1 on the I_0/I axis, and a slope of K_{SV}. If, however, both static and dynamic quenching are present, equation 3.8 may be rewritten as [27]

$$I_0 / I = 1 + (K_{SV} + K_{eq})[Q] + K_{eq}K_{SV}[Q]^2 \qquad 3.13$$

where K_{eq} is the dissociation constant for the binding of the quencher to the luminescent species. If the τ_0/τ and I_0/I plots versus [Q] are linear and coincide, quenching is purely collisional i.e. $K_{eq} = 0$. However, if I_0/I is everywhere greater than τ_0/τ, static quenching

is present. Therefore, from the analysis of both intensity and lifetime quenching data, the determination of the static and dynamic quenching contributions may be carried out.

An alternative method of determining the relative contributions of dynamic and static quenching is by examining the influence of temperature on the Stern Volmer curve. For collisional quenching, an increase in temperature results in the quencher molecule having greater energy and thus a greater probability of a collisional encounter. This means that the dynamic quenching process is more efficient at higher temperatures. For similar reasons, other quenching processes such as solvent quenching come into effect at higher temperatures. In contrast, an increase in temperature is likely to result in decreased stability of complexes and thus lower static quenching contributions. These effects can be seen on a Stern Volmer plot as an increase in slope for dynamic quenching, and as a decrease in slope for static quenching. This is illustrated in figure 3.7 [23].

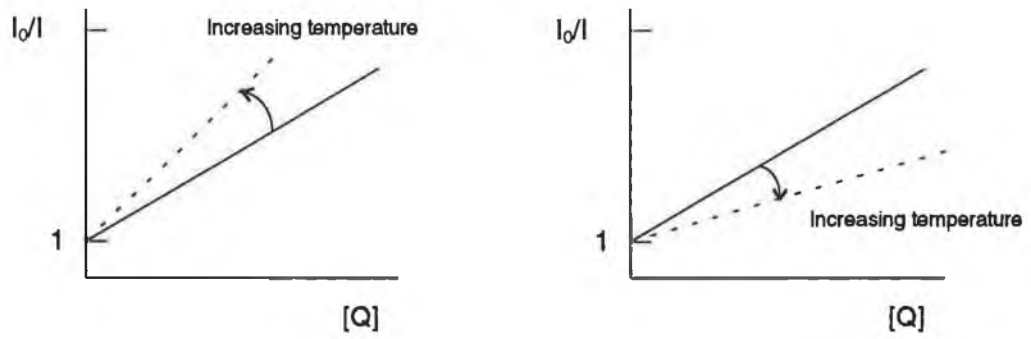

(a) Dynamic quenching (b) Static quenching

figure 3.7 Increasing temperature influence on dynamic and static quenching

3.2.3 The Stern-Volmer Equation

The Stern-Volmer equation (i.e. equation 3.8) relates the extent of collisional quenching (I_o/I) to quencher concentration [Q]. The derivation of the Stern-Volmer equation can be carried out as follows [28]. When a fluorophore is excited by a pulse of light of suitable wavelength, a certain fraction of the fluorophore population will be excited. The excited molecules will then de-excite according to equation 3.5 with a rate constant, K, where K is composed of a sum of several rate constants:

$$K = k_r + k_{nr} + k_t[Q] \qquad 3.13$$

where k_r and k_{nr} are respectively the radiative and non-radiative decay constants, k_t is the rate constant for the transfer of energy from the excited fluorophore to the quenching agent and [Q] is the concentration of quencher molecules in the bulk fluorophore. It can be shown, from equation 3.3, that the fluorescence quantum yield, η, is given by:

$$\eta = \frac{k_r}{k_r + k_{nr} + k_t[Q]} \qquad 3.14$$

When the only available de-excitation process is fluorescence, k_{nr} and k_t are equal to zero, giving η=1. However as the de-excitation processes characterised by k_{nr} and k_t become available η diminishes. Therefore, the ratio of η_0 (the fluorescence quantum yield in the absence of quencher, e.g. oxygen) to η (the fluorescence quantum yield in the presence of quencher) can be expressed as:

$$\frac{\eta_0}{\eta} = \frac{(k_r / k_r + k_{nr})}{(k_r / k_r + k_{nr} + k_t[Q])} = 1 + \left(\frac{1}{k_r + k_{nr}}\right) k_t[Q] \qquad 3.15$$

$$= 1 + \tau_0 k_t[Q] \qquad 3.16$$

Then using equation 3.4 gives the Stern-Volmer expression

$$I_0 / I = 1 + K_{SV}[Q] \qquad 3.17$$

where K_{SV} (= $k_t\tau_0$) is the Stern-Volmer constant. Further, in the case of dynamic quenching $I_0/I = \tau_0/\tau$, and therefore

$$\tau_0 / \tau = 1 + K_{sv}[Q] \qquad 3.18$$

A linear Stern-Volmer is generally indicative of a single class of fluorophore, all of which are equally accessible to the quencher. However, if two fluorophore populations are present, and one is less accessible to the quencher than the other, then the Stern-Volmer plot deviates from linearity. This result is frequently found when Ru(II) complexes are immobilised in microheterogeneous environments such as silicone rubber [27], polymeric material [29], silica [29] or silica gel [30]. In this situation the Stern-Volmer quenching equation is often rewritten in terms of a two-site model as follows[27]

$$I_0 / I = \frac{1}{f_{01} / (1 + K_{SV1}[Q]) + f_{02} / (1 + K_{SV2}[Q])} \qquad 3.19$$

where the f_{01} and f_{02} are the respective fractions of the total emission from each of the two components under unquenched conditions and the K_{SV}'s are the associated Stern-Volmer quenching constants for each component.

3.2.4 Temperature dependence of fluorescence

One of the potential disadvantages of using luminescent based sensing techniques is that many fluorescent compounds are very sensitive to temperature variation. For accurate fluorescence-based sensing measurements, it is necessary either to provide temperature regulation or to incorporate temperature compensation within the signal processing of the sensing system. The temperature dependence of fluorescent transition metal complexes has been studied extensively [13, 30]. Because the deactivating ^{3}d-d state (see figure 3.5) is thermally activated, there is an increase in the deactivation rate as the temperature is raised. Thus $Ru(bpy)_3^{2+}$ shows a strong change in lifetime above room temperature [32]. A thermal deactivation model which describes the temperature dependence of fluorescence lifetime has been described by Van Houten et al. [13] and by Demas et al.[31], Assuming $k_t = 0$, then the observed fluorescence decay constant, K_{obs}, is given by

$$K_{obs} = k_r + k_{nr} + k_{nr'}(T) \qquad 3.20$$

where $k_{nr'}(T)$ is the temperature dependent non-radiative decay constant and k_{nr} and k_r are respectively the temperature independent decay rate constants for non-radiative decay and radiative decay. (see section 3.2.1). The temperature dependent term, $k_{nr'}$, can be written in terms of the Arrhenius equation as follows [31]:

$$k_{nr'}(T) = A_i \exp\left(\frac{-\Delta E}{kT}\right) \qquad 3.21$$

where A_i is the Arrhenius pre-exponential factor for thermal activation of the ^{3}d-d state, k is the Boltzmann constant, T is the absolute temperature and ΔE is the energy gap between the ^{3}d-d state and the emitting ^{3}MLCT state. The observed fluorescence lifetime τ_{obs} is then given by

$$\tau_{obs} = \frac{1}{K_{obs}} = \frac{1}{k_r + k_{nr} + A_i \exp(-\Delta E / kT)} \qquad 3.22$$

This model assumes that decay from the ^{3}d-d state occurs much faster than return to the ^{3}MLCT state. Equation 3.22 was used successfully by Van Houten et al. [13] and by Demas et al. [31] to model the lifetime dependence on temperature. However, the suitability of this model for microheterogeneous environments remains to be tested. In this work, temperature dependence studies were carried out on a sol-gel immobilised $Ru(Ph_2phen)_3^{2+}$ complex and are detailed in section 7.9.

3.2 Fluorescence lifetime sensing

Most optical oxygen sensing detection systems monitor the quenching of the intensity of fluorescence emitted by an appropriate fluorophore. Although these fluorescence intensity-based sensors exhibit promising results [33,34,35,36,37], they are susceptible to a number of errors including photobleaching of dye, possibility of fouling, leaching of indicator, and any parameter that can alter the intensity of the detected signal independently of oxygen concentration. The signal, S_I, obtained from a fluorescence intensity sensor can be expressed as follows [37]:

$$S_I = I_S k_{I1}(1-10^{-c\varepsilon_e l_e})\varphi \times 10^{-c\varepsilon_f l_f}(k_{I2}s_d) \qquad 3.23$$

where I_S is the intensity of the light source, k_{I1} the light throughput of the optical system in the excitation spectral region, c the concentration of the indicator, ε_e the absorptivity of the indicator at the exciting wavelength, l_e the optical pathlength for the exciting light in the sensor element, φ the fluorescence quantum efficiency, ε_f the absorptivity of the indicator at the emission wavelength, l_f the optical pathlength in the sensor for the emitted light, k_{12} the light throughput of the optical system in the emission spectral region and s_d the detector sensitivity. Every parameter in equation 3.23 contributes an uncertainty to the sensor response. This results in the need for frequent recalibration and other corrections [37]. To avoid these problems wavelength ratiometric probes have been developed, where the ratio of signals at two excitation or emission wavelengths are measured [38,39]. An alternative and more advantageous measurement method is one that depends on the luminescent lifetime of an indicator rather than its intensity [37,40,41,42]. The fluorescence lifetime, τ, of an excited-state population does not depend on any of the parameters of equation 3.23. The measured signal of a lifetime-based sensor, in the most general case can be written as [37]:

$$S_\tau = S(t_s, k_{\tau 1}, \tau, k_{\tau 2}, k_d) \qquad 3.24$$

i.e. the sensor signal depends not only on the decay time τ but also on the time constant t_s of the light source, any time distortions in the excitation and emission optics represented by $k_{\tau 1}$ and $k_{\tau 2}$, respectively, and the rise time of the detector, t_d. The lifetime measuring sensor output should therefore be independent of indicator concentration, excitation source intensity, and photobleaching of dye. As lifetimes are absolute quantities such an approach offers the possibility of inherent referencing. Fluorescence lifetime-based sensors have now been developed for many important analytes including pH [43,44,45], calcium [45], glucose [46] and potassium [45]. Since oxygen quenching reduces the mean fluorescence lifetimes of fluorophores, such as ruthenium complexes, according to

equation 3.9, it is clear that oxygen concentration can be monitored by measuring the quenched lifetime.

Fluorescence lifetime measurements are frequently necessary in fluorescence spectroscopy since they can reveal, for instance, the frequency of collisional encounters with quenching agents, the rate of energy transfer or the rate of excited state reactions [23]. There are two widely used methods for the measurement of fluorescence lifetimes. These are the pulse method and the phase-modulation method. In the pulse method the fluorescence sample is excited with a short pulse of light, and the time dependent decay of the fluorescence intensity is measured (see equation 3.5). The fluorescence lifetime can then be determined from the slope of the natural log of the intensity curve following pulsed excitation. Although this method of lifetime measurement is accurate, it requires the use of rather sophisticated equipment. The pulsed method is also a slow process that is unsuitable for real-time lifetime sensing. In the alternative phase modulation method, the fluorescent sample is excited with a sinusoidally modulated light. The resultant fluorescence is phase shifted and is demodulated, relative to the incident light and may be used to calculate the fluorescence lifetime. This method of lifetime measurement is known as phase fluorimetry and is discussed in detail in the following section.

3.3 Phase fluorimetry

In 1927 Gaviola described the use of a continuous, sinusoidally modulated excitation combined with phase sensitive detection, as a method of fluorescence lifetime measurement [47]. In this method, the fluorescence species is excited with light having a time dependent intensity, E(t), of the form

$$E(t) = B + A\sin\omega t \qquad 3.25$$

where B is the d.c. intensity component of the exciting light (see figure 3.8). The degree of modulation is defined as M = A/B, and ω is the angular modulation frequency ($\omega = 2\pi f$, where f is the linear modulation frequency). The resultant time-dependent emission is modulated at the same frequency as the excitation. Because of the finite lifetime of the

excited state, the modulated emission is delayed in phase by an angle ϕ, relative to the excitation. Furthermore, the emission is demodulated relative to the excitation as illustrated in figure 3.8. The resultant phase shifted fluorescence emission, R(t), is written as follows for the specific case of a single exponential decay

$$R(t) = b + a\sin(\omega t - \phi) \qquad 3.26$$

Either the phase shift ϕ, or the demodulation factor m, [where m = (a/b)/(A/B)] can be measured and used to calculate the fluorescence lifetime τ. The following relationships have been shown to exist between phase shift, demodulation factor and modulation frequency [42].

$$\phi = \arctan(\omega\tau) \qquad 3.27$$

$$m = [1+\omega\,\tau^2]^{-1/2} \qquad 3.28$$

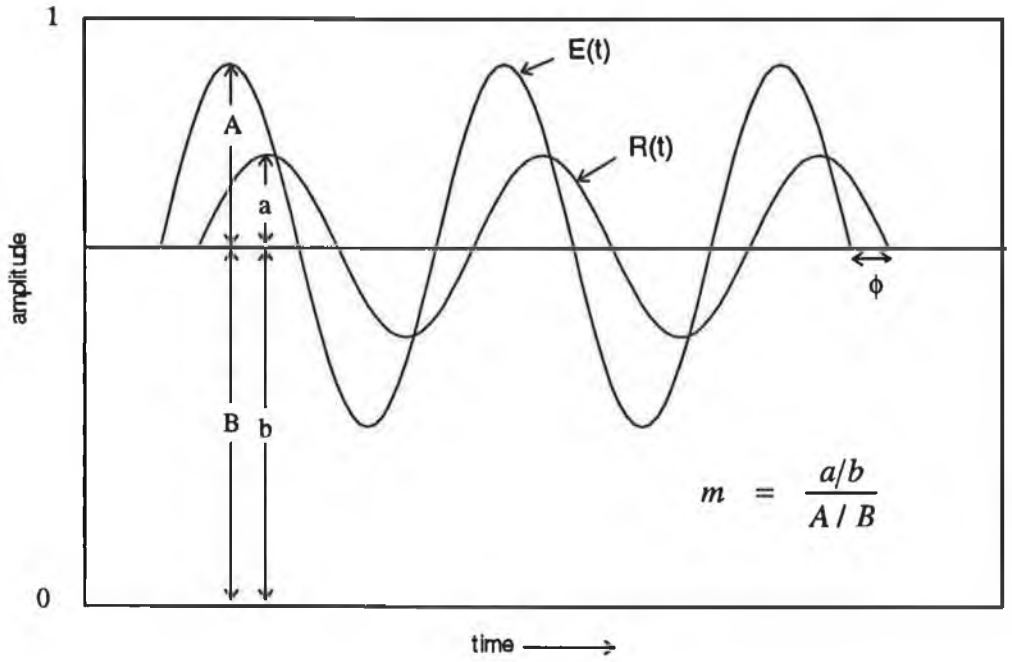

figure 3.8 Schematic description of phase and modulation lifetime measurements. (In general, b ≠ B.)

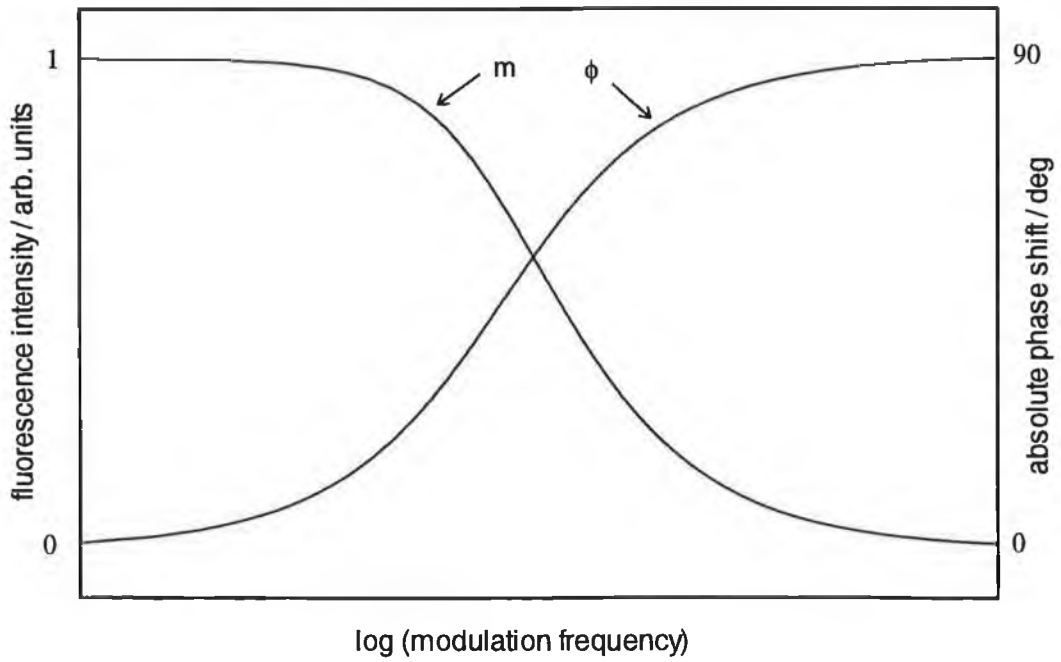

figure 3.9 Demodulation factor, m, and phase shift, ϕ versus modulation frequency

These well known phase fluorimetric relationships are derived in appendix A. A phase fluorimetric system response illustrating the variation of absolute phase shift, ϕ, and demodulation factor, m, with modulation frequency f is shown in figure 3.9. From the diagram it is clear that the phase shift increases with frequency whereas the degree of modulation decreases with frequency. The experimental apparatus for this type of fluorescence lifetime sensing is detailed in sections 6.3.2 and 6.3.3.

3.3.1 Multi-exponential decays

When a fluorophore exhibits multi-exponential decay, such as is observed when a Ru(II) complex is immobilised in a microheterogeneous environment, the observed decay is expressed as a sum of i exponential functions

$$F(t) = \sum_i \alpha_i \exp(-t/\tau_i) \qquad 3.29$$

where α_i is the pre-exponential factor representing the fractional contribution to the time-resolved decay component with a lifetime τ_i. The fractional intensity values (f_i), of each contribution can then be given by [23]

$$f_i = \frac{\alpha_i \tau_i}{\sum_i \alpha_i \tau_i} \qquad 3.30$$

It is important to note that solid state matrices such as polymers or gels may provide numerous different kinds of environments for a fluorophore [48,49]. There may generally be a distribution of distances between the fluorophore molecules and the interacting parts of the immobilising matrix (i.e. spatial disorder) as well as a distribution of interaction energies (i.e. energetic disorder) [50]. These types of disorder may cause fluorescence decay distributions which are non-exponential in profile. James et al. [51] have shown that such type of complex decay profile can, with the usual achieved level of accuracy, be fitted to a sum of two exponential functions. It is important to realise that the quantities α_1, α_2 and τ_1, τ_2, in this case, may have no physical significance with respect to the environment of the fluorophores.

For multiexponential decays, the phase fluorimetric relationships of equations 3.27 and 3.28 are expressed as follows, where the resultant phase shift $\langle\phi\rangle$, and the resultant demodulation factor $\langle m\rangle$ are given by [23]

$$\tan\langle\phi\rangle = \frac{\sum_{i=1}^{n} f_i \sin\phi_i \cos\phi_i}{\sum_{i=1}^{n} f_i \cos^2\phi_i} \qquad 3.31$$

$$\langle m\rangle = \left[\left(\sum_{i=1}^{n} f_i \sin\phi_i \cos\phi_i\right)^2 + \left(\sum_{i=1}^{n} f_i \cos^2\phi_i\right)^2\right]^{1/2} \qquad 3.32$$

where ϕ_i is the phase angle associated with the decay time τ_i. Therefore, if the lifetimes of the individual components of a multi-exponential decay are known, it is possible to

predict the resultant phase shift and degree of modulation. This type of analysis is carried out for sol-gel immobilised ruthenium complexes in section 7.4.

3.4 Conclusion

Ruthenium complexes have been introduced and their suitability for optical oxygen sensing has been described. Two methods of using these complexes have been described. These are the measurement of fluorescence intensity, and the monitoring of their fluorescence lifetimes. The latter method has been shown to be potentially the more advantageous, due to the fewer number of variable parameters within such a measuring system. Finally, phase fluorimetry as a method of real-time lifetime measurement has been treated, both for a single exponential lifetime decay and the more realistic situation of a multi-exponential decay. This method of fluorescence lifetime sensing has been be applied by us to oxygen sensing, and is described experimentally in chapter 6.

References:

1. Gilbert A., Baggot J., Wagner P.J.: '**Essentials of molecular photchemistry**', Blackwell Scientific Publications, Oxford, 1991

2. Juris A., Balzani V., Barigelette F., Campagna S., Belser P., Von Zelewsky A.: '**Ru(II) polpyridine complexes ; photophysics, photochemistry, electrochemistry and chemiluminescence**', Co-ordination Chemistry Reviews, 1988, Vol. 84, pp. 85-277.

3. Bergmann I.: '**Rapid response atmospheric oxygen monitor based on fluorescence quenching**', Nature, 1968, Vol. 218, p.396

4. Gruber W.R., Klimant I., Wolfbeis O.S.: '**Instrumentation for optical measurement of dissolved oxygen based on solid state technology**', Lakowicz J.R. (Ed.), Proc. SPIE, 1993, Vol. 1885, pp.

5. Wehry E.L.: '**Modern fluorescence spectroscopy 4**', 1991, Plenum Press, New York

6. Demas J.N., Harris E.W., McBride R.P.: '**Energy transfer from luminescent transistion metal complexes to oxygen**', Journal of the American Chemistry Society, 1977, Vol. 99, p. 3547

7 Kroneis H.W., Marsoner H.J.,: '**A fluorescence-based sterilizable oxygen probe for use in bioreactors**', Sensors & Actuators, 1983, Vol. 4, pp. 587-592

8. Peterson J.I., Fitzgearld R.V., Buckhold D.K.: '**Fiber-optic probe for in vivo measurement of oxygen partial pressure**', Analytical Chemistry, 1984, Vol. 56, pp. 63-67

9. Gehrich J.L., Lübbers D.W., Opitz N., Hausmann D.R., Miller W.W., Tuas J.K., Yafuso M.: '**Optical fluorescence and its application to an intravascular blood gas monitoring system**', 1986, IEEE Transactions of Biomedical Engineering, BME-33, pp. 117-132

10. Opitz N., Graf H.J., Lübbers D.W., '**Oxygen sensor for the temperature range 300 to 500°K based on fluorescence quenching of indicator-treated silicone rubber membranes**', Sensors & Actuators, 1988, Vol. 13, pp. 159-163

11. Demas J.N., DeGraff B.A., '**Design of transitions metal complexes as luminescence probes**', Chemical, Biochemical and Environmental Fiber Sensors, Lieberman R.A.: Wladarczyk M.T. (Eds.), Proc. SPIE, Vol. 1172, 1989, pp. 217 - 224

12. Demas J.N., DeGraff B.A., '**Design and applications of highly luminescent transition metal complexes**', Analytical Chemistry, 1991, Vol. 63, No. 17, pp.829-837

13. Van Houton J., Watts R.J.: '**Temperature dependence of the photophysical and photochemical properties of the tris(2,2'-bipyridyl) ruthenium (II) ion in aqueous solution**', Journal of the American Chemical Society, 1976, Vol. 98, No. 16, pp. 4853-4858

14. Durham B., Caspar J.V., Nagre K.K., Meyer T.J.: '**Photochemistry of $Ru(bpy)_3^{2+}$**', Journal of the American Chemical Society, 1982, Vol. 104, pp. 4803-4810

15. Lee J.D.: '**A new concise inorganic chemistry**', 1977, 3rd Ed., Van Nostrand Reinhold Company Ltd.

16. Wilkinson G., Gillard R.D., McCleverty J.A.: '**Comprehensive co-ordination chemistry: middle transition elements**', Vol. 4, pp. 327-335

17. Kiernan P.: '**Oxygen sensitivity of ruthenium-doped sol-gel derived silica films**', Dublin City University, Thesis presented for degree of Masters, 1994

18. Hughes P., Marin D., Bell S., McGarvey J.J., Vos G.V., '**Photophysical and photochemical properties of dinuclear Ru(II) complexes containing 2,2'-bipyridine and 1,10-phenanthroline moieties**', Inorganic Chemistry, 1993, Vol. 3, No. 20, pp. 4402-4408

19. Hage R.: '**Osmium complexes containing triaxole ligands, synthesis, structures, electrochemical and photophysical properties**', 1991, Ph.D. Thesis

20. Section 6.1

21. Section 7.2.2

22. Demas J.N., Crosby G.A., '**Quantum efficiencies of transition metal complexes II, Charge transfer luminescence**', Journal of the American Chemical Society, 1971, Vol. 93, No. 12, pp. 2841-2847

23. Lakowicz J.R.: '**Principles of fluorescence spectroscopy**', 1983, Plenum Press, New York, pp 257-301

24. Guilbault G.G., '**Practical fluorescence, theory, methods and techniques**', Marcel Dekker Inc., New York.

25. Kautsky H.: '**Quenching of luminescence by oxygen**', Transactions of the Faraday Society', 1939, Vol. 35, pp. 216-219

26. Gilbert A., Baggot J.: '**Essentials of molecular photochemistry**', Blackwell Scientific Publications Oxford.

27. Carraway E.R., Demas J.N., DeGraff B.A. Bacon J.R.: '**Photophysics and photochemistry of an oxygen sensor based on luminescence transition-metal complexes**'. Analytical Chemistry, 1991, Vol. 63, pp. 337-342

28. McFarlane R., Hamilton M.C.: '**A fluorescence based dissolved oxygen sensor**', Seastar Instruements LTD.

29. Wenying X., McDonough R.C., Langsdorf B., Demas J.N., DeGraff B.A.: '**Oxygen sensors based on luminescence quenching: Interactions of metal complexes with the polymer supports**', Analytical Chemistry, 1994, Vol. 66, No. 23, pp. 4133-4141

30. Mingoarranz F.J., Moreno-Bondi M.C., Garcia-Fresnadillo D, De Dios C., Orellana G.: '**Oxygen sensitive layers for optical fiber devices**', 2nd European Conference on Optical Sensors and Biosensors, Florence, April 1994.

31. Demas J.N., DeGraff B.A.: '**On the design of luminescence based temperature sensors**', 1992, Proc. SPIE, Vol. 1792, pp. 71-75

32. Bacon J.R., Demas J.N.: '**Determination of oxygen concentrations by luminescence quenching of a polymer-immobilised transition-metal complex**', Analytical Chemistry, 1987, Vol. 59, No. 23, pp. 2780-2785

33. Wolfbeis O.S, Weis L.J., Leiner M.J.P., Ziegler W.E.: '**Fiber-optic fluorosensor for oxygen and carbon dioxide**', Analytical Chemistry, 1988, Vol. 60, pp. 2028-2030

34. Bacon B.R., Demas J.N.: '**Determination of oxygen concentrations by luminescence quenching of a polymer-immobilized transition-metal complex**', Analytical Chemistry, 1987, Vol. 59, pp. 2780-2785

35. Hauser P.C., Tan S.S.: '**All solid state instrument for fluorescence-based fibre optic sensors**', Analyst, 1993, Vol. 118, pp. 991-995

36. Opitz N., Lübbers D.W.: '**Oxygen transport to tissue**', 1984, Plenum Press, New York, Vol. 6, pp. 757-762

37. Lippitsch M.E., Draxler S.: '**Luminescence decay-time-based optical sensors: principles and problems**', Sensors and Actuators B, 1993, Vol. 11, pp. 97-101

38. Theriault G.A., Newberry R., Andrews J.M., Apitz S.E., Lieberman S.H.: '**Fiber optic fluorometer based on a dual wavelength laser excitation source**', 1992, Proc. SPIE, Vol. 1796, pp. 115-123

39. Lee E.D., Werner T.C., Seitz W.R.: '**Luminescence ratio indicators for oxygen', Analytical Chemistry**', 1987, Vol. 59, No. 2, pp. 279-283

40. Lippitsch M.E., Pusterhofer J., Leiner M.J.P., Wolfbeis O.S.,: '**Fibre--optic oxygen sensor with the fluorescence decay time as the information carrier**', Analytica Chimica Acta, 1988, Vol. 205, pp. 1-6

41. Demas J.N.: '**Fluorescence lifetime sensing**', Laser Focus World, May 1992, pp. 60-80

42. Demas J.N.: '**Excited state lifetime measurements**', Academic Press Inc., 1983

43. Draxler S., Lippitsch M.E., Leiner M.J.P.: '**Optical pH sensors using fluorescence decay time**', Sensors & Actuators B, 1993, Vol. 11, pp. 421-424

44. Thompson R.B., Lakowicz J.R.: '**Fiber optic pH sensor based on phase fluorescence lifetimes**', Analytical Chemistry, 1993, Vol. 65, No. 7, pp. 853-858

45. Lakowicz J.R., Szmacinski H.: '**Fluorescence lifetime-based sensing pH, Ca^{2+}, K^{+} and glucose**', Sensors & Actuators B, 1993, Vol. 11, pp. 525-530

46. Papkovsky D.B., Olah J., Nurochkin I.N.: '**Fibre-optic lifetime-based enzyme biosensor**', Sensors & Actuators, 1993, Vol. 11, pp. 525-530

47. Gaviola Z., '**Ein fluorometer. Apparat zur messung von fluoreszenzabklingung-szeiten**', Z. Phys, Vol. 42, pp. 853-861

48. James D.R., Liu Y.S., de Mayo P., Ware W.R.: '**Distributions of fluorescence lifetimes: Consequences for the photophysics of molecules adsorbed on surfaces**', Chemical Physics Letters, 1985, Vol. 120, No. 4,5, pp. 460-465

49. Liu Y.S., Ware W.R.: '**Photophysics of polycyclic aromatic hydrocarbons adsorbed on silica surfaces: Fluorescence lifetime analysis: an ill-conditioned problem**', Journal of Physical Chemistry, 1993, Vol. 97, pp. 5980-5986

50. Sienicki K., Blonski S., Durocher G.: '**Relaxation distributions of fluorescence decays**', Journal of Physical Chemistry, 1991, Vol. 95, pp. 1575-1579

51. James D.R., Ware W.R.: '**A fallacy in the interpretation of fluorescence decay parameters**', Chemical Physics Letters, 1985, Vol. 120, No. 4,5, pp. 455-459

Chapter Four - The Sol-Gel Process

4.1 Introduction

In 1846, Ebelmen made the first observation of the sol-gel process [1]. However, it was not until the mid-seventies that this new technology began to attract considerable research interest. The sol-gel process may be described as a chemical phenomenon in which a single or multi-component metal oxide *sol*ution undergoes *gel*ation to form a coherent rigid network of the oxides present [2]. The reason it is of interest is that it can be used to produce 'tailor-made' glasses and ceramics with wide ranging applications. Furthermore, it allows for lower temperature treatments than is normally possible in the production of conventional glasses [2]. Sol-gel literature is concerned almost equally with the production of bulk glasses, fibres, monoliths and thin films. A number of industrial applications of the process have been reported, including the development of rear view mirrors for automobiles, anti-reflective coatings, lenses, and optical filters [3,4,5,6]. The sol-gel process is to-day a potentially inexpensive route to the manufacture of a wide variety of devices which depend on the integration of new materials and technologies. These include Y-couplers, gratings, sensors, frequency doublers, lenses, interferometers, etalons, amplifiers and thin films [6].

The preparation of glass substrates by traditional methods of melting silica require extreme temperatures. In contrast, the sol-gel process involves low temperature hydrolysis of an alkoxide precursor followed by condensation to yield a polymeric SiO_2 network. During the process molecules of the corresponding alcohol are liberated. The initial hydrolysis and polycondensation reactions occurring in localised regions lead to formation of colloidal particles. As the connectivity of these particles increase, the viscosity of the sol starts to increase and leads to the formation of a solid gel. Although the nature of individual events is random and the geometry and pore-size distribution of the final gel are difficult to determine, the nature of the final polymeric gel can be regulated to a certain extent by controlling the rates of the individual steps [7].

4.2 Details of process

The main reaction components in a typical sol-gel process are a metal alkoxide[1], water, a solvent and a catalyst. Preparation of sol-gel glasses is based on the hydrolysis and condensation polymerisation of the metal alkoxide solution, followed by a temperature programme which controls the glass densification process. There are three distinct stages to the sol-gel process:

i) Mixing of the precursors in solution to achieve intimacy on a molecular scale.

ii) Gelling of the solution in a manner which will retain the chemical homogeneity achieved in step (i).

iii) Thermal treatment to further age the gel or to convert the gel to a glass.

The chemistry and physics of sol-gel processing is well documented in the literature [2,8]. In this chapter some of the relevant details of the process are discussed under the following headings: i) hydrolysis and condensation polymerisation, ii) influence of catalyst and pH, iii) influence of solvent, iv) influence of water, v) gelation, vi) aging, vii) drying, viii) stabilisation of microstructure, ix) encapsulation of organic molecules in a sol-gel glass, and x) preparation of a $Ru(Ph_2phen)_3^{2+}$ doped gel.

4.3 Hydrolysis and condensation polymerisation

The formation of a typical silica sol-gel can be described by the following reactions.

$$Si(OR)_4 + nH_2O \underset{\text{Esterification}}{\overset{\text{Hydrolysis}}{\rightleftharpoons}} Si(OR)_{4-n}(OH)_n + nROH \qquad 4.1$$

$$\equiv Si\text{-}OH + RO\text{-}Si\equiv \underset{\text{Alcoholysis}}{\overset{\text{Alcohol condensation}}{\rightleftharpoons}} \equiv Si\text{-}O\text{-}Si\equiv + ROH \qquad 4.2$$

$$\equiv Si\text{-}OH + OH\text{-}Si\equiv \underset{\text{Hydrolysis}}{\overset{\text{Water condensation}}{\rightleftharpoons}} \equiv Si\text{-}O\text{-}Si\equiv + H_2O \qquad 4.3$$

In the preparation of such a sol-gel derived silica, one starts with an appropriate alkoxide [e.g. $Si(OC_2H_5)_4$, tetraethylorthosilicate or TEOS] which is mixed with water. A mutual solvent such as alcohol is normally used as a homogenising agent, due to the fact that

[1] MOR, where M is any electropositive element and R is an alkyl group C_xH_{2x+1}

water and alkoxysilanes are immiscible. Hydrolysis reactions lead to the formation of silanol groups (i.e. Si-OH). These species are intermediates as they further react to form siloxane groups (i.e. Si-O-Si). The processes of hydrolysis and condensation are, in general, difficult to separate [9]. There are several parameters that influence the rate of hydrolysis and condensation polymerisation reactions including the ambient temperature, the solution pH, the presence of a catalyst, the particular alkoxide precursor, the solvent, and the relative concentrations of the alkoxide precursors, water and solvent. The relative rates of the hydrolysis and condensation reactions are considered to be the parameters that define the initial nature of the gel [10]. It is therefore important to be able to control the relevant reaction rates.

As the metal alkoxide and water are mixed, hydrolysis and polycondensation reactions initiated at numerous sites within solution. The mechanisms for the hydrolysis of a silicon alkoxide have been widely investigated and depend on the reaction conditions. Possible reaction pathways under acidic and basic conditions are generally accepted as follows: For acidic conditions hydrolysis takes place by a molecular S_N2 nucleoplilic substitution reaction. In this reaction, the alkoxide is protonated by the acid, thus increasing the acidity of the group and allowing the central silicon atom to be attacked from the rear by a water molecule as illustrated in figure 4.1(a). The positive charge of the protonated alkoxide is correspondingly reduced, making alcohol a better leaving group [11]. The rate of reaction will not be particularly sensitive to the inductive effect of other groups bonded to the silicon atom, since the flow of charge will be predominantly

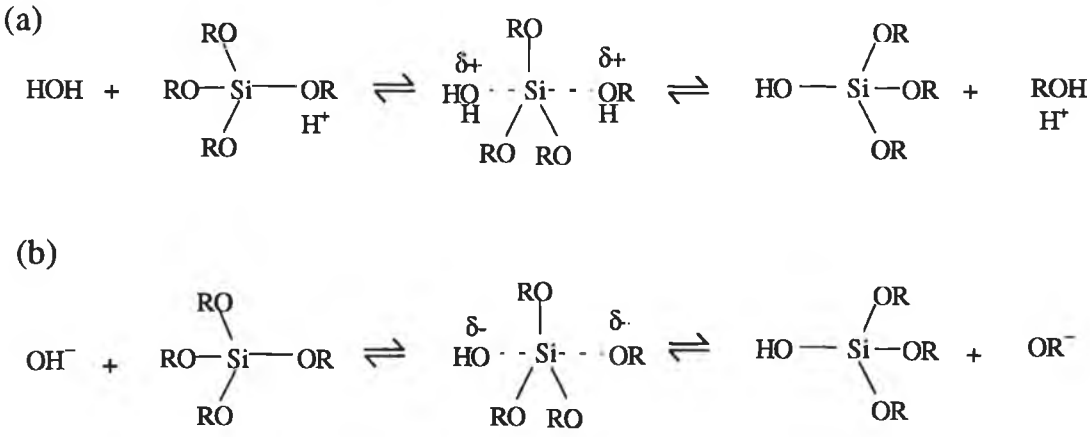

figure 4.1 (a) Acid and (b) base catalysed mechanisms for hydrolysis of a sol-gel mixture

from the protonated alkoxy to the water molecule. The ease with which electrophiles can approach the silicon complex will, however, have a significant effect on the rate of reaction and so steric factors will have the greatest effect on the hydrolysis reaction [2].

Under basic conditions, water dissociates to produce a nucleophilic hydroxyl anion. The hydroxyl atom then attacks the silicon atom. Because the silicon atom aquires a negative charge in the transition state (see figure 4.1(b)), the mechanism is quite sensitive to inductive charge as well as steric effects. Keefer [12] proposed an S_N2 nucleophilic substitution reaction mechanism, in which the OH^- displaces OR^-.

The most widely accepted mechanism for the condensation reaction involves the attack of a deprotonated silanol on a neutral silicate species:

$$\equiv Si\text{-}O^- + Si(OH)_4 \rightleftharpoons \equiv Si\text{-}O\text{-}Si\equiv + OH^- \qquad 4.4$$

This reaction pertains above the isoelectric point of silica i.e. pH ≈ 2 (where the electron mobility and the surface charge is zero) where surface silanols may be deprotonated depending on their acidity. The acidity of a silanol group depends on the inductive effect acting on the silicon atom.

4.4 Influence of Catalyst and pH

Hydrolysis is most rapid and complete when catalysts are employed. Changing the catalyst can have large influence on the microstructure of the gels formed as well as on the rate of the gelation process. The most commonly used catalysts are HCl, HF, NH_4OH and KF. Pohl et al. [11] carried out an investigation to determine the influence of pH on hydrolysis. The rate constants obtained for γ-glycidoxypropyltrialkoxysilane are shown in figure 4.2 as a function of pH. The hydrolysis appears to be both hydronium ion specific and hydroxyl ion specific i.e. hydrolysis rate is greatest for low pH and high pH.

The pH-dependence of the time to gelation is often used as a measure of the overall condensation rate for sol-gel systems (gel time ∝ 1/ (average condensation rate)). Such a study carried out by Coltrain et al. is shown in figure 4.3 [13]. The minimum at ~ pH2 corresponds to the isoelectric point of silica. As a result, in an acid catalysed reaction, condensation is likely to occur before the monomer is fully hydrolysed and the

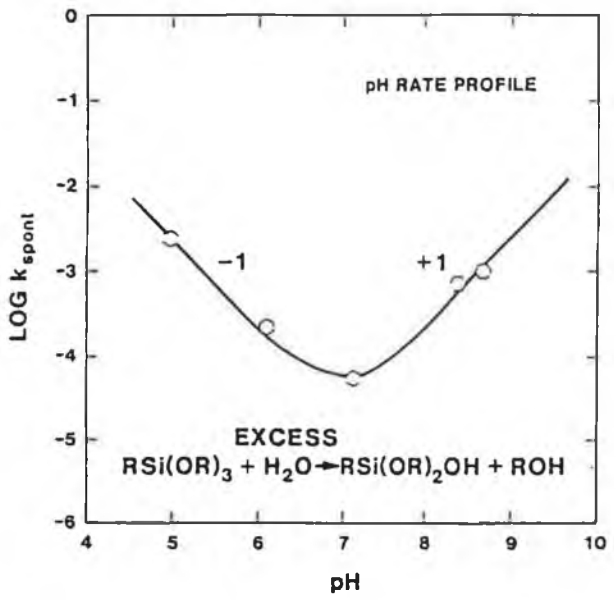

figure 4.2 Hydrolysis rate as a function of pH [11].

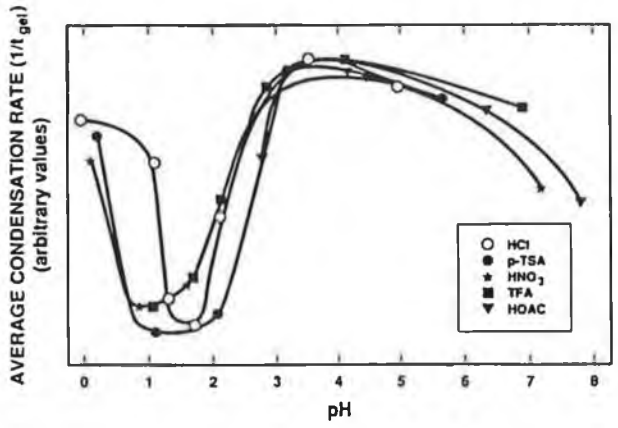

figure 4.3 Average condensation rates (1/time to gelation) for TEOS as a function of pH [13].

resulting polymer will tend to be lightly cross-linked i.e. primarily linear. In the base catalysed reaction, however, the hydrolysis of the alkoxide molecule tends to go to completion, such that the condensation will result in a more densely crosslinked polymer giving rise to branched clusters. Porosity, which is related to the extent of cross-linking, is therefore, one property which may be controlled by the appropriate choice of pH [2].

4.5 Influence of Solvent

The solvent most commonly reported in sol-gel work is ethanol. The influence of the solvent is important not only because it can take part in the reverse of reactions 4.1 and 4.2, but also because its removal during drying determines to a great extent the final morphology of the gel. Solvents may generally be classified as polar or non-polar and as protic[1] or aprotic. The important characteristics of solvents with regard to solvating power are its polarity and the availability of labile protons. The polarity largely determines the solvating ability for polar and non-polar species. The availability of labile protons determines whether anions or cations are solvated more strongly through hydrogen bonding and whether or not the solvent can participate in dissociative reactions such as alcoholysis or hydrolysis. Because hydrolysis is both hydroxyl and hydronium ion catalysed, solvent molecules which hydrogen bond to hydroxyl ions or hydronium ions reduce catalytic activity under basic and acidic conditions, respectively. Therefore, aprotic solvents, which do not hydrogen bond to hydroxyl ions, have the effect of making hydroxyl ions more nucleophilic, whereas protic solvents make hydronium ions more electrophilic. The availability of labile protons also influences the extent of the reverse reactions (equations 4.1 to 4.3): reesterfication, alcoholysis or hydrolysis. Aprotic solvents do not participate in reverse reactions such as reesterification, because they lack sufficiently electrophilic protons and are unable to be deprotonated to form sufficiently strong nucleophiles. Therefore, compared to alcohol or water, aprotic solvents such as THF or dioxane do not take part in sol-gel processing reactions [2].

The vapour pressure of the solvent has an important effect on the time required to gel and on the surface area of the resulting gel. When the vapour pressure is low, the solution gels with a larger amount of liquid, so the dried gel has a more porous structure.

4.7 Influence of water

Another parameter that influences the relative hydrolysis and condensation rates is the R value[2]. A R value of 2 is theoretically sufficient for complete hydrolysis and condensation to yield anhydrous silica as shown in the net reaction [2]:

---

[1] Containing a labile proton

[2] The relative concentration of water and alkoxide precursor is often referred to as the R value i.e. $R=[H_2O]/[TEOS]$

$$nSi(OR)_4 + 2nH_2O \rightarrow nSiO_2 + 4nROH \qquad 4.5$$

Generally, however, the reactions do not go to completion under these conditions because of the formation of intermediate species [2]. The most obvious effect of increasing the R value is the promotion of hydrolysis according to equation 4.1. Equations 4.2 and 4.3 suggest two further effects of the R value. With 'under-stoichiometric' additions of water (R<2), the alcohol-producing condensation reaction is favoured, whereas the water-producing reaction is favoured when R>2. Excess water, however, is expected to promote depolymerization according to the reverse of equation 4.3. Although increased R values generally promote hydrolysis, when R is increased while maintaining a constant solvent : silicate ratio, the silicate concentration is reduced. This in turn reduces the hydrolysis and condensation rates, causing an increase in the gelation time. This effect has been shown by Colby et al. [14] (see figure 4.4) and by McDonagh et al. [15].

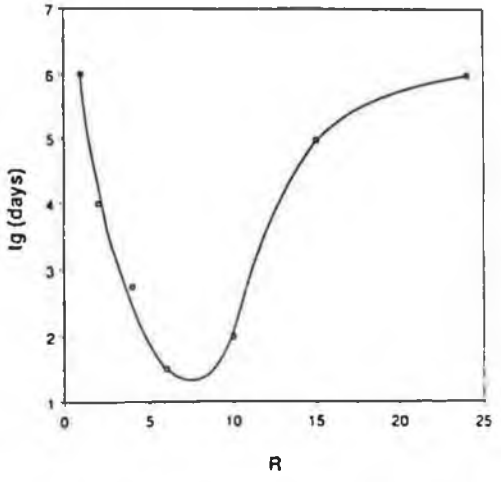

figure 4.4 Gelation time as a function of R-value[14].

4.7 Gelation

When sufficient interconnected Si-O-Si bonds are formed in a region, they respond co-operatively as colloidal particles or a sol[1]. With time the colloidal particles

[1] A suspension containing colloidal particles is called a sol.

and the condensed silica species link to form a 3-dimensional network. The gelation point is marked by a sharp increase in viscosity and the result is a solid structure in the shape of the mould. The product of this process at the sol-gel transition is called an alcogel. After the sol-gel transition, the solvent phase is removed from the interconnecting pore network. If it is removed by conventional drying the gel network is drawn together due to capillary forces, resulting in considerable shrinkage of the gel. In effect, the gel material becomes more condensed with smaller pores because of the drying. Air-dried gels, which are known as xerogels, may shrink up to one-eighth of their original gel volume [7]. Further heating at higher temperature of xerogels leads to the formation of a densified glass structure equivalent to fused quartz or silica. The steps involved in the sol-gel processing of a densified glass are illustrated in figure 4.5.

	LIQUID PHASE	alkoxide precursor
hydrolysis, condensation	↓	
	SOL	colloidal submicron particles
aging	↓	
	GEL	3D network
drying	↓	
	XEROGEL	large area small pores
high T	↓	
	DENSIFIED GLASS	

figure 4.5 Steps involved in the manufacture of a sol-gel glass

4.8 Aging

Aging, also known as prepolymerisation, is the term used to indicate the on-going hydrolysis and polymerisation reactions in a sol-gel system both before and after gelation has taken place. During aging, the gel structure is evolved resulting in the thickening of interparticle necks and decreases in porosity. Much work has been carried out to model this process. Some of the mechanisms that have been reviewed include

treating the system with percolation theory, molecular orbital calculations and molecular dynamic simulations [2].

4.9 Drying

During drying the liquid is removed from the interconnected pore network. If the pores are small (<20nm) large capillary stresses develop during drying. These stresses may cause the gels to crack catastrophically unless the drying process is controlled by decreasing the liquid surface tension by the addition of surfactants, by elimination of very small pores by hypercritical evaporation, or by obtaining monodisperse pore sizes by controlling the rates of hydrolyses and condensation. The process of drying of a porous material can be divided into 3 stages.

i) The first stage of drying is called the *constant rate period* because the rate of evaporation per unit area in independent of time [2]. The compliant gel network is deformed by the large capillary forces. The body shrinks by an amount equal to the volume of liquid that evaporates and the liquid-vapour interface remains at the exterior surface of the body. As the gel shrinks, the tension in the pores increases and the vapour pressure of the liquid in the pores decreases. If the network remains compliant, shrinkage could continue until the pores collapse completely. In practice, however, the network stiffens as it shrinks, and at some point becomes able to withstand the capillary pressure. Shrinkage stops at the critical point [9].

ii) The second stage is known as the *first falling rate period.* This begins when the body becomes too stiff to shrink and the liquid recedes into the interior, leaving air-filled pores near the surface. During this stage the rate of evaporation decreases. As air invades the pores, a continuous funicular liquid film supports liquid flow to the exterior, so evaporation continues to occur from the surface of the body [9].

iii) As the meniscus recedes into the body, the exterior does not become completely dry right away, because liquid continues to flow to the outside surface. This continues as long as the flux of liquid is comparable with the evaporation rate, and the funicular condition is preserved. However, as the distance from the exterior surface and meniscus increases, the flux decreases. Eventually, it becomes so slow that the liquid near the outside of the body is isolated in pockets, so flow to the surface stops and liquid is removed from the body only by diffusion of its vapour. The temperature of the surface

now approaches ambient temperature and the rate of evaporation becomes less sensitive to exterior conditions. At this stage, drying is said to enter the *second falling rate period* [9].

One of the problems with using sol-gel derivatives is that they are liable to crack. If the pressure in the liquid within the gel network were uniform, there would be no tendency for the gel to crack. However, the low permeability of the gel gives rise to a pressure gradient, so the tension in the liquid is greater near the drying surface and the contraction of the network is consequently greater. The difference in shrinkage rates between the inside and the outside of the body is the cause of drying stress which can lead to cracking. Brinker and Scherer have shown quantitatively that it is the difference in shrinkage rate between the inside and outside of a drying body that results in a tensile drying stress [2]. They show that the tensile stress (σ_x) as a function thickness (L) can be expressed as follows:

$$\sigma_x(L) \approx \frac{L\eta_L V_E}{3D} \qquad 4.6$$

where η_L = viscosity of the liquid, V_E is the evaporation rate, and D is the permeability of the network. This equation shows that as the thickness of a gel (L) increases or the evaporation rate , V_E, increases, the probability of cracking increases. Cracking may also be attributed to the existence of a pore size distribution in the gel. When larger pores are emptied by evaporation, the wall between adjoining pores is subjected to uneven stress that can cause cracking. Cracking during stage 1 of the drying process is rare unless the gel has not been sufficiently aged and therefore does not posses the dimensional stability to withstand the increasing compressive stress. Most failure occurs after the critical point. The possibility of cracking occurring at this stage is high due to the high stresses and low strain tolerance of the material.

However, there exists a number of methods to alleviate the problem of cracking. Firstly, the aging of a gel before drying helps to strengthen the network and thereby reduce the risk of fracture (see section 4.4). Surfactants can be added to the pore liquid to reduce the interfacial energy and thereby decrease the capillary stress. The shrinkage at the critical point is also reduced by the surfactant. This will have a beneficial

effect on the permeability of the gel and also reduces the stress that occurs during stage 1. Another group of chemicals, known as drying control chemical additives (DCCA), reduce the risk of occurrence of cracks. Examples are formamide (NH_2CHO) or glycerol, which replace some of the solvent ordinarily used. The resulting gel is found to be harder and to have a larger and more uniform pore size. All of these features help to reduce cracking. The success of this type of chemical additive is attributed to coarsening of the microstructure and strengthening of the network. They also provide a medium through which volatile components (e.g. water and alcohol) can diffuse, thereby allowing diffusion to reduce the pressure differential with in the body.

Since shrinkage and cracking are produced by capillary forces, Kistler [16] reasoned that these problems could be avoided by removing the liquid from the pores above the critical temperature and critical pressure of the liquid. During this process no interfacial tension is created. However, the high temperatures and pressures make the process expensive and dangerous. Glass structures produced using this technique are known as aerogels. An alternative method of avoiding the presence of the liquid-vapour interface is to freeze the pore liquid and sublime the resulting solid under vacuum. This type of glass is called known as cryogel.

4.10 Stabilisation of microstructure

It is imperative to achieve thermal and chemical stabilisation of the sol-gel derived glass structure before it can be used as optical component. Chemical stabilisation involves the removal of remaining silanol groups to a level which the surface does not rehydroxylate during use. Thermal stabilisation involves reducing the surface area sufficiently to enable the material to be used at a given temperature without reversible structural changes occurring.

A problem in producing silica optical components is the removal of gel surface hydroxyl groups and hydrogen bonded water. These entities give rise to atomic vibrational energy absorption in almost the entire of U.V. to I.R. wavelengths and so decrease the optical application of silica gel monoliths. To achieve dehydration it is necessary to recognise that water is present in two forms, i.e. physisorbed and chemisorbed water. Dehydration at temperatures up to a few hundred degrees centigrade

is reversible and physisorbed water is readily removed. Chemisorbed water is more difficult to remove and does not take place to any significant extent until temperatures higher than 400°C are used [2].

4.11 Encapsulation of organic molecules in a sol-gel glass

Sol-gel technology is being considered for a number of applications among which is as a support matrix in fibre optic chemical sensors. Because sol-gel manufacture is a low temperature process, organic and biological molecules with poor thermal stability may be encapsulated intact in the organic glass. Zusman et al. [17] have shown the potential of doped gels for chemical analysis. They entrapped a range of dyes sensitive to selected analytes in sol-gel derived glass blocks. By monitoring the characteristic colour changes in the doped gels, they showed that metal ions such as Fe^{3+}, Al^{3+}, Co^{2+}, Ni^{2+}, Cu^{2+} and Pb^{2+} as well as changes in pH could be detected successfully, albeit with long response times. Recent research has also demonstrated that silicate glasses obtained by the sol-gel method, can provide matrices suitable for the immobilisation of biomolecules, such that they retain many of the characteristics of the liquid state, despite the fact that the molecule is trapped in a solid material [2,18,19,20]. In 1991, the first fibre optic chemical sensors prepared by sol-gel thin film coatings were reported by MacCraith et al.[21] and shortly afterwards by Ding et al.[22]. Both groups immobilised pH indicators in a silica gel matrix as described in section 1.4. The work presented in this thesis uses the sol-gel process to immobilise oxygen sensitive ruthenium complexes in films attached to optical fibres. The advantages of sol-gel derived glass as an immobilisation technique for chemical reagents in optical sensor applications can be summarised as follows:

i) The glass matrix is transparent down to 250nm, making it suitable for quantitative spectrophotometric and spectrofluorimetric studies [16]

ii) The glass is chemically inert, and suitable for chemically harsh environments [23].

iii) The manufacturing process is inherently simple without the need for expensive equipment.

iv) Sol-gel manufacture offers the ability to vary the chemical nature of optical materials, in order to tailor the properties of the microstructure (e.g. refractive index, porosity/pore size, pH and hydrophobicity).

v) The sol-gel process allows the synthesis of materials of controlled porosity which can be impregnated by optically active organic dyes. The open porosity makes these molecules accessible to other reagents.

However some disadvantages of the process should be noted:

i) Complex nature of interdependencies of process parameters.

ii) A complete knowledge of the effect of varying the chemical and physical parameters of the sol-gel process is still evolving.

4.12 Preparation of a $Ru(Ph_2phen)_3^{2+}$ doped gel

A typical preparation of a dye doped gel is shown by the following reaction:

$$TEOS + 2H_2O + 3C_2H_5OH + (DYE) \xrightarrow[pH1]{HCl} (SiO_2)_n : Dye \qquad 4.7$$

This particular recipe was obtained from a collaborating group working in the Department of Pure and Applied Physics, Dublin University, Trinity College Dublin. It emerged from a systematic study of the sol-gel process parameters, the main criterion being the ability to achieve good optical quality thin films. The method of preparation is as follows: 0.0324 grams (27.67 μmoles) of ruthenium dye was placed in a clean vial. To the vial 3.9803 grams (0.086 μmoles) of ethanol were added. These were stirred using a magnetic bob until the ruthenium dye dissolved. 1.0375 (0.058 μmoles) of water was then added. The pH of the water was adjusted to 1 using hydrochloric acid. This was then stirred for a few minutes, taking care that no splashing occurred. Finally, 6.0000 grams (0.028 μmoles) of TEOS was added dropwise. The mixture was stirred for one hour in the vial. Aging of the sol was carried out at a temperature of 70°C for a duration of about 16 hours. During this time, it was important to keep the vial tightly sealed. However, the plastic covered vials were punctured with a pin, to allow a certain amount of evaporation to take place. If the sols were left uncovered, they were found to solidify

A parameter of importance in the preparation of these gels is the ruthenium dye concentration. It is difficult to define exactly the final concentration of ruthenium complex in a thin film. However, there exists a number of possible methods to express this e.g. i) molarity with respect to the total precursor solution, ii) molarity with respect to TEOS, and iii) parts per million of ruthenium complex with respect to silicon. The third method is used throughout this thesis. In the preparation just described 0.0324 grams of ruthenium complex corresponds to 40,000ppm of ruthenium weight per weight of silicon. An investigation into the optimum Ruthenium dye concentration is discussed in section 5.3.2.

4.13 Conclusion

The sol-gel process and the parameters that control the rates of the chemical reactions involved, have been described. The choice of using the sol-gel method as an immobilization technique over other possible methods, has been primarily governed by the fact that the process is inherently simple to carry out, and that it offers the possibility of altering the physical nature of the final glass structure by varying the reaction parameters. However disadvantages of using the technique include the fact that there exists many variables in the production of the glass and that the complexities of the process are not completely understood. Questions that need to be addressed with regard to the use of the sol-gel immobilization technique for sensing applications include the effect of temperature and relative humidity (and other environmental conditions) on the glass structure. These questions are addressed in section 7.5.

References:

1. Ebelmen : '**Annales de Chemie et de Physique**', 1846, No. 3, Vol. 57, pp. 319-355

2. Brinker C.J., Scherer G.W.: '**Sol-gel Science**', 1990, Academic Press, New York

3. Prospect Glas ohne Reflexe. Deutsche Spezialglas AG, Grünenplan, Germany

4. Prospect Calorex®. Das absolut farbneutrale Sonnenreflexionglas von Schott Glaserke, 1983, Mainz, Germany

5. Bell J.: '**Sol-gel halves optical filter prices**', Opto & Laser Europe, Nov. 1993, Issue 8, p. 9

6. 'Sol-gel reclassifies materials for optics', Opto & Laser Europe, Feb. 1994, Issue 9, pp. 20-22

7. Dave B.D., Dunn B., Valentine J. S., Zink J.I.: '**Sol-gel encapsulation methods for biosensors**', Analytical Chemistry, 1994, Vol. 66, No. 22, pp. 1120A-1127A

8. '**Sol-gel Optics - Processing and applications**', Klein L.C., (Ed.), Kluwer Academic Publishers, 1994

9. Hench L.L., West J.K.: '**The Sol-Gel Process**', Chemical Reviews, 1090, Vol. 90, pp. 33-72

10. Harrison C.C.: '**Sol-gel chemistry principles and applications**', Tutorial notes, May 1993, Sira communications Ltd., Kent, England.

11. Pohl E.R., Osterholtz F.D.: '**Molecular characterisation of composite interfaces**', Ishida H., Kumar G., (Ed.), 1985, Plenum, New York, p. 157

12. Keefer K.D.: '**Better ceramics through chemistry**', Brinker C.J., Clark D.E., Ulrich D.R., (Eds.), 1984, North-Holland, New York, pp. 15-24

13. Coltrain B.K., Melpolder S.M., Salva J.M.: '**IVth International Conference on Ultrastructure Processing of Ceramics, Glasses, and Composites**', Proc., Feb. 19-24, 1989, Arizona, Hench L.L., Ulrich D.R. (Eds.)

14. Colby M.W., Osaka A., MacKenzie J.D., Journal of non-Crystalline Solids, 1986, Vol. 82, p.37

15. McDonagh C., Sheridan F., Butler T., MacCraith B.D.: '**Characterisation of sol-gel-derived silica films**', submitted to Journal of non-crystalline solids, 1995

16. Kistler S.S., Journal of Physical Chemistry, 1932, Vol. 36, pp. 52-64

17. Zusman R., Rottman C., Ottolenghi M., Avnir D.: '**Doped sol-gel glasses as chemical sensors**', Journal of non-crystalline solids, 1990, Vol. 122, pp. 107-109

18. Ellerby L.M., Nishida C.R., Nishida F., Yamanaka S.A., Dunn B., Valentine J. S., Zink J.I.: '**Encapsulation of proteins in transparent porous silicate glasses prepared by the sol-gel method**', Science, Vol. 255, pp. 1113-1115

19. Braun S., Rappoport S., Zusman R., Avnir D., Ottolenghi M.: '**Biochemically active sol-gel glasses: the trapping of enzymes**', Materials Letters, 1990, Vol. 10, p. 1-5

20. Lev O., Tsionsky M., Rabinovich L., Glezer V., Sampath S., Pankratov I., Gun J.: '**Organically modified Sol-gel sensors**', Analytical Chemistry, 1995, Vol. 67, No. 1, pp. 22A-30A

21. Mac Craith B.D., Ruddy V., Potter C., '**Optical waveguide sensor using evanescent excitation of a fluorescent dye in a sol-gel glass**', Electronic Letters, 1991, Vol. 14, No. 27, pp. 1247-1248

22. Ding J.Y., Shahriari M.R., Sigel Jr. G.H.: '**Fibre-optic pH sensors prepared by sol-gel immobilisation technique**', Electronic Letters, 1991, Vol. 17, No. 27, pp. 1560-1561

23. Butler T., MacCraith B.D., McDonagh C.M: '**Development of an extended range fibre optic pH sensor using evanescent wave absorption of sol-gel entrapped pH indicators**', Proc. Chemical, Biochemical, and Environmental Fibre Sensors VII, Munich, 1993, 19-23 June, 2508-21

Chapter Five - Fibre Sensor Fabrication

5.1 Introduction

The fabrication of the fibre sensor devices forms an important section of the work undertaken in this thesis. The aim of this investigation is to develop a method of producing sol-gel coated optical fibres which are suitable for use as oxygen sensors. These sensors should be capable of detecting low concentrations of oxygen, have fast response times and have good long term stability. Among the parameters involved in producing such a device is the sol-gel process itself, which has been described in chapter 4. Other preparation steps involved include polishing of fibre ends, optimisation of sol-gel coating length and thickness, as well as optimisation of the ruthenium dye concentration within the sol-gel glass layer. Optimisation of the optical parameters, including the numerical aperture of launch/collection lens is also discussed as well as the effect of tapering the optical fiber.

5.2 Preparation of optical fibres for fluorescence sensing

The type of fibre used in this work is a plastic clad silica (PCS) fibre, of core/cladding diameter 600/760μm which is manufactured by Ceramoptec Inc., Enfield, CT, U.S.A. (NA = 0.4; n_{core} = 1.460; £3.50 per meter). Reasons for choosing this relatively large silicone cladded step-index fibre are as follows:

i) It is relatively easy to remove the cladding material from a plastic cladded fibre.

ii) The large fibre is relatively easy to handle and is more durable than smaller fibre such as single moded fibre.

iii) Even though the coupling efficiency decreases for the bulk case, with core diameter according to Egalon's treatment (see table 2.1). It would be expected that the overall captured fluorescence signal would increase with core diameter which is suggested by equation 2.23.

iv) Larger fibre diameters permit ease of coupling of light from semiconductor sources.

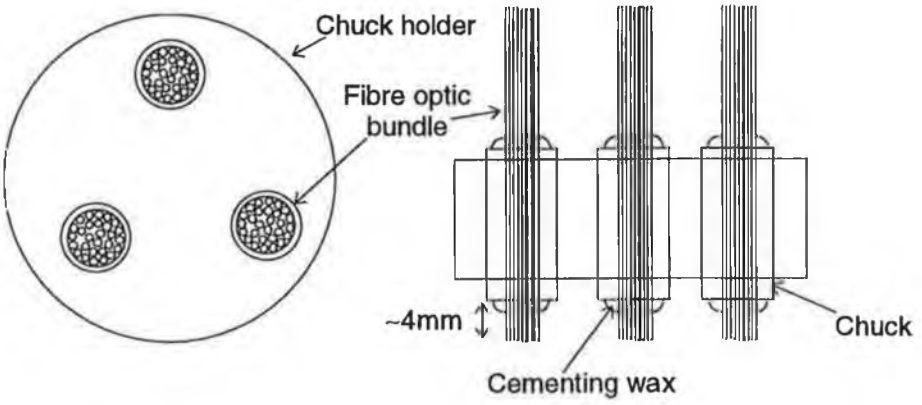

figure 5.1 Plan view and side view of polishing chuck

As standard fibre optic cleaving tools are not available to accommodate this relatively large diameter fibre, the fibres must first be broken and then polished at each end. The fibre was cut using a fibre cutter with due care taken to ensure that minimum damage occurred during the cutting procedure as this reduced the polishing time. A typical fibre length was 11cm. Approximately 40 of these rods were put into a chuck and held firmly in place using a cementing wax. The rods were left standing proud of the polishing chuck by approximately 4mm. Caution was taken to ensure the fibre ends were parallel to the lower face of the chuck. Three of these chucks were then placed in a chuck holder as illustrated in figure 5.1. The chuck holder containing all of these rods was then placed on a Logitech PM2A polishing rig as shown on figure 5.2. The rig has two large polishing plates available for different applications (a steel plate for use with both 9 μm and 3 μm polishing suspensions and a polyurethane plate for use with a 0.125μm suspension). A cam linkage system links a mechanical arm which sweeps across the radius of the polishing plate. The function of this arm is to induce a spinning action into the chuck holder thereby enhancing the uniformity of the finished polished fibres. The chuck holder is kept in place by a semi-circular arm and the motion of the polishing wheel. The machine also has a rotating drum mechanism which is used to deposit polishing suspensions onto the rotating wheel. Various grades of polishing fluids are supplied with the polisher. The 9μm Al_2O_3 fluid was initially used until the majority of the cracks were removed from the fibre end face. The grinding action of this fluid, combined with the rotation of the cast iron polishing plate for a duration of about 3 hours, polishes the end

faces of the rods. The process was then continued using the 3μm Al_2O_3 solution. At this point the steel wheel was replaced with the polyurethane wheel together with a 0.125μm polishing suspension. The feed rate for this suspension was controlled by restricting the flow tube of a gravity feed system. After approximately 3 hours and microscopic examination, the rods are then taken out of the chucks, inverted and the above is repeated for the other end face. The result is a bundle of 10 cm long PCS rods with both end faces polished.

Each rod is then cleaned, first with water and then with alcohol, to remove the remaining aluminium oxide and cementing wax. The rods are then examined individually for the polishing quality. Any non-standard rods are rejected. The primary coating is then carefully removed from ~8cm of the fibre length using a scalpel, ensuring that the fibre core is not damaged in the process. The silicone cladding is removed by etching with a commercially available chemical solvent (Lumer, Bagnolet, France), based on a methylene chloride / sulphuric acid mixture. The rods are left in contact with the etchant for about 15 minutes and are then washed in water. The rods are quickly placed in ethanol and each rod is then cleaned with an ethanol soaked lens tissue. Care is taken to prevent direct excitation of the fluorescent coating, by covering the tip with a black opaque epoxy resin (Epo-tek, Epoxy technology Inc., Billerica, MA, U.S.A.). (See figure 5.4.)

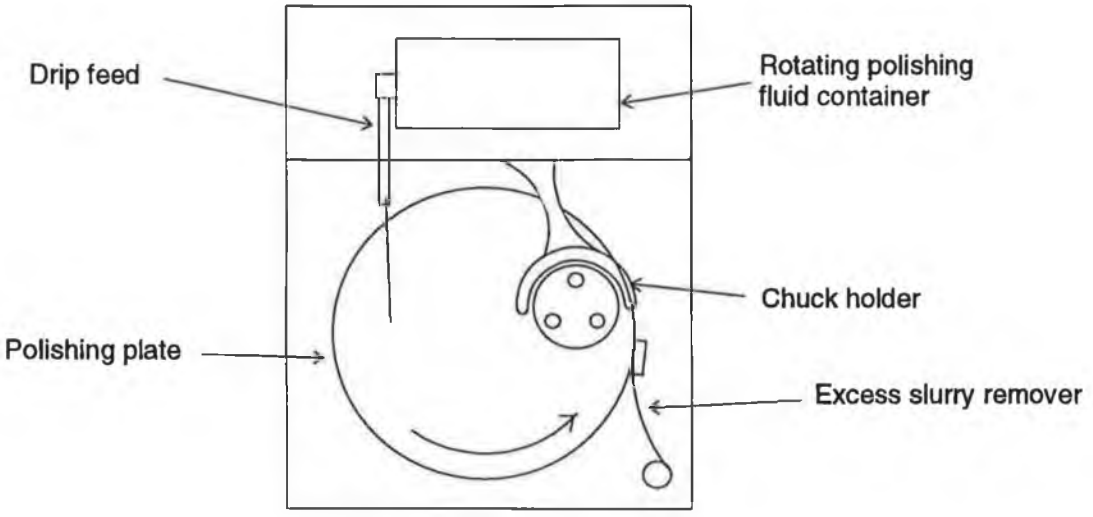

figure 5.2 Plan view of polishing rig

5.3 Dip-coating of fibres

Compared to conventional thin film forming processes, such as CVD, evaporation or sputtering, sol-gel film formation is much simpler and requires considerably less equipment. In general three methods of liquid coating that are available when laying down thin layers of precise thickness [1]. These are spin and dip coating, which are the most widely used, and meniscus coating which is comparatively new. The method used in this work is the dip-coating technique also known as drain-coating. An illustration of the apparatus used is shown in figure 5.3. It consists of a vertically moveable platform, in which a container of coating sol is firmly held. The movement of the platform is controlled using a D.C. motor which rotates a threaded bar, and thus moves the platform up and down as required. A P.C. controls the direction and speed of movement. To achieve good quality films the motor should be of the highest quality with an absolutely smooth movement. The apparatus is placed on vibration damping mats to ensure that the liquid surface remains completely stable during the dipping process. The optical fibre is held vertically in place using a septum. The platform is raised such that a certain length of the optical fibre is immersed in the sol. The platform is then dropped at a constant velocity, leaving a sol-gel thin film on the fibre. The fibre is then carefully removed and put in an oven to dry, typically at 70°C for 16 hours. A typical sensor structure obtained in this manner is shown in figure 5.4

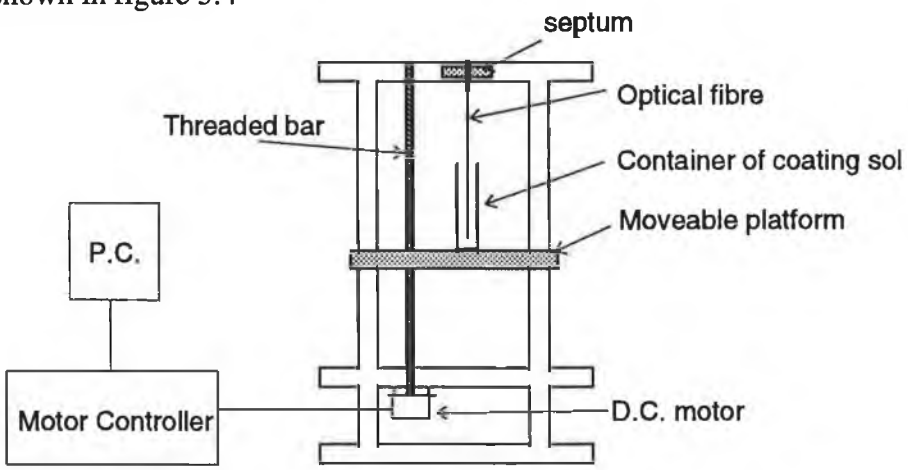

figure 5.3 Dip-coating apparatus

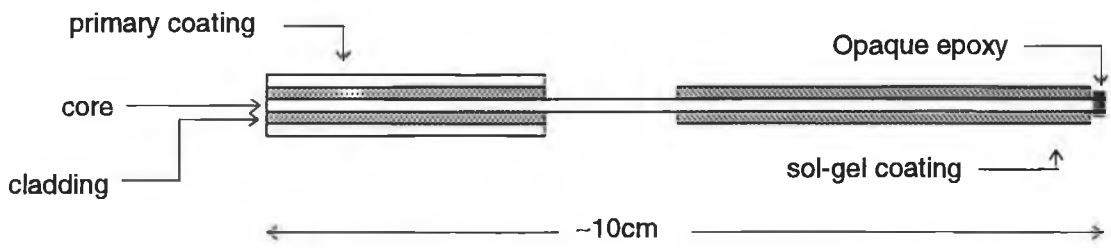

figure 5.4 Typical sensor configuration

5.2.1 Thin film thickness

A number of parameters affect the thickness of the sol-gel film. Scriven who has carried out detailed work on the dip-coating process, divides it into five stages: immersion, start-up, deposition, drainage and evaporation [2]. With volatile solvents such as alcohol, evaporation normally accompanies the start-up, deposition and drainage steps. As illustrated in figure 5.5, the moving sol-container entrains liquid in a fluid mechanical layer carrying some of the liquid toward the deposition region A, and some of the liquid out of the container with the substrate. The boundary layer is then split in two. The inner layer moves upwards with the substrate, while the outer is returned to the container. The thickness of the deposited film is related to the position of the streamline dividing the upward and downward moving layers. Up to six forces in the film deposition region govern the film thickness and position of the streamline [2]. These include i) the viscous drag upward on the liquid by the moving substrate, ii) gravity, and iii) the inertial force of the boundary layer liquid arriving at the deposition region.

When the liquid viscosity (η) and substrate speed (U) are high enough to lower the curvature of the meniscus, the deposited film thickness (t) is the thickness that balances the viscous drag ($\propto \eta U/t$) and gravity force per unit area (ρgt), where ρ is the density of the liquid and g the acceleration due to gravity. Therefore at balance

$$t = c_1 (\eta U / \rho g)^{1/2} \qquad 5.1$$

where the proportionality constant c_1, is about 0.8 for Newtonian liquids [3]. When the substrate speed and liquid viscosity are not high enough, as is often the case in sol-gel

processing, this balance is modulated by the ratio of viscous drag to liquid vapour tension (γ_{LV}) according to the following relationship [4].

$$t = 0.94(\eta U / \gamma_{LV})^{1/6}(\eta U / \rho g)^{1/2} \qquad 5.2$$

rearranging these terms gives

$$t = \frac{0.94(\eta U)^{2/3}}{\gamma_{LV}^{1/6}(\rho g)^{1/2}} \qquad 5.3$$

Equations 5.2 to 5.3 assume constant Newtonian viscosity and ignore the effects of evaporation. However, to a first approximation the dependence of film thickness on process parameters can be written as follows:

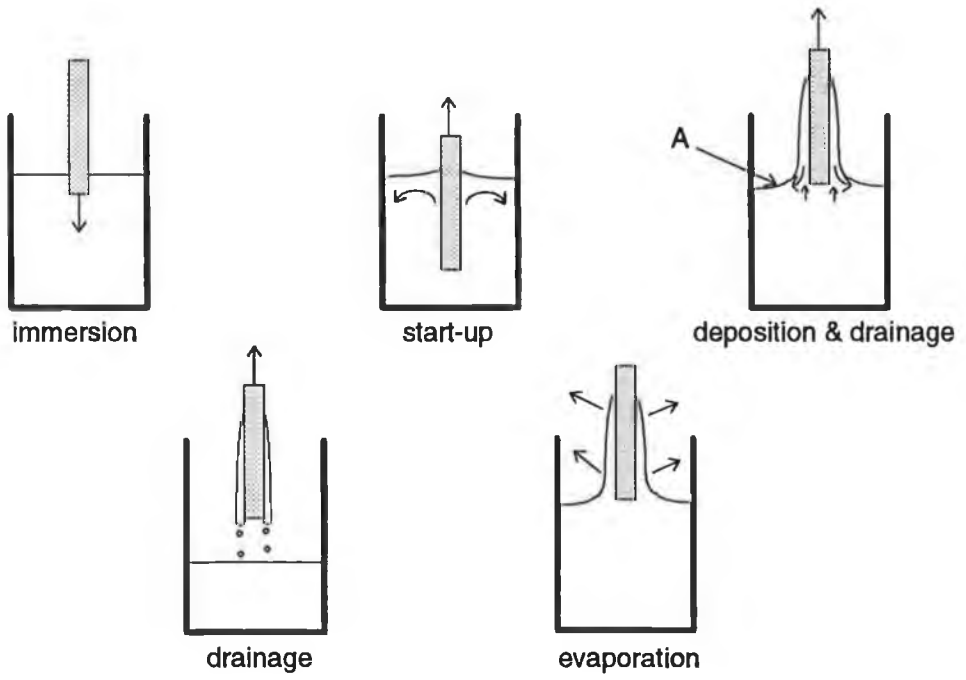

figure 5.5 Stages of the dip coating process [2].

$$thickness \propto \left[\frac{(viscosity)(withdrawal\ rate)}{(liquid\ density)}\right]^{2/3} \qquad 5.4$$

Clearly, if the viscosity and density remain constant, the film thickness is proportional to the withdrawal rate to the power of 0.6. i.e. thicker coatings are obtained at higher withdrawal rates. Several studies have been carried out on the thickness-withdrawal rate relationship. The power dependence of the thickness was found to be between 0.5 and 0.65 on the withdrawal rate [5,6].

A thickness-withdrawal rate dependence study was carried out in this laboratory to examine the validity of equation 5.4. A range of sol-gel films were prepared at pH 1 for R values of 2,4,6 and 7, respectively. Sol aging time was 5 hours in each case. R = 4,6 and 7 films were found to have a 0.6 ± 0.02 power dependence, while the R=2 had a 0.4 ± 0.03 power dependence[7].

5.3 Optimisation of physical parameters

5.3.1 Ruthenium concentration

The ruthenium dye concentration was varied with in the sol-gel coating in order to identify the optimum concentration. Optimisation criteria were first maximum fluorescence intensity from the doped sol-gel, and, second, maximum quenching of signal in the presence of oxygen.

In solution, the fluorescence signal from a fluorophore is related to the dye concentration by the following equation:

$$I_f = \eta I_0[1-\exp(-\varepsilon L c)] \qquad 5.5$$

where I_0 is the intensity of the incident radiation, ε is the molar extinction coefficient, L is the optical path length in the sample, c is the dye concentration and η is the fluorescence quantum efficiency. For low concentrations ($\varepsilon\eta c << 1$), the fluorescence intensity is directly proportional to the dye concentration i.e.

$$I_f = \eta I_0 \varepsilon L c \qquad 5.6$$

However, at higher concentrations the observed fluorescence intensity is no longer linearly proportional to the dye concentration. This is due to a number of factors, including: i) the inner filter effect, ii) photodecomposition and iii) quenching. The inner filter effect results in a reduction in observed fluorescence, due to the overlap between the fluorescence and absorption spectral distributions. The effect is also observed at high fluorophore concentrations as each layer of the of the sample absorbs some of the excitation light, such that the incident intensity is progressively reduced as it passes through the sample. The photo-decomposition process also competes with the emission process. A complete understanding of this process is not available, however, it is thought to be mainly due to the photon energy being comparable with the band disassociation energy of the absorber. The absorber molecule does not recover from photo-decomposition and it is thought that the structure of the fluorescent molecule is irreversibly damaged.

In the case of a fluorescence intensity sensor, the observed signal can be written as follows [8]:

$$I_f = \eta I_o k_{I1}\left[1-\exp(-\varepsilon_e L_e c)\right]\times\left[\exp(-\varepsilon_f L_f c)\right](k_{I2} s_d) \qquad 5.7$$

where k_{I1} is the light throughput of the optical system in the excitation spectral region, ε_e the molar absorptivity of the indicator at the exciting wavelength, L_e the optical pathlength for the exciting light in the sensor element, η the fluorescence quantum efficiency, ε_f the molar absorptivity of the indicator at the emission wavelength, L_f the optical pathlength in the sensor for the emitted light, k_{I2} the light throughput of the optical system in the emission spectral region and s_d the detector sensitivity. This expression takes account of absorption and emission contributions of a fluorescence sensor but ignores the effect of quenching and photo-decomposition. The following investigation was carried out to identify an optimum ruthenium complex concentration in a sol-gel film for use in fluorescence-based oxygen sensing.

The ruthenium dye concentration was varied within the sol-gel films from 5000ppm (weight of ruthenium complex relative to silica), up to 60000ppm. This concentration range was chosen as values less than 5000ppm were found to give weak fluorescence signals; 60000ppm was chosen arbitrarily. Three optical fibres were coated at a speed of 0.97mm/sec (see section 5.4.3) from the appropriate sols. After drying, the fibres were placed in the experimental system described in section 6.3.2 and a fluorescence intensity reading was recorded for each fibre in the presence of ambient air. The results are plotted in figure 5.6, where the standard deviation of the recorded measurements from 3 fibres are illustrated by the error bars. The results indicate that the greatest increases in fluorescence signal with ruthenium concentration, occur at the lower concentration levels. However, the rate of increase levels off to an extent, at the higher concentration levels as suggested by equations 5.5 and 5.6.

It is important to emphasise that as the ruthenium concentration in the sol-gel increases, it is expected that the refractive index of the sol-gel cladding, as well as its thickness, also increase. These effects were recorded while using the commercially

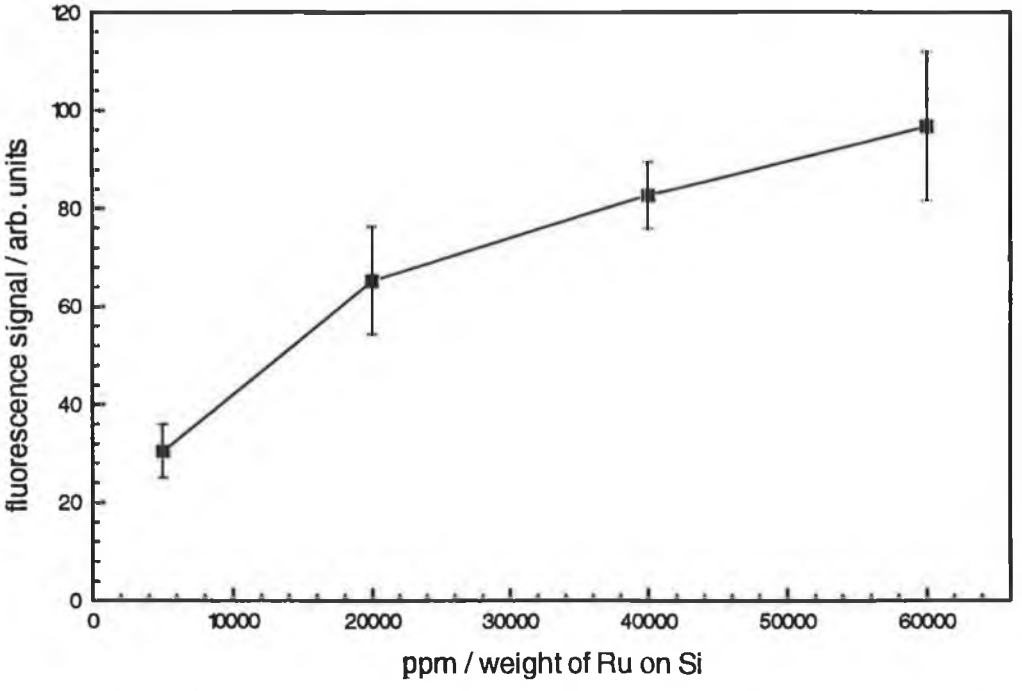

figure 5.6 Captured fluorescence signal as a function of $Ru(Ph_2phen)_3^{2+}$ concentration, in a sol-gel coated fibre.

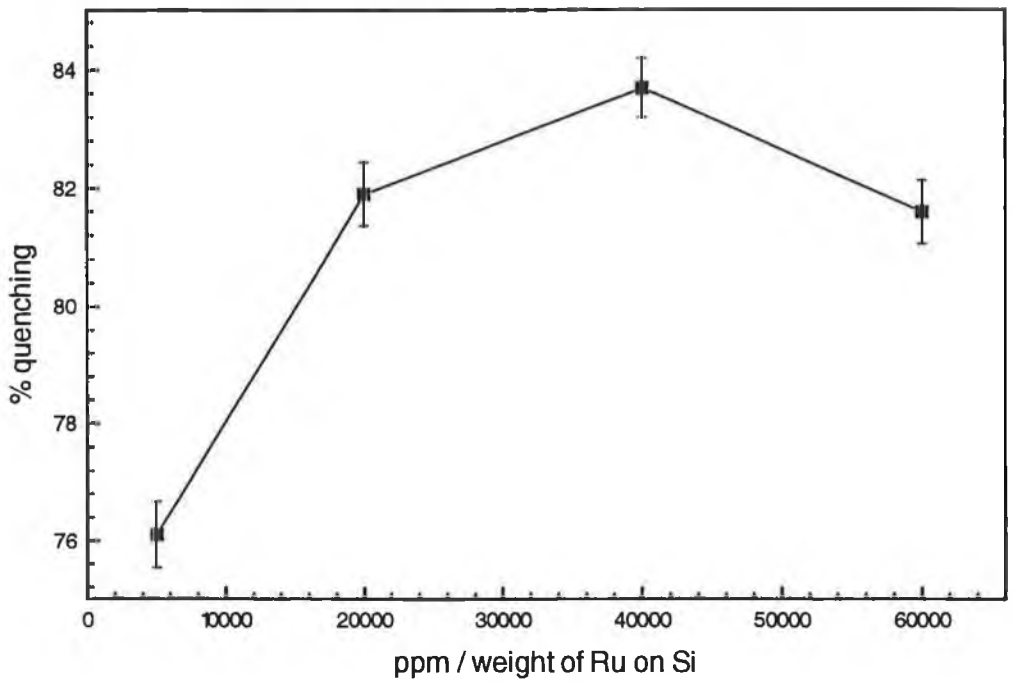

figure 5.7 Percentage fluorescence signal quenching observed for $Ru(Ph_2phen)_3^{2+}$ doped sol-gel coated optical fibres, during a change from a N_2 to an O_2 environment.

available sol-gel known as Liquicoat [9] Films manufactured using this material were doped with varying concentrations of the same ruthenium complex. As the percentage by weight of dopant in the SiO_2 liquicoat was varied from 0 to 0.6, the refractive index was found to change from 1.431 to 1.454 . The film thickness of the same samples increased from 140nm to 245nm for a coating speed of 0.97mm/sec [9]. These measurements were carried out using ellipsometric techniques on coated silicon wafers. In the data shown in figure 5.6, the percentage ruthenium complex in TEOS was varied from 0.067 for 5000ppm, to 0.809 for 60000ppm. This change in ruthenium concentration would be expected to result in a similar change in the refractive index and film thickness of the coated optical fibres. The effect of the refractive index change would lead to a decrease in Δn, or a decrease in the fluorescence coupling efficiency as predicted by Egalon's work. (A more detailed investigation of the effect of changing Δn is presented in section 5.3.4). In conclusion, the data in figure 5.6 may be considered as a combination of 4 effects.

i) An increase in fluorescence signal as predicted by equations 5.5, 5.6 and 5.7.

ii) A decrease in coupling efficiency due to the increase in cladding refractive index, or a decrease in Δn.

iii) An increase in evanescent absorption according to equation 5.9.

iv) The fourth effect is due to change in film thickness resulting from the increase in ruthenium concentration. However, as described in section 5.3.3, such a change in film thickness results in very little change in captured fluorescence signal and may therefore be neglected in the interpretation of this data.

The percentage fluorescence signal quenching due to a change from a nitrogen to an oxygen environment was also monitored for the same fibers using the system described in section 6.3.2, and is shown in figure 5.7. The data exhibit an increase from 76.1% quenching at 5000ppm to 81.6% at 60000ppm, with an optimum quenching of 83.7% occurring at 40000ppm. The error bars show the standard deviation of 3 fibres. The exact interpretation of these data is not trivial. However, the following explanation is proposed. At low ruthenium complex concentrations, the probability of quenching interactions occurring will be relative low resulting in a low percentage quenching being detected. As the concentration reaches zero, the percentage quenching being detected will go to zero such that the curve in figure 5.7 will intersect the origin. As the ruthenium complex concentration is increased, we would expect to observe an increase in percentage quenching or oxygen sensitivity as indicated by the first two points in figure 5.7. At the higher concentrations, however, the circumstances are unclear. The data might suggest that an equilibrium has been reached between ruthenium complex concentration and the probability of a quenching interaction occurring. However, a decrease in observed quenching at the higher concentrations observed. As already mentioned, a full interpretation of the underlying processes has yet to be established. Throughout the work presented in this thesis, a concentration of 40000ppm weight of ruthenium complex on silica, was used as the dopant concentration in the fabrication of the oxygen sensors.

5.3.2 Coating length

An investigation was also carried out to determine the relationship between sol-gel film coating length and captured fluorescence signal. As previously carried out, each set of three optical fibres was coated with a different length of film. The recorded data are shown in figure 5.8, where the error bars illustrate the standard deviation of the three fibres for each coating length. From the treatment of Love et al., one would expect to see

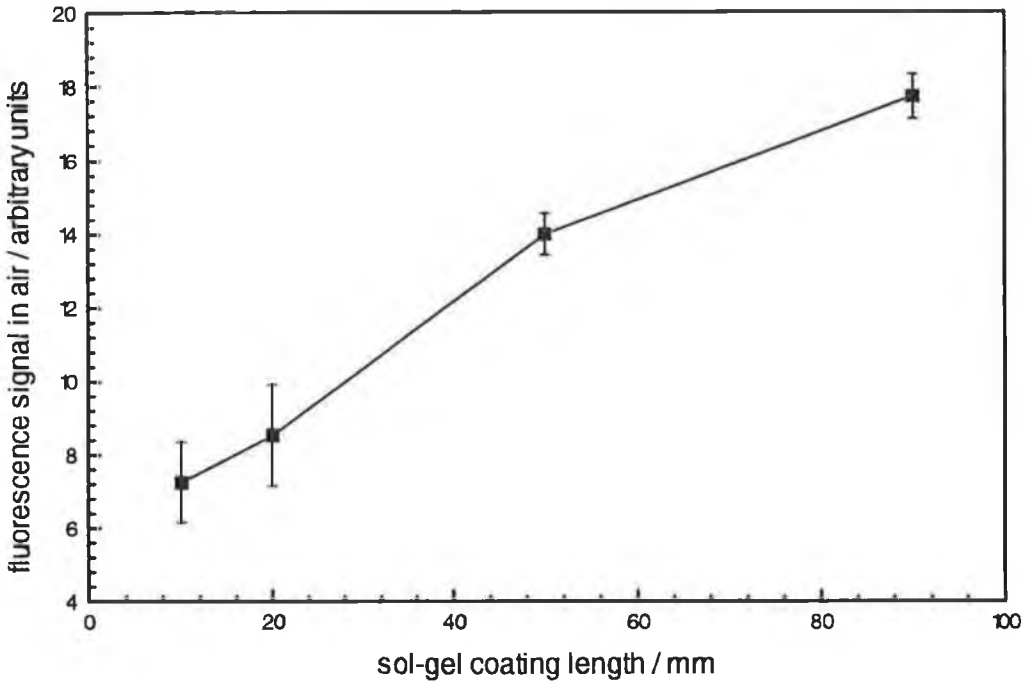

figure 5.8 Captured fluorescence signal from an optical fiber, as a function of sol-gel coating length.

a linear dependence of captured fluorescence signal on length of fluorescence coating. However, a log/log plot of the experimental data here shows that captured fluorescence signal has a 0.43 power dependence on coating length. This deviation from linearity is probably due to the decrease in transmitted power by the optical fibre, caused by the absorbing sol-gel medium [10], which is unaccounted for in Love's analysis (which assumes low absorption). The power transmitted by such an optical fibre whose cladding has been replaced locally by an absorbing medium may be written in the form

$$P(z) = P(0)\exp(-\gamma z) \qquad 5.8$$

where z is the distance along the declad length, P(0) is the power transmitted in the absence of an absorbing species and γ is an evanescent absorption coefficient. This phenomenon could be seen by closely examining an optical fibre which was being excited by an appropriate light source (see chapter 6). It was noted that the excited region of the fibre did not have a uniform intensity along its length, rather, the region closest to the

excitation source glowed brightest. If however, the excitation power was evenly distributed along the sensing region of the fibre, one would expect to observe uniform fluorescence intensity along the fibre length. In this situation the captured fluorescence signal would be expected to be directly proportional to the coating length. It should also be noted that the feed-through of the optical filter combination which is discussed in detail below may account for the D.C. offset inherent in the data i.e. If a straight line is fitted to the data in figure 5.8 and is extrapolated to zero coating length, then the line would intersect the Y-axis at a point above the origin. The distance between the intersection point and the origin would give an indication of the amount of light transmitted through the filter combination. However, this was not checked experimentally.

The same fibres were examined in terms of dependence of oxygen sensitivity on coating length. It was expected to find an independent relationship. On the contrary, however, it was discovered that greater sensitivity to oxygen was noted for longer sol-gel coating lengths. The data shown in figure 5.9 exhibits this dependence where the R_{fl}-value (i.e. fluorescence signal measured in the presence on nitrogen divided by

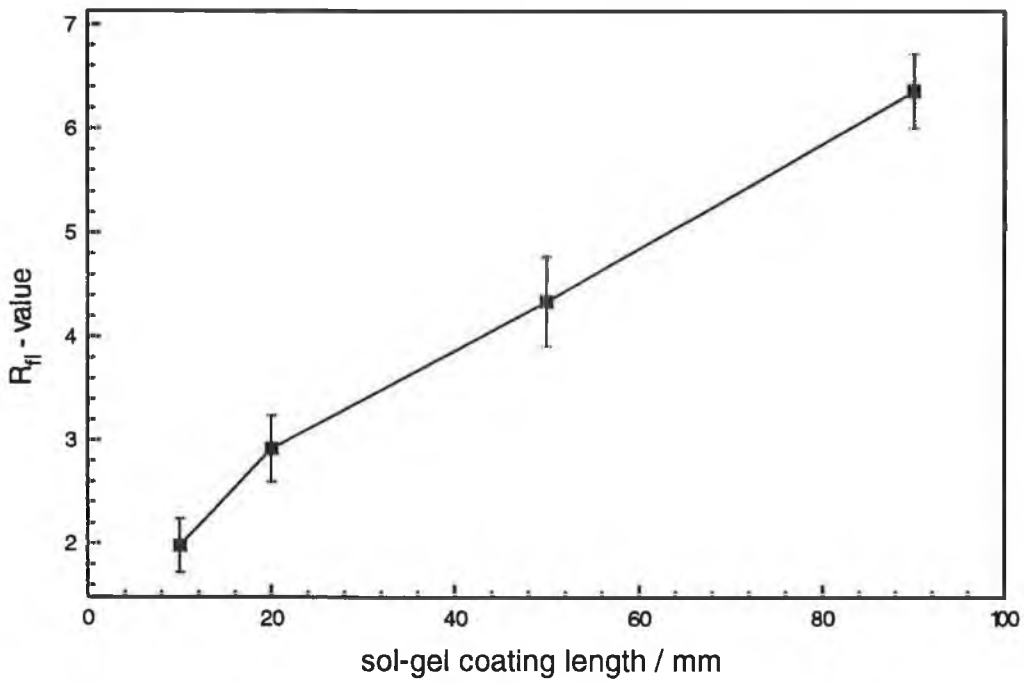

figure 5.9 Oxygen sensitivity measured in terms of R-value as a function of fluorescence coating length.

fluorescence signal in an oxygen environment) is plotted as a function of length. The standard deviation of measurements performed on three fibres is shown by the error bars. These results may possibly be accounted for by examining the experimental system which is detailed in section 6.3.2. The filter combination A and C of figure 6.9 was chosen to have a low transmittance. However, 0.1% transmittance does occur at 580nm and this results in a background signal in addition to the fluorescence signal. Consequently, for a short coating length, a larger D.C. background due to transmitted excitation light will be present. Similarly, for long lengths this background will be much smaller. This may result in an apparent higher quenching ratio for longer coating lengths than for the shorter lengths. If it were possible to achieve zero transmittance for the filter combination a constant R_{fl}-value would be expected to be seen.

5.3.3 Coating thickness

We know from equation 5.4 that the sol-gel film coating thickness may be varied by adjusting the speed of the dip-coating apparatus. For an undoped sol-gel prepared with an R-value of 2, film thicknesses were found to vary linearly from 350nm to 600nm by adjusting the dipping speed from 0.49mm/sec to 1.66mm/sec [11]. These values were measured using ellipsometry techniques on sol-gels that were aged for 17 hours and dried for 17 hours. Using both the same range of dipping rates and curing parameters, optical fibres were coated with ruthenium doped sols (40000ppm) and were examined for variation in absolute fluorescence signal and oxygen sensitivity using the experimental configuration as described in section 6.3.2. The results of the experiment are shown in table 5.1.

Coating rate (mm/sec)	**Film thickness (nm) from ref. [11]**	**Fluorescence signal (arb. units)**	**O_2 sensitivity (%)**
0.49	362 ± 20	70.87 ± 11.53	91.1 ± 0.71
0.97	433 ± 20	56.43 ± 3.50	92.0 ± 1.1
1.38	560 ± 20	54.60 ± 8.55	80.6 ± 0.50
1.66	602 ± 20	84.77 ± 17.17	84.6 ± 3.5

table 5.1 Variation of absolute signal and oxygen sensitivity of fibres with dip-coating speed.

The table also shows undoped sol-gel film thicknesses taken from reference [11] As mentioned in section 5.3.1, the doped films would be expected to have thicknesses in the order of 100nm greater than those cited from reference [11]. The third column of the table shows the absolute fluorescence signal as measured in an nitrogen atmosphere for the optical fibre sensors ± the standard deviation of 3 such samples. No obvious trend can be interpreted from the data shown. Similarly, the data recorded for the oxygen sensitivity of the fibres shows no obvious trend. The erratic nature of the data seems to be more of an artefact of the variation from fiber to fiber rather than a function of film thickness. Parameters which may account for this variation, assuming that those of equation 5.7 are held constant include the following:

i) Fibre polishing quality:- Even though fibre quality is examined prior to usage, it may occur that cracks within the optical fibre cause variation in the fluorescence signal from fibre to fibre. This variation in fluorescence signal would not be expected to be present in the phase fluorimetric measurement system.

ii) Launching position of fibre:- The ability to position an optical fibre at the correct working distance from the launching microscope objective is critical in achieving fibre to fibre repeatability. In an attempt to alleviate this problem Feldman et al. described a system in which they used a perforated mirror which was placed between the launching optics and the proximal end of a fibre probe [12]. A pair of achromat lenses then formed a real, magnified image of the fiber face, which could be viewed using a microscope eyepiece. This system allows one to adjust accurately the position of the fibre relative to the working distance of the fibre probe. However, in the case of the oxygen sensor being described, this approach is not practical, as the miniaturisation of the optical system is a priority.

iii) Other parameters that may account for the irregular nature of the above data include the error in achieving equal sol-gel coating lengths on the optical fibres, as well as the ability to repeatably obtain good quality sol-gel films on the optical fibres.

iv) It should also be noted that at the slower coating rates, films of lesser quality are produced. This is due to the fact that stepping movement of the D.C. motor becomes more pronounced at these speeds.

Furthermore, it is known that the slowest coating speed of 0.49mm/sec produces a thin film of the order of 450nm which approximately equals the penetration depth of the evanescent wave (see equation 2.13). Changes in captured fluorescence signal due to film thickness variation would therefore be expected to occur for films thinner than this. To achieve this the dipping apparatus would have to be altered by either introducing a gear mechanism, or by alternatively by replacing the motor with a finer step movement.

5.3.4 Refractive index of coating

In 1989 Thompson at el. described an experiment in which they investigated the effect of varying the V-number on the sensitivity of an evanescent wave fiber optic

biosensor. [13]. They argued that two important sensor parameters possess different dependencies on the fibre V-number. Firstly there is the proportion of power present in the evanescent wave which decreases with V-number according to Gloge[1] [14].

$$r = \frac{4\sqrt{2}}{3V} = \frac{P_{clad}}{P_{tot}} \qquad 5.9$$

where P_{clad}, and P_{tot} are respectively, the optical power in the cladding and the total power in the fibre. Secondly, there is the efficiency with which fluorescence excited by the evanescent wave at the core surface is coupled back into the fibre. As described in chapter 2, this efficiency, increases with V-number according to Marcuse [15]. More specifically, Egalon's treatment shows that it increases with Δn [16]. According to Thompson et al., these opposite V-number dependencies suggest that there may be an optimum V-number (or range of V-numbers) for a specific fibre sensor. They tested this hypothesis by labelling a declad silica fibre, with a fluorophore, and measuring the evanescent-excited fluorescence while systematically varying the V-number of the fibre. This was done by immersing the labelled fibre end either in oils having accurately known refractive indices, ethanol or air. This procedure afforded V-numbers ranging from 100 for a 200μm core fibre to greater than 3500 for a 600μm fibre in air. The normalised fluorescence intensities were found to go through maxima corresponding to particular V-numbers for each fibre tested. These results suggest that the above hypothesis is valid.

A similar type of experiment was reported in 1994 by Albin et al [17]. This work was carried out in an attempt to experimentally verify Egalon's theory, which predicts an increase in the coupling efficiency for higher differences in refractive indices between core and cladding. The experimental apparatus consisted of a declad optical fibre 50cm long, coated with a thin film of europium-doped yttrium oxide. The configuration differs from the work of Thompson et al. in that the fluorescent material, in this case, is excited with side illumination, perpendicular to the fibre axis. (Thompson et al. used evanescent wave excitation.) Part of the excited fluorescence was injected into the core and guided to a detector. The signal was measured for several different cladding refractive indices.

[1] This ratio was later corrected to 4/3V [18].

The cladding consisted of sugar dissolved in water and the refractive index was changed by varying the sugar concentration in the solution. The results indicate that the power injected into the rod, due to evanescent wave excitation, increases with difference in refractive index, which is in qualitative agreement with theory.

An attempt was made to repeat this experiment using the commercially available sol-gel, known as Liquicoat. (E. Merck, Darmstadt, Germany). By mixing Liquicoat Silica and Liquicoat Titania in specific ratios the refractive index of the sol-gel was be accurately controlled between the values of 1.42 and 1.90 [9]. It was also observed that as the percentage TiO_2 in SiO_2 was increased, the sol-gel film thickness decreased. Therefore, throughout this experiment, the coating speed of the fibres was adjusted so as to maintain a constant film thickness of 250nm from fibre to fibre. The Liquicoat fibers, all doped with the same $Ru(Ph_2phen)_3^{2+}$ concentration were tested in the experimental apparatus shown in figure 5.10. An argon-ion laser (λ = 488nm) was directed perpendicularly onto the coated end of optical

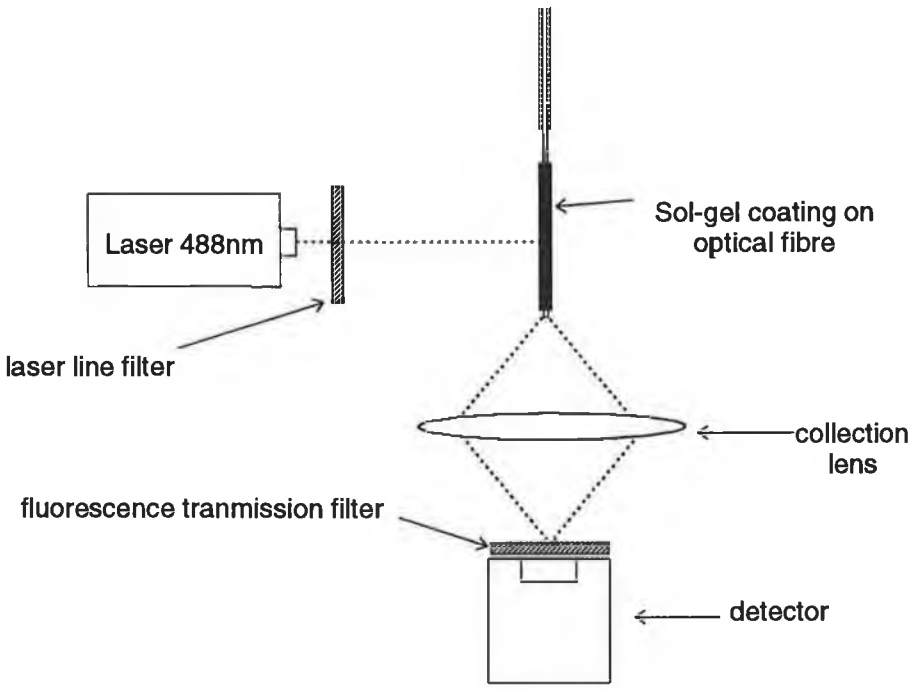

figure 5.10 Experimental configuration used to measure fluorescence signal as a function of n_{core}-n_{clad}.

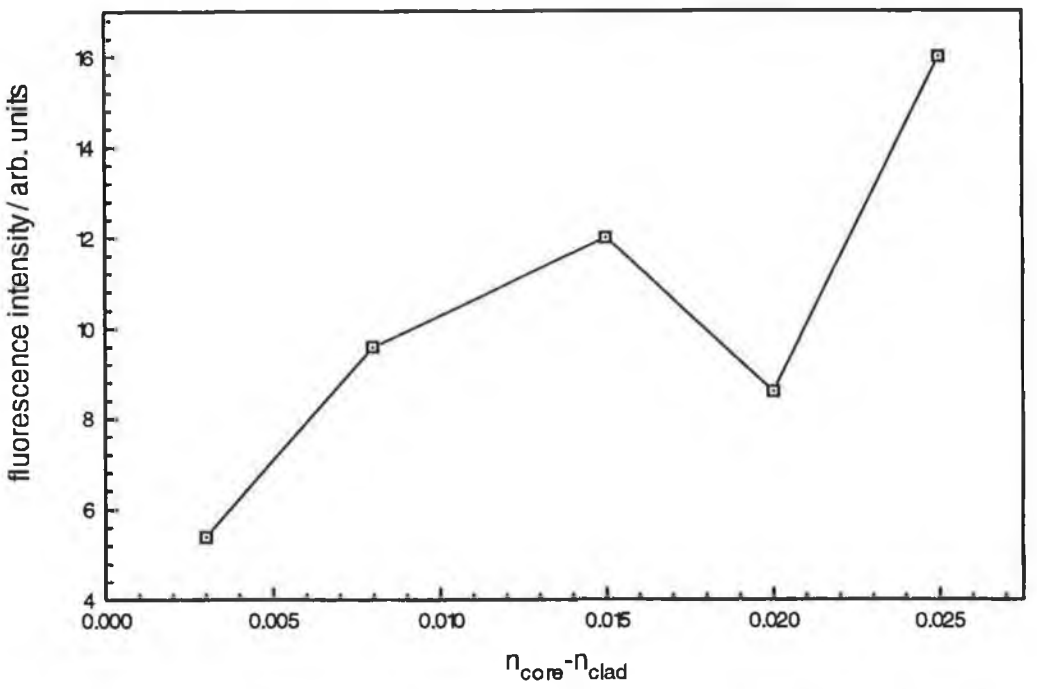

figure 5.11 Variation of captured fluorescence signal against the difference in refractive index, n_{core}-n_{clad}.

fibre and the resultant fluorescence was focused through a band pass filter onto a detector. Care was taken to ensure that each fibre was placed in the same position, relative to the laser beam and detector. The resulting data is plotted in figure 5.11. With the exception of data point #4, it was found that the captured fluorescence signal increased with Δn, which again is in qualitative agreement with Egalon's predictions.

5.4.5 Conclusion

With regard to the optimisation of the principal parameters involved in sol-gel based fluorescence sensors, the following conclusions may be deduced from the investigations described above:

i) The fluorescence signal from a typical sol-gel coated optical fibre increases with concentration of ruthenium complex in the sol-gel coating. Clearly this effect will reach saturation at sufficiently high concentrations.

ii) The oxygen sensitivity of fibre sensors increase with ruthenium complex concentration. This increase in sensitivity levels off at a concentration of ~20000ppm weight of ruthenium complex on silicon.

iii) The fluorescence signal from a fibre increases with sol-gel coating length over the short lengths examined here.

iv) Oxygen sensitivity was also found to increase with sol-gel coating length. This unexpected effect is related to the feed-through of the optical filter combination used in the measurement system.

v) No substantial change in fluorescence signal or oxygen sensitivity was recorded as a function of film thickness. This, however is probably due to the fact that the thin film thicknesses examined were all greater than the evanescent wave penetration depth.

5.5 Optimisation of optical parameters

5.5.1 Numerical aperture of launch/collection lens

An experiment was carried out to examine the modal dependence of fluorescence coupling efficiency of a coated fibre. In particular, the angles at which the fluorescence is coupled out of a typical sol-gel coated optical fibre. The experimental configuration was set-up as shown in figure 5.12. Light from an argon-ion air-cooled laser was expanded as shown, using microscope objective X and biconvex lens Y, to fill the 0.65 numerical aperture microscope objective Z. The doped sol-gel coated optical fibre was positioned at the working distance of the microscope objective for launching. A rotation stage was positioned centrally underneath the distal tip of the fibre. The rotation stage allowed measurements of rotation angles to 0.5 degree accuracy. The signal from the apertured (~1mm) photodiode attached to the rotation stage was amplified, and synchronously detected using a lock-in amplifier as illustrated. It is noted that the fibre optic sensor configuration of figure 5.4 is not suitable to observe the fluorescence modal pattern. The reason for this is that fluorescence from the sol-gel coating on the side of the fibre swamps the fluorescence signal of interest, originating from the core of the fibre. To overcome this, the fibre structure shown in figure 5.12 was used in the experiment i.e. the

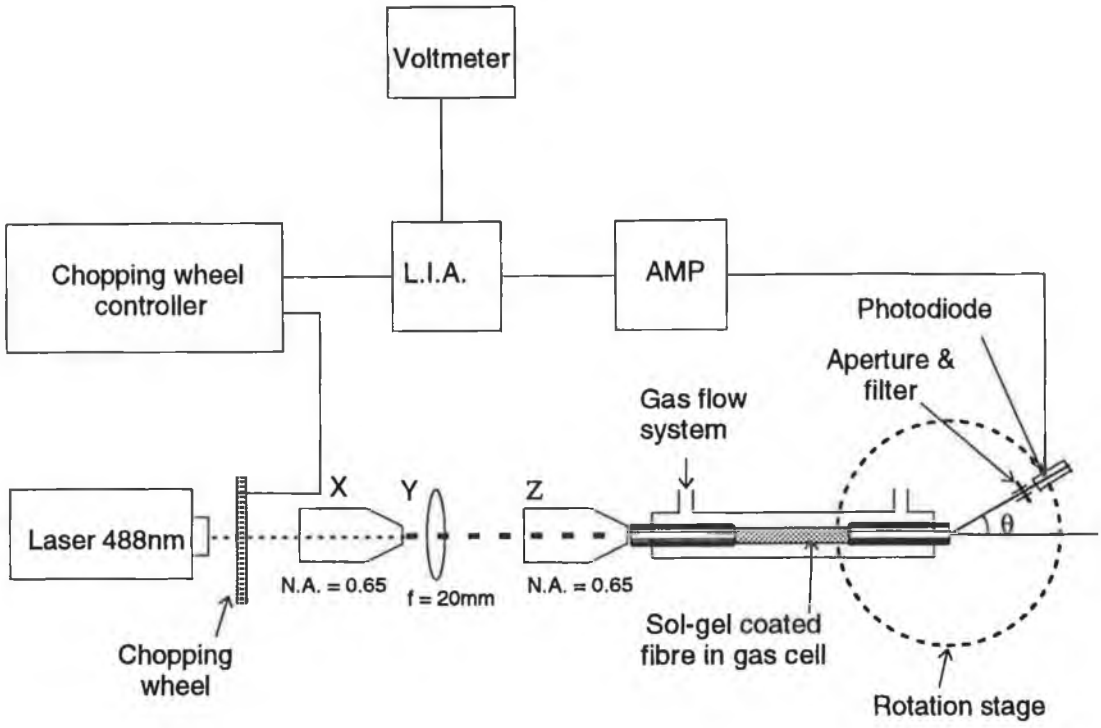

figure 5.12 Experimental configuration to measure polar distribution of fluorescence from a sol-gel coated fibre.

primary coating was removed from the central section of a fibre, leaving approximately 15mm of primary coating at both launching and distal ends. Cladding etching was carefully carried out in a petri dish, in a manner which the etchant did not come into contact with the remaining primary coating. With this sensor positioned in the experimental system, all the red/orange fluorescence reaching the photodiode originates from the fibre core. Holding white paper behind the red glass filter showed that the fluorescence modal pattern is predominately in the high order modes. The measurement of this pattern was carried out and the data recorded are shown in figure 5.13. Two sets of data are shown, one recorded in the presence of a nitrogen atmosphere and one in the presence of oxygen. The fluorescence quenching in the presence of oxygen in obvious from the data shown. A number of important points may be deduced from these data:

i) Evanescent wave excited fluorescence couples predominately into the high order modes of the fibre.

ii) From measurements and manufacturers data we know the refractive index of the sol-gel coating and cladding to be approximately 1.43 and 1.40, respectively.

Consequently, the V-number or NA of the sensing region is less than the V-number of the cladded fibre. Therefore one can assume that, all the fluorescence coupled via the evanescent tail of the guided modes into the fibre, exits the distal end (see section 5.5.2). In addition we can deduce the NA of the sol-gel coated region of the fibre to be 0.34. This yields a refractive index of 1.42 for the sol-gel coating. This value corresponds favourably to ellipsometric measurements of 1.43 [11].

iii) The NA of 0.34 (in the vicinity of 600nm) for the sol-gel coated fibre implies that a collection lens of NA $\geq$ 0.35 is sufficient to collect all the fluorescence light exiting the end of the optical fibre. However, it also suggests that an excitation numerical aperture $\geq$ 0.35 is sufficient.

iv) Figure 5.13 also suggests that a higher degree of quenching due to change from a nitrogen to an oxygen environment may be measured by inserting an annular modal mask within the collection optics so as to block the lower angle modes and transmit the higher ones. The influence of such a mask was interpreted by integrating the area under the curves in figure 5.13. The results are plotted in figure 5.14, where the X-axis shows the maximum blocking angle of the mask in degrees. Zero degrees correspond to having no mask in place. As the mask diameter increases, the analysis shows that the percentage quenching should increase from 71.1% at a mask angle of 0.6° to a maximum of 91.2% at 34.6°. However, increasing the mask angle also has the effect of reducing the overall detected fluorescence signal. An increase from 0.6° to 34.6° in mask angle reduces the overall unquenched fluorescence signal by 96.5 %. The choice of optimum mask angle would depend on the particular SNR and sensitivity requirements of each application.

5.5.2 Tapering of optical fibre

One of the problems that may arise during evanescent-wave fibre optic fluorescence sensing is mismatch between the V-number of the sensing region of the fibre, V_{sens}, and the cladded region of the fibre, V_{clad}. The only function of the remaining cladding is to enable holding of the fibre without absorbing evanescent wave energy. In many biosensing applications the sensing region is immersed in aqueous samples which have a refractive index less than that of the optical fibre cladding. This causes an abrupt change in the V-number between the sensing region and the cladded fibre, resulting in

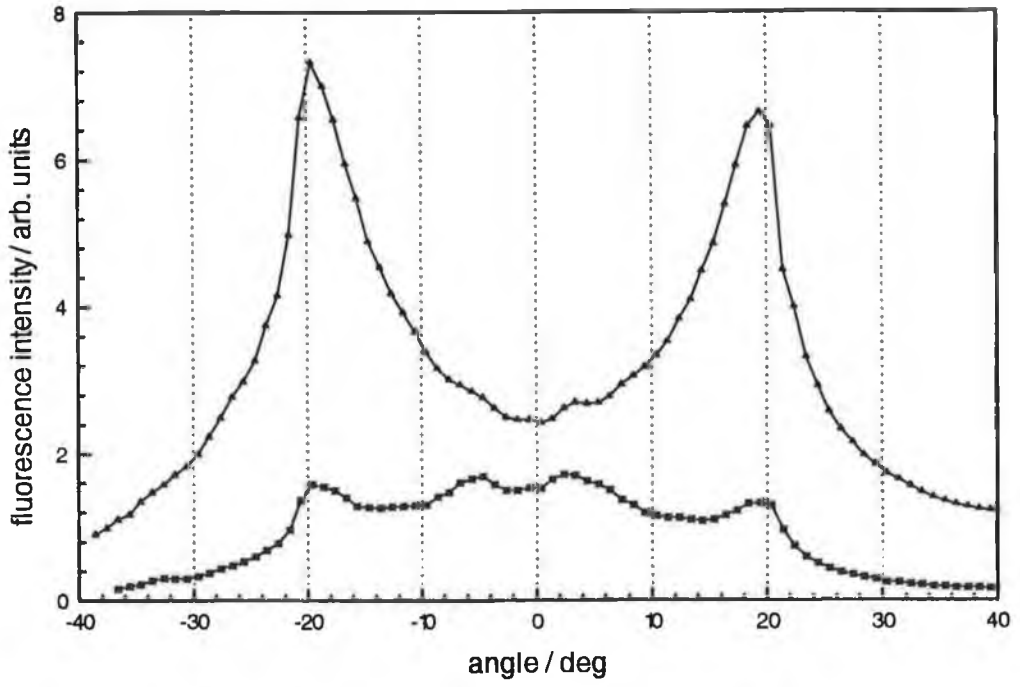

figure 5.13 Polar distribution of evanescently excited fluorescence light from fibre core, measured both in nitrogen and oxygen atmospheres.

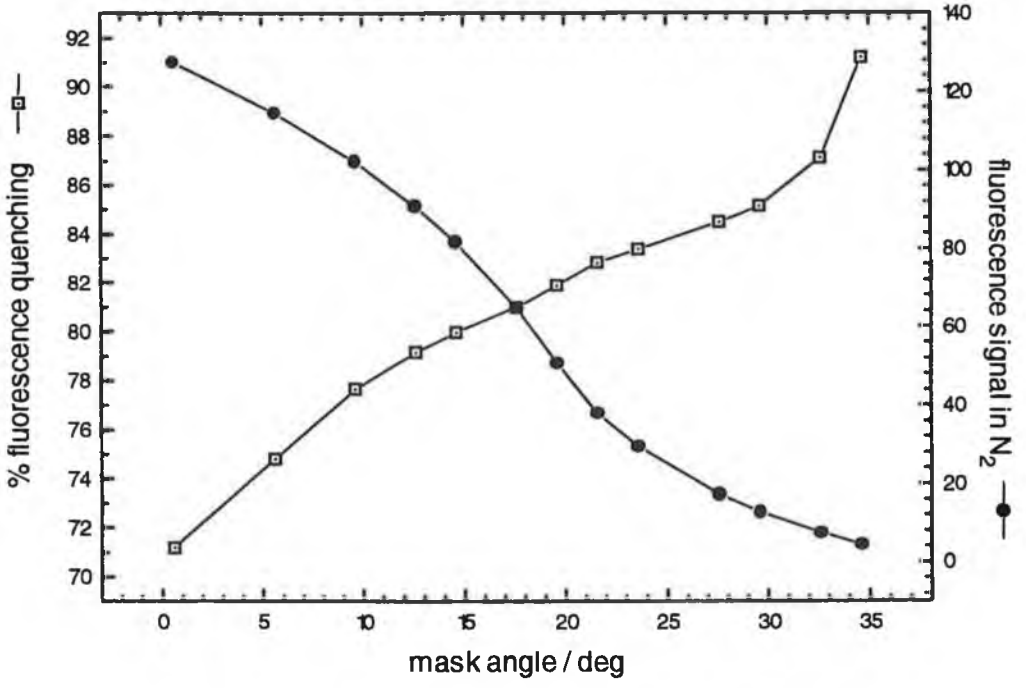

figure 5.14 Percentage quenching and fluorescence signal in nitrogen as a function of mask angle. Data taken from figure 5.13.

fluorescence light guided by the high order modes being lost. This problem is compounded by the fact that the fluorescence which couples into the fibre is carried primarily by the high order modes, as confirmed by the data in figure 5.13. Two methods have been examined in an attempt to overcome this problem.

i) Lackie et al. discussed a method of overcoming this problem by removing the cladding and using a thin ring to hold and align the proximal end of the fibre while preserving the NA of the sensing region [19].

ii) The alternative and more widely used method is to taper the fibre core. This was first proposed by Thompson et al. in 1989 [13]. The principle of tapering involves the reduction of the fibre sensing radius r_{sens}, so as to produce a V-number less than or equal to that of the cladded fibre [20]. The radius should be reduced such that

$$V_{sens} \leq V_{clad} \qquad 5.10$$

and therefore

$$r_{sens} \leq r_{cl}\left[\frac{\left(n_{co}^{\,2} - n_{cl}^{\,2}\right)}{\left(n_{co}^{\,2} - n_{sens}^{\,2}\right)}\right]^{1/2} \qquad 5.11$$

to avoid signal loss from V-number mismatch between the sensing region and the cladded region of the fibre. Anderson et al. reported a 10-fold increase in detection limits by using a continously tapered fiber rather than a non-tapered one [21]. Taper geometries have been controlled by varying the speed at which the optical fibre is immersed in a HF solution [21]. An alternative method of producing quality fibre tapers for relatively large diameter fibres has been described using butane torches to heat the fibre core which is then exposed to tensile stress [22].

In the analysis of the current situation, it was found unnecessary to taper the fibre probe due to the fact that the refractive index of the sol-gel layer is greater than that of the fibre cladding.

5.6 Conclusion

The processes involved in the fabrication of a sol-gel based fibre optic oxygen sensor have been discussed. Parameters which require optimisation include dye concentration within the sol-gel layer, coating speed of optical fibre and length of sensing region have been detailed. The investigation of optical parameters has also been carried out. Issues such as the optimisation of the numerical aperture of the collection lens, the effect of using a modal mask, and the effect of tapering fibres have been identified and their relevance discussed in specific applications.

References:

1. Thomas I.M.: '**Optical coating fabrication**', Sol-Gel Optics Processing and Application, Chapter 6, Klein C.K. (Ed.), Klumer Academic, 1994, pp 141-158

2. Scriven L.E.: '**Better Ceramics Through Chemistry III**', Clark D.E., Brinker C.J., Ulrich D.R. (Eds.), 1988, pp. 717-729

3. Brinker C.J., Scherer G.W.: '**Sol-gel Science**', Academic Press, New York, 1990

4. Strawbridge I., James P.F., Journal of Non-Crystalline Solids, 1986, Vol. 82, pp. 366-372

5. Sakka S., Kamiya K., Marita K., Yamamoto Y., Journal of Non-Crystalline solids, 1984, Vol 63, p.223

6. Yoldas B.E.: '**Investigation of porous oxides as an antireflective coating for glass surfaces**', Applied Optics, 1980, Vol 19, pp. 1425-1429

7. McDonagh C., Sheridan F., Butler T., MacCraith B.D.: '**Characterisation of sol-gel derived films**', To be published in Journal of Non-Crystalline Solids.

8. Lippitsch M.E., Draxler S.: '**Luminescence decay-time-based optical sensors: principles and problems**', Sensors & Actuators B, Vol. 11, 1993, pp. 757-762

9. Murphy V.: '**Sol-gel thin film characterisation**', 4th year Project Report, March 1994, Degree in Applied Physics, Dublin City University, Ireland.

10. Ruddy V., Mac Craith B.D., Murphy J.A.: '**Evanescent wave absorption spectroscopy using multimode fibers**', Journal of Applied Physics, 1990, Vol. 67, No. 10, pp. 6070-6074

11. Personal communication with Thomas Butler, School of Physical Sciences, Dublin City University, Ireland.

12. Feldman S.F., Uzgiris E.E.: '**Determination of the kinetic response and absolute sensitivity of a fiber-optic immunoassay**', Procs. SPIE, Vol. 2068, Chemical, Biochemical and Environmental Sensors V, Boston, 1993, pp. 139-144

13. Thompson R.B., Kondracki L.: '**Waveguide parameter for waveguide-binding fiber optic biosensors**', Proc. IEEE EMBS 11th International Conference, Kim Y., Spelman F.A. (Eds.), 1989, New York, pp. 1102-1103

14. Gloge D.: '**Weakly guiding fibers**', Applied Optics, 1971, Vol. 10, pp. 2252-2258

15. Marcuse D.: '**Launching light into fiber cores from sources located in the cladding**', Journal of lightwave technology, 1988, Vol. 6, No. 8, pp. 1273-1279

16. Egalon C.O.: '**Injection efficiency of bound modes**', NASA Contractor Report 4333, 1990

17. Albin S., Bryant A.L., Egalon C.O., Rogowski R.S., '**Injection Efficiency from a side-excited thin-film fluorescent cladding f a circular waveguide**', Optical Engineering, 1994, Vol 33, No. 4, pp. 1172-1175

18. Hale Z.M., Payne F.P.: '**Fluorescent sensors based on tapered single-mode optical fibres**', Sensors & Actuators B, 1994, Vol. 17, pp. 233-240

19. Lackie S.J., Glass T.R., Block M.J.: '**Instrumentation for Cylindrical Waveguide Evanescent Fluorosensors**', in Biosensors with Fiberoptics, Wise D.L., Winegard L.B.(Eds.), Humana Press, 1991, pp. 225-251

20. Golden J.P., Shriver-Lake., Anderson G.P., Thompson R.B., Ligler.: '**Fluorometer and tapered fiber optic probes for sensing in the evanescent wave**', Optical Engineering, 1992, Vol. 31, No. 7, pp. 1458-1462

21. Anderson G.P., Golden J.P., Ligler F.S., '**A fiber optic biosensor: combination tapered fibers designed for improved signal acquisition**', Biosensors & Bioelectronics, 1993, Vol. 8, pp. 249-256

22. Cryan C.: '**An optical fibre refractometer**', 4th year Project Report, April 1989, Degree in Applied Physics, Dublin City University, Ireland.

Chapter Six - Experimental Systems

6.1 Introduction

The requirements of the experimental systems to measure the fluorescence intensity and phase fluorimetric response of the sol-gel coated fibres are discussed in this chapter. A schematic diagram of a typical fluorescence intensity measuring system is shown in figure 6.1. It consists of a light source of a particular wavelength range which overlaps the absorption band, $\Delta\lambda_{abs}$, of the fluorescent material. An optical arrangement is usually necessary to couple light from the source into the fluorescent material, along with an excitation filter which transmits the excitation band of wavelengths, $\Delta\lambda_{ex}$, while blocking any light in the fluorescence region. The fluorescence emitted from the material at the higher wavelength band, $\Delta\lambda_{em}$, is then captured and focused onto a suitable photo-detector. The emission filter is used to prevent excitation light from reaching the detector. The photo-detector and associated processing electronics thus record the fluorescence intensity of the material as a function of time. This type of system can be changed to a phase fluorimetric type system by modulating the light source and adjusting the detection electronics to measure the phase shift between the modulator and the detected fluorescence. A phase fluorimetric system thus records phase angle as a function of time.

In setting up such experimental systems, the first requirement is to choose a suitable light source. As the sol-gel immobilised ruthenium complex was found to have a broad absorption band with a maximum occurring at 450nm (see figure 6.2), an argon-ion air-cooled laser with a 488nm line was suitable to excite its fluorescence. The complete experimental systems using the laser as excitation source in fluorescence intensity mode and in phase fluorimetric mode are described in sections 6.2.1. and 6.2.2, respectively. Although a laser is shown to work well as an excitation source, a number of disadvantages are noted:

i) the physical size of the laser lends itself for use only in a laboratory based measurement system.

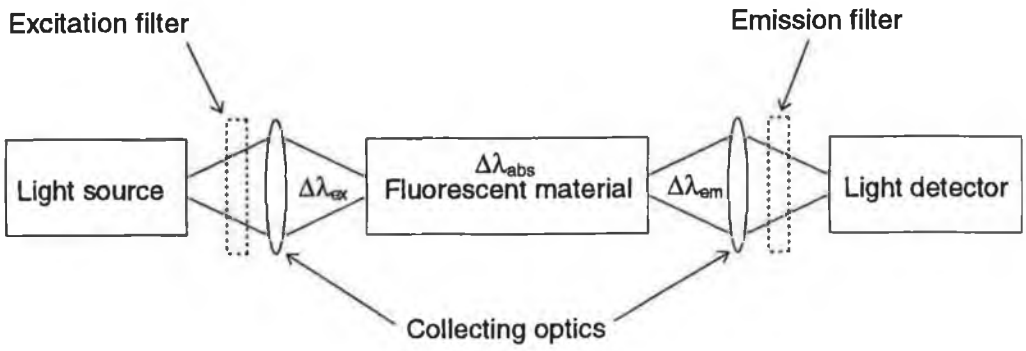

figure 6.1 Typical fluorescence intensity measurement system

ii) the high power consumption of such a laser results in relatively high running costs.

iii) the system is relatively expensive.

iv) optical density filters are often required to reduce the effect of photobleaching in fluorescent material.

v) modulation of excitation light is required to carry out lock-in detection.

Alternative excitation sources for use in fluorescence sensors were therefore investigated. The use of light emitting diodes (LED's) as radiation sources is an attractive alternative. LED's have many operational advantages over other sources:

i) because direct electronic intensity modulation is feasible, moving parts are not required.

ii) they are inexpensive due to mass production.

iii) they are small in size and mechanically stable.

iv) their low power consumption makes them suitable for battery operation.

v) they have stable output intensities.

A lot of research is currently being carried out to develop LED sources in the blue region of the spectrum. Up to recently, although LED sources at longer wavelengths have been readily available, blue LEDs were not available. In 1992, 15 mcd blue LED's, manufactured by Ledtronics Inc, CA, U.S.A., became available commercially. In 1993, the maximum luminous intensity of these devices was increased to 30 mcd. These blue LEDs with a peak wavelength of 467nm (see figure 6.2) matched the absorption of the immobilised ruthenium complexes extremely well. The availability of these LEDs allowed

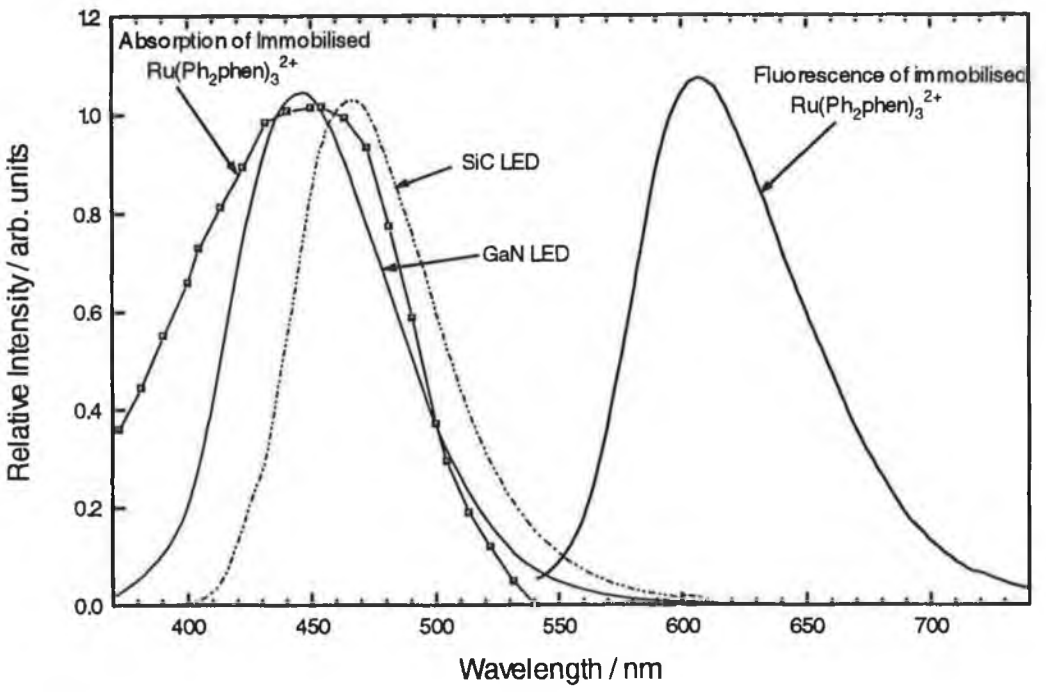

figure 6.2 Spectroscopy of oxygen sensor showing emission overlap both of a silicon carbide and a gallium nitride blue LED with the absorption spectrum of a sol-gel immobilised ruthenium complex. The fluorescence emission from such a complex is also shown, where λ_{peak} = 607nm.

the construction of miniaturised optical oxygen sensors. However, their very low emission intensity required the use of a photomultiplier tube or equivalent to achieve adequate signal to noise ratios (SNR). In early 1994, further improvements in blue LED technology resulted in the availability of a 1000 mcd device. This resulted in an increase from 0.5µW to 1mW in total output power of the LEDs, for a forward current of 35mA. These new devices also had the advantage that their peak power was at 446nm which matched exactly the absorption peak of the ruthenium complexes as shown in figure 6.2. Their availability made possible an all-solid-state portable oxygen sensor. Fluorescence signals from a typical sol-gel coated fibre were now found to yield high SNRs when detected using a standard photodiode. Section 6.3 describes the use of these LEDs in an experimental system that measures both the fluorescence intensity and the phase fluorimetric response of the fibre optic oxygen probes. The construction of an all-solid-state portable sensing device is completed by the use of a balanced demodulator as a lock-in amplifier. This work is detailed in section 6.4.

The final sections (6.6, 6.7) of this chapter includes a discussion on the various techniques used in phase measurements which were used in the phase fluorimetric experimental system.

6.2 Laser based system

6.2.1 Fluorescence intensity mode

The laser based experimental system used to characterise the multimode oxygen sensors in terms of fluorescence intensity variation is shown in figure 6.3. The experimental system shown is equivalent in principle to that illustrated in figure 6.1. Light at a wavelength of 488nm from an air-cooled argon-ion laser (Cathodeon, Oxford, U.K.), is passed through expanding optics, microscope objective X and collimating lens Y, as shown, and is then reflected from a Raman holographic edge filter C, (Physical Optics Corporation, Torrance, CA, U.S.A.), via a microscope objective, Z, to the coated PCS600 fibre which is mounted in a gas cell. The expanded and collimated laser beam is signified using the thicker dotted line in the diagram. The holographic filter is designed to be used off-axis from 5-20 degrees. Mirrors A and B are therefore adjusted such that the angle α has a value of 12°. This corresponds to 0% transmission at 488nm and 80% transmission at 607nm (see appendix B for specifications of filter), the peak fluorescence wavelength of the sol-gel-immobilised ruthenium complex (see figure 6.2). The gas flow system consists of a combination of cylinders of oxygen, nitrogen and air (if required), mass-flow controllers and a mixing unit, which enables precise gas mixtures to be passed at selected flow rates, through the gas cell. The gas cell is held in a metal frame which is attached to a X-Y-Z positioner, thus allowing optimisation of the launching position of the fibre. The evanescent field of the guided radiation excites the entrapped ruthenium complex and a fraction of this resultant fluorescence is captured by the fibre. Some of this guided fluorescence is transmitted back through the holographic edge filter, which rejects scattered or reflected laser radiation, and is then focused onto the scanning monochromator slit (or optical filter arrangement). The focal length of lens W is 100mm, which combined with a diameter of 25mm, closely matches the f-number of the monochromator. The ruthenium complex fluorescence is detected by a Hamamatsu PMT (serial number R1414), whose signal is amplified using an Ithaco current sensitive

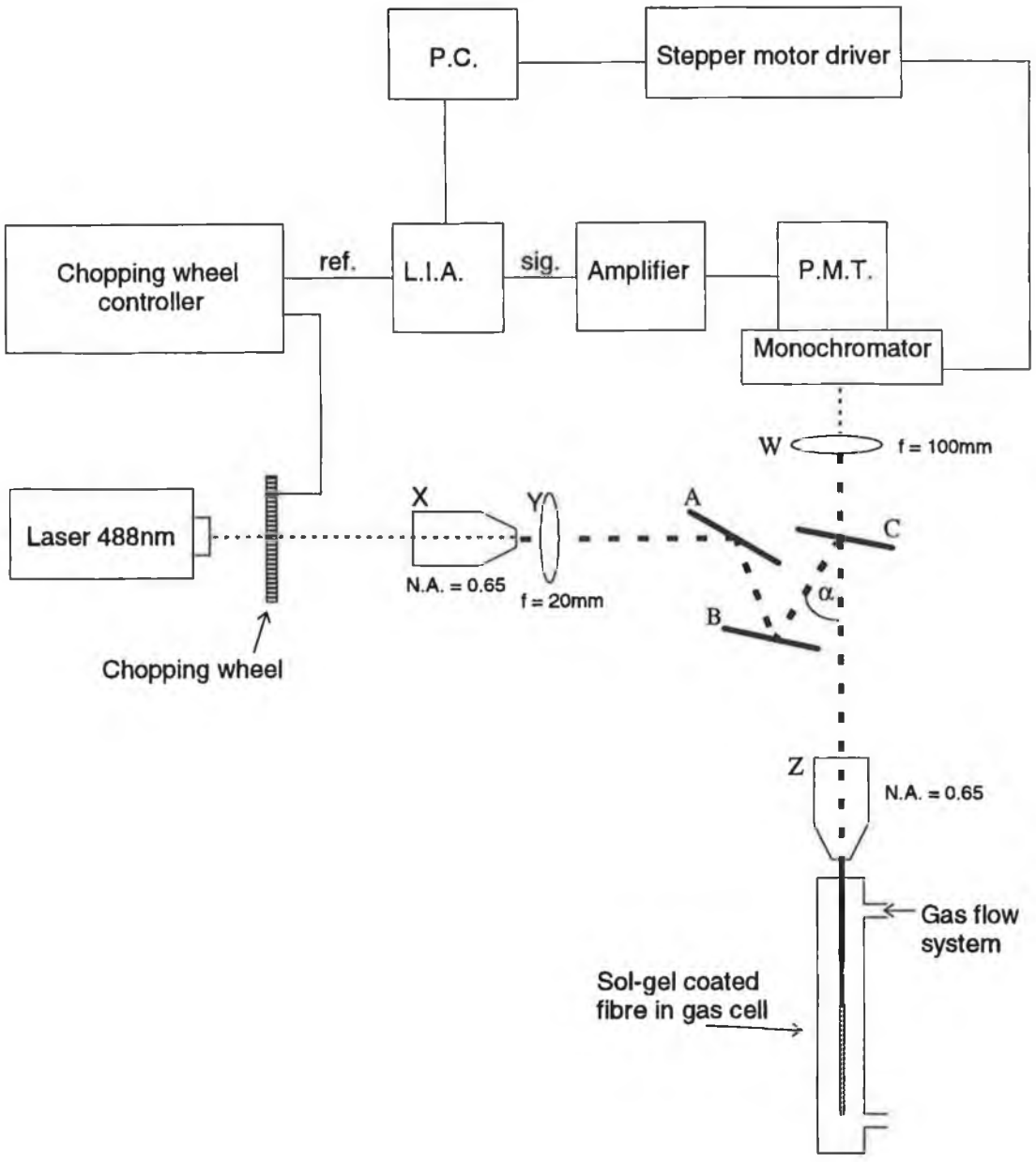

figure 6.3 Fluorescence intensity measurement system using an argon-ion laser as excitation source

amplifier (model number 1642), and fed into a lock-in amplifier (Stanford Research Systems, model SR510), for synchronous detection. Software was written to control a Bytronics mutifunction input/output card (model number MPIBM3), which converts the detected analogue signal to digital format, which is then passed to the P.C. for storage. Software was also written to control the monochromator such that, if required, a fluorescence spectra of 0.90nm resulution could be obtained using a slit width of 150μm.

However, during normal mode of operation the monochromator is replaced with a longwave pass filter (catalogue number SOG-550, CVI Laser Corporation, Albuquerque, N.M., U.S.A.). This filter has a transmission of 99% above 600nm. The only signal therefore being detected by the lock-in amplifier should be the fluorescence signal from the evanescently excited ruthenium complex. However, in practice this is not entirely the case, as some of the scattered 488nm light is detected by the PMT. This leads to a D.C. background level in the detected fluorescence signal. One way of reducing this offset is by placing the chopping wheel between the microscope objective Z, and the optical fibre as carried out by Ligler et al. [1]. However, due to the high fluorescence signals that were being detected and the short working distance of lens W, this was not carried out. Alternatively, the D.C. background level can be eliminated by using the 'offset' function within the lock-in amplifier. The fluorescence signal is recorded as a function of time. The gas in the cell is alternated between oxygen and nitrogen or a controlled mixture of the two gases. As the oxygen enters the cell environment and displaces the nitrogen, a dramatic decrease in detected signal is observed, due to the quenching process. The observed response of the oxygen probes is presented in chapter 7.

6.2.2 Phase fluorimetric mode

The experimental apparatus used in characterising the optical fibre oxygen sensor in phase fluorimetric mode is very similar to that illustrated in figure 6.3. However, due to the mechanical limitation in modulation frequency of the chopping wheel (maximum of ~2kHz), an alternative method of light modulation had to be used. An acousto-optic modulator (Hoya Electronics Co., Ltd., Tokyo, Japan) was therefore used to modulate the light. The experimental set-up is illustrated in figure 6.4. The radio frequency generator sets up an acoustic wave in the tellurite crystal, which behaves like a sinusoidal grating [2]. The incident laser beam passing through this grating is thus diffracted into several orders as illustrated [3]. Analogue modulation of the radio frequency results in the transmitted laser beam being modulated. Due to the fact that only one of the beams can be used, an iris is required to block the remaining beams. By appropriate adjustment of the analogue signal from the signal generator, square wave or sinusoidal wave

modulation of the laser beam can be achieved up to frequencies of ~10MHz as required. The light that passes through the iris is then expanded to a beam diameter of 5mm (so as to fill microscope objective Z), as shown in figure 6.3. The remaining phase fluorimetric experimental system is equivalent to that of figure 6.3. The sole difference is that the lock-in amplifier is replaced with a phase detector which monitors the phase angle between the modulating excitation beam and the detected fluorescent light. As oxygen replaces nitrogen in the gas cell, a decrease in phase shift occurs between the modulation of the excitation beam and the resultant fluorescence. The phase shift that occurs can be measured using a number of approaches. Various phase detecting systems are discussed in section 6.6.

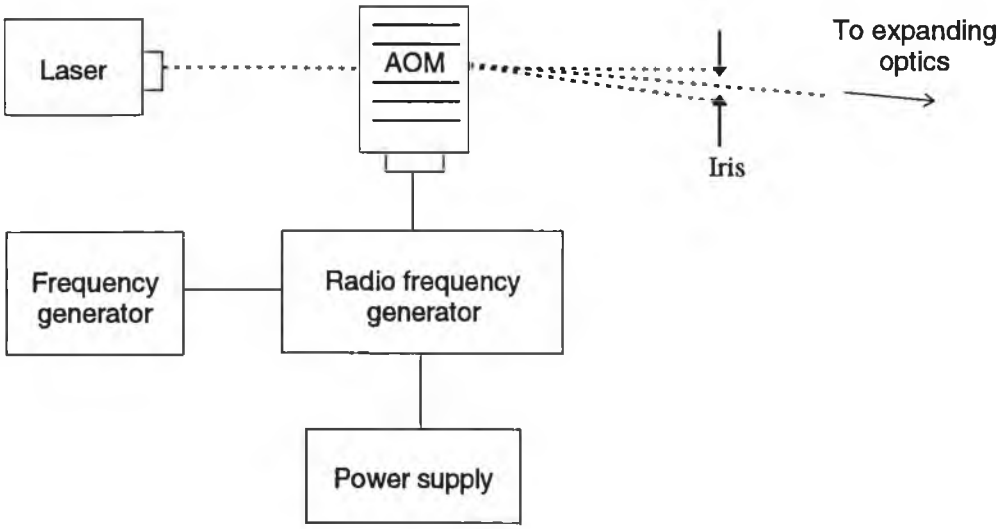

figure 6.4 Acousto-optic modulation of laser beam

6.3 LED based system

6.3.1 Introduction

Because of their many advantages, there is a strong desire to use LED's in optical systems. Commonly available LED's cover a wavelength range from about 555nm to the near-infrared spectral region. However, most fluorescence chemistries require excitation wavelengths of less than 500nm. The typical semiconductor materials used in the manufacture of these longer wavelength LEDs are III-V compounds such as gallium

arsenide phosphide ($GaAs_{1-x}P_x$), gallium phosphide (GaP) and gallium aluminium arsenide ($Ga_{1-x}Al_xAs$) [4]. For emission in the blue region of the spectrum, these materials are not suitable because their band gaps are too small. However, there are alternative compounds that are of interest in the production of blue LED's. These include gallium nitride (GaN), zinc sulfide (ZnS), zinc selenide (ZnSe), and silicon carbide (SiC) [4]. The low intensity LEDs of 15 mcd and 30 mcd, which were previously mentioned, are fabricated from silicon carbide, whereas the newer ultra bright blue LEDs use gallium nitride.

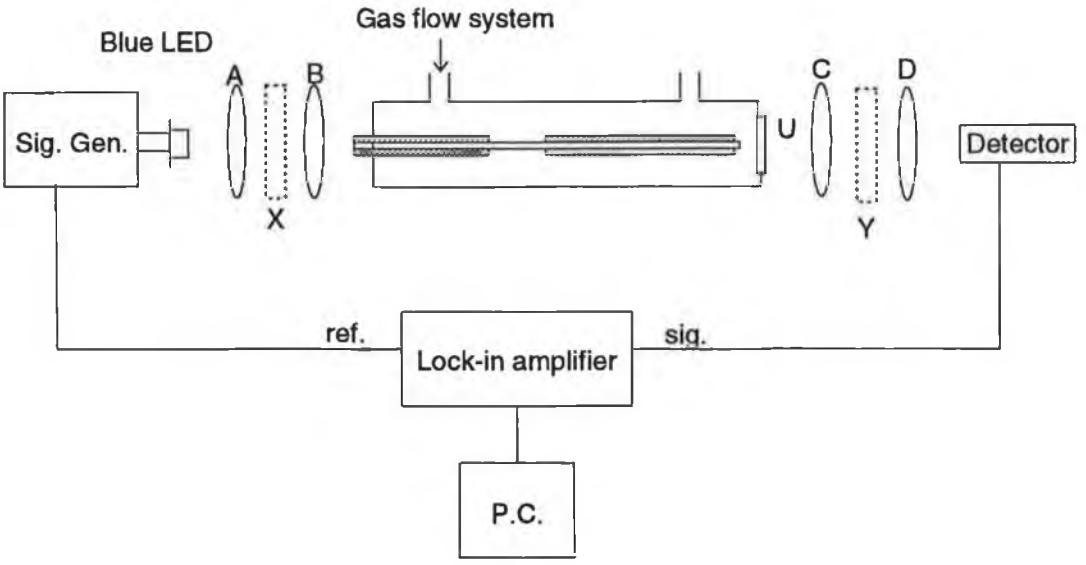

figure 6.5 LED based fluorescence intensity system (I)

6.3.2 Fluorescence intensity mode

The LED-based fluorescence intensity system was originally set-up using the weaker SiC blue LEDs. To achieve SNRs of the order of 1000, a PMT was required. The system is illustrated in figure 6.5. A signal generator was used to modulate the LED for lock-in amplification and detection. Various configurations for launching the LED light into the optical fibre were investigated. The simplest coupling scheme, whereby the fibre is butted directly against the surface of the LED, is not very efficient because the beam diameter of the LED at the dome surface, is in the order of 4 times greater than the fibre core diameter. Significant launching improvements which involving either tapering the fibre end or placing a microlens between the LED and fibre have been reported in the

past [5]. However, in the present situation, it was found necessary to use the optical filter X, between the LED and fibre to remove the portion of the LED emission that overlaps the region of the fluorescence. Optimum launching of the LED light was achieved, by first polishing the 5mm diameter LED down to a level close to the emitting surface.

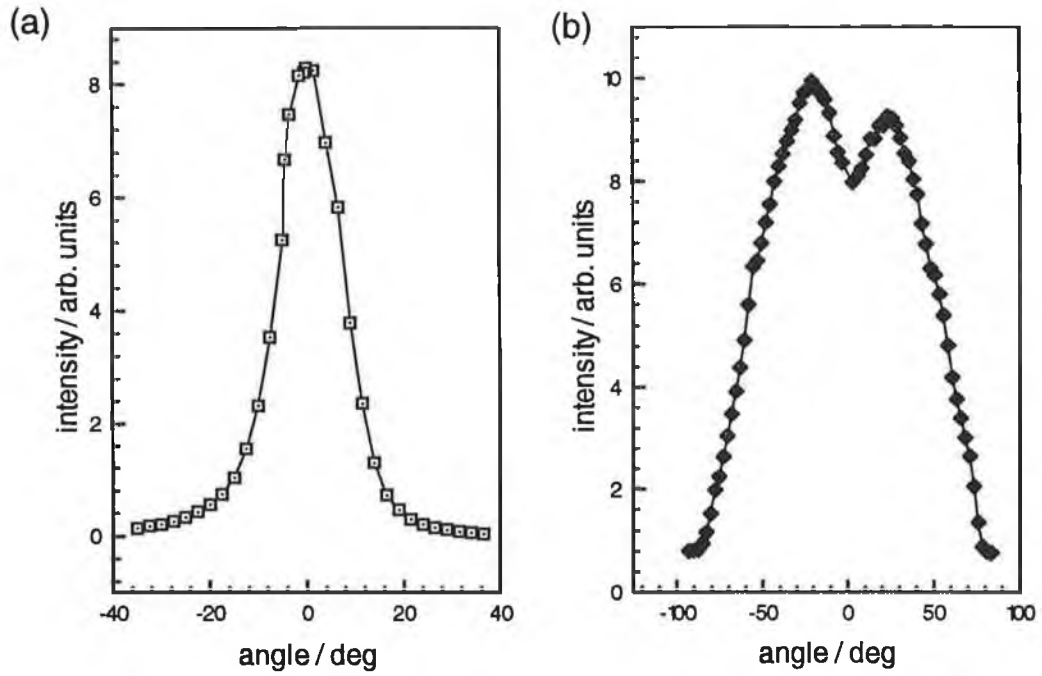

figure 6.6 Polar distribution of radiation from (a) an unpolished SiC LED and (b) a polished SiC LED.

Various grades of optical polishing paper were used to achieve a good quality finish on the LED surface. The effect of polishing the dome of the LED can be seen from the polar distribution of light intensities shown in figure 6.6. In figure 6.6(a), the majority of the radiation from the unpolished LED is directed within a 10° light cone. However, polishing the LED dome removes this high directivity, and results in a highly diffuse emitting surface as shown in figure 6.6(b). The dip in intensity observed at 0° is due to the circular structure of the semi-conductor junction. A 10mm focal length convex lens was placed 10mm from the LED surface, to achieve a collimated beam of diameter 5mm, which filled the aperture of the microscope objective lens B. Filter X (Infrared Engineering, Essex, London) is a band pass filter ($\lambda_{cut\text{-}on}$ = 400nm and $\lambda_{cut\text{-}off}$ = 505nm, see appendix C for specifications). A scan of the blue LED emission, plus filter X is shown in figure 6.7. Light from the 0.65 NA microscope objective was launched into the fibre. The fluorescence coupled back into the fibre was then collected through the glass window U. A convex lens C, of diameter 25mm and focal length 20mm was used to collimate the collected fluorescence (NA = 0.52, which is sufficient to collect all the fluorescence, see section 5.5.1). This was

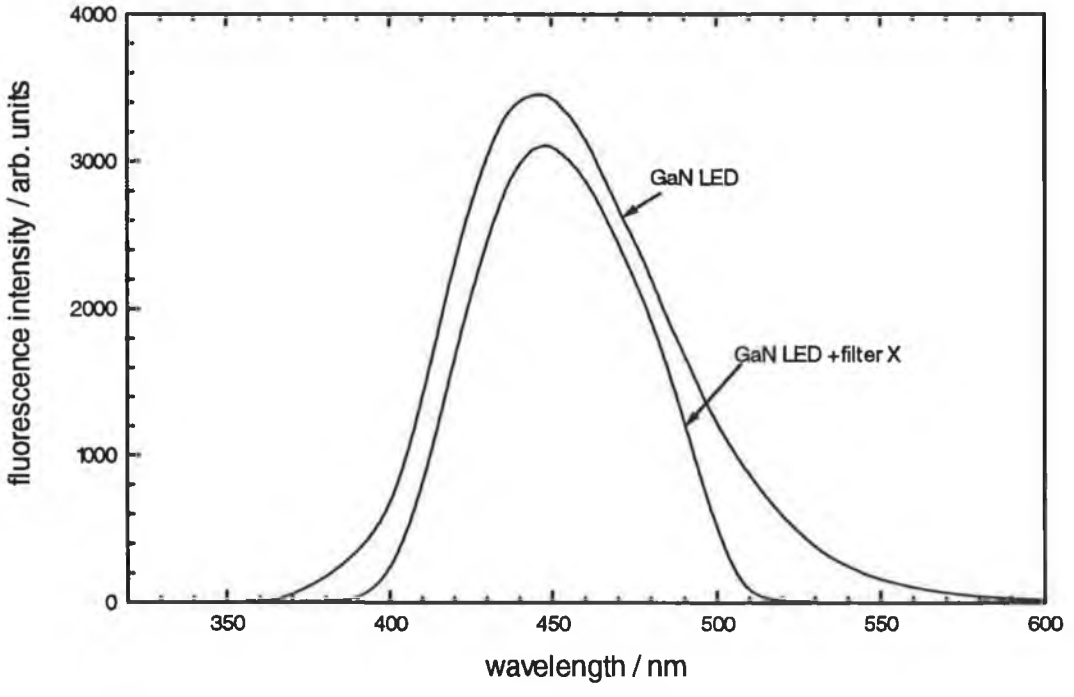

figure 6.7 Blue LED emission with and without filter X

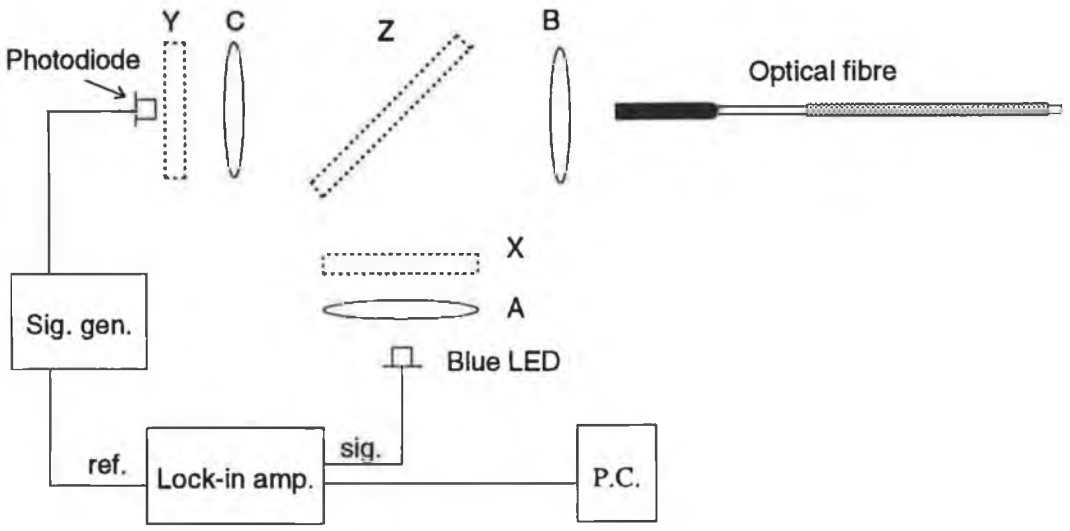

figure 6.8 LED based fluorescence intensity system (II)

then focused onto the PMT through filter Y. (Filter Y is equivalent to the fluorescence-transmitting filter used in the laser based system). It is important that the filter combination XY has close to zero transmittance. A spectrophotometer was used to test this. The results showed that a maximum of 0.1% transmittance occurred at 580nm.

An alternative LED based experimental arrangement was also investigated. Up to this point the fluorescence has been excited from the proximal end and collected at the distal end of the fibre. Since the fluorescence photons in the waveguide have no preferential direction, the signals that exit the opposite ends of the fibre are equal in power [6]. There are a number of advantages in collecting the fluorescence from the proximal end, just as was carried out in the case of the laser excitation:

i) in the order of 90% of the excitation light launched into the waveguide exits at the distal end. Therefore the signal-to-background ratio is higher for proximal end than for distal end collection.

ii) having the distal end free makes the installation and alignment of the sensor easier.

iii) only the proximal end requires focusing optics.

iv) it allows for the use of long fibre lengths, suitable for remote sensing applications.

The introduction of the higher power LEDs also made the set-up and alignment of this experimental system easier to accomplish. The new system is illustrated in figure 6.8. Corresponding components of this system are equivalent to those used in figure 6.5. However, high SNRs were achievable using a photodiode as detector. The photodiode used was a Hamamatsu silicon detector (type number S1133-14). A portable 4-rail structure was designed and constructed, onto which all the components could be placed. Linear adjustment of the components was easily achieved. This rail system is shown in Appendix B. The remaining optical component in figure 6.8 which has not already been discussed is filter Z. It is a colour separation filter with a transmission range from 535 to 2600nm and a blocking range from 443 to 565nm (Reynard Corporation, San Clemente, CA, U.S.A.). This filter reflects the incident blue light into the microscope objective lens B and into the optical fibre. The resultant fluorescence then passes through filter Z and is focused onto the photodiode. The response of this experimental set-up to oxygen is discussed in chapter 7.

6.3.3 Phase fluorimetry mode

The modulation of LEDs at the frequency required for phase fluorimetric characterisation is not a problem as it can be carried out electronically. The GaN LED has a frequency response of 4-5Mz [7]. However, it was necessary to use a low bias current operational amplifier to amplify the signal detected by the photodiode. The OPA128 device manufactured by Burr Brown, Tucson, AZ, U.S.A. allows an amplification of up to 10^8 and has an ultra low bias current of 75fA [8]. These amplified signals were then fed into a phase sensitive detector. The experimental configuration for phase fluorimetric measurements is identical to that depicted in figure 6.8 with direct detection replaced by phase-sensitive.

6.4 All-solid-state system

Due to the availability of high intensity blue LED's, it was now feasible to construct an all-solid-state fluorescence-intensity monitoring device. The remaining commercial instruments used in the experimental system and which needed replacement were the frequency generator to drive the LED, and the lock-in amplifier. The frequency generator can be replaced by a voltage-to-frequency converter circuit, using an integrated

circuit manufactured by Analog Devices (i.e. AD654). Appendix C illustrates the electronic circuit lay-out. Discrimination against ambient light may be carried out using the Analogue Devices Balanced Modulator/Demodulator (AD630), which can be configured to operate as a lock-in amplifier. The circuit was built as shown in appendix D. The frequency of modulation of the LED is set at 780Hz due to the fact that optimum operation of the AD630 i.c. is at frequencies up to 1 kHz [9]. The D.C. output voltage of the lock-in amplification circuit was fed to a local display (3½ digit LCD digital panel meter, RS 255-979), which gives a voltage reading that corresponds to the fluorescence intensity of the immobilised ruthenium complex. The portable fluorescence intensity oxygen sensor with local display is shown is appendix D.

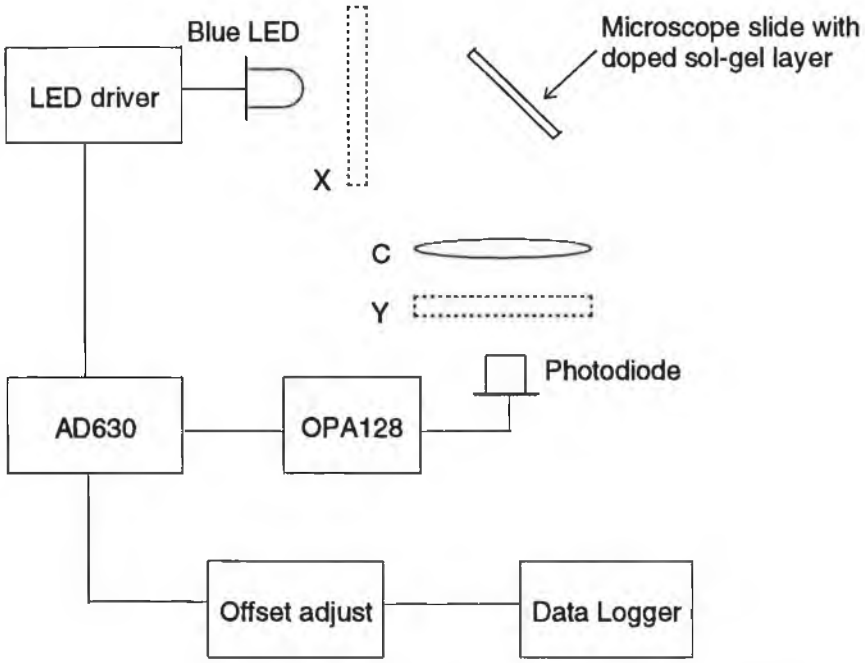

figure 6.9 long term stability instrument

6.5 Instrument for long term stability studies

During the course of the work it was necessary to build a instrument which could monitor the long term stability of the doped sol-gel coatings. With this in mind an instrument was constructed which is based on the all-solid state system. An illustration of the system is shown in figure 6.9. A section (5mm × 15mm) of a microscope glass slide was dip-coated in a sol-gel containing a ruthenium complex. The slides were prepared

exactly as described in the case of optical fibres. It was unnecessary to polish the LED dome in this case, as the 10° diverging LED beam was sufficient to excite the coated slide, which was placed at an angle of 45° to the incoming beam. A biconvex lens (C), was used to collect a portion of the fluorescence and focus it onto the photodiode. An offset adjustment feature was also put in place such that the baseline could be adjusted if required. The detected voltage which represented the fluorescence intensity of the immobilised ruthenium complex was stored using a data-logger. The complete system with data logger was placed in light-tight box and placed in a room for monitoring over a period of time. The recorded data could be down-loaded from the data-logger to a P.C. and analysed. Data obtained from this system is discussed in detail in section 7.2.4.

6.6 Phase measurement systems

6.6.1 Introduction

In the phase fluorimetric systems described, it is necessary to be able to measure the phase angle between two sinusoidal signals. There are many methods of carrying out this measurement. In the work presented in this thesis, two techniques of phase measurement were investigated. Firstly, a dual phase LIA is used to measure the phase angle. The second technique employed 2 zero cross detectors with an exclusive OR gate. This system is detailed in section 6.6.3.

6.6.2 Dual phase LIA

A dual phase lock-in amplifier can be used to measure the phase difference between two sinusoidal signals. The principle of operation of such a phase measuring system is described as follows. The signal waveform, sig, and reference waveform, ref, can be represented by the following expressions[10]:

$$sig = V_{sig} \sin(\omega_{sig} t + \theta_{sig}) \qquad 6.1$$

$$ref = V_{ref} \sin(\omega_{ref} t + \theta_{ref}) \qquad 6.2$$

where V_{sig} and V_{ref} are respectively the signal and reference amplitudes, and ω_s and ω_r are respectively the signal and reference frequencies. A lock-in amplifier amplifies the signal waveform and then multiplies it by the reference using a phase sensitive detector or multiplier. When the frequencies of both signals are equal i.e. when $\omega_{ref} = \omega_{sig}$, the low pass filtered output of the phase sensitive detector (V_{PSD1}) is a D.C. signal which can be expressed as follows:

$$V_{psd1} \propto V_{ref} V_{sig} \cos(\theta_{sig} - \theta_{ref}) \qquad 6.3$$

In a dual phase lock-in amplifier, a second phase sensitive detector (PSD2) multiplies the signal by the reference phase-shifted by 90°. The output can then be expressed as

$$V_{psd2} \propto V_{ref} V_{sig} \sin(\theta_{sig} - \theta_{ref}) \qquad 6.4$$

V_{psd1} and V_{psd2} represent the signal as a vector relative to the lock-in reference, where V_{psd1}, the 'in phase' component is X, and V_{psd2}, the 'quadrature' component is Y, as shown in figure 6.10. The phase between the signal and lock-in reference can thus be measured according to

$$\theta = \theta_{sig} - \theta_{ref} = \tan^{-1} \frac{V_{psd2}}{V_{psd1}} \qquad 6.5$$

Two dual phase lock-in amplifiers were available for use during the work carried out, i) EG&G Princeton Applied Research, model #5210 and ii) Stanford Research Systems, DSP model #SR630. One of the advantages of using the dual phase lock-in amplifier to measure phase angle is that very low signals (nanovolts) can be measured. Furthermore, the LIA outputs are calibrated with respect to angle e.g. 18°/1V.

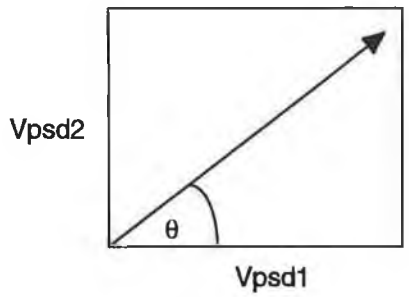

figure 6.10 Vector representation of dual phase LIA

6.6.3 Zero-crossing system

A circuit containing two zero cross detectors (ZCD), an exclusive OR gate (ExOR) and a lowpass filter was built for the purpose of relative phase measurements. A diagrammatic representation of the circuit is shown in figure 6.11. The two sinusoidal waveforms are connected to the inputs of the zero cross detectors, which give a corresponding square wave output. The ExOR gate output goes high when the incoming square waves are in phase. The low pass filtering of this signal produces a D.C. voltage signal corresponding to the in phase components of the original sinusoidal waves. A calibration curve of the circuit is shown in figure 6.12. Calibration was carried out by measuring the circuit output with signals supplied from a variable phase oscillator.

For this instrument to work satisfactorily, it is necessary to have very little noise in the detected fluorescence signal i.e. the SNR must be above parity and preferably much higher. To accomplish this, it was found necessary to use a photomultiplier tube as detector. To further decrease noise inherent in the sensor output signal, it is possible to increase the low pass filter time constant. However, this competes with the sensor response time. The use of a photodiode as detector is considered possible only if a frequency filter is incorporated prior to the ZCD, so as to remove noise in the signal.

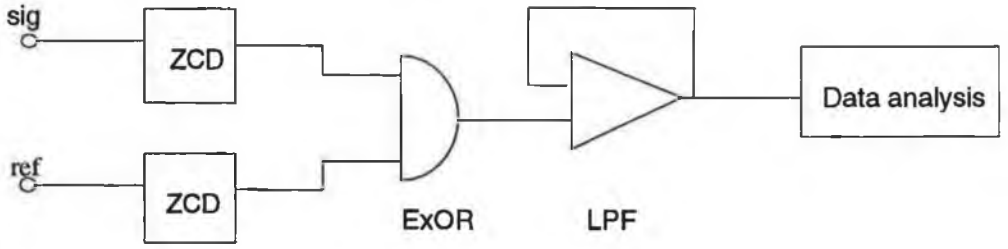

figure 6.11 Schematic diagram of phase measurement circuit using two zero cross detectors with an ExOR gate with low pass filter.

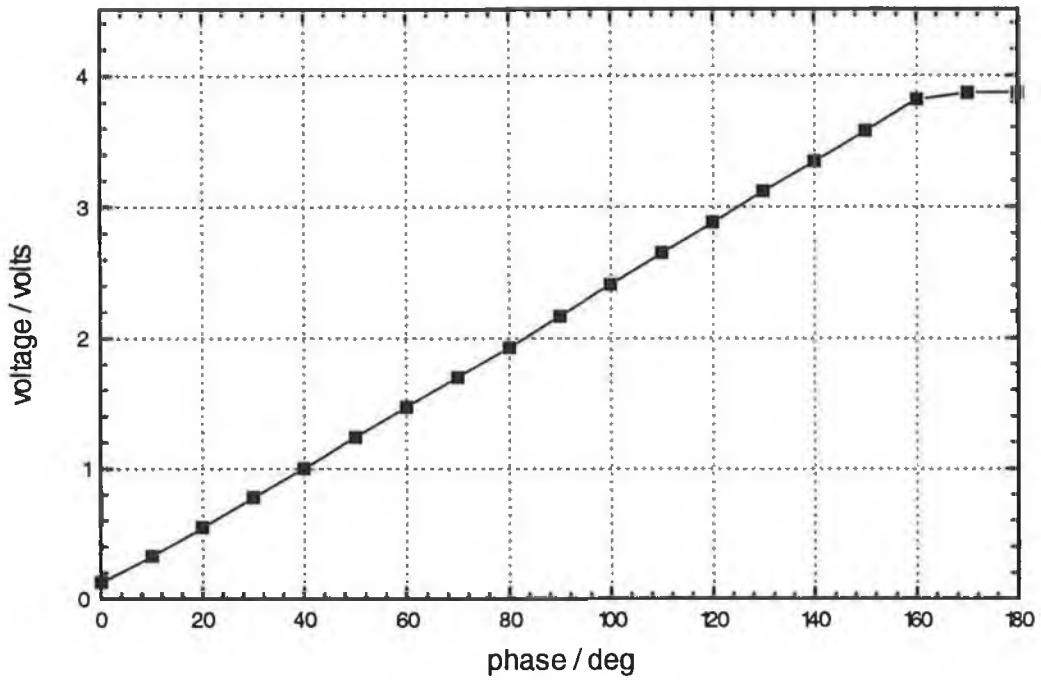

figure 6.12 Calibration curve of ZCD and ExOR phase sensitive detector

6.7 Phase locked detection of fluorescence

An alternative method of measuring the fluorescence lifetime of the ruthenium complex was developed in collaboration with the department of Electrical, Electronic and Information Engineering, City University, London [11]. The system, based on phase locked loop technology, measures the fluorescence lifetime and converts it to a repetitive signal, which also serves as the modulation signal for the excitation source. Therefore lifetime measurements, or oxygen concentration determination, can be made by monitoring the period, or modulation frequency of this repetitive signal. These are parameters which can be measured with high precision.

The phase locked detection system is presented schematically in figure 6.13. A rectangular pulse, Q2, is used to excite the fluorescence material. The rectangular pulse carries more excitation power from the light source than a sinusoidal one, and therefore a higher SNR can be achieved from the corresponding fluorescence response [11]. Using the theory of linear phase locked loops, Zhang et al., have shown that the introduction of a phase lag, α, between the modulation and reference signal results in the system being theoretically immune to excitation source leakage [11]. They show mathematically that

optimum responses from such a phase sensitive detection system are achieved, when the phase lag has a value of 0.117. A phase lag of 0.125 is introduced in the present system, between modulation signal Q2, and the reference signal Q1 using a dual D-type edge-triggered flip flop (LS74) and a bit binary counter (LS93) as illustrated by the timing diagram in figure 6.14. Zhang et al. also found that by introducing an analogue switch, better measurement reproducibility was achieved. This switch is incorporated in the electronics by using the dual monolithic analogue switch HI200 (RS 309-559). The output of the phase sensitive detector is now only determined by the decay process of the fluorescence material. The resulting modulation waveform has a period proportional to the lifetime of the fluorescent material. This system was implemented and built as shown in appendix E.

To measure the period of the this signal a tachometer was used. A tachometer was built based on an i.c. available from Radionics (RS 302-047) [12]. A calibration

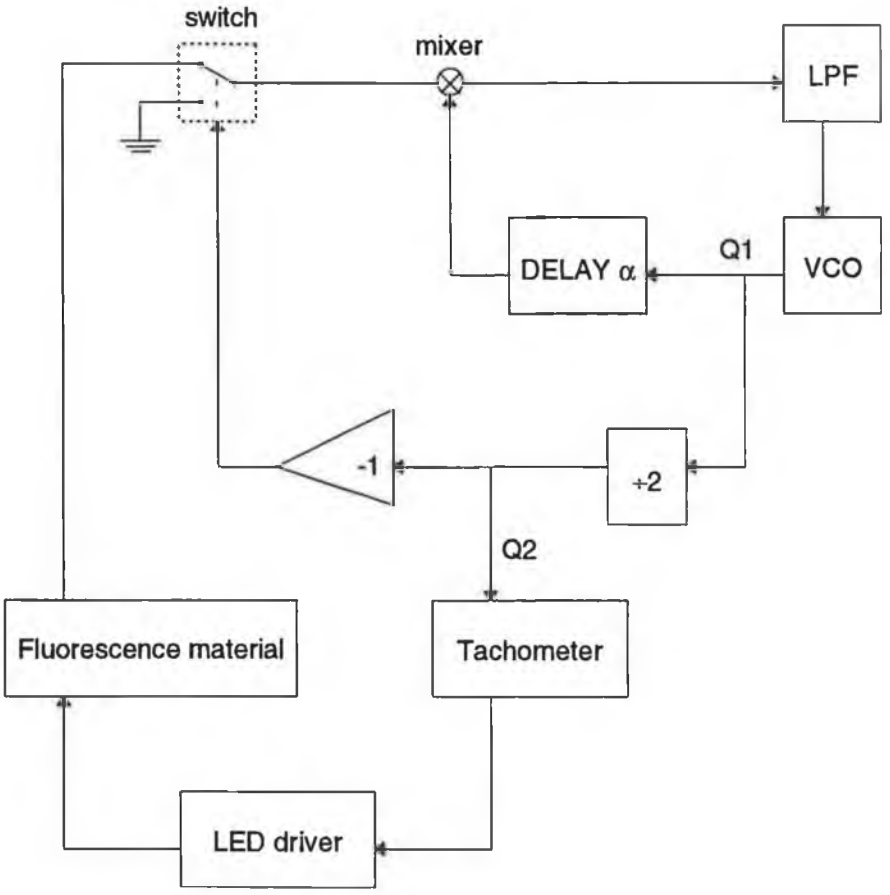

figure 6.13 Pulse modulated phase locked detection with two reference signals.

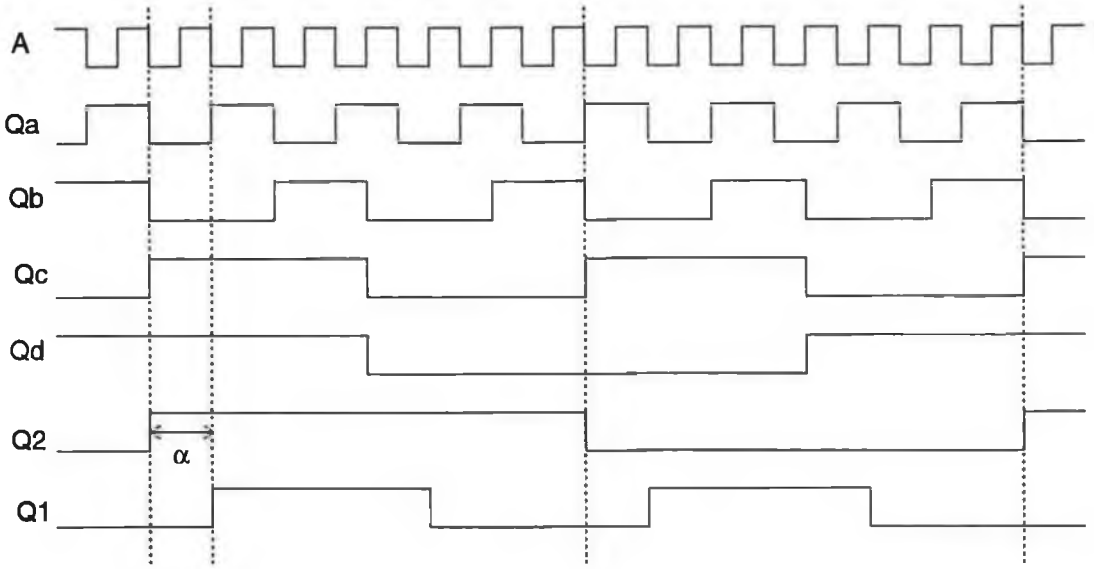

figure 6.14 Timing diagram for phase sensitive detection of fluorescence system [11]. (Signal labels refer to appendix E).

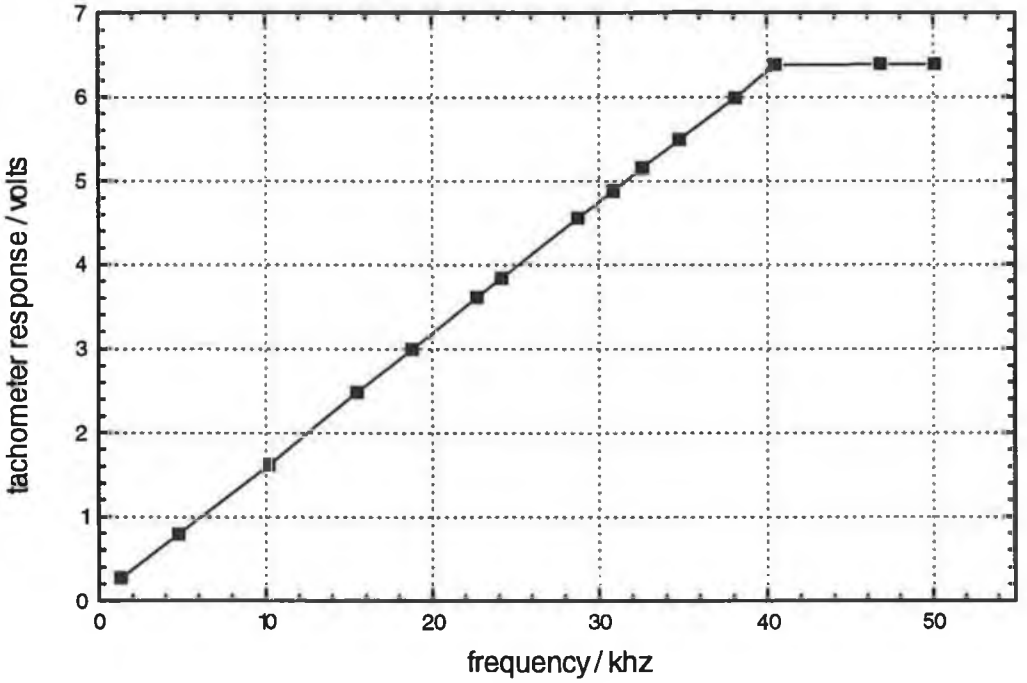

figure 6.15 Tachometer calibration

curve of such a tachometer is shown in figure 6.15.

6.8 Conclusion

In chapter 6 the various experimental systems used in this work are detailed. The progress from the initial laser/photomultiplier tube laboratory based system to a LED/photodiode hand held portable sensor is described, for both fluorescence intensity and phase fluorimetric measurements. Various techniques of phase measurement have been described. The response of the various systems to oxygen is presented in chapter 7.

References:

1. Golden J.P., Shriver-Lake, Anderson G.P., Thompson R.B., Ligler F.S: '**Fluorimeter and tapered fiber optic probes for sensing in the evanescent wave**', Optical Engineering', 1992, Vol. 31, No. 7, pp. 1458-1462

2. Noble M.: '**Acousto-optic devices: Diverse applications**', Lasers and Optronics, March 1992, pp. 27-30

3. Yariv A.: '**Optical Electronics**', 4th Ed., Saunders College Publishing, 1991, Chapter 12, pp. 461-478

4. Weyrich C.: '**Blue light emitting silicon-carbide diodes, materials, technology, characteristics**', Siemens Optoelectronic Data Book 1993, pp. 11(84) - 11(86)

5. Gabardi D.R., Shealy D.L.: '**Coupling of domed light-emitting diodes with a multimode step-index optical fiber**', Applied Optics, 1986, Vol. 25, No. 19, pp. 3435-3442

6. Christensen D., Andrade J., Wang J., Ives J., Yoshida D.: '**Evanescent-wave coupling of fluorescence into guided modes : FDTD analysis**', Chemical, Biochemical and Environmental sensors, Proc. SPIE, 1989, Vol. 1172, pp. 70-74

7. **New super bright blue LED** - Data sheet, Ledtronics Inc., Torrance, CA., U.S.A.

8. **Difet® electrometer-grade operational amplifier** - Data sheet, OPA128, Burr-Brown, Tucson, AZ., U.S.A.

9. **Balanced modulator/demodulator** - Data sheet, AD630, Analog Devices, Norwood, MA., U.S.A.

10. **What is a Lock-in Amplifier?**, SR830 - Reference manual, Stanford Research Systems Inc., Sunnyvale, CA., U.S.A.

11. Zhang Z., Grattan K.T.V., Palmer A.W.: '**Phase-locked detection of fluorescence lifetime**', Review of scientific instruments, 1993, Vol. 63, No. 9, pp. 2531-2540

12. **Tachometer ic 2917**, RS data sheet J4901, Issued March 1992

Chapter Seven - Experimental Results

7.1 Introduction

The experimental results obtained from the investigation of evanescent wave-excited fluorescence from ruthenium complex doped sol-gel coated optical fibres are presented in this chapter. The primary use of the data is to determine the possibility of producing a viable evanescent wave gas sensor. Criteria for such a sensing device have been established and are detailed in section 1.3. In this chapter, the performance of the evanescent-wave fiber optic sol-gel based oxygen sensor is investigated in the context of these criteria. The progress from the initial laser/PMT based characterisation system to the LED/photodiode system is detailed in terms of a direct fluorescence intensity monitoring system and also in terms of the various fluorescence lifetime monitoring systems, which have been described in chapter 6. Sensor characterisation is also carried out in terms of long term stability, temperature and relative humidity dependencies, cross-interferents and response time.

When considering the results presented in this chapter, it should be noted that experiments were not always carried out using the same sol-gel coated optical fibre (due to breakages and fibre damage). Therefore, film-to-film and fibre-to-fibre variability may give rise to some variation in sensor performance.

7.2 Fluorescence intensity monitoring

7.2.1 Laser based system

A laser based experimental system was first used to characterise the fiber optic oxygen sensors in terms of fluorescence intensity variation. This fluorescence intensity measurement system was set up as illustrated in figure 6.4. A bright orange/red glow was clearly visible from the sol-gel coated region of the optical fibre. Using mass flow controllers, nitrogen gas was passed at a rate of 500cm^3/min, through the gas cell containing the sol-gel coated fibre. Fluorescence intensity data obtained from sensors with sol-gel doped bipyridine ($Ru(bpy)_3^{2+}$) and diphenyl-phenanthroline ($Ru(Ph_2phen)_3^{2+}$)

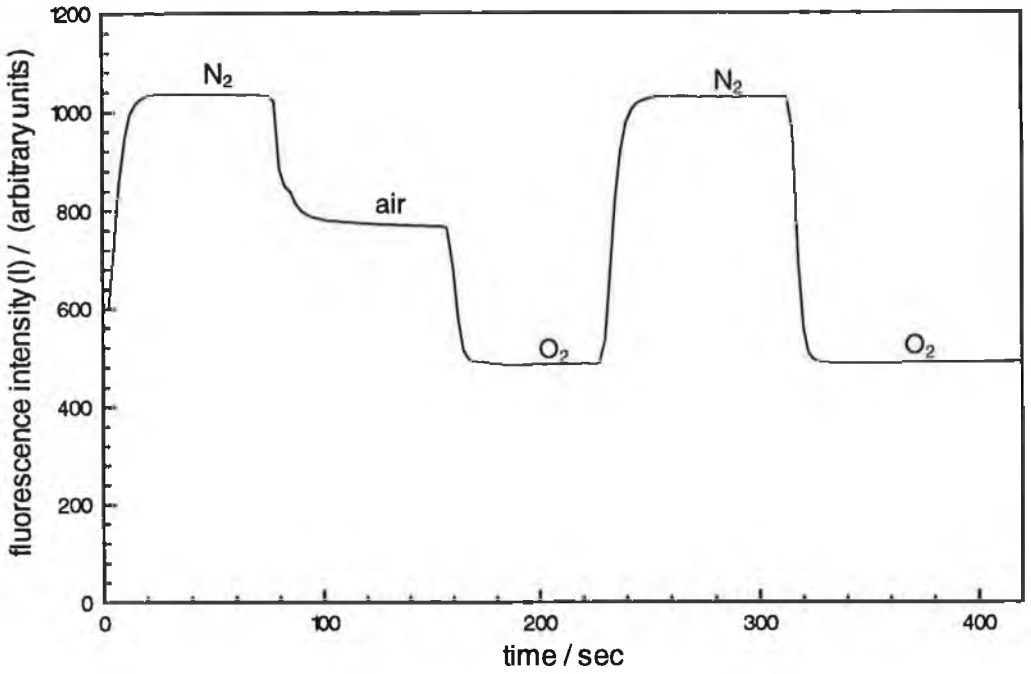

figure 7.1 Response of sensor coated with sol-gel film containing $Ru(bpy)_3^{2+}$ complex; measured using the laser based system.

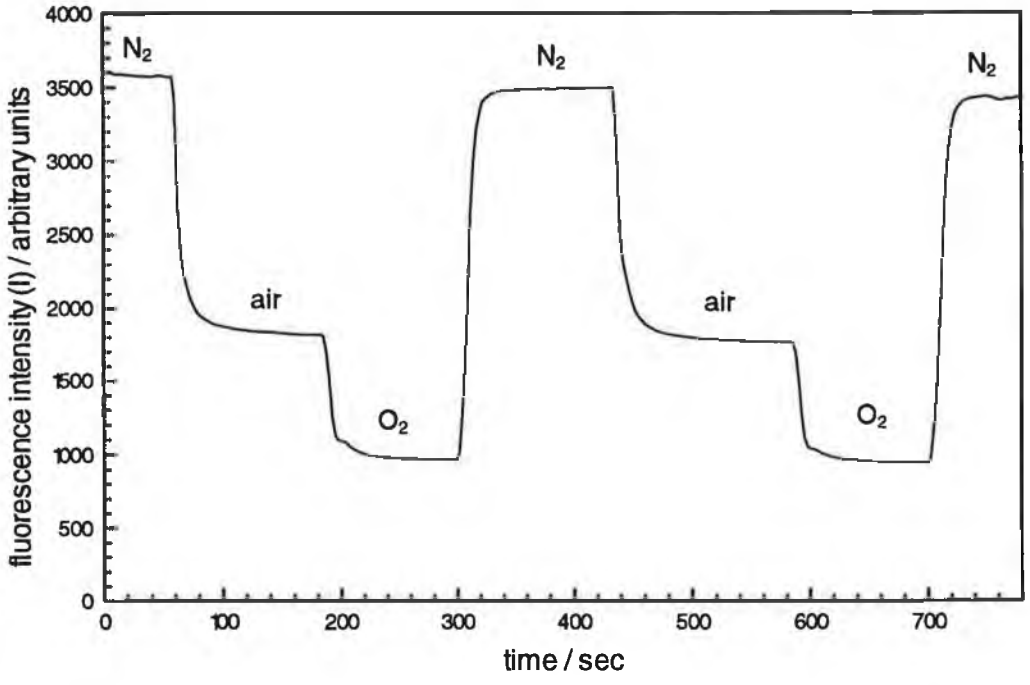

figure 7.2 Response of the sensor coated with sol-gel containing $Ru(Ph_2phen)_3^{2+}$; measured using the laser based system.

complexes are shown in figures 7.1 and 7.2. As the nitrogen in the gas cell is replaced with air, fluorescence quenching occurs as expected. Further quenching is observed when the air is replaced by oxygen. The ratio $R_{fl} = I_0/I_{100}$, where I_{100} represents the detected fluorescence signal in 100% oxygen and I_0 is the fluorescence signal in 0% oxygen, can be used as an approximate measure of the oxygen sensitivity of the sensor. In figure 7.1, the performance of a sensor coated with a sol-gel film containing bipyridine complex is shown (τ_0 = 685ns). The sol-gel recipe used to prepare these films is as detailed in section 4.7, i.e. ruthenium complex concentration of 40,000ppm, and a water/TEOS ratio of 2:1. Although the response varies in a repeatable manner with oxygen concentration, the sensitivity is relatively low with an R_{fl} value approximately of 2.0. The diphenyl-phenanthroline complex, known to have a longer excited-state of lifetime than the bipyridine complex (τ_0 = 5600ns), would therefore be expected to show higher oxygen sensitivity. This is confirmed by figure 7.2 where the response of a sensor coated with a film containing the diphenyl-phenanthroline complex is shown. An increase in R_{fl} value to approximately 3.7 was observed. Both plots show high values of signal-to-noise ratios with little evidence of photobleaching or hysteresis. The plots may not be used to deduce

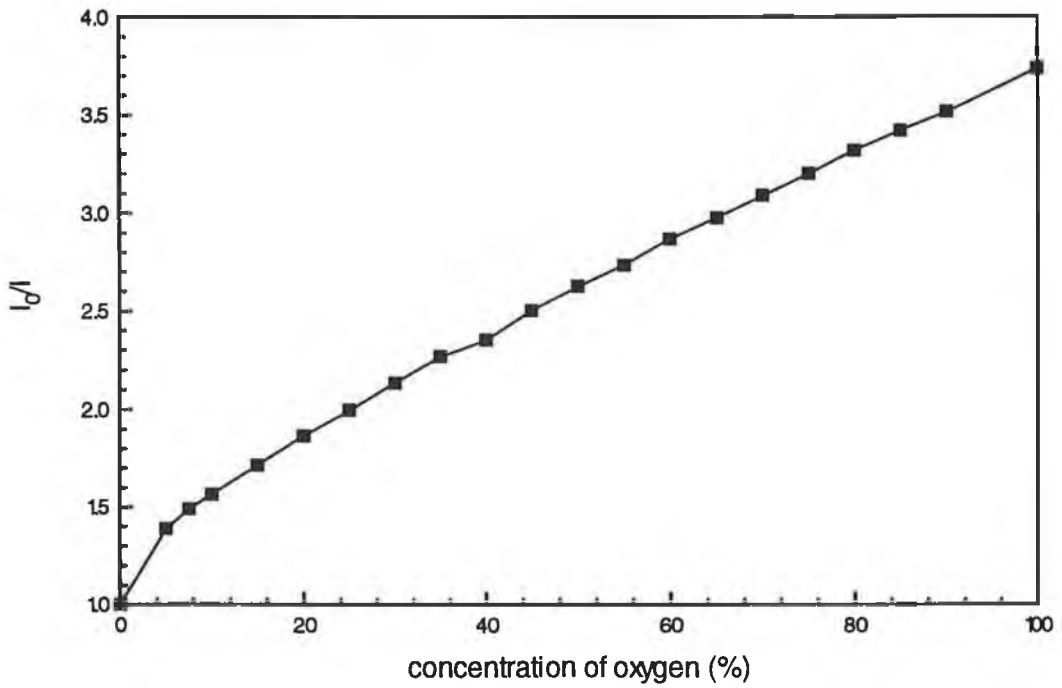

figure 7.3 Typical Stern-Volmer plot obtained using laser based system.

the sensor response time, as the transition regions are mostly indicative of the time taken to achieve manually adjusted stable gas concentrations. A more detailed discussion on the sensor response time is presented in section 7.7.4. A typical Stern-Volmer plot obtained using the diphenyl-phenanthroline material is shown in figure 7.3. Two features should be noted from these data. Firstly, the data is approximately linear over most of its range; the source of its deviation is unclear. Secondly, the highest sensitivity to oxygen using this particular sol-gel coating is obtained in the range 0% to 10% oxygen, as predicted by the Stern-Volmer equation (i.e. equation 3.17).

7.2.2 Blue LED based system

When LEDs of sufficient output power became available, they were used to replace the argon-ion laser source of the previous section. A LED based fluorescence intensity characterisation system was set up based on the illustration shown in figure 6.6. Initially 15 mcd and 30 mcd silicon carbide blue emitting LED's were used as excitation sources. However, results from the higher power gallium nitride (1000mcd) LED are shown here, with the exception of the data of figure 7.5 which was recorded using the

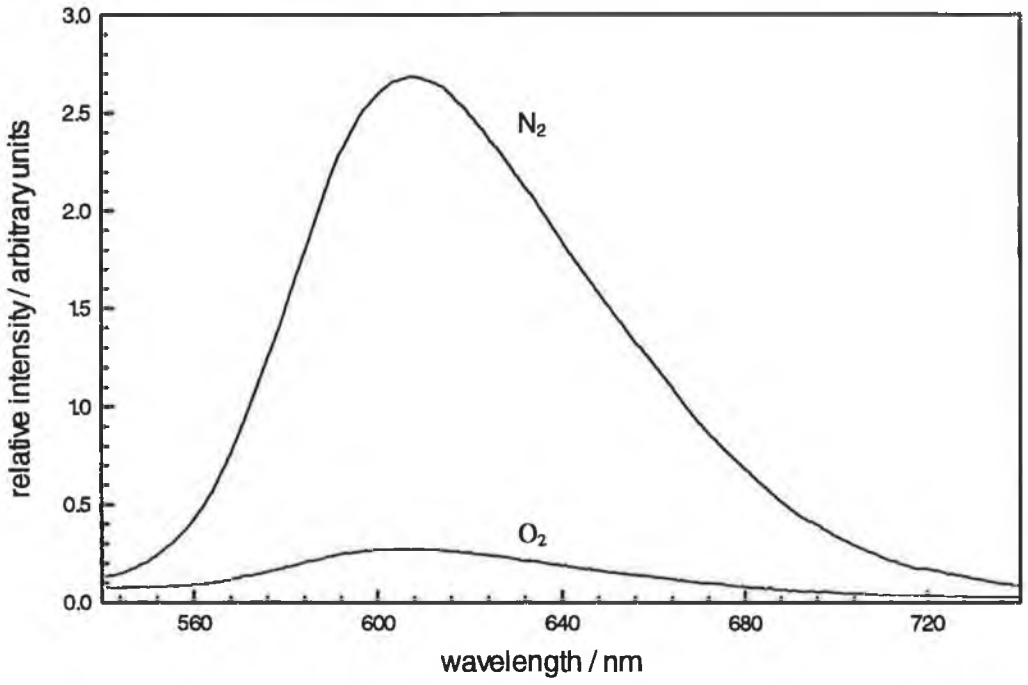

figure 7.4 Fluorescence quenching of $Ru(Ph_2phen)_3^{2+}$ in the presence of oxygen.

lower power silicon carbide LED. With the photomultiplier tube in place as shown in figure 6.5, and the longwave pass filter Y (99% transmission above 600nm) replaced by a monochromator, the fluorescence spectrum of a sol-gel coated optical fibre in a nitrogen atmosphere was recorded. Oxygen was then passed through the gas cell containing the optical fibre. The fluorescence spectrum from the fibre was again recorded. Results demonstrate fluorescence quenching of the entrapped ruthenium dye as expected. Both spectra are shown in figure 7.4. The sol-gel entrapped ruthenium complex fluorescence was found to peak at 607.5nm. A high degree of quenching of 89.8% was found, corresponding to an R_{fl} value of 9.8. This value corresponds to a substantial increase in sensitivity from the laser based system, which possibly is partially due to the improvement in spectral filtering in the LED-based system, and also due to improvements in producing better quality sol-gel thin films.

Real-time fluorescence signal monitoring was carried out with the longwave pass filter Y in place of the monochromator. The sensor response at 10% intervals over the range 0%-100% oxygen is shown in figure 7.5. The lower power silicon carbide blue LED was used as an excitation source in the recording of these data with photomultiplier

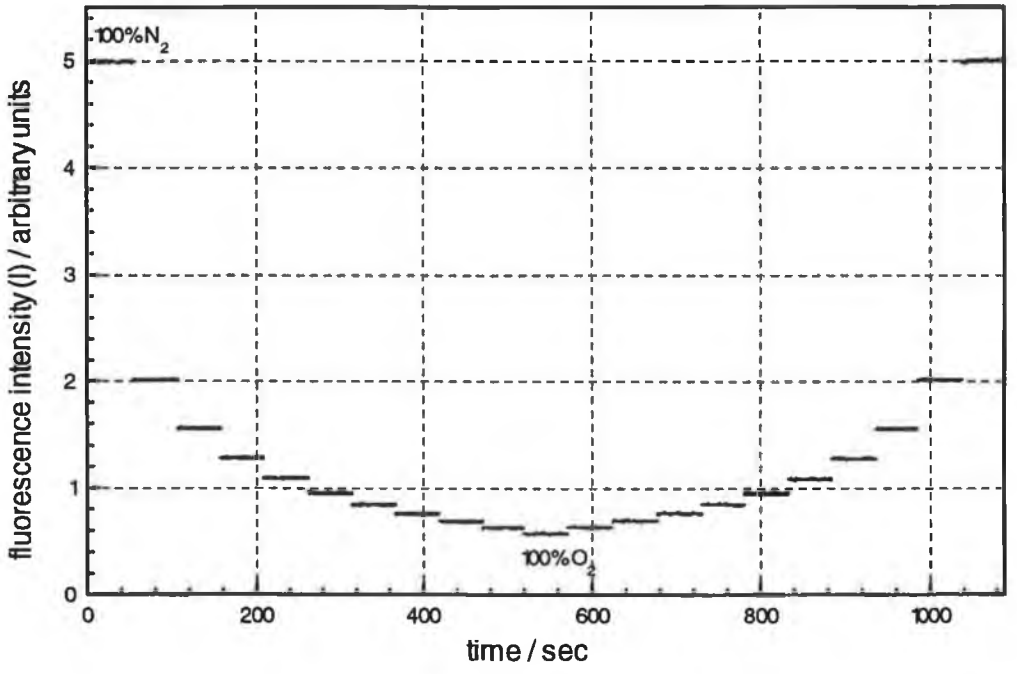

figure 7.5 Sensor calibration data in 10% increments from 0% to 100% oxygen : LED excitation/PMT detection.

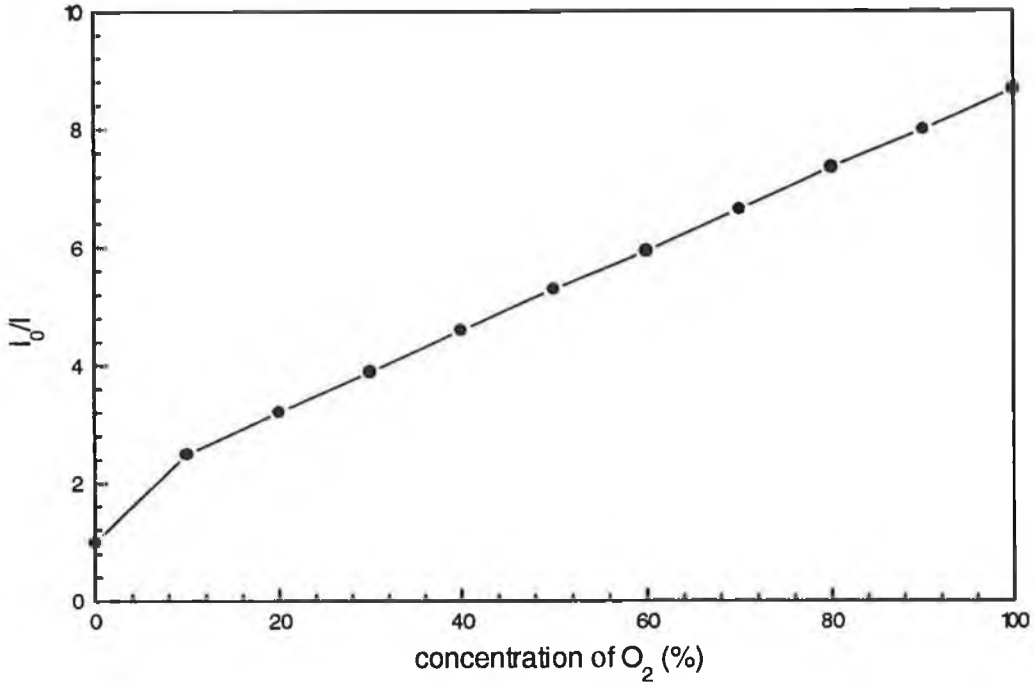

figure 7.6 Stern Volmer plot of data shown in figure 7.5

tube as detector. These data show a high level of repeatability of the measurement process and a high signal-to-noise ratio (~300 for 100% nitrogen). The extremely high sensitivity of the system in the lower oxygen concentrations would be very suitable for use in either the anaerobic or personal sensing systems as discussed in section 1.3. A Stern-Volmer plot of this data is shown in figure 7.6. The Stern-Volmer data was found to be linear over most of the oxygen concentration range. The source of the deviation from linearity at low oxygen concentrations in unclear, however it may be accounted for by considering the multiple exponential nature of the immobilised ruthenium complexes. Section 7.3 describes the lifetime analysis of a typical sol-gel-coated fibre, for which a good mathematical fit is found for a double exponential decay. The bimolecular quenching constant k, of each fluorescent lifetime component, which characterises the non-linear quenching response, depends on the rate of diffusion of the oxygen molecules through the microporous structure. By adjusting the sol-gel process parameters, it should be possible therefore, to control the coating microstructure in order to optimise sensitivity in a concentration region of interest.

7.2.3 All-Solid state system

The all-solid-state fluorescence intensity monitoring system described in section 6.4 was built and used to test sol-gel coated fibres in a manner equivalent to above. The system response to alternate environments of 100% nitrogen and 100% oxygen is shown in figure 7.7, and to intermediate oxygen/nitrogen values in figure 7.8. Synchronous detection with the LED pulsing signal is achieved by use of a balanced demodulator (AD630) which enables effective lock-in detection and discrimination against ambient light. These data again show the high level of repeatability of the measurement process. The combination of the LED light source, photodiode detector and balanced demodulator lock-in amplifying system is a major advancement of the system from the initial laser-based design, in terms of sensor performance, cost effectiveness and portability.

7.3 Lifetime Analysis

Fluorescence decay analysis was performed by exciting the sol-gel coated fibres with 15ns pulses from a frequency-doubled Nd:YAG laser (λ=532nm). The resultant fluorescence decay profiles were captured and averaged using a 100MHz oscilloscope (HP 54600A). This data was then down-loaded to an Apple Macintosh for analysis using Kaleidagraph. The immobilised fibres were mounted in the gas cell and a range of oxygen partial pressures was achieved by precise mixing of 100% oxygen and 100% nitrogen using mass flow controllers and a mixing unit. All measurements were carried out on diphenyl-phenanthroline complex doped sol-gel fibres. Figure 7.9 shows fluorescence decay curves for the sol-gel immobilised ruthenium complex in the presence of 100% oxygen and 100% nitrogen respectively.

As expected, the observed fluorescence decays were not single exponential. The lifetime data measured at a range of concentrations from 0% to 100% oxygen, were analysed, and in all cases the data provide an approximate mathematical fit to a double exponential decay. This behaviour may be considered consistent with a two-site model for ruthenium complexes, where the two sites have different levels of accessibility to oxygen. Alternatively, this behaviour may represent an approximate fit to a continuous distribution of lifetimes due to a heterogeneous sol-gel enviroment. For each oxygen concentration, short and long lifetime components were extracted from the lifetime data.

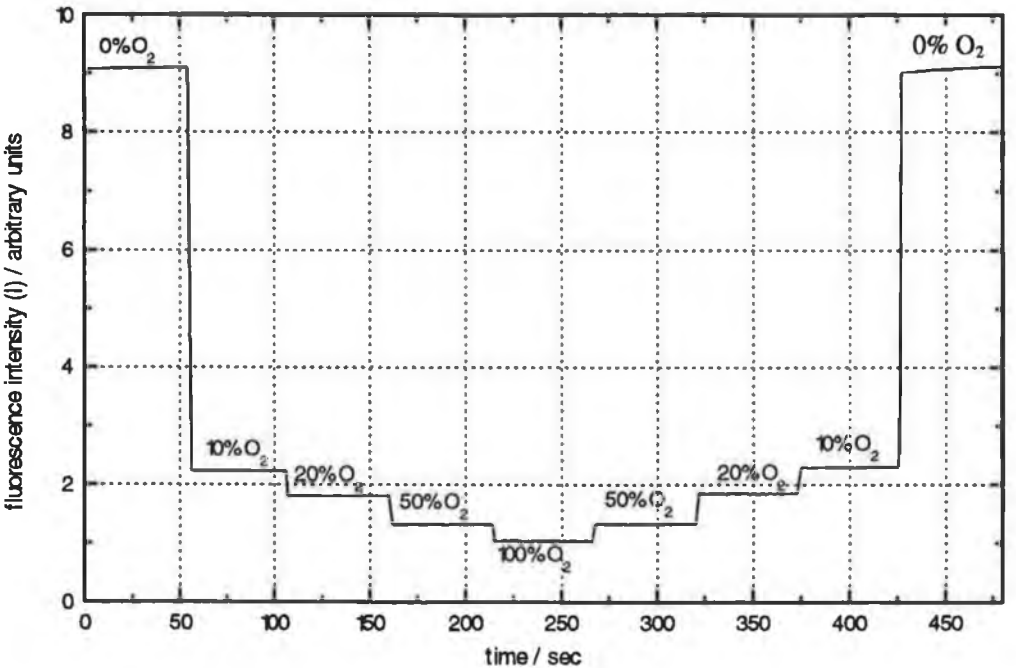

figure 7.8 Stepped response of all-solid state system.

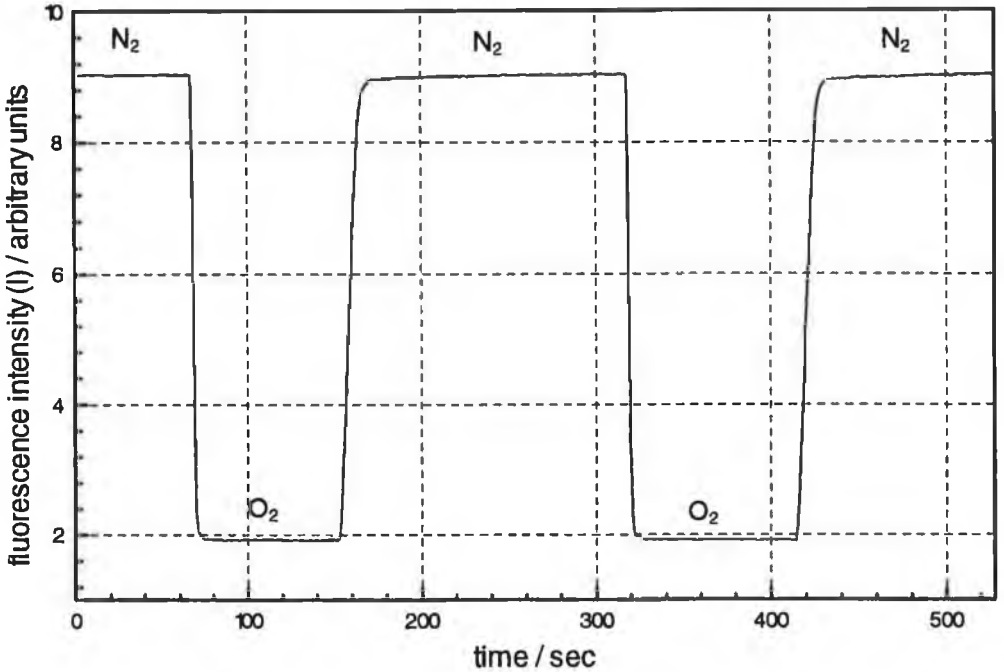

figure 7.7 Fluorescence intensity response of all-solid state system.

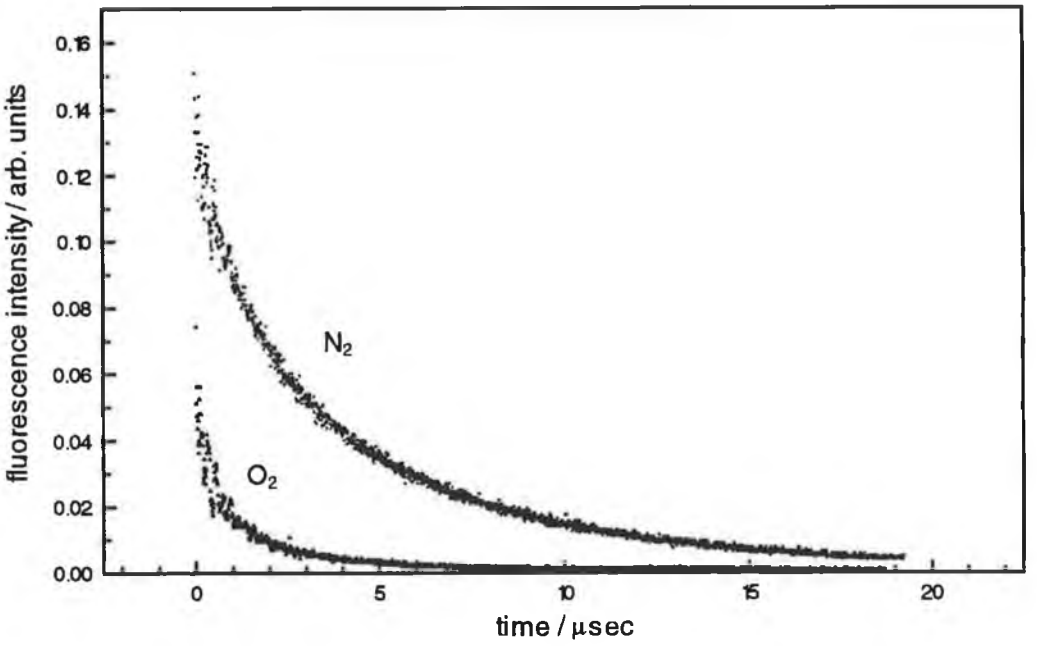

figure 7.9 Sol-gel immobilised ruthenium fluorescence decay curves corresponding to (a) quenched lifetimes of 356ns and 2.217μs in 100% O_2 and, (b) unquenched lifetimes of 933ns and 5.613μs in 100% N_2.

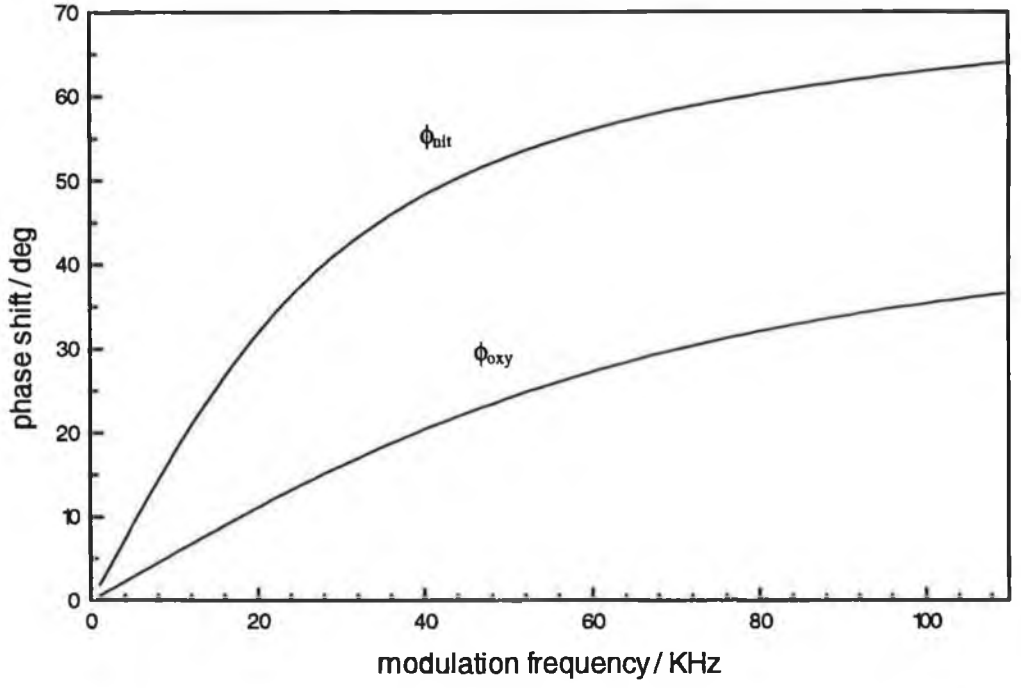

figure 7.10 Phase shift as a function of modulation frequency calculated using equation 3.31 for oxygen and nitrogen.

In 100% nitrogen, values of 5.613μs (R = 0.9803)[1] and 933ns (R = 0.8590), respectively, were found to give the best fit. Short and long lifetime components of 2.217μs (R = 0.9742) and 356ns (R = 0.7839), respectively, were found for 100% O_2. Pre-exponential factors were also determined from the analysis [3].

Using the measured lifetime data and equations 3.21 and 3.22, the expected phase shift for 0% and 100% oxygen concentrations can be calculated for a given modulation frequency. The phase shift will be smallest for a concentration of 100% oxygen and greatest for a concentration of 0% oxygen. Software was written based on equation 3.31 such that the fluorescence lifetime data and calculated pre-exponential factors could be used to generate the phase shift both for oxygen and nitrogen as a function of modulation frequency. Figure 7.10 shows the calculated phase shifts between modulation signal and resultant fluorescence for oxygen and nitrogen environments. The data shows that the phase shift increases with modulation signal and that the phase shift will be smallest for a concentration of 100% oxygen (ϕ_{oxy}), and be greatest for a concentration of 0% oxygen (ϕ_{nit}), i.e. 100% nitrogen. The calculated phase shift difference between these two extremes of the measurement range, ϕ_{diff}, where $\phi_{diff} = \phi_{nit} - \phi_{oxy}$, is plotted as a function of modulation frequency in figure 7.11. From the diagram, it is noted that, for a change from an oxygen to a nitrogen environment a maximum phase difference of 27° is predicted to occur at 48kHz, and that the response levels off close to 100kHz.

The optimum modulation frequency for maximum phase shift was also determined experimentally to an accuracy of 0.1 of a degree, using the dual-phase lock-in amplifier and LED based phase fluorimetric system as described in section 6.3.3. The LED modulation frequency was varied by adjusting the LED driving circuitry. For each frequency, the resulting phase difference was recorded as the sensor environment was alternated between 0% and 100% oxygen. These experimental phase difference results are also plotted in figure 7.11. Given the approximation inherent in the double exponential decay model used, these results are in reasonable agreement with the theoretical predictions. The agreement is sufficiently close to enable selection of the optimum operating frequency range when a decay time analysis has been performed.

[1] Where R represents the correlation coefficient

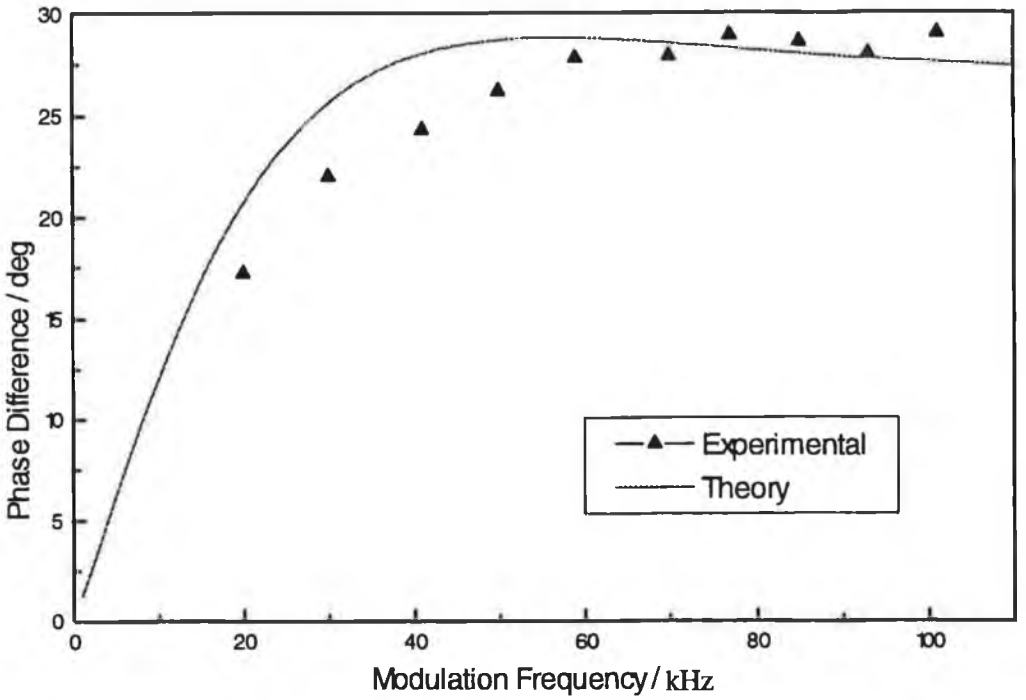

figure 7.11 Theoretical and experimental phase difference, ϕ_{diff}, between the phase shift for O_2 and the phase shift for N_2, plotted against modulation frequency.

7.4 Phase Fluorimetric Sensor Performance

7.4.1 Laser based system

Fluorescence signals from the laser-based phase fluorimetric system were recorded on an oscilloscope and are shown in figure 7.12. The nitrogen signal is phase shifted by an amount, ϕ_{nit}, from the excitation signal. A smaller phase shift, ϕ_{oxy}, exists when the oxygen replaces nitrogen in the gas cell. The real time response of the sensor when exposed alternately to environments of 100% oxygen and 100% nitrogen is shown in figure 7.13. These results were also obtained using the laser-based phase fluorimetric system with the laser modulated sinuisoidally at a frequency of 48kHz. Although it is clear from the data in figure 7.11 that a slightly greater phase difference could have been achieved at higher modulation frequencies, the measurement system exhibited lower signal-to-noise ratios at these frequencies. An explanation for this is given in section 7.6. The data shown in figure 7.13 illustrates a number of important features of the sensor.

First, the sensor exhibits a high level of repeatability and short response time. A typical calibration curve for sensors fabricated in this manner is shown in figure 7.14. The data have been offset to yield a phase angle of 0° at 100% oxygen concentration. The sensor again exhibits greatest sensitivity at the lowest oxygen concentrations (0% - 10%), as predicted by the Stern-Volmer equation.

7.4.2 LED based system

A LED/photdiode based phase fluorimetric system was set-up as described in section 6.3.3. The system response to alternate environments of 100% oxygen and 100% nitrogen is shown in figure 7.15. These data are again offset such that in an oxygen environment a phase shift close to 0° occurs. At a modulation frequency of 48kHz a maximum phase shift of 24° was recorded. This value matches closely the experimental and theoretical values of figure 7.11. It should be noted however, in comparing these values that the data was recorded from different optical fibres. The all-solid-state phase fluorimetric system exhibits a high SNR, good repeatability and fast response time. This is the first reported intrinsic phase fluorimetric solid-state sensor using LED excitation and photodiode detection. Even though, these data were recorded using a commercial dual phase lock-in amplifier, other phase measurement systems which lend themselves to miniaturisation may possibly be configured in the system. Such systems are investigated in the following section.

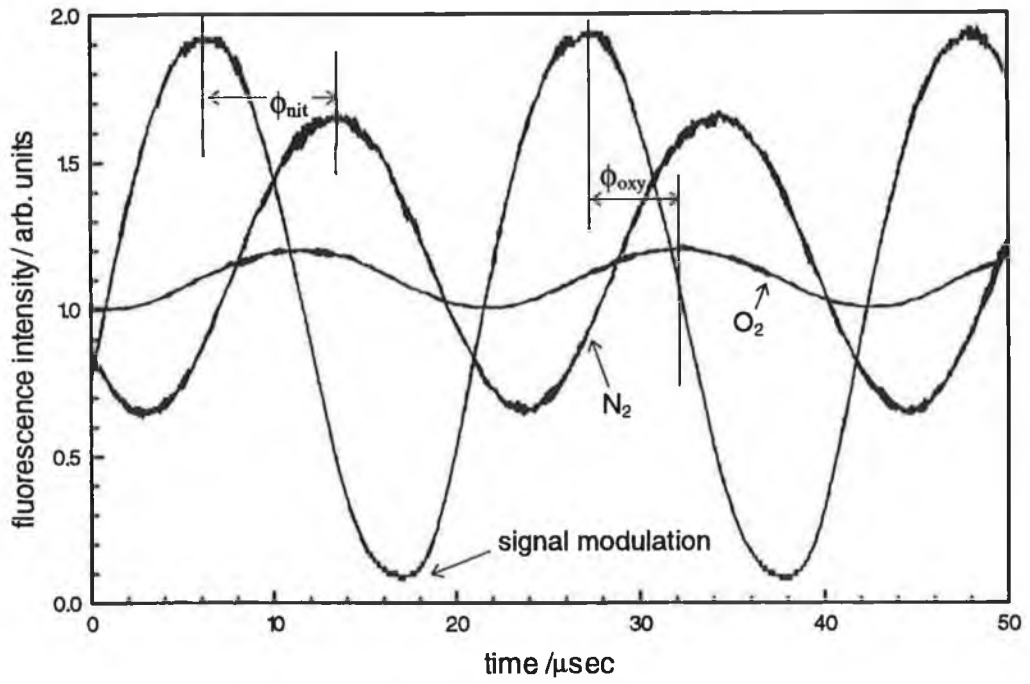

figure 7.12 Phase fluorimetric response of sensor; including laser modulation and resulting phase shifts of fluorescence in the presence of 100% oxygen and 100% nitrogen.

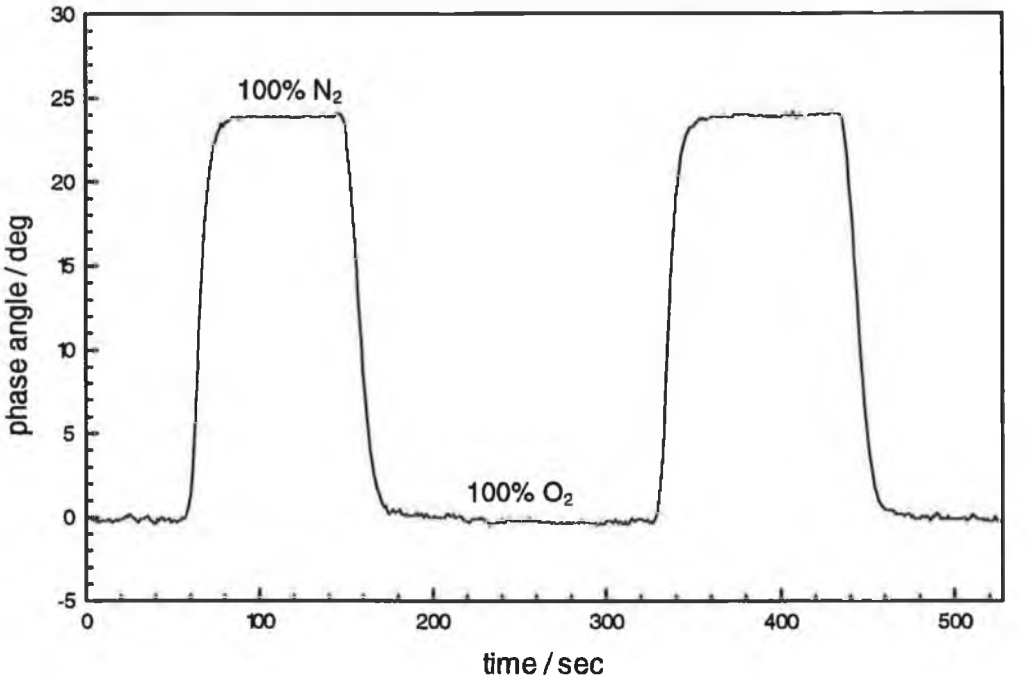

figure 7.13 Phase fluorimetric sensor laser excited / PMT detected.

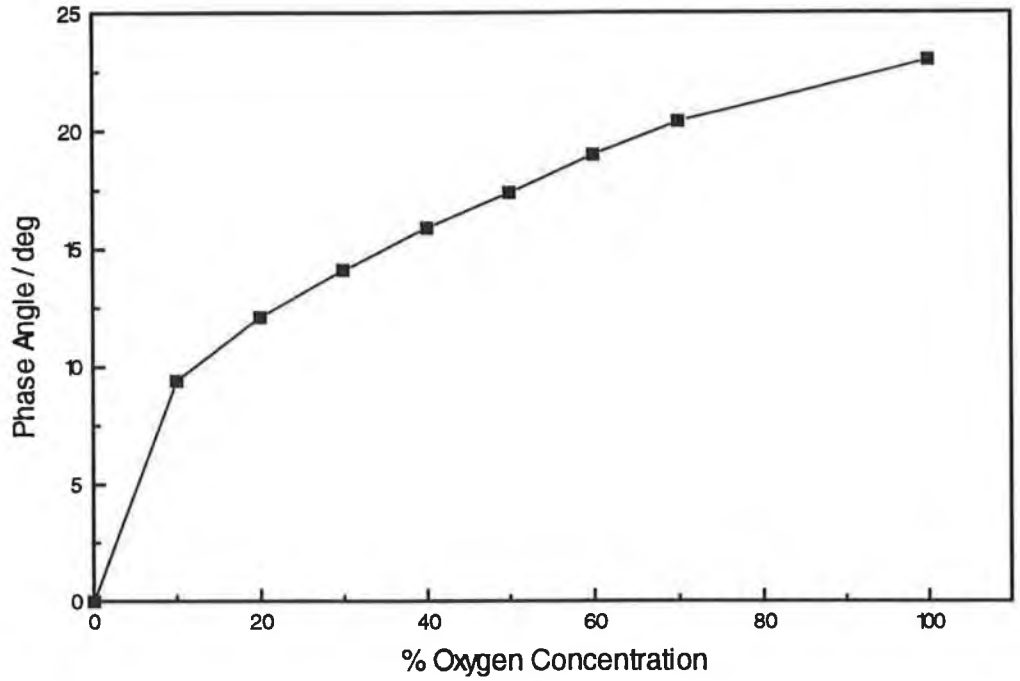

figure 7.14 Calibration curve for the phase fluorimetric oxygen sensor.

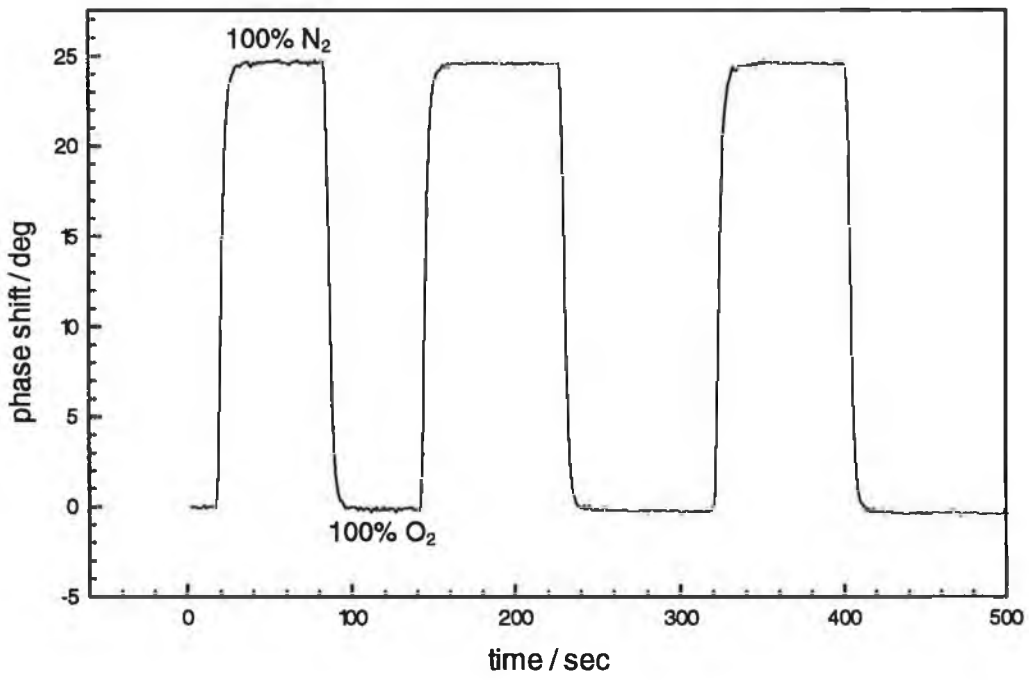

figure 7.15 Phase fluorimetric sensor LED excited/ photodiode detected.

7.5 Alternative methods of lifetime sensing

7.5.1 Zero crossing system

A circuit for measuring the phase shift between a reference modulation signal and resultant fluorescence signal containing two zero cross detectors, an exclusive OR gate and lowpass filter was built as shown in figure 6.11. The system produces a voltage output which increases with the in-phase component of the two sinusoidal signals, as shown by the calibration curve of figure 6.12. The laser excitation combined with the PMT detection phase-fluorimetric characterisation system, which is detailed in section 6.2.2, was set up so as to test the zero crossing system in sensing mode. The phase shift between the reference signal from the acousto-optic crystal and the detected fluorescence signal was monitored as a function of modulation frequency in the presence of nitrogen and oxygen respectively. The response of the system is shown in figure 7.16. The phase shift for oxygen and nitrogen was found to increase with modulation frequency in a manner similar to figure 7.10. A range of measured phase shifts for specific modulation frequencies using the zero crossing system are compared to the theoretical values of figure 7.10 and are shown in table 7.1. The voltage signal from the zero crossing system

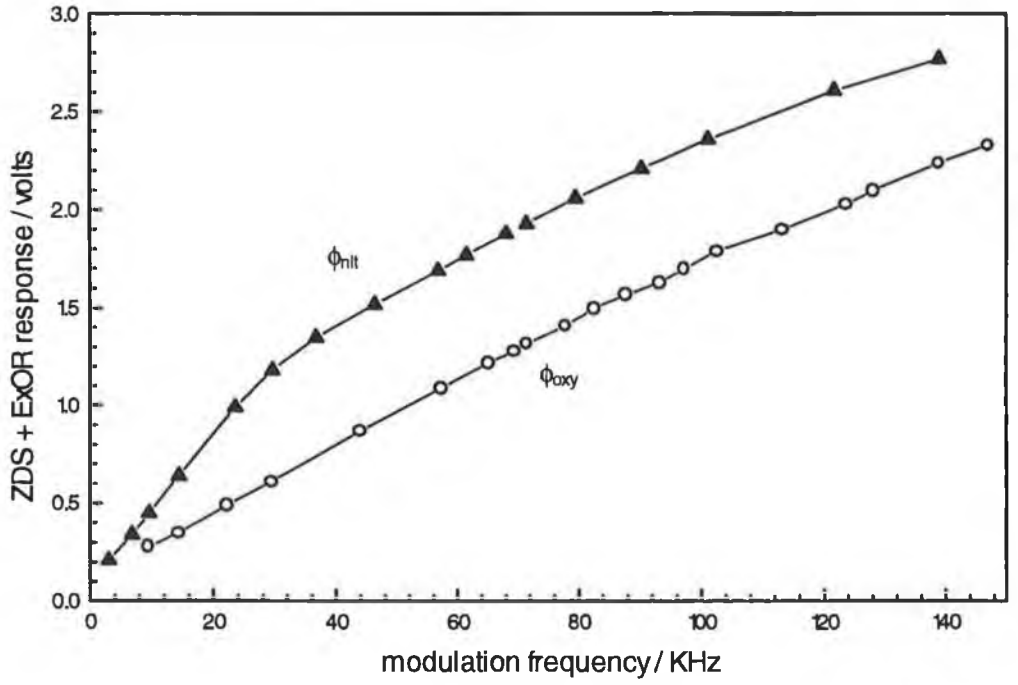

figure 7.16 ZDS + ExOR system response to frequency variation for oxygen and nitrogen

Modulation Frequency (kHz)	ZCS + ExOR[1]			Theoretical values[2]			Dual-phase LIA
	ϕ_{oxy}(deg)	ϕ_{nit}(deg)	ϕ_{diff}(deg)	ϕ_{oxy}(deg)	ϕ_{nit}(deg)	ϕ_{diff}(deg)	ϕ_{diff}(deg)
10	8.2	16.3	**8.1**	5.69	17.71	**12.01**	**8.5**
20	15.3	33.1	**17.8**	11.12	31.82	**20.70**	**17.22**
40	30.7	57.5	**26.8**	20.43	48.33	**27.91**	**24.14**
60	45.2	71.7	**26.5**	27.29	56.07	**28.77**	**27.62**
80	59.4	85.4	**26.0**	32.07	60.26	**27.49**	**28.57**

table 7.1 Comparison of phase shift and phase difference values measured using the zero crossing system, and theoretical values which were calculated from the fluorescence lifetime analysis of a fibre. Phase difference values recorded using a dual phase LIA are also included which were extrapolated from figure 7.11.

was converted to degrees using the calibration curve of figure 6.12. The difference, ϕ_{diff}, between the phase shift in the presence of oxygen, ϕ_{oxy}, and the phase shift in the presence of nitrogen, ϕ_{nit}, was found to increase with frequency and stabilise above 40kHz approximately. This is in close agreement with both the theoretical and experimental data presented in figure 7.11, as illustrated by table 7.1. The measured values of phase difference are also compared to those values measured using the more reliable method of a dual-phase lock-in amplifier. Good agreement was found between the three sets of data. It must be noted, however, that when comparing the data in table 7.1, that each experiment was carried out using different sol-gel coated fibres. To conclude, this analysis shows that a zero crossing system, which may be easily built using standard electronic components is a possible method of performing phase angle measurements. The system performance compared well to theoretical phase measurements and also to an independent method of carrying out phase measurements, that of a dual-phase LIA. Even though the system lends itself to high performance phase measurements, system miniaturisation and inexpensive manufacture, it does require SNR levels which are higher than those achievable from a LED/photodiode based system. However, by using a frequency filter set at the operational modulation frequency for the

[1] Phase shifts calculated using calibration curve of figure 6.12

[2] Theoretical values of phase shift were extrapolated from figure 7.10.

specific measurement system, unwanted frequencies components may be removed resulting in the production of higher SNR's, thus possibly allowing the use of a LED/photodiode based phase fluorimetric system in conjunction with a zero crossing phase measurement system.

7.5.2 Phase locked detection of fluorescence lifetime

An alternative method of oxygen sensing based on the phase locked detection of fluorescence lifetime of the ruthenium complex was investigated. The phase locked detection of fluorescence experimental system, was constructed as described in section 6.7. A tachometer circuit was built to monitor frequency changes as a function of oxygen concentration. The calibrated response of this system is shown in figure 6.15. A LED excited, PMT-detected characterisation system was set up and configured as illustrated in figure 6.13. A typical response of such a system to various oxygen concentrations is shown in figure 7.17. Using figure 6.25 to calibrate against frequency, a frequency change from 2.8 kHz in oxygen to 4.6 kHz in nitrogen was measured. This frequency was found to be dependent on the signal amplification used in the detection part of the

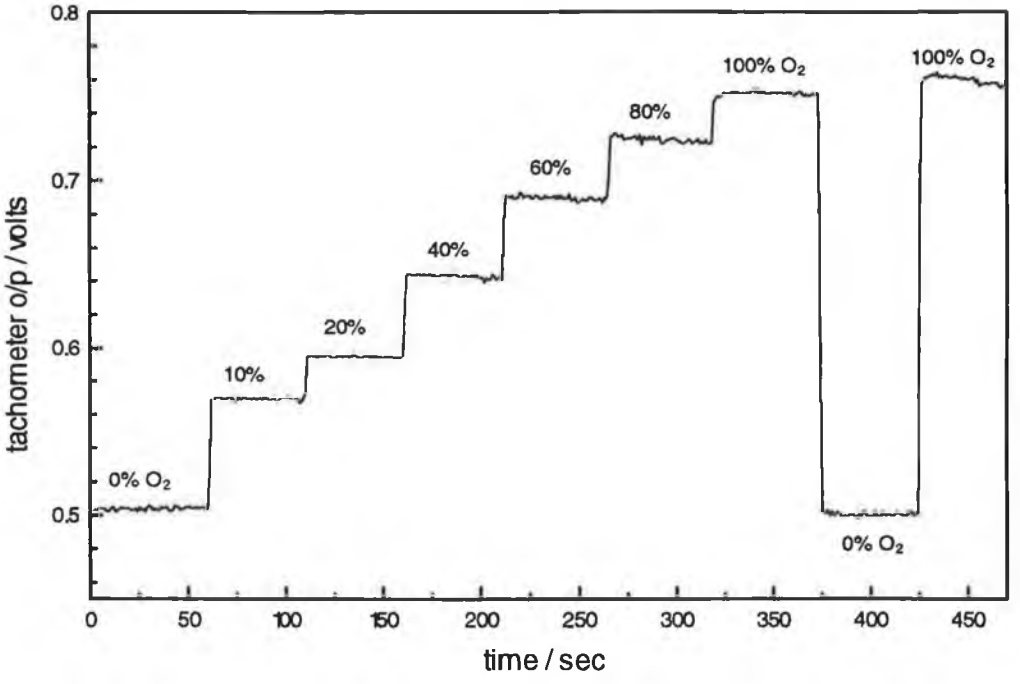

figure 7.17 System response to various oxygen concentrations

system. In order to carry out absolute fluorescence lifetime measurements, a sample of known fluorescence lifetime would first be required to calibrate the system against lifetime. The phase locked detection system response could then be used to directly monitor lifetime changes as its output is directly proportional to fluorescence lifetime [4]. Response time of the system was found to be of the order of a few seconds for a change from 100% nitrogen to 100% oxygen. System repeatability was also found to be high. Maximum sensitivity to oxygen concentration was found to be in the lower oxygen concentration region as predicted by the Stern-Volmer equation. The SNR of ~63 is considerably lower than that of the fluorescence intensity measurement systems or lock-in amplification based phase fluorimetric systems, resulting in a higher limit of detection using this system. A compromise, however, between SNR and sensor response time may achieved by adjusting the time constant of the tachometer circuit to suit the specific requirements of the measurement being performed.

7.6 Optimisation of modulation frequency for fluorescence intensity measurement system

During the phase fluorimetric analysis, it was observed that a fall off in SNR occurred at the higher modulation frequencies. In an attempt to explain this observation the following experiment was carried out using the LED / photodiode fluorescence intensity system of section 6.4. During the experiment, the fluorescence intensity was recorded as a function of modulation frequency in the presence of nitrogen and air. The results are shown in figure 7.18. The data suggest that an optimum modulation frequency exists close to 5kHz. At this frequency a maximum oxygen sensitivity is observed i.e greatest decrease in signal was measured by changing from a nitrogen to an air environment. Maximum fluorescence signal, both for nitrogen and air environments, was also measured at this modulation frequency. The decaying part of the curves is predicted by equation 3.32, where a decrease in demodulation factor, or fluorescence intensity occurs with modulation frequency. The exact source of the initial increase in fluorescence signal with frequency up to 5kHz is unclear.

We may conclude, however, that an optimum modulation frequency for a fluorescence intensity based sensor is close to 5kHz, whereas in the case of a phase fluorimetric sensor, optimum phase shift occurs close to 45kHz (from figure 7.11).

However, the higher the frequency the lower the SNR, therefore a compromise between high SNR and magnitude of phase shift has to be taken into consideration for each specific measurement.

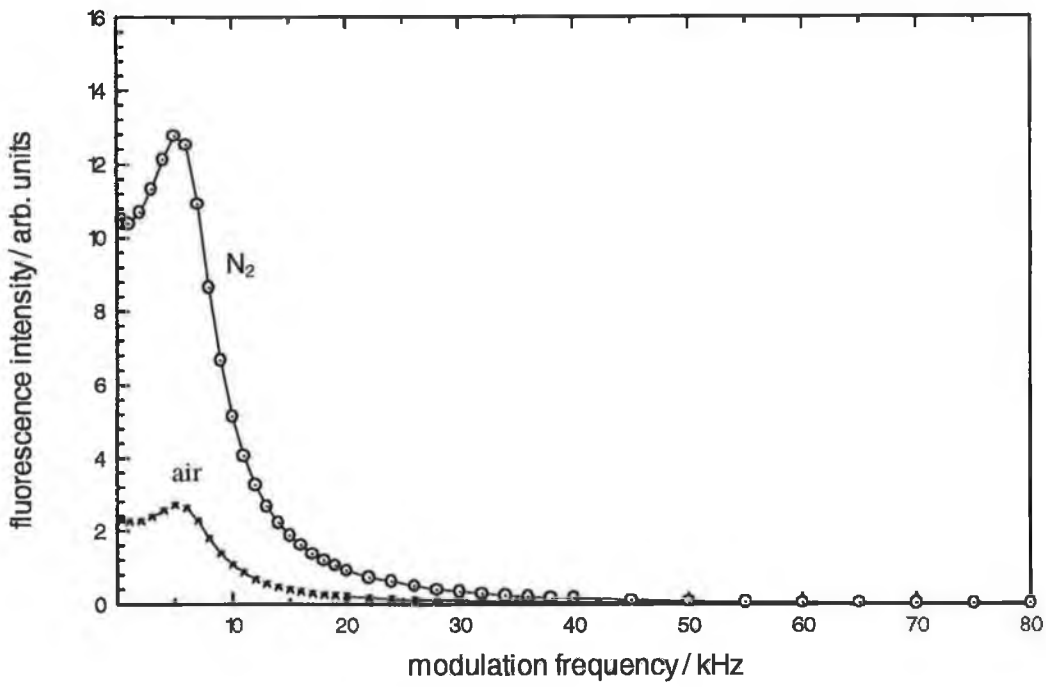

figure 7.18 Frequency response of fluorescence intensity system

7.7 Summary of the various oxygen sensing techniques

The performance of the various oxygen sensing systems may be tabulated as shown in table 7.2.

Sensing Configuration	Characterisation System	Optimum Operational Frequency	S/N	Minimum detectable O_2 conc. in the 20% region
Fluorescence intensity	laser/PMT	~6kHz	284	.007%
	LED/photodiode	~6kHz	237	.008%
Phase Fluorimetry (Dual Phase LIA)	laser/PMT	~48kHz	60	.033%
	LED/photodiode	~48kHz	82	not measured
Phase Fluorimetry (ZCS)	laser/PMT	30 - 40kHz	not measured	not measured
Phase Locked Detection	LED/PMT	NA	63	0.32%

table 7.2 Summary of performance of various oxygen sensing systems

7.8 Sensor characterisation

7.8.1 Long term stability studies

In order to determine the long term stability of the sol-gel coatings doped with ruthenium complexes, the system described in section 6.4 was built. Sol-gel-coated microscope glass slide sections were placed in the instrument and their fluorescence emission was monitored as a function of time and of ambient temperature. Typical data retrieved over a 16 hour period are shown in figure 7.19. The upper plot shows the ambient temperature variation and the lower plot represents the measured fluorescence output. Close examination of this data reveals an increase of 3.6% in fluorescence signal over the monitoring period. For the same period a decrease of 3.6°C occurred in the ambient temperature. This decrease in fluorescence intensity with temperature would be expected according to the discussion in section 3.2.4. These data suggest the necessity of carrying out temperature compensation in real oxygen sensing applications. This subject is discussed in detail in section 7.7.2. Subsequent measurements on the temporal stability

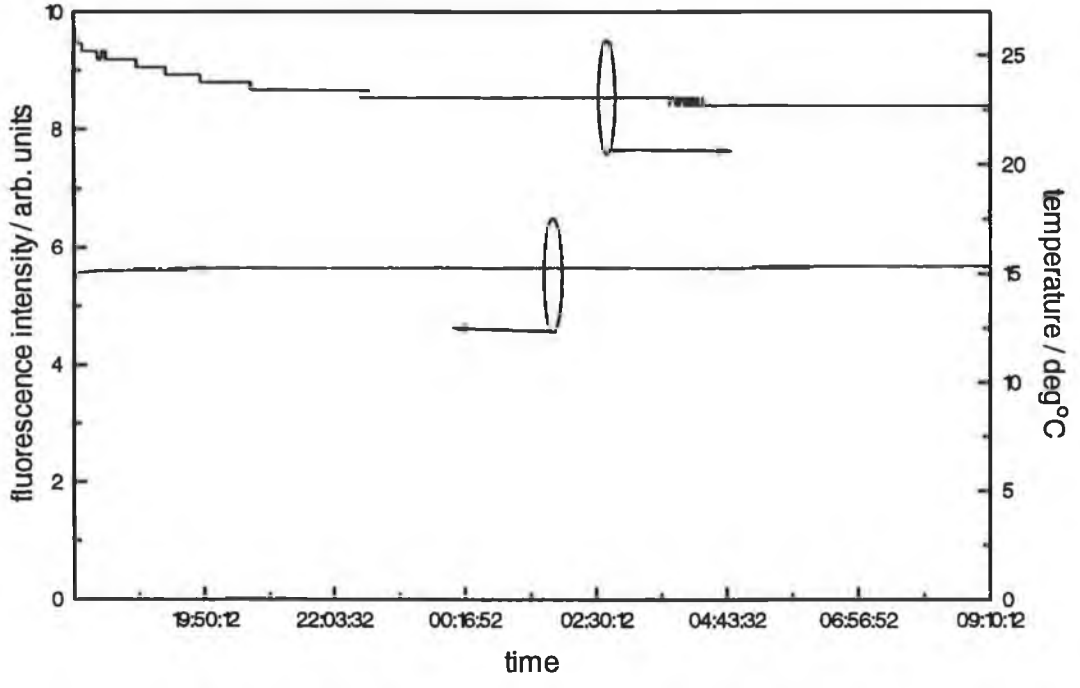

figure 7.19 Long term stability instrument response, and ambient temperature for a period of 16 hours.

of film thickness indicated that for the recipe used, the film microstructure was still evolving during the period of these tests. These findings are further discussed at the end of section 7.7.2.

7.8.1 Temperature and relative humidity dependence studies

In order to investigate the viability of using the sensors in various climatic conditions, a range of environmental tests were carried out on the probes. These included investigations to determine the susceptibility to temperature and relative humidity (RH) variation as well as to potential interfering gases. All temperature and relative humidity studies of the sensor were carried using in a climatic chamber (*Fisons*, type 22280CT/C/R10/IND). Using this chamber it was possible to pre-program any desired temperature variation (0°C to 100°C), over a period of time. Unfortunately, the RH controller in the instrument was not in proper working order and therefore could not be used. Consequently, the RH varied with temperature. To monitor the two parameters a *Vaisala* temperature/RH probe (model #MI 32) was used. This produced voltage outputs proportional both to the temperature and RH values being measured. The optical block and fibre sensor of the all-solid state system were placed in the climatic chamber for the duration of a temperature cycle. A data logger was used to simultaneously monitor variation of the sensor output, temperature and RH.

The initial temperature studies were carried out by measuring the fluorescence intensity from the sol-gel immobilised ruthenium complex. All sol-gel coated fibres were doped with the diphenyl phenanthroline complex, immobilised in a 2:1 water/TEOS sol-gel. It should be noted that the measured fluorescence signal is the temperature/RH combined response of the complete optical system, i.e. response of the LED, photodiode and optics are included. Figure 7.20, shows a typical temperature/RH dependence of the system. From the data a 59% signal decrease occurred while increasing the temperature from 0.98°C to 67.60°C, The relative humidity changed as shown.

Two questions to be answered when considering temperature/RH dependence are as follows. Firstly, is the fluorescence signal repeatable with temperature? Secondly, does the oxygen sensitivity of the sensor change after exposure to a temperature program? Experiments were carried out to examine these questions under the following conditions:

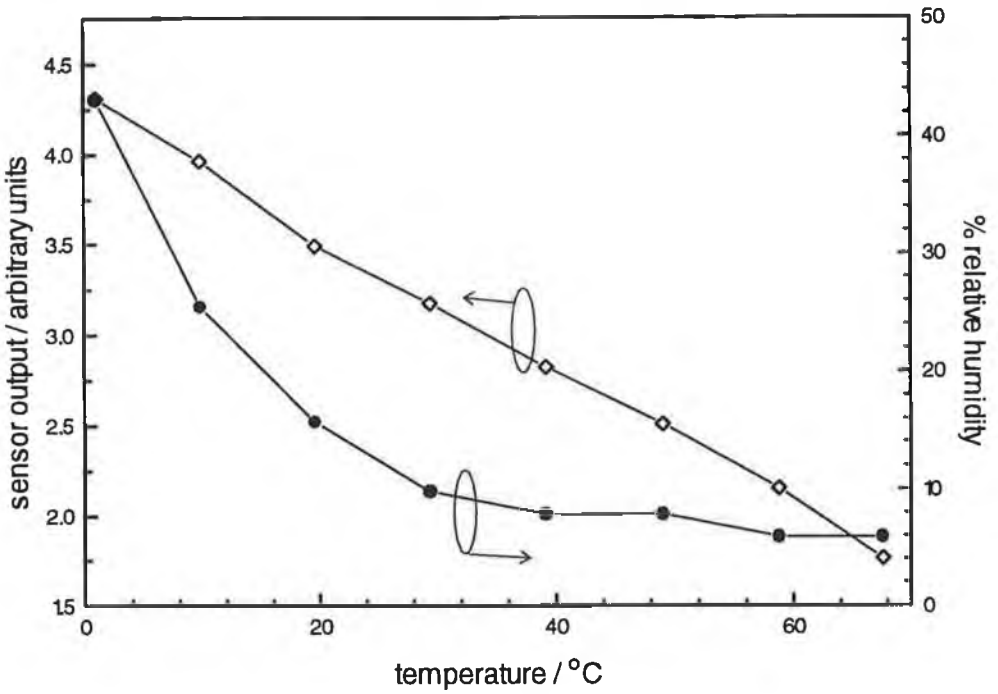

figure 7.20 Sensor response to temperature and humidity variation.

i) O°C - 70°C ; RH off[1]

ii) 10°C - 50°C ; RH off

iii) 10°C - 40°C ; RH off

i) O°C - 70°C ; RH off

The response of the complete optical block plus fibre sensor to a 0°C - 70°C temperature cycle is shown in figure 7.21. The following temperature programme was used:

0°C - 3 hours; 30°C - 2 hours; 70°C - 2 hours

The temperature cycle was set to begin during the 0°C to 30°C transistion. It should also be noted that the response time of the climatic chamber was not instantaneous and that a certain amount of time was required for the chamber to reach the programmed temperature. This delayed temperature response of the chamber is obvious from the middle plot of figure 7.21. The measured fluorescence signal is plotted on the top plot of figure 7.21, temperature on the

[1] RH controller was turned off, resulting in the RH not being constant, rather it followed temperature variation

middle plot and relative humidity on the lower plot of figure 7.21. The scan has a duration of about 2.96 days. As can be seen from the sensor output, the sensor response varies in a repeatable manner with temperature and RH. However, the overall signal drops considerably for the first three 9 hour temperature cycles or so, before a more gradual decrease in signal is observed. This behaviour can be seen more clearly in figure 7.24 in which the peak fluorescence signal of each 9 hour cycle is plotted against time. Sensitivity to oxygen, however, was found to change considerably during this temperature program. Prior to the temperature program, sensitivity of ~65% was measured for the specific fibre sensor. This decreased to 22% within 1 hour and immediately following the program the sensitivity measured 6%. This decrease in sensitivity to oxygen is also shown in figure 7.24.

ii) 10°C - 50°C ; RH off

Figure 7.22 shows a similar experiment, where the temperature programme set as follows:

10°C - 2 hours; 30°C - 2 hours; 50°C - 2 hours

In this case, the fluorescence signal again stabilises over the first day. The fluorescence peak signal of each of the 6 hour temperature cycles are plotted in figure 7.24. The rate of decrease in signal is quite significantly less than the previous experiment. Oxygen sensitivity changes from an initial value of 70% to 23% at 15 hours to a final value of 20%.

iii) 10°C - 40°C ; RH off

The equivalent experiment was carried out for a temperature range of 10°C to 40°C, for a duration of 18 hours. The system performance is shown in figure 7.23. A sensitivity change from 82% to 67.4% was recorded over the duration of the experiment. This decrease is quite a small change when compared to the two previous experiments as displayed in figure 7.24. It is also obvious from the graph that the variation in fluorescence signal is quite repeatable with temperature and therefore offers the potential of temperature compensation. This is in contrast with the two previous environmental tests during which decreases in fluorescence signal were observed over the same measurement periods. It seems likely that the repeatability with temperature is due to the narrower temperature range to which the sensor

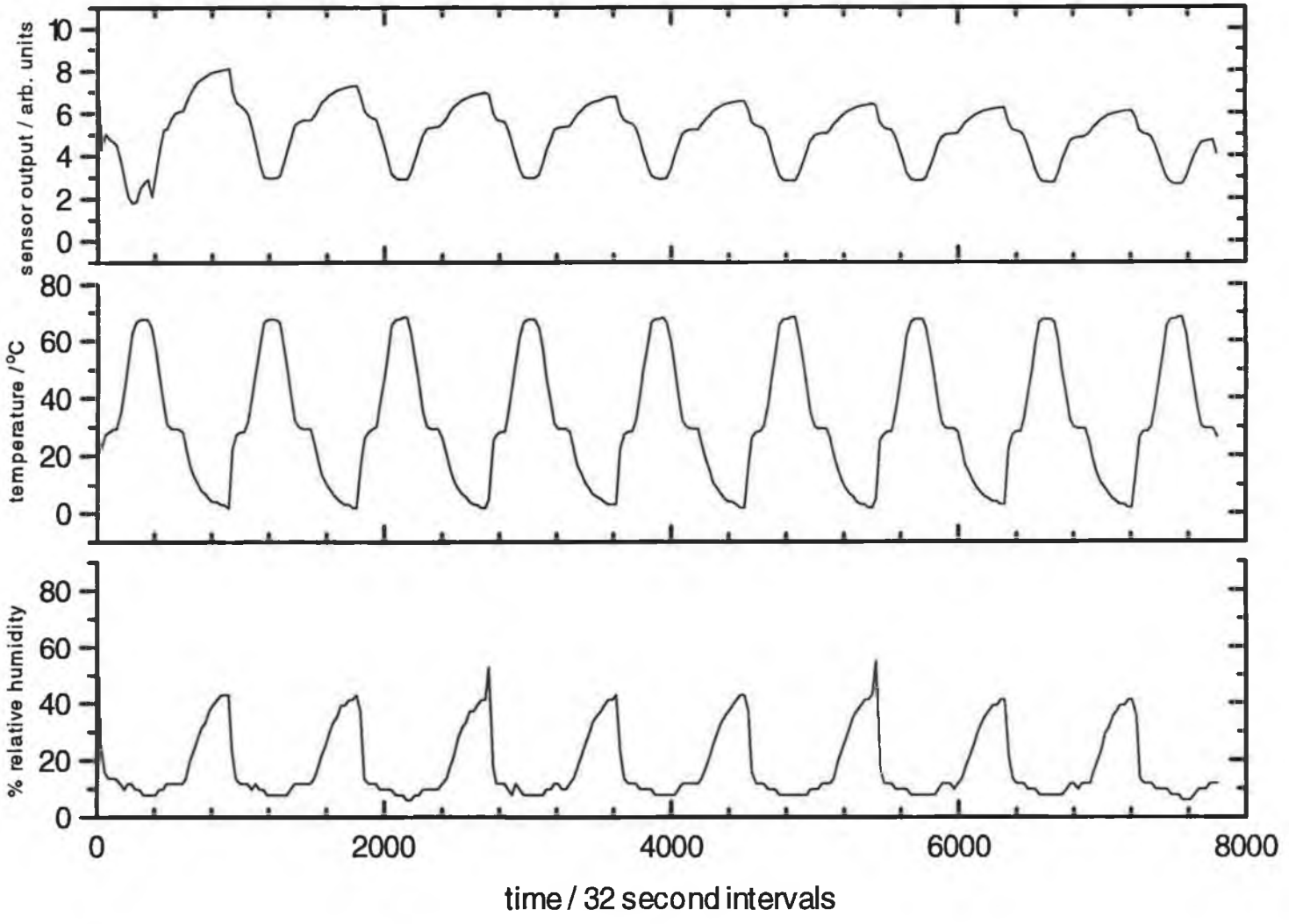

figure 7.21 Sensor response to a 0°C to 70°C temperature cycle over a period of 2.96 days; temperature and relative humidities are included.

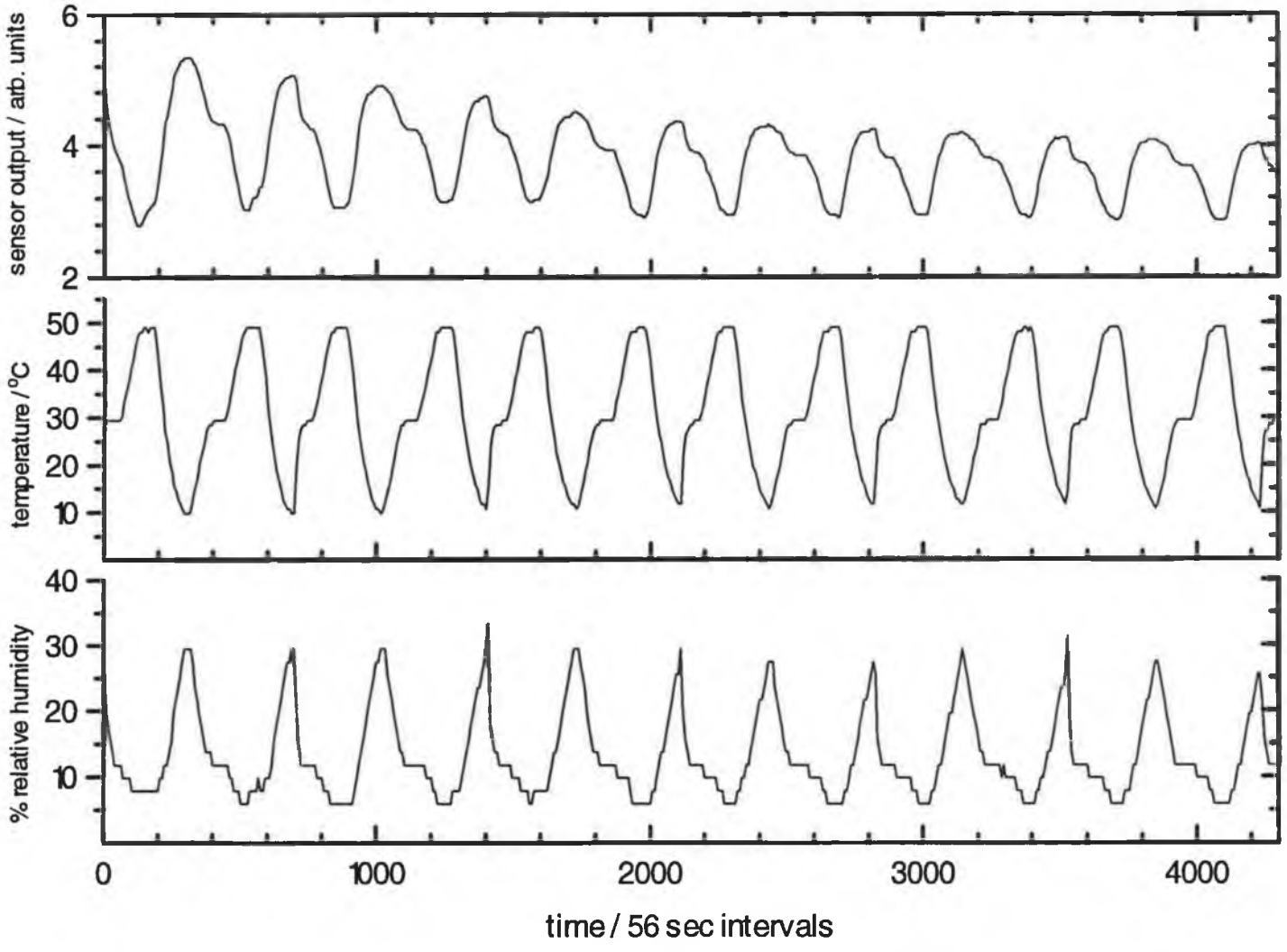

figure 7.22 Sensor response to a 10°C to 50°C temperature cycle over a period of 2.78 days; temperature and relative humidities are included.

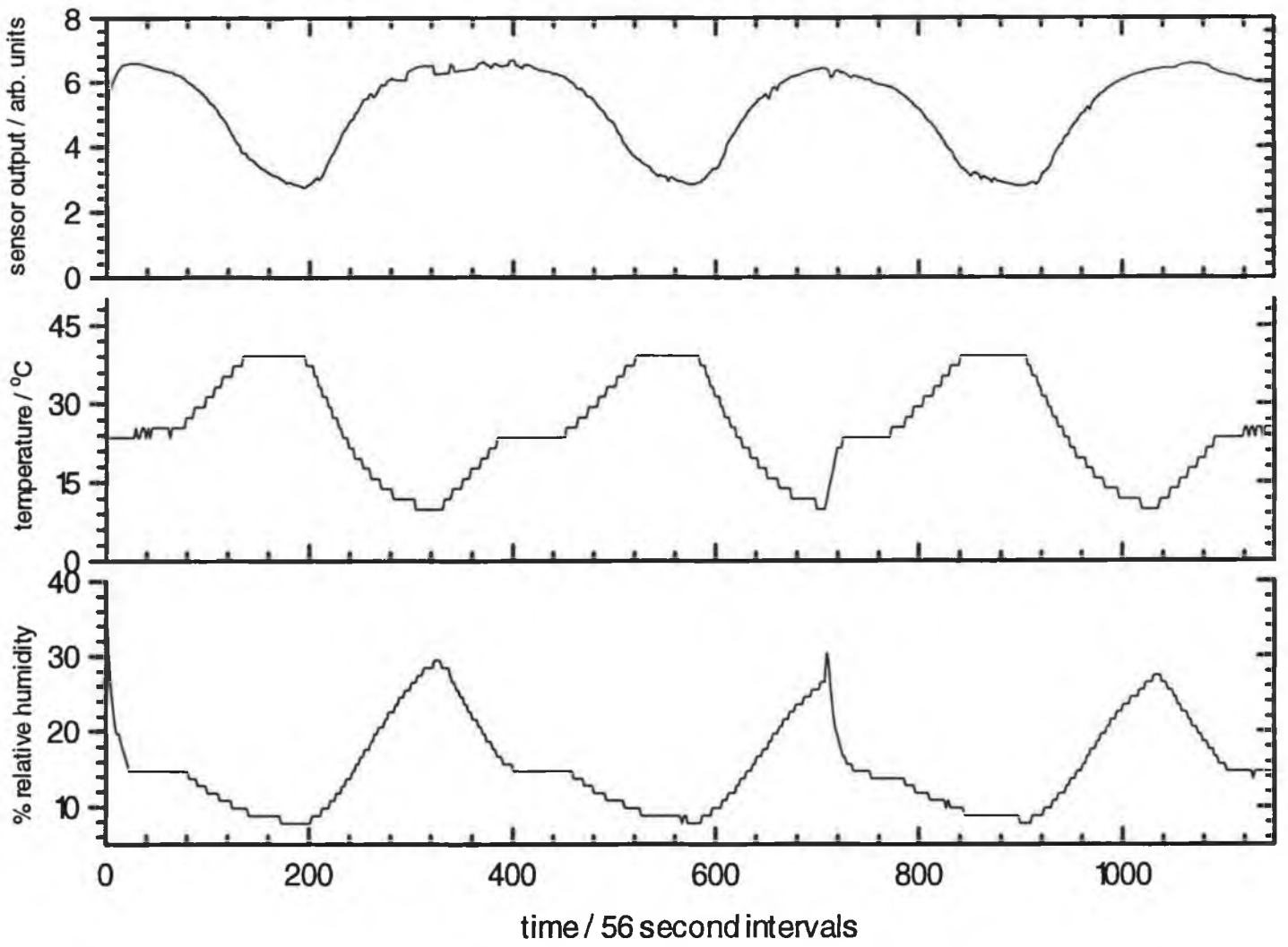

figure 7.23 Sensor response to a 10°C to 40°C temperature cycle over a period of 0.75 days; temperature and relative humidities are included.

has been exposed. This temperature response of the sensing probe to the less harsh temperature cycle may possibly be related to the evolution of the sol-gel microstructure of sensor.

As previously mentioned, the RH controller of the climatic chamber was not in proper working order. However, one experiment was carried out using an alternative chamber which had RH control. During the experiment, the temperature was kept constant at 25.5°C, and the RH was varied as shown in the lower plot of figure 7.25. It is clear from these data that the sensor output is very dependent on the relative humidity.

It is difficult to arrive at precise conclusions from the temperature/RH dependency studies which have been presented. If it were possible to completely separate temperature and RH dependencies a clearer understanding might be achievable. However a number of important points can be noted from these experimental results:

i) Fluorescence intensity does decrease with temperature as predicted by equation 3.14.

ii) Significant changes in sensor response occurred during the harsher temperature programs of 0°C to 70°C and 10°C to 50°C including large decreases in oxygen sensitivity and decreases in overall fluorescence signal.

iii) The 10°C - 40°C temperature programme had very little effect on the repeatability of absolute fluorescence intensity and only slightly effected its oxygen sensitivity. This temperature range is typical of the quoted operating range of -15° to +40°C of electrochemical oxygen sensing cells [2]. Most sensors have a certain amount of variation with temperature. However, it is critical that the variation is repeatable so as to allow proper temperature compensation. Figure 7.23 suggests that temperature compensation is possible over that specific temperature range.

iv) The sensor response to RH variation at a constant temperature is shown in figure 7.25. From these data it is possible to determine the sensors dependence on RH variation. However it is unclear from the data, if the variation between the two parameters is totally repeatable. To clarify this, a RH cycling programme such as those carried out to test the temperature dependence of the sensor would be necessary. The data of figure 7.25 suggest the need of a RH sensor for use with the oxygen sensor. A decrease in fluorescence signal with a decrease in RH may possibly be accounted for by the fact that at low RH the sol-gel pores are free from condensation and therefore allow the diffusion of oxygen throughout the

porous structure. This results in fluorescence quenching taking place and a decrease in sensor output signal as observed. At high RH the opposite would be expected to occur i.e. the formation of condensation within the sol-gel structure will force oxygen molecules from the microstructure and will also impede the diffusion of oxygen molecules within the structure. This would be expected to result in an increase in fluorescence signal as was observed. There are however, a number of possible means by which this problem can be alleviated. Firstly, the use of a hydrophobic membrane around the optical fibre would restrict moisture from forming on the sol-gel layer. Alternatively the use of a heating element close to the fibre would also restrict the formation of condensation. This method of restricting condensation is used by Sieger Ltd., in the design of their infrared gas sensor - *Searchpoint* [5]. Finally, a third possibility is to silanise the sol-gel surface and thus make it hydrophobic.

The susceptibility to RH and temperature of the sol-gel sensor could retard the future commercialisation of such an optical sensor. It would be hoped that the sensing sol-gel layer would be completely stable during its use and if not, then vary in a repeatable manner with temperature and RH. It should be noted that the temperature cycles of figures 7.21, 7.22 and 7.23 may reflect, firstly, the temperature dependence of the ruthenium complex which is expected according to equation 3.22. This variation with temperature would be expected to be repeatable. The second source of variation with temperature, which possibly may account for the lack of repeatability of fluorescence signal which was observed in figures 7.21 and 7.22, may be attributed to recent investigations at Dublin City University into the temporal evolution of the sol-gel glasses microstructure. These studies have suggested that 2:1 water/TEOS sol-gel coatings are unstable as previously discussed in section 4.6. This instability has been attributed to unreacted silanol groups hydrolysing with water molecules from the atmosphere. It has also been discovered that the 2:1 sol-gel film thickness reach equilibrium over a period of 50-60 days. This suggests that the sol-gel films used in the above temperature/RH studies had not yet reached equilibrium with regard to stabilisation of their microstructure. Had they reached equilibrium, it might be plausible to assume that less of a variation with temperature and RH would be observed. More stable sol-gel films are now routinely being produced with a higher TEOS/water ratio. These films were found to stabilise over a 10 day period. Susceptibility to temperature variation remains to be tested.

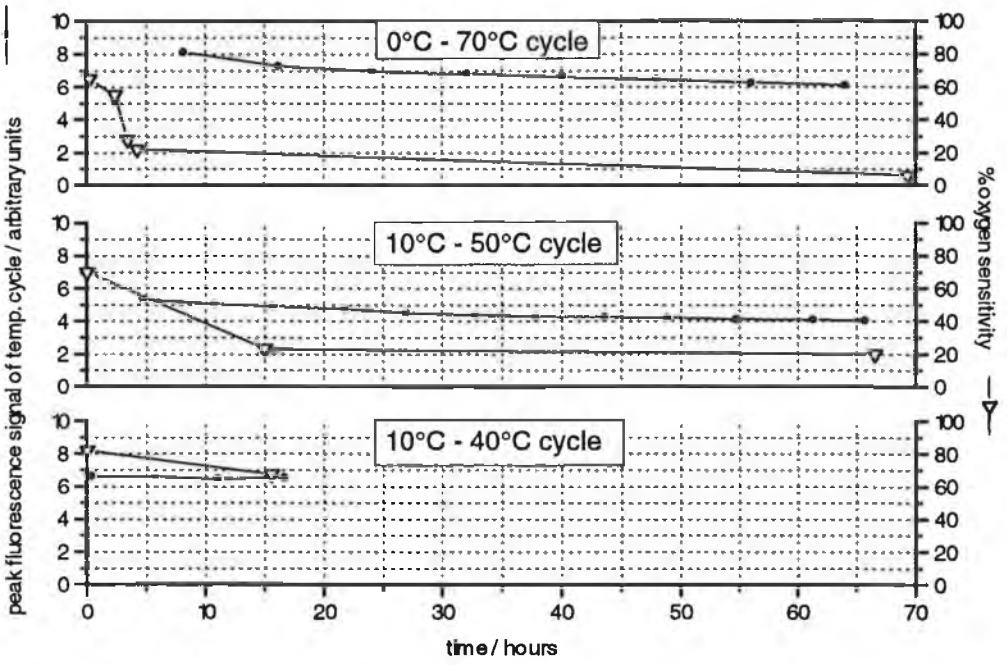

figure 7.24 Peak fluorescence signal and sensitivity to oxygen variation of above temperature programs.

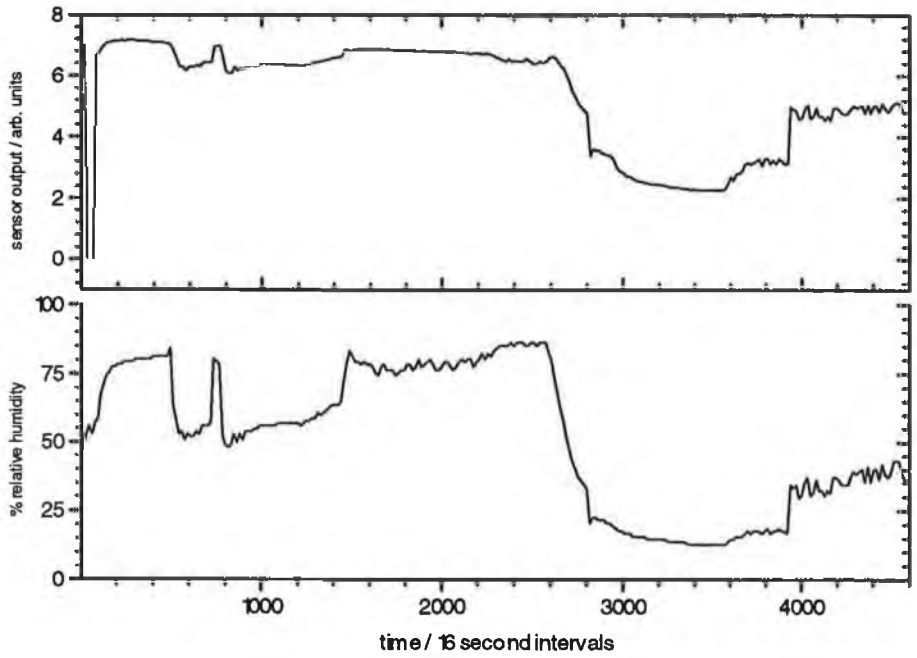

figure 7.25 Sensor response to humidity variation cycle over a period of 18 hours; temperature was kept constant at 25.5°C.

7.8.3 Gas interferent studies

The susceptibility of the sensor to other gases potentially interfering gases was also investigated. The all-solid state sensor system response was tested in the presence of 50% LEL methane in air and in 50% LEL butane in air. No detectable change was observed in fluorescence intensity, and no poisoning of the sensor occurred. An interference test was also carried out with CO_2. Pumping 5% CO_2 in nitrogen reduced the fluorescence signal by 3%, and reduced the fibre sensitivity by 7%. When the concentration of CO_2 was increased from 5% to 50% in nitrogen, the fluorescence signal decreased by a further 1%. However, its sensitivity was found to have reduced by a further 31%. In the interpretation of this data it should first be noted that the percentage by volume of CO_2 in dry air is 0.03 [6]. Therefore, the variation of CO_2 in air around 0.03% will possibly have very little effect on the sensor output. The testing of the interference of CO_2 could not be carried out at these low concentrations as the mass flow controllers used allow an accuracy of 1%. Finally, it should also be noted that manufacturer's data for typical oxygen sensing electrochemical cells state that the presence of CO_2 results in an enhanced sensor signal of about 0.3% per 1% CO_2.

7.8.4 Sensor response time

Throughout the analysis of the oxygen sensor, a flow rate of 500cm^3/min was achieved using mass flow controllers. In order to analyse the sensor's response time, solenoid valves were included in the gas flow system. The use of these valves allowed the switching of the flowing gases to occur instantaneously rather than with the adjustment of the mass flow controllers as was previously required. Gas piping length was kept to a minimum between the switching valves and the oxygen sensor, such that the effect of their filling time could be minimised. The LED / PMT fluorescence intensity system was set up using a commercial lock-in amplifier to discriminate against background light. The time constant feature of the lock-in amplifier was reduced to a value of 10ms such that the true response time of the sensing material would be detected. Using a flow rate 500cm^3/min of nitrogen through the sensing cell, the fluorescence signal was monitored as the flowing gas was changed to oxygen. The quenching signal was recorded as a function of time as previously described in section 6.2.1. Neglecting the switching time of the solenoid valves, a response time of 3.1 seconds was measured for the sensor output

to change completely from a stable nitrogen signal to a stable oxygen signal. A slower time of 13.3 seconds was measured for a transistion from oxygen to nitrogen at the same flow rate. The same experiment was carried out for various gas flow rates as shown in figure 7.26. At a flow rate of 15.6 cm^3/ min, a large difference of 268 seconds occurred between a N_2 to O_2 transistion and an O_2 to N_2 transistion. The interpretation of these data may be carried out as follows:

i) A major parameter in the interpretation of the above data, is the physical size of the gas cell in which the oxygen sensor is held, i.e. the gas cell filling time should be considered. At the maximum flow rate of 500cm^3/min, the time to fill the gas cell (volume = 30 cm^3) is about 0.06 seconds. Whereas at the minimum rate of 15.6cm^3/min the gas cell filling time is in the region of 2 minutes. At the low flow rates the length of extra gas piping also affect the measured response times. Taking these parameters into consideration it is difficult to extract true sensor response times from the data in figure 7.26. However, at the maximum gas flow rate, the gas cell filling time is negligible when compared to the sensor response time. The values of 3.1 seconds for the turn-on time

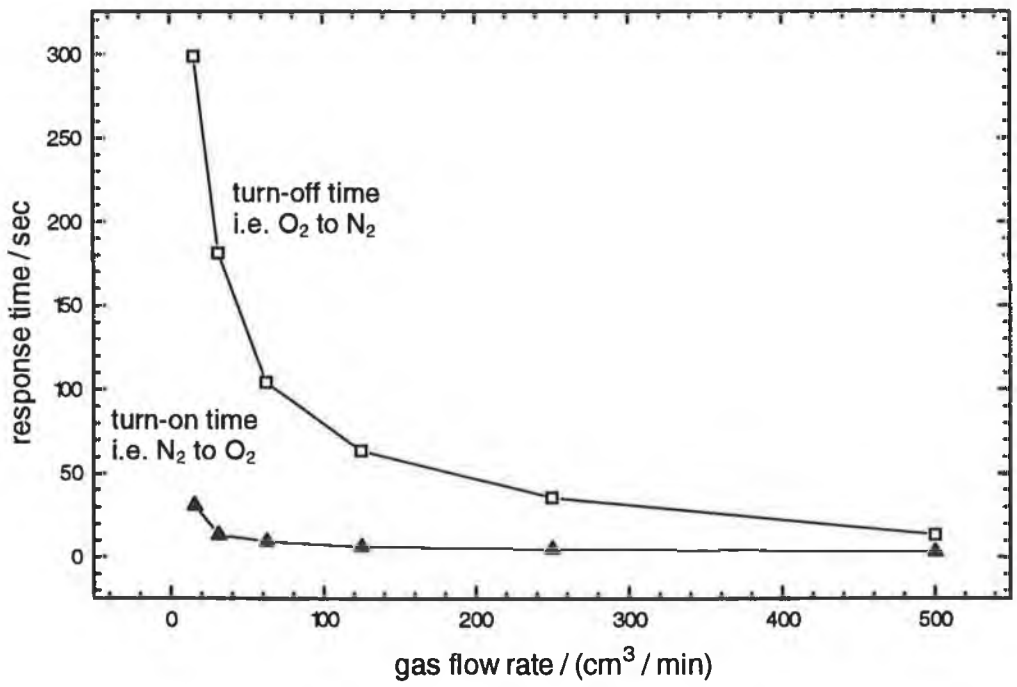

figure 7.26 Sensor turn-on and turn-off times as a function of gas flow rate.

and 13.3 seconds for the turn-off time are therefore closest to the true response times of the sensing material.

ii) One obvious feature from the data, however, it the fact that the sensor turn-off time is much greater than its turn-on time. These data may reflect the greater affinity of oxygen for the water layer over nitrogen within the sol-gel microstructure, as is evident by their differing mole fraction solubility values[1] for water (oxygen : 2.756×10^{-5}, nitrogen : 1.386×10^{-5} [7]). In addition it may also reflect the greater reactivity of oxygen compared to nitrogen. The ratios of turn-off to turn-on response times, as a function of flow rate, are shown in table 7.3. Greatest errors in the measurements would be expected to be present in ratio-values calculated for the fast response times. Therefore, if the first two data points in the table are neglected, a near constant ratio of sensor turn-off time to turn-on time would result. A more accurate method of determining response times of fluorescence coatings, which allows an accuracy of up to 10μs has been described by Baron et al. [8]. Using a system such as this, less of a deviation from the average ratio would be expected to be observed.

Flow rate ccm/min	turn-off / turn-on
500	4.3
250	7.7
125	10.3
62.5	11.4
31.3	13.7
15.6	9.8

table 7.3 Gas flow rate as a function of the ratio of sensor turn-off response time to sensor turn-on response time.(Data taken from figure 7.26).

7.9 Conclusion

Chapter seven describes the response of a sol-gel derived evanescent-wave fiber optic oxygen sensor. High sensitivity to the presence of oxygen has been demonstrated using a laser / PMT characterisation system. Greatest sensitivity to oxygen was reported

[1] Values refer to a partial pressure of 101.325 KPa and a temperature of 288.15°K.

using the diphenyl-phenanthroline ruthenium complex which has a relatively long fluorescence lifetime. Good repeatability of signal, high SNR and fast response times were also demonstrated for the same system using the phase fluorimetric measurement technique. This system was shown to possibly be more advantageous than the direct fluorescence intensity measurement system. The laser excitation source was replaced with the recently available high intensity blue LEDs combined with photodiode as detector. This miniaturised, all-solid-state portable system was shown to operate again with high signal repeatability, good sensitivity to oxygen, high SNR and fast response times for both a direct fluorescence intensity and a phase fluorimetric type measurement system. This is the first reported intrinsic phase fluorimetric all-solid-state sensing system. In the analysis the frequency response of the system for both measurement configurations have been examined. Alternative measurement techniques which are based on the fluorophore lifetime are also detailed.

Sensor characterisation was also carried out in terms of susceptibility to temperature and relative humidity variation using the all-solid-state fluorescence intensity monitoring system. A number of temperature cycling tests were performed on the oxygen sensor. The data shown exhibited a lack of repeatability for both a 0°C - 70°C and a 10°C - 50°C temperature programme. However promising results were found for a temperature programme of 10°C - 40°C where good repeatability of fluorescence signal from the sensor was recorded with temperature variation. Possible methods of temperature compensation have also been discussed. The sensors response to variation in relative humidity was detailed. A fall-off in fluorescence signal was recorded as the percentage relative humidity decreased. This was attributed to the formation of condensation within the sol-gel microstructure, resulting in the expulsion of air from the sol-gel environment and therefore a reduction in fluorescence signal. The sensor was also characterised in terms of potential interfering gases and sensor response time.

References:

1. Crowcon Detection Instruements, Fixed systems and portable instrumentation for safety gas monitoring, Oxfordshire, England.

2. Citicel - Product Data Handbook, City Technology Limited, Quality gas detection, April 1993, Issue 1.7.

3. Personal communication with Aisling McEvoy, School of Physical Sciences, Dublin City University, Ireland.

4. Zhang Z., Grattan K.T.V., Palmer A.W.: '**Phase-locked detection of fluorescence lifetime**', Review of Scientific Instruements, 1993, Vol. 63, No. 9, pp. 2531-2540

5. Sieger Gas Detection Portfolio, Poole, Dorset, United Kingdom.

6. Mortimer C.E.: '**Chemistry**', 6th Ed., Wadsworth Publishing Company, 1986, p.611

7. '**Handbook of Chemistry and Physics**', Lide D.R., (Ed.), 72nd Edition, CRC Press Inc., 1991, pp. 6/3 - 6/3

8. Baron A.E., Danielson J.D.S., Gouterman M., Wan J.R., McLachlan B.: '**Submillisecond response times of oxygen-quenched luminescent coatings**', Review of Scientific Instrumentation, 1993, Vol. 64, No. 12, pp. 3394-3402

Chapter Eight - Evanescent Wave Biosensing

8.1 Introduction

Biosensing is an emerging technology that has been shown to have practical applications in fields such as clinical diagnostics, environmental monitoring and process control [1,2,3]. In a biosensor, biological molecules provide the recognition of a substance to be detected. The use of such biological molecules, especially antibodies, offers excellent selectivity for detecting many analytes of interest, for example enzymes, proteins, hormones and toxins. The basis for the specificity of immunoreactions is the antigen-antibody binding reaction, which is a key mechanism by which the immune system detects and eliminates foreign matter from the body. Antibodies are complex biomolecules made up of hundreds of individual amino acids arranged in a highly ordered sequence [1], and are also known as proteins. The antibodies are produced by immune system cells, when such cells are exposed to molecules which are called antigens. The antibodies produced following antigen exposure have recognition/binding sites for specific substructures of the antigen. This unique property of antibodies results in their particular suitability for use in sensors their use in sensors, which can identify an analyte of interest, present even in an extremely small amounts. Fluorescence-based fibre-optic immunoassays have been the subject of much research in recent years with some groups

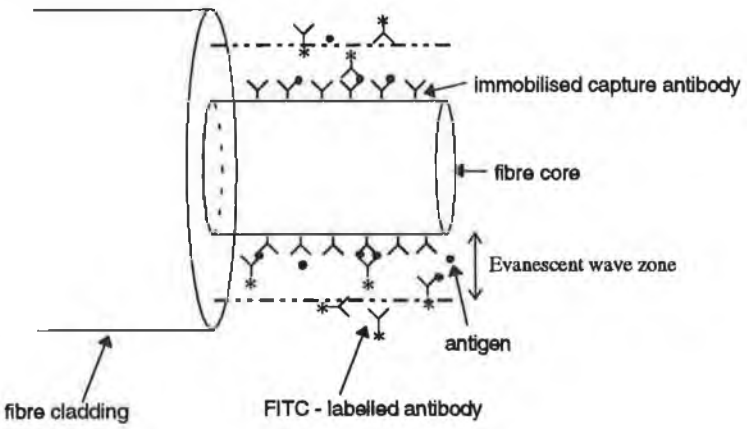

figure 8.1 Fibre optic fluorescence immunosensor based on the evanescent wave technique

being particularly prominent [4,5]. In this chapter work similar to this, which has been carried out in collaboration with the School of Biological Sciences in Dublin City University is described. The system utilises the evanescent wave of a fibre optic waveguide, in combination with a sandwich immunoassay which is performed at the surface of an optical fibre. Antibodies specific for an analyte of interest are immobilised on the exposed silica based core of the optical fibre as shown in figure 8.1. The analyte of interest (antigen) binds to this immobilised antibody, removing the molecules from solution and holding them with-in a few hundred angstroms of the fibre core. The rate of antigen - antibody binding is proportional to the antigen concentration present, as long as the immobilised antibody is in excess. A second antibody labelled with a fluorophore (FITC, i.e. fluorescein isothiocyanate) binds to the antigen and the fluorophore is detected due to its interaction with the evanescent wave. Evanescent wave radiation at the appropriate wavelength excites the fluorescent molecules within its penetration depth. Fluorescently labelled antibodies in the bulk solution are therefore generally not excited. They may however, lead to a constant D.C. background level. The rate of increase of the fluorescence can therefore be directly related to the antigen concentration. Antibody-antigen binding can thus be measured in real-time.

Optically detected signals from evanescent wave fluorescence immunoassays are typically derived from a number of sources, as illustrated in figure 8.2. The background signal is composed of scattered excitation light (1), fluorescence from the waveguide itself (2), and unbound labelled antibody in solution (3). These background contributions will vary from system to system depending on for example, the spectral filtering and

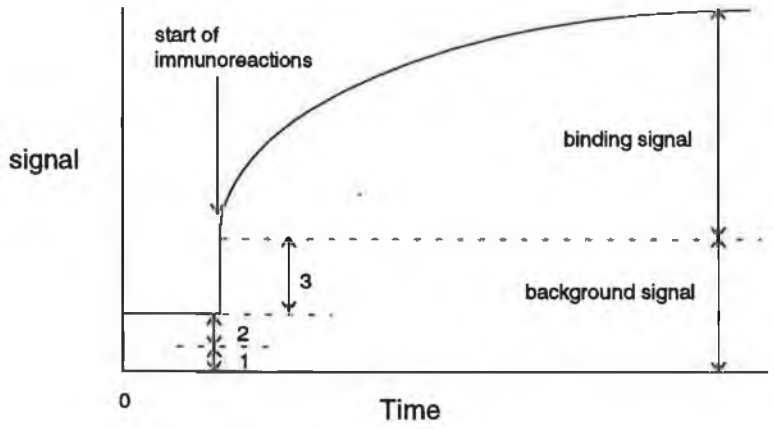

figure 8.2 Origin of evanescent wave immunoreaction signals [6].

choice of fibre. Initiation of the immunoreactions is taken as the point when the gradual increase in detected fluorescence signal occurs. The slope of the signal response curve, which corresponds to the initial rise of the number of labelled antibodies attracting themselves via the antigen molecules to the immobilised antibodies on the fibre surface, is proportional to the concentration of antigen in solution.

The work described here concerns the detection of Lactate Dehydrogenase (LDH). LDH is a clinically important diagnostic marker enzyme for many diseased states. Different isoenzyme forms of LDH are found in different organs and tissues of the body. Damage to these tissues will result in increased levels of certain isoenzymes in the blood. LDH is generally measured on the basis of its activity 24-48 hours following tissue damage. Such results, however, should be viewed with caution as the catalytic activity of such enzymes decrease with sample age. Because of the immunoassay's lesser susceptibility to conformational changes at the active site, measurement on the basis of mass content rather than catalytic activity is more suitable for diagnostic measurements [7].

8.2 Sensor preparation

PCS optical fibre of 600μm diameter was cut into 11cm lengths, polished, partially declad and etched as described previously in chapter 5. The exposed silica core was acid-cleaned using a 1:1 mixture of concentrated HCl and methanol. Following washing several times with ultra pure water, the fibres were immersed in concentrated H_2SO_4 for 30 minutes and washed again in ultra pure water for further cleaning. The fibres were then hydroxylated by placing them in a bath of boiling ultra pure water for 30 minutes. The fibres were then allowed to air-dry.

In the past, antibodies have been attached to glass, by surface adsorption or by covalent attachment directly to surface hydroxyl groups [8]. However, a method of immobilisation of antibody onto the optical fibre surface based on the silanisation of the fibre surface has been described by Bhatia et al. [8]. This process was carried out on the optical fibres by co-workers in the School of Biological Sciences. Dublin City University.

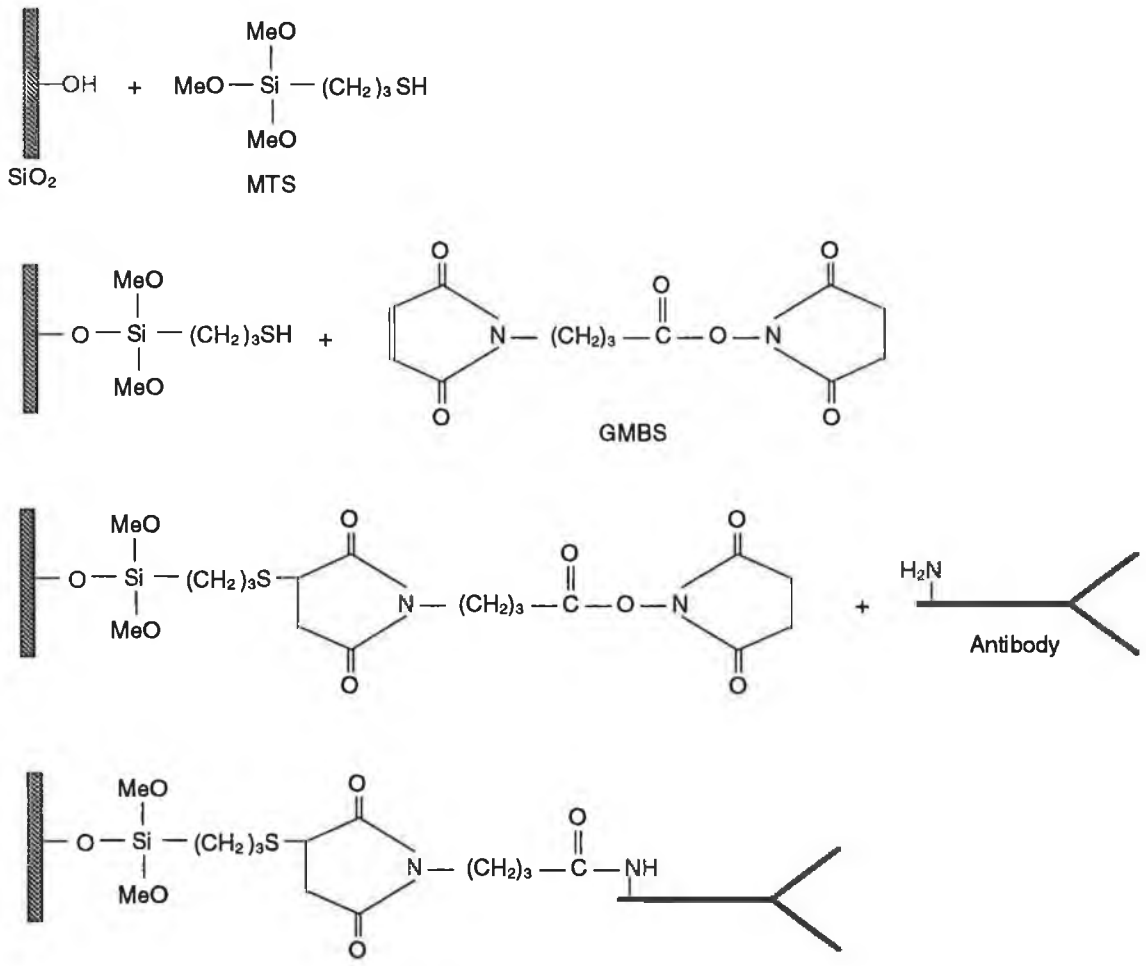

figure 8.3 chemistry of antibody immobilisation [8].

The heterobifunctional crosslinker[1] γ-maleimidobutyric acid N-hydroxysuccinimide ester (GMBS) is coupled to the silane (3-mercaptopropyltrimethoxysilane i.e. MTS) through one end, and the free end of the crosslinker is reacted with a terminal amino group of the antibody via an amide linkage. A schematic diagram of the chemistry of this process is shown in figure 8.3 The prepared fibres were stored in phosphate buffered silane (PBS), containing preservative until required for use.

8.3 Experimental system

The system used to carry out this work is essentially equivalent to that described in section 6.2.1. Figure 8.4 shows the absorption spectrum of FITC for emission at 520nm, which is suitable for excitation at 488nm using an argon-ion laser. Its

[1] A molecule with different reactive sites on each end

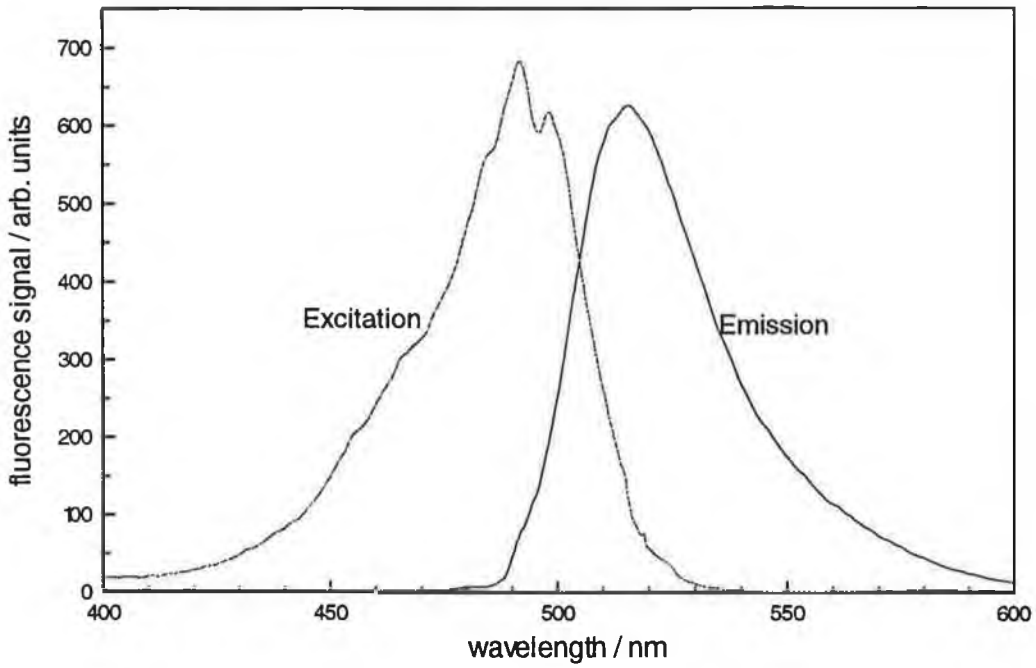

figure 8.4 FITC absorption and fluorescence bands

fluorescence peak occurs at 517nm. A glass filter which blocks 488nm to 0.01% and transmits 520nm at 95% was used in place of the monochromator shown in figure 6.4 [9].

Figure 8.5 shows the glass flow cell which has both ends threaded. It is important that the fibre is held firmly in place in the flow cell, such that it is not moved out of position during the flow of liquid through the cell. Rubber septa are used on either side of the cell as illustrated, to position the optical fibre along the cell's central axis. The septums are held in position by two screw-on plastic caps. Sample waste was reduced by

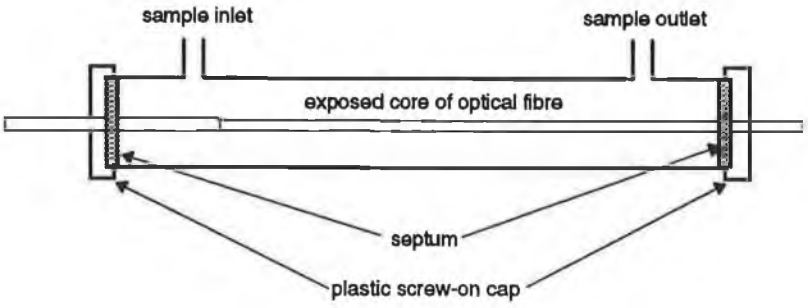

figure 8.5 Immunoassay flow chamber

keeping the cell volume to a minimum ($1.5cm^3$). Samples were passed through the cell using a peristaltic pump. Care was taken to ensure that air bubbles did not enter the sample flow stream during usage. The glass structure was mounted in a X-Y-Z micro-positioner to enable the adjustment of fibre launching position.

8.4 Control experiment

There are at least three possible sources of fluorescence signal when a fibre probe is exposed to a solution containing fluorescently labelled antibody [10]. The first is due to specific binding of antigen to antibody. The second is non-specific binding of antigen due to proteins or other substances on the fibre probe. However, the occurrence of this process is more or less eliminated by the use of Tween20, which is a detergent that disrupts weak bonds and therefore minimises the effect of any such non-specific binding. As previously mentioned the probe may generate a signal originating in the bulk solution. When a fibre coated with anti-LDH antibody is exposed to a non- specific antigen, no specific binding should take place. Thus any detectable signal would be due to non-specific binding or would originate in the bulk solution. Figure 8.6 shows

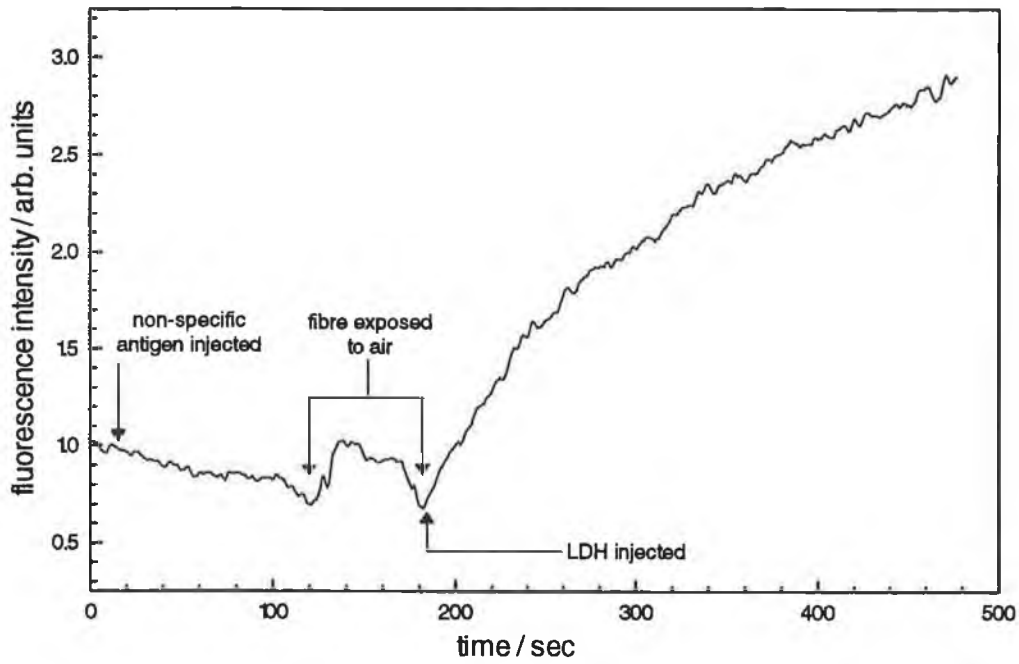

figure 8.6 Fibre specificity for LDH

an example of the results when the probe was exposed to non-specific antigen. No response was observed. After flushing, the probe was then exposed to specific antigen, to ensure that the null result was not due to a defect in the probe or in the optical instrumentation. Based on the absence of any signal except when the probe was exposed to specific antigen, the conclusion is that the signal in figure 8.6, is due to specific binding of the FITC labelled anti-LDH to the LDH.

8.5 Two step Immunoassay

Optical fibres with anti-LDH antibodies immobilised on their surface were incubated with various concentrations of LDH (30-1000ng/ml) for 2 hours at room temperature to ensure equilibrium was established. The fibres were then washed 3 times with a PBS/Tween20 mixture. The fibres were stored in 0.1M PBS, pH 7.3 on ice until they were ready for use in the evanescent wave fluorescence characterisation system. Alignment of the fibre was carried out in the optical system and the flow chamber was filled with 1% bovine serum albumin (BSA) so that a baseline could be monitored. D.C. background signals were nulled by using the 'offset' feature of the Lock-in amplifier.

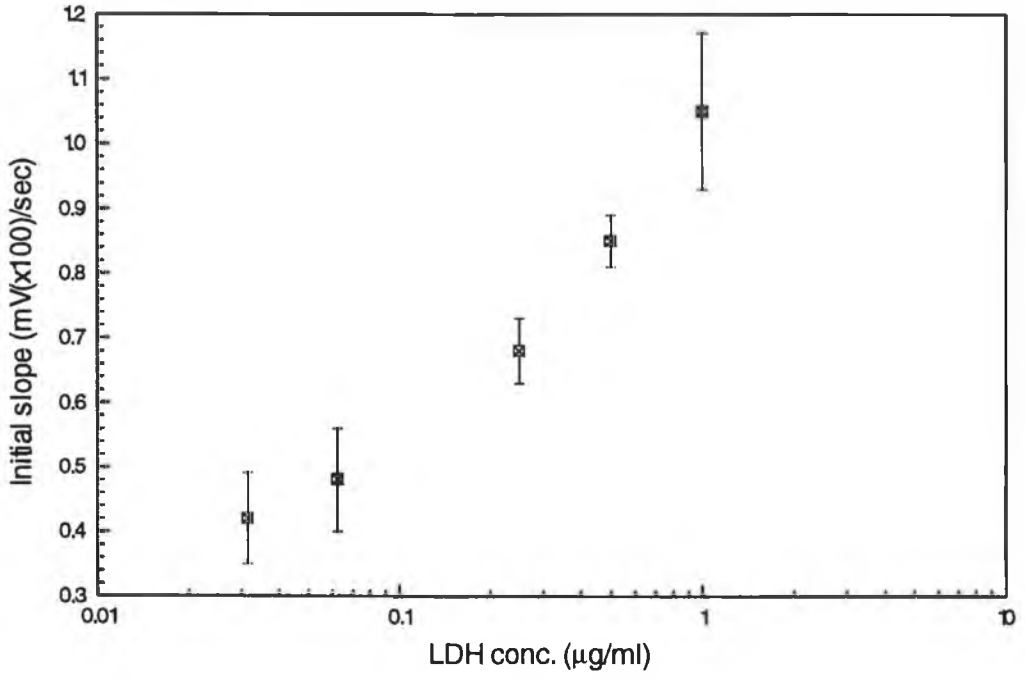

figure 8.7 Two-step immunoassay

Once a steady baseline was obtained, an excess of FITC labelled anti-LDH (~20μg/ml) prepared in 1% BSA was pumped into the flow cell until the fibre was completely immersed in the second antibody solution. The rate of fluorescence signal accumulation was monitored for 4.5 minutes.

Figure 8.7 shows the initial slope (measured over 100 seconds) obtained in such a two step immunoassay evanescent wave experiment, for various LDH concentrations. The samples were run in triplicate. Standard deviation of the 3 samples is depicted by the error bars. Such results are typical of this type of assay [11].

8.6 One-step Immunoassay

The sandwich immunoassay was also performed as a one-step process with similar results. Various LDH concentrations were prepared in 1% BSA. The anti-LDH coated fibres were aligned in the flow cell and the baseline monitored until a steady baseline was observed. The LDH sample to be tested, was premixed with an excess of FITC labelled anti-LDH antibody just prior to injecting it into the flow cell. The binding

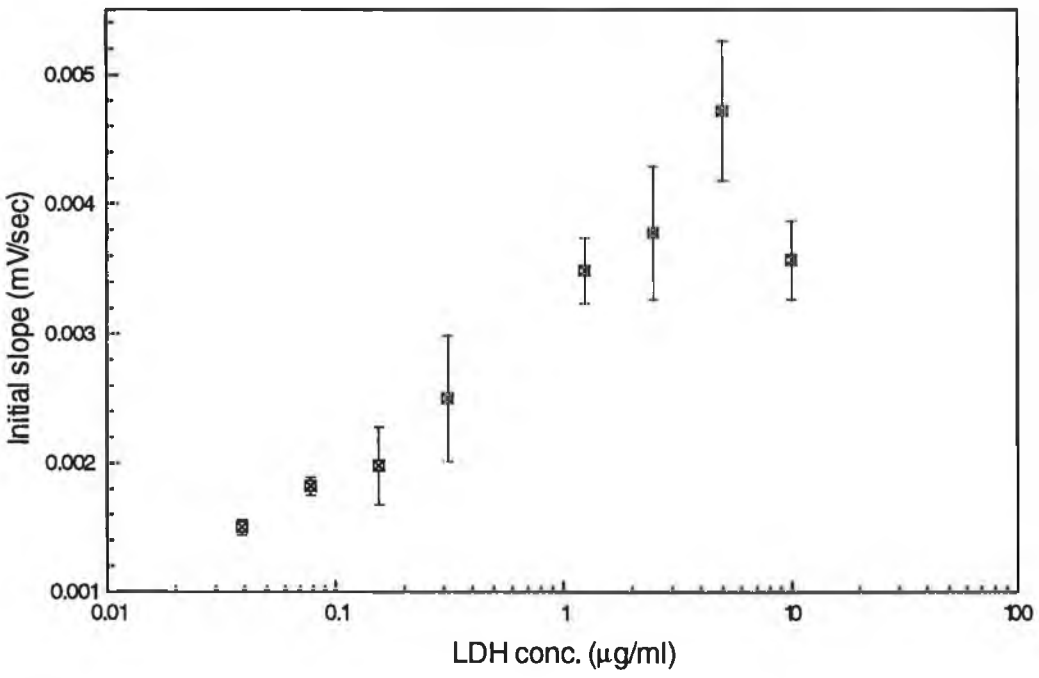

figure 8.8 One-step immunoassay

of the LDH/FITC anti-LDH complex to the capture antibody was monitored via the resulting fluorescence signal.

Figure 8.8 shows the initial slope obtained in the one-step evanescent wave immunoassay experiment for various LDH concentrations. The samples were again run in triplicate, and calculated standard deviations are depicted by the error bars. Sensor response again increases with concentration except for the high concentration of 10μg/ml. This departure from linearity may be explained by the fact, that at these high concentrations, there may not be enough fluorescently labelled antibody present in the system to bind to all the antigen, resulting in the decrease of fluorescence signal as observed. To overcome this problem a higher concentration of labelled antibody would be required in the assay.

Errors in this type of assay are often analysed in terms of coefficient of variance (CV). Most modern day assays performed in the laboratory would be expected to exhibit a maximum CV of 5% [11]. Both the one-step and two-step immunoassay experiments have an average CV of double this value ranging from 3% to 16% However, when considering the number of experimental variables present, these can be considered quite reasonable values. Sources of error include; i) alignment of fibre, ii) air bubbles in the flow chamber, iii) cleaning and polishing of fibres, iv) chemical immobilisation of capture antibody, v) contamination and degradation of biomolecule samples.

8.7 Conclusion

The use of silane with a heterobifunctional crosslinker was shown to be a successful method of immobilising antibodies on optical fibres for immunoassay development. Specific antibody-antigen binding was displayed, leading to a method of detection of the enzyme LDH. Evanescent wave excitation and collection of the fluorescence from the labelled antibody was carried out successfully, using the laser based optical system which has been described in chapter 6.

References

1. Wolfbeis O.S.: '**Fiber optic chemical sensors and biosensors**', Vol. 1, CRC Press, Boca Raton 1991

2. Wolfbeis O.S.: '**Fiber optic chemical sensors and biosensors**', Vol. 2, CRC Press, Boca Raton 1991

3. Wise D.L., Wingard L.B.(Eds.): '**Biosensors with fiberoptics**', Humana Press, Clifton NJ, 1991

4. Walczak I.M., Love W.F., Cook T.A., Slovacek R.E.: '**The application of evanescent wave sensing to a high-sensitivity fluoroimmunoassay**', Biosensors & Bioelectronics, Vol. 7, 1992, pp. 39-48

5. Shriver-Lake L.C., Ogert R.A., Ligler F.S.: '**A fiber-optic evanescent-wave immunosensor for large molecules**', Sensors & Actuators B, Vol. 11, 1993, pp. 239-243

6. Masuda K., Shigemori K., Sugimura M., Matano M.: '**Study of the sensitivity of evanescent wave immunoassay**', Book of Abstracts, Europt(r)ode II, 2nd European Conference on Optical Sensors and Biosensors, Florence, Italy, April 19-21, 1994

7. McCormack T., O'Kennedy R., O'Keeffe G., MacCraith B.D.: '**Evanescent wave fiber optic immunosensor for the determination of lactate dehydrogenase**', Biosensors '94, New Orleans, June 1-3, 1994

8. Bhatia S.K., Thompson R.B., Shriver-Lake L.C., Levine M., Ligler F.S.: '**Fiber optic-based immunosensors: A progress report**', Proc. SPIE Vol. 1054 - Fluorescence Detection III, 1989, pp. 184-190

9. Reynard Corporation, San Clemente, California, U.S.A., Optical components/Thin film coatings/Optical Instruements - Catalogue, 1992-93

10. Feldman S.F., Uzgiris E.E.: '**Determination of the kinetic response and absolute sensitivity of a fiber-optic immunoassay**', Proc. SPIE, Vol. 2068, Chemical, Biochemical and Environmental Sensors V, Boston, 1993, pp. 139-144

11. Personal Communication with Teresa McCormack, School of Biological Sciences, Dublin City University.

Chapter Nine - Conclusion

The work presented in this thesis describes the development of fibre optic oxygen sensors based on evanescent-wave excitation of ruthenium complexes which are encapsulated in thin microporous coatings fabricated by the sol-gel process. The sensing process is based on the quenching of fluorescence from ruthenium complexes. In the work described, Ru(II) tris(4,7-diphenyl-1, 10-phenanthroline) was chosen as the sensing species due to its particularly long unquenched lifetime of ~5μs and its strong absorption in the blue-green region of the spectrum.

The sol-gel process and the parameters that control the rates of the chemical reactions involved, were described. The choice of using the sol-gel method as an immobilization technique over other possible methods, has been primarily governed by the fact that the process is inherently simple to carry out, and that it offers the possibility of altering the physical nature of the final glass structure by varying the reaction parameters. However, some disadvantages of using the sol-gel immobilization technique were found to exist. These include the fact that there exists many variables in the production of such a glass substrate and that a complete knowledge of the chemical and physical processes involved is still evolving.

Parameters which require optimisation in the fabrication of fluorosensors, including dye concentration within the sol-gel layer, coating speed of optical fibre and length of sensing region were investigated. It was found that the fluorescence signal from a sol-gel coated fibre increases with concentration of ruthenium complex within the sol-gel coating, and that it reaches saturation at higher concentrations. It was also found that oxygen sensitivity of the optical fibre sensors increased with ruthenium complex concentration before reaching saturation. No substantial change in fluorescence signal or oxygen sensitivity was observed as a function of thin-film thickness. This was probably due to the fact that the thicknesses of the films examined were greater than the penetration depth of the evanescent wave. Both the fluorescence signal and oxygen sensitivity were found to increase with sol-gel coating length. The increase in oxygen sensitivity was attributed to the feed-through of the optical filter combination used in the measurement system. The optimisation of relevant optical parameters was also carried

out. The theoretical prediction of the coupling of fluorescence into the higher order modes was verified experimentally which may be used as means of achieving higher sensitivity.

Two methods of measurement which may be used with fluorosensors were studied. Firstly, the direct monitoring of fluorescence intensity and secondly, the monitoring of the phase shift between a sinuisoidally exciting signal and its resultant fluorescence signal (i.e. phase fluorimetry), were characterised. Both the degree of fluorescence quenching and the phase shift were shown to be dependent on the fluorescence lifetime of the fluorophore, and therefore on the oxygen concentration. However, the latter method was shown to be potentially more advantageous, due to the fewer number of variable parameters within such a measuring system. Phase fluorimetry as a method of real-time lifetime measurement was treated, both for a single exponential lifetime decay and the more realistic situation of a multi-exponential decay. This method of fluorescence lifetime sensing was applied to oxygen sensing. A fluorescence lifetime analysis of the sol-gel immobilised ruthenium complex was carried out, from which a good mathematical fit was achieved for a double exponential decay profile. The measured lifetime components were applied to predict a phase shift for the phase fluorimetry characterisation system. Good agreement between the predicted values and experimentally determined values was found. Alternative circuits for phase shift measurements, were also developed and were both shown to operate as accurately as commercially available phase angle measurement systems, and also to lend themselves to the construction of inexpensive, miniaturised fluorescence lifetime-based measurement systems. Sensor characterisation was initially performed using a laser excitation source with photomultiplier tube detection. However, these rather bulky and expensive components were later replaced with the recently available high intensity blue LEDs combined with photodiode detection.

The oxygen sensor exhibited high sensitivity to the presence of oxygen using a laser / photomultiplier tube fluorescence intensity characterisation system. The presence of 100% oxygen was shown to produce a decrease in fluorescence signal of about 75%, with highest sensitivity in the lower oxygen concentration region, as predicted by the Stern-Volmer equations. High sensitivity to oxygen (~27° phase shift at a modulation frequency of 48 kHz), good repeatability of signal, high SNR (~150 for 100% nitrogen)

and fast response times (<3 seconds) were also demonstrated for the same system, using the phase fluorimetric measurement technique. The all-solid-state (LED with photodiode) system was also shown to operate with good sensitivity to oxygen (~80% decrease in fluorescence signal in 100% oxygen), high signal repeatability, high SNR (~300 and ~200 for 100% nitrogen in the fluorescence intensity and phase fluorimetric systems, respectively) and fast response times (<3 seconds) both for a direct fluorescence intensity and a phase fluorimetric type measurement system. This is the first reported intrinsic phase fluorimetric all-solid-state sensing system. In the analysis, the frequency response of the system for both measurement configurations was examined and shown to have an optimum value of 5kHz and 45kHz for the fluorescence intensity and phase fluorimetric systems, respectively.

Sensor characterisation was performed in terms of susceptibility to temperature and relative humidity variation using the all-solid-state fluorescence intensity monitoring system. A number of temperature cycling tests was performed on the oxygen sensor. The results presented exhibit a lack of repeatability for both a 0°C - 70°C and a 10°C - 50°C temperature programme. However, more promising results were found for a temperature programme of 10°C - 40°C where good repeatability of fluorescence signal from the sensor was recorded with temperature variation. The sensor output as a function of relative humidity was also detailed. A decrease in fluorescence signal was recorded as the percentage relative humidity decreased. This was attributed to the formation of condensation within the sol-gel microstructure, resulting in the expulsion of air from the sol-gel environment and therefore a reduction in fluorescence signal. The sensitivity to oxygen as a function of relative humidity was not examined.

The main challenge in the possible future commercialisation of sol-gel based evanescent-wave oxygen sensors is in the production of ruthenium complex doped sol-gel films which are immune to temperature and relative humidity variation. As discussed in chapter seven, the unrepeatable nature of the variation of the sensor response with temperature, may possibly be due to the fact that the sol-gel films had not reached structural stabilisation at the time of measurement. Had the sensors responded in a repeatable manner to temperature variation, then the realisation of temperature compensation would be trivial, resulting in the ability to perform evanescent-wave oxygen sensing during variations in ambient temperature. The temperature and relative

humidity response of newly developed stabilised sol-gel films has yet to be investigated. Other possible future work which would be of interest may include the development of a distributed oxygen sensor, using the work described in this thesis as a basis. The development of sol-gel-derived oxygen planar waveguide sensors would also be of potential interest.

List of Publications & Conference Presentations:

Oral Presentations

i) Evanescent-Wave Sensors Based on Sol-gel Derived Porous Glass Coatings. *Irish Optoelectronics Group Conference*, Dublin, 23th - 24th April, 1992.

ii) LED Based Fibre Optic Oxygen Sensor using Sol-Gel Entrapped Dyes. *Sensors & their Applications VI*, Manchester, 12th - 15th September, 1993.

iii) Development of a LED Based Phase Fluorimetric Oxygen Sensor Using Evanescent Wave Excitation of a Sol-Gel Immobilised Dye. *2nd European Conference on Optical Chemical Sensors and Biosensors*, Florence, 19th - 21st April, 1994.

Poster Presentations

i) Evanescent Wave Fiber Optic Immunosensor for the Determination of Lactate Dehydrogenase in Serum Samples, *Biosensors '94*, New Orleans, June 1st - 3rd, 1994

ii) Development of an Intrinsic Phase Fluorimetric Oxygen Sensor using a High Intensity Blue LED. *10th Optical Fibre Sensors Conference*, Glasgow, 11th - 13th October, 1994.

Conference Publications

i) MacCraith B.D., McDonagh C.M., O'Keeffe D.G., Vos J.G., O'Kelly B., McGilp J.F.: 'Evanescent-Wave Oxygen Sensing using Sol-Gel Derived Porous Coating' *Proc.* SPIE Proceedings, Boston, 1992, Vol. 1796, pp. 167-175.

ii) MacCraith B.D., O'Keeffe D.G., McDonagh C.M.: 'Evanescent-Wave Fibre Optic Oxygen Sensors Based on LED-Excited Fluorescence in Sol-Gel-Derived Coatings'. *9th Optical Fibre Sensors Conference*, Post Deadline Paper, Florence, May 1993.

iii) O'Keeffe D.G., MacCraith B.D., McDonagh C.M.: 'LED Based Fibre Optic Oxygen Sensor Using Sol-gel Entrapped Dyes'. *Sensors VI, Technology, Systems and Applications*, IOP Publishing, 1993, pp. 75-78.

iv) MacCraith B.D., O'Keeffe D.G., McEvoy A.K., McDonagh C.M.: 'Development of a LED-Based Fibre Optic Sensor Using Sol-Gel-Derived Coatings', SPIE Proceedings, San Diego, Vol. 2293, *Chemical, Biochemical and Environmental Fibre Sensors VI*, 1994, pp. 110-120.

v) MacCraith B.D., McDonagh C.M., O'Keeffe D.G., McEvoy A.K., Butler T., Sheridan F.R.: 'Sol-Gel Coatings for Optical Chemical Sensors and Biosensors', SPIE Proceedings, San Diego, Vol. 2288, *Sol-Gel Optics III*, 1994, pp. 518-528.

vi) MacCraith B.D., McDonagh C.M., O'Keeffe D.G., McEvoy A.K., Butler T., O'Kelly B., McGilp J.F.: 'Fibre Optic Chemical Sensors based on Evanescent Wave Interactions in Sol-Gel-Derived Porous Coatings', *Journal of Sol-Gel Science & Technology*, Vol. 2, Nos. 1-3,1994, pp. 661-665.

Refereed Publications

i) MacCraith B.D., McDonagh C.M., O'Keeffe D.G., Keyes T.K., Vos J.G., O'Kelly B., McGilp J.F.: 'Fibre Optic Oxygen Sensor Based on Fluorescence Quenching of Evanescent-Wave Excited Ruthenium Complexes in Sol-gel Derived Coatings', *The Analyst*, 1993, Vol. 118, pp. 385-388.

ii) MacCraith B.D., O'Keeffe D.G., McDonagh C.M., McEvoy A.K.: 'LED-Based Fibre Optic Oxygen Sensor Using Sol-Gel Coating'. *Electronic Letters*, 1994, Vol. 30, 11, pp. 888-889.

iii) MacCraith B.D., O'Keeffe D.G., McEvoy A.K., McDonagh C.M., O'Kelly B., McGilp J.F., O'Mahony J.D., Cavanagh M.: 'LED-Based Oxygen Sensing using Evanescent Wave Excitation of a Dye-Doped Sol-Gel Coating'. *Optical Engineering*, 1994, Vol. 33, No. 12, pp. 3861-3866.

iv) O'Keeffe D.G., MacCraith B.D., McEvoy A.K., McDonagh C.M.: 'Development of a LED-Based Phase Fluorimetric Oxygen Sensor using Evanescent Wave Excitation of a Sol-Gel Immobilised Dye', *Sensors & Actuators*, To be published, 1995.

Appendix A :

Derivation of Phase shift formula.

This treatment is taken from Lakowicz, reference [41], chapter three. If the excitation of a fluorophore with an infinitely short pulse of light is considered, which results in an initial population, N_0, of fluorophores in the excited state. Then the rate of decay of the initially excited population is

$$\frac{dN(t)}{dt} = -(k_{nr} + k_r)N(t) \qquad A.1$$

where N(t) is the number of excited molecules at time t following excitation, k_r and k_{nr} are the radiative and non-radiative decay constants respectively. If the excitation of the sample fluorophore, is considered, with sinusoidally modulated light whose time-dependent intensity is

$$E(t) = a + b\sin\omega t \qquad A.2$$

The fluorescence emission is forced to respond with same frequency, but is phase shift and modulation will be different. It is assumed that

$$N(t) = A + B\sin(\omega t - \phi) \qquad A.3$$

The determination of the relationship between fluorescence lifetime and the phase shift (ϕ) and the modulation (m) may be carried out as follows. Under conditions of sinusoidal equation A.1 becomes

$$\frac{dN(t)}{dt} = -\frac{1}{\tau}\cdot N(t) + E(t) \qquad A.4$$

Substitution of equation A.3 into equation A.4 yields

$$\frac{dN(t)}{dt} = -\frac{1}{\tau}[A + B\sin(\omega t - \phi)] + a + b\sin\omega t \qquad A.5$$
$$= B\cos(\omega t - \phi)$$

Expansion of the sine and cosine functions, followed by equating the coefficients of $\sin\omega t$, $\cos\omega t$, and the constant terms, yields

$$a - \left(\frac{1}{\tau}\right)A = 0 \qquad A.6$$

$$\omega\cos\phi - \left(\frac{1}{\tau}\right)\sin\phi = 0 \qquad A.7$$

$$\omega\sin + \left(\frac{1}{\tau}\right)\cos\phi = b / B \qquad A.8$$

From equation A.7 one obtains the relation

$$\frac{\sin\phi}{\cos\phi} = \tan\phi = \omega\tau \qquad A.9$$

Squaring equations A.7 and A.8, followed by addition , yields

$$\left[\omega^2 + \left(\frac{1}{\tau}\right)^2\right] = \left(\frac{b}{B}\right)^2 \qquad A.10$$

Recalling from equation A.6 that $A = a\tau$, we obtain

$$m = \frac{B / A}{b / a} = [1 + \omega^2\tau^2]^{1/2} \qquad A.11$$

which is the usual relationship between lifetime and the demodulation factor.

Appendix B :

Specifications of Raman Holographic Edge Filter.

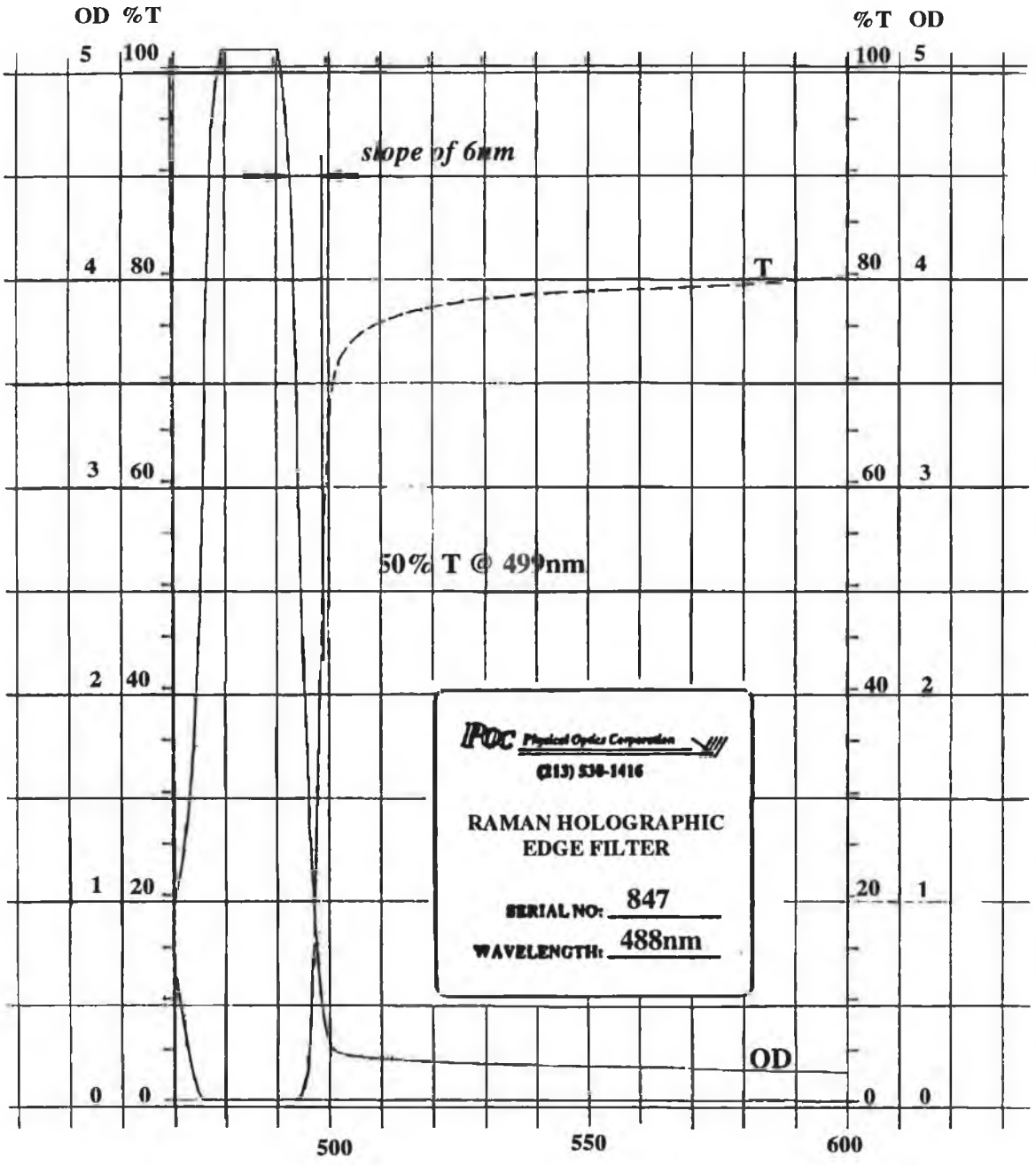

Appendix C :

Specifications of Wide Band Pass Filter.

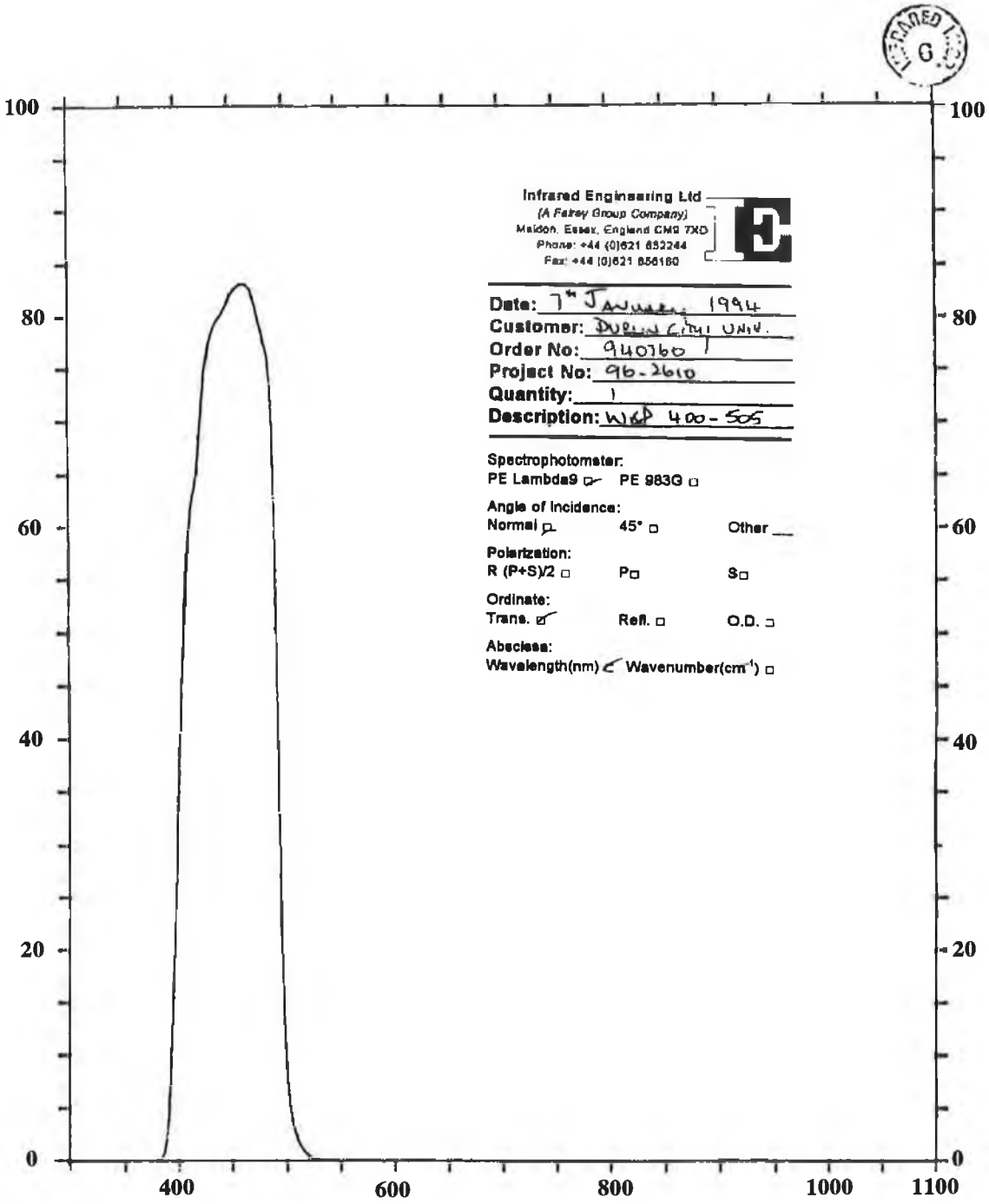

Appendix D :

Photograph of stand-alone LED/photodiode fluorescence intensity-based oxygen sensor.

Appendix E :

LED driver circuit design using AD654.

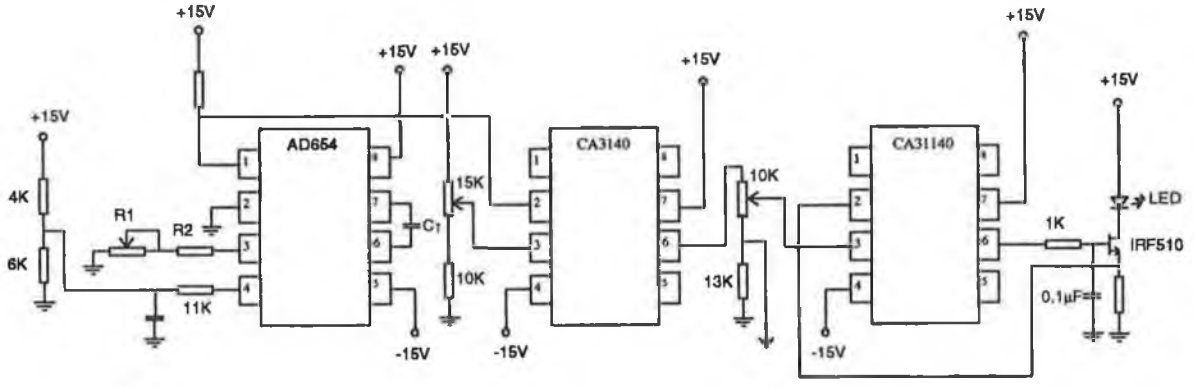

Appendix F :

AD630 based lock-in amplication circuit design.

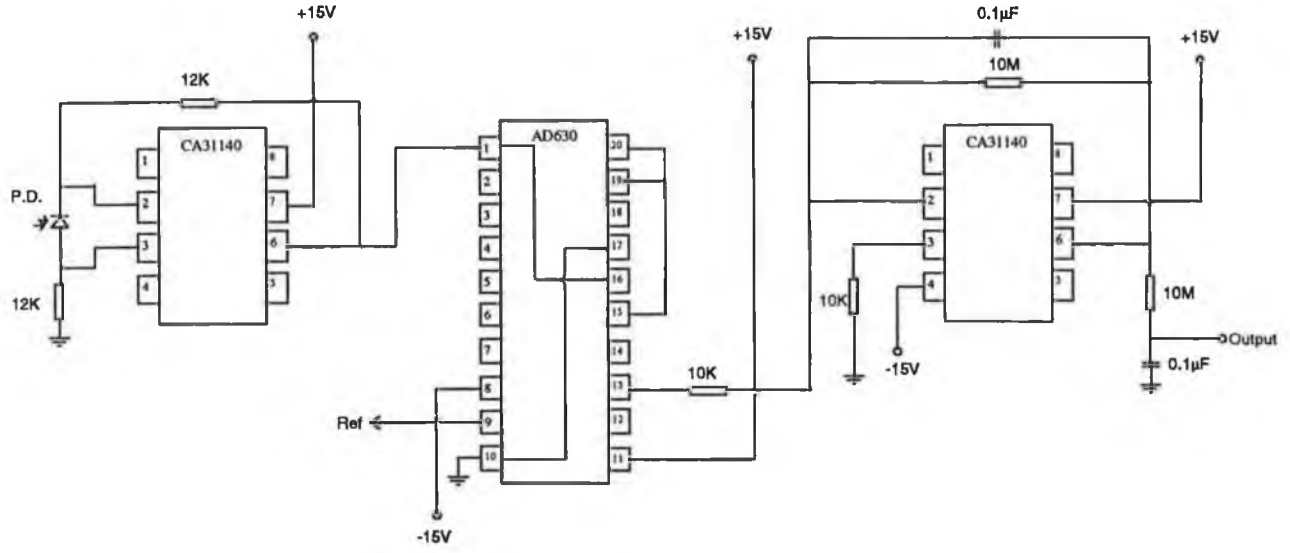

Appendix G :

Circuit design of phase locked detection of fluorescence system.